Phillips, Monifa Louise (2018) Spectroscopic investigation of resistive switching mechanisms in pulsed laser deposited metal-oxide thin films. PhD thesis.

https://theses.gla.ac.uk/38989/

Copyright and moral rights for this work are retained by the author

A copy can be downloaded for personal non-commercial research or study, without prior permission or charge

This work cannot be reproduced or quoted extensively from without first obtaining permission in writing from the author

The content must not be changed in any way or sold commercially in any format or medium without the formal permission of the author

When referring to this work, full bibliographic details including the author, title, awarding institution and date of the thesis must be given

Enlighten: Theses
https://theses.gla.ac.uk/
research-enlighten@glasgow.ac.uk

Spectroscopic Investigation of Resistive Switching Mechanisms in Pulsed Laser Deposited Metal-Oxide Thin Films

Monifa Louise Phillips

Submitted in fulfilment of the requirements for the Degree of Doctor of Philosophy

School of Physics & Astronomy
College of Science and Engineering
University of Glasgow

University of Glasgow

September 2018

Inspirational Pledge

I pledge my mind to positive thinking,

I aim to do my best at everything I do,

To respect and love myself,

To treat others as I expect to be treated,

These things I will do,

For myself, my family and my community.

- Student pledge written by the supplementary school director at the Claudia Jones Organisation, a charitable centre that supports and empowers women and families of African Caribbean heritage in London.

Abstract

Today, CMOS-compatible Flash memory technology dominates the non-volatile memory storage market due to high density and low fabrication costs. However, with CMOS approaching fundamental scaling limits, research into novel emerging non-volatile memory storage technologies that exploit materials properties including resistance, spin and polarisation, has significantly progressed. The ideal non-volatile memory technology would compete with Flash, offering high-density memory storage at low costs, however it would outperform Flash due to its faster operating speeds, lower energy requirements, greater endurance and greater potential for scaling. Of all the emerging technologies, resistive RAM (RRAM) elements, in which reproducible (switchable) and distinct high and low resistance states are the basis of memory storage, are considered most advantageous due to their superior potential for scaling, fastest exhibited operating speeds and extremely low energy requirements. Despite progress in the field of RRAM research, the underlying mechanisms that allow a device to switch between high and low resistance states remains unclear in many materials systems and is the key motivation behind this work. Here, Pulsed Laser Deposited (PLD) RRAM devices that incorporate resistive switching transition metal oxide thin films were studied using Electron Energy Loss Spectroscopy (EELS). Basic metal/oxide/metal RRAM heterostructures that incorporated strongly oxidising titanium electrodes and polycrystalline ZnO and manganese-doped ZnO were investigated in Chapter 3. These devices were designed for direct comparison to a device in presented the literature which displayed the simultaneous co-switching of resistance and magnetisation states. In the devices fabricated here, EELS analysis revealed Mn-phase segregation both at grain boundaries both above and below the

top and bottom electrodes, which supported the proposed co-switching mechanism. In Chapter 4, epitaxial single crystal perovskite oxide $Pr_{0.48}Ca_{0.52}MnO_3$ was incorporated into a novel metal/oxide/tunnel-oxide/metal RRAM structure, where the thickness of the interfacial Yttria-stabilised Zirconia tunnel oxide varied the output current density. In both the ZnO and $Pr_{0.48}Ca_{0.52}MnO_3$ devices, EELS analysis revealed that the observed resistive switching was mediated by the field-induced exchange of oxygen vacancies between the bulk oxide and an interfacial oxide. Despite this similarity, the overall device resistance was governed by different effects: for the polycrystalline ZnO-based devices, this was the oxygen-vacancy induced formation and dissolution of a highly resistive TiO_2 interfacial layer; in contrast, for the epitaxial $Pr_{0.48}Ca_{0.52}MnO_3$ device, this was the oxygen-vacancy induced charge accumulation and dissipation in the tunnel oxide, which modulated the tunnel barrier height.

Declaration

This thesis is a record of the work carried out by myself in the Materials and Condensed Matter Physics group based in the School of Physics and Astronomy at the University of Glasgow during the period 2014-2018 under the supervision of Dr. Donald MacLaren. The work described herein is my own, with the exception of the LabView code that runs the probe station, which was developed by Dr. Gary Paterson, and the STEM-EELS data acquisition, which was acquired by Dr. Donald MacLaren.

Some of the work presented in Chapter 4 can be found in the following paper:

- B. Arndt, F. Borgatti, F. Offi, M. Phillips, P. Parreira, T. Meiners, S. Menzel, K. Skaja, G. Panaccione, D. A. MacLaren, R. Waser, R. Dittmann, *"Spectroscopic Indications of Tunnel Barrier Charging as the Switching Mechanism in Memristive Devices"*. Adv. Funct. Mater. 2017, 27, 1702282.

An award winning oral presentation of the work presented in Chapter 4 was delivered at the following international conference:

- Microscience Microscopy Congress – Manchester, UK – July 2017

Contents

Abstract iii

Declaration v

Contents vii

List of Figures xi

List of Tables xxix

1 Introduction 1

1.1 Principles of Memory Storage 1

1.1.1 Emerging Non-Volatile Memories 5

1.2 Resistive Switching 10

1.2.1 Memristor Theory 10

1.2.2 Resistive Switching Mechanisms 11

1.2.3 Electrochemical Memory 12

1.2.4 Thermochemical Memory 16

1.2.5 Valence Change Memory 18

1.2.6 Interfacial oxides for Valence Change Memory 24

1.3 Scope of Research 26

1.3.1 Thesis Outline 28
Bibliography 29

2 Instrumentation 35

2.1 Physical Vapour Deposition 36
2.2 Pulsed Laser Deposition 36
2.2.1 Laser-Matter Interaction 39
2.3 Metallisation 41
2.3.1 Photolithography 41
2.3.2 Electron-beam Evaporation 43
2.4 Focused Ion Beam Lamella Fabrication 44
2.5 Transmission Electron Microscopy 48
2.5.1 Inelastic and Elastic Scattering 49
2.5.2 Diffraction 51
2.5.3 Electron Sources 53
2.5.4 Electromagnetic Lenses 54
2.6 Electron Optical System 57
2.6.1 Bright-Field and Dark-Field Imaging 59
2.6.2 Scanning Transmission Electron Microscopy 60
2.7 Electron Energy Loss Spectroscopy 62
2.7.1 Electron Energy Loss Spectrum 62
2.7.2 Basic EELS Processing Steps 66
2.7.3 Elemental Ratio Normalisation 67
2.7.4 Deconvolution 72
2.7.5 Principle Component Analysis 72
2.7.6 Multiple Linear Least-Squares Fitting 73
2.7.7 Electron Energy Loss Magnetic Spectrometer 74
2.8 Hard X-Ray Photoelectron Spectroscopy 76
2.9 Atomic Force Microscopy 77
2.10 Electrical Probe Station 80
Bibliography 82

3 Polycrystalline Manganese-Doped Zinc Oxide RRAM Device 89

3.1 Properties of Zinc Oxide 90

3.2 Resistive Switching in Zinc Oxide 93

3.2.1 Simultaneous Magnetisation- and Resistive-Switching in Mn:ZnO 95

3.3 Principles of Thin Film Growth 96

3.4 Thin Film Considerations for Zinc Oxide RRAM 101

3.5 Zinc Oxide and Manganese-doped Zinc Oxide RRAM 104

3.5.1 RRAM Heterostructure Fabrication 105

3.5.2 AFM Analysis 107

3.5.3 Electrical Characterisation 110

3.5.4 Electron Microscopy Characterisation 122

3.5.5 TEM-EELS Analysis 126

3.6 Conclusion 139

Bibliography 143

4 Crystalline $Pr_{0.48}Ca_{0.52}MnO_3$ Tunnel Oxide RRAM device 157

4.1 Resistive Switching in Crystalline Perovskite Oxides 158

4.1.1 Resistive Switching in Crystalline $Pr_{1-x}Ca_xMnO_3$ 160

4.2 Crystalline Tunnel Oxide $Pr_{0.48}Ca_{0.52}MnO_3$ RRAM 163

4.3 Electrical Characterisation 165

4.4 STEM-EELS Analysis 169

4.4.1 Static Device Characteristics 171

4.4.2 Comparison of HRS and LRS 180

4.5 HAXPES Analysis 187

4.6 Conclusion 190

Bibliography 194

5 Summary and Outlook 201

Bibliography 206

List of Figures

1.1 *Computer memory hierarchy. Here, cache processing requires memory technologies with extremely fast operating speeds, which have only been achieved by low density, high speed, (SSD) SRAM. Main memory has lower speed requirements than Cache, and currently employs (SSD) DRAM. In contrast to computational memory, storage technologies must be non-volatile, and have the lowest operating speed and highest storage density requirements. The most widely used storage technologies are (SSD) Flash and HDD.* 2

1.2 *(a) Labelled cross-section of a Flash memory cell and (b)-(d) its working principles. (b) A voltage applied across the source and drain electrodes forms a conduction channel. Charge carriers are represented by yellow circles. (c) Write process where a positive control gate voltage stimulates the tunnelling of charged carriers into the floating gate; due to the surrounding insulator layers, the charges becomes trapped. (d) Erase process in which the control gate is grounded and the substrate is positively biased. This stimulates the tunnelling of charge carriers back into the conduction channel.* 4

1.3 *(a) Cross-section of a FeRAM cell. (b) Evolution of the polarisation resolution as a function of the voltage applied across the top and bottom electrodes. Parallel arrows indicate the polarisation saturation of the ferroelectric active layer where distinct positive and negative saturation states are achieved at positive and negative bias respectively.* 6

1.4 *(a) Cross-section of an MRAM cell. (b) Evolution of the magnetoresistance response to the voltage applied across the top and bottom electrodes. Whilst the pinned layer remains saturated in one direction, the ferromagnetic active layer can be saturated to the same or opposite direction, which affects the magnetoresistance.* 7

1.5 *(a) Cross-section of a PRAM cell. (b) During the set process, a short pulse length at high temperatures is sufficient to trigger a transition to the amorphous phase. In contrast, during the erase process long pulses at low temperatures stimulates a transition to the crystalline phase.* . . 7

1.6 *(a) Cross-section of a Metal-Insulator-Metal RRAM cell. (b) Evolution of the resistance state as a function of the voltage applied across the top and bottom electrodes. Here, the Low Resistance State (LRS) and the High Resistance State (HRS) are highlighted by a dashed line.* . . . 8

1.7 *Example of a simplified 3D RRAM Crossbar array. Here, individual RRAM cells can be accessed by isolating specific top and bottom electrode intersections.* 9

1.8 *Two basic modes of resistive switching in which the LRS and HRS are shown in green and red respectively, and the switching process is shown in grey. The SET and RESET voltages highlighted in both images, and the compliance current, used to prevent damage, is shown as a green dashed line. (a) illustrates bipolar RS, and (b) illustrates unipolar RS. Adapted from [5].* 12

1.9 *IV curve obtained from an ECM cell in the four key stages of RS are illustrated in four device cross-sections presented in insets (a)(b)(c) and (d). In (a), a positively biased active electrode induces M^+-migration in the direction shown by the curved white arrows, where M^+ cations are represented by blue circles. In (b), the active electrode has reached a voltage sufficient to SET the device to the LRS which corresponds to the formation of a conductive M^+ filament. In (c), a sufficient negative voltage has induced M^+-migration in the direction indicated by the white arrows, rupturing the filament. Image (d) represents the final HRS reached after the full dissolution of the filament. Adapted from [5].* . . . 13

1.10 *RS reproducibility map depicting the dependence of reproducible RS on applied voltage.* . . . 15

1.11 *(a)-(c) Stages of RS that occur in Joule-heat-dissolution TCM; each image corresponds to a different point in the unipolar IV curve, which has been separated into a SET voltage sweep and a RESET voltage sweep for clarity. The red region in (a) illustrates the hot conduction channel formed as a result of the thermoelectric breakdown of the insulator material, which is shown in pink. This causes oxygen anions to migrate out of the hot channel in the direction indicated by the black arrows, and leaves behind chemically reduced insulator material, which is shown in dark blue. (b) Formation of a conductive filament. (c) Localised dissolution hotspot that ruptures the filament, resetting the device.* . . . 16

1.12 *'Faucet' model for unipolar TCM showing (a) the HRS and (b) the LRS. Here, switching is governed by a highly resistive 'faucet' region at the interface, which is shown here in dark red. Conductive regions consistent of reduced, non-stoichiometric oxide are shown here in white. In both states, multiple filaments bridge the top and bottom inert electrodes, but the 'faucet' governs the overall resistance state of the device.* . . . 18

1.13 *(a) Electroforming process of a n-type oxide material and (b)(c) filamentary-VCM RS in a MOM heterostructure. This process is governed by the electromigration of $V_{\ddot{O}}$, which are shown in white, and move in the direction of the white arrows. (a) During electroforming, the migration of $V_{\ddot{O}}$ towards the anode forms a 'virtual cathode'. Within the vicinity of the anode, highlighted by the black dashed box in (a), filamentary RS occurs and is shown in (b) and (c). (b) shows the LRS in which $V_{\ddot{O}}$ migrate towards the anode (top electrode) and form a complete conductive path. At opposite polarity, (b) shows the HRS in which the $V_{\ddot{O}}$-filament is ruptured due to the migration of $V_{\ddot{O}}$ towards the cathode (anode electrode). $V_{\ddot{O}}$-migration occurs in the direction opposite to O^{2-}-migration, which is shown in brown.* 19

1.14 *RS in a Schottky contact/oxide/Ohmic contact MOM heterostructure in which an n-type oxide is employed. RS is depicted in terms of (a)(b) interface-VCM and (c)(d) Schottky barrier modulation. (a) and (c) represent the LRS in which $V_{\ddot{O}}$ -migration towards the anode leads to the accumulation of $V_{\ddot{O}}$ at the interface. This leads to the formation of an oxygen-rich region, which is shown here in dark red, and the reduction of the depletion width W_d of the Schottky Barrier, which promotes tunnelling. (b) and (d) represent the HRS at opposite polarity; here, $V_{\ddot{O}}$-migration in the opposite direction leads to a reduction in the number of $V_{\ddot{O}}$ at the Schottky interface and an increase in W_d which prevents tunnelling.* 21

1.15 *Example of a bipolar, interface resistive switching IV curve where the LRS is highlighted in green and the HRS is highlighted in red. As current increases gradually, compliance currents are not always employed.* . . . 22

1.16 *'Reverse' valence change memory in an n-type MOM cell. $V_{\ddot{O}}$-rich regions are shown in white, and O_2-rich regions are shown in dark red. (a) LRS of an interface-VCM RS device where the Schottky interface is located below the active electrode. This is the same set-up shown in Fig.1.14(a) and is included for comparison. (b) HRS of reverse-interface-VCM RS device, which is achieved at the same polarity as (a), but at a larger voltage magnitude. This increased voltage further depletes the of an oxygen-rich ($V_{\ddot{O}}$-deficient) region at the inert electrode, forming a second Schottky interface that dictates the RS state of the device.* . . 23

1.17 *(a) Redox-formed CrO_x interfacial oxide formed in a Cr/ZnO/Pt device discussed in [35]. Here, the oxidation of the Cr electrode causes a reduction of the nearby ZnO film, forming a ZnO_{1-x} layer. (b) Dedicated functional oxide that was deposited during fabrication.* 25

2.1 *Schematic diagram of a UHV vacuum that accommodates pulsed laser and magnetron sputtering deposition systems. Laser pulses are guided into the deposition chamber through a window and onto a target that is held on a motorised target carousel system; the purple arrows represent possible motion. The substrate is also attached to a motorised holder which can be resistively heated and can move in the directions represented by the red arrows. A turbo-molecular vacuum pump was used to evacuate the chamber via the outlet highlighted by the green arrows, and a mass flow controller was used to control gas flow into the deposition chamber through the gas inlet highlighted by the single blue arrow.* 38

2.2 *The four stages of laser-matter interaction during the ablation of a PLD target. At high laser fluence, the interaction passes through stages (a),(b),(c),(d) and (e) consecutively, whereas at low laser fluence, stage (f) follows stage (b). Stages (a) and (b) depict the melting and subsequent vaporisation of the target, which at high-fluence is followed by the creation of a plume of ejected material, partly thermally ionised. This is followed by stages (d) and (e) where the plume becomes increasingly ionised due to shock wave collisional ionisation and further laser irradiation. In contrast, at low-fluence, the vaporisation stage is followed by the re-solidification of melted material, as shown in (f).* . . 40

2.3 *Steps required for photolithography after photoresist spinning are shown in images (a)-(c), where (a) depicts the use of a mask to prevent/allow UV exposure on specific regions of the photoresist, (b) illustrates structural changes in the photoresist as a result of photo-irradiation, and (c) shows the remaining patterned photoresist after the dissolution of the exposed photoresist. Images (d) and (e) depict the final metallisation steps described in Section 2.3.2; (d) shows the deposition of metal onto the patterned photoresist, and (e) shows the final metallised pattern obtained after agitation in acetone.* 42

2.4 *SEM image of e-beam evaporated Ti/Pt top electrode contacts deposited after photolithographic patterning. Top electrode contacts had diameters 10µm, 20µm, 50µm, 100µm, 200µm, and 300µm* 43

2.5 *Diagram showing vertical ion-beam column used in the FIB-SEM DualBeam instrument. A liquid metal ion source is shown in yellow and sits at the top of the column. Ga^{+} ions are accelerated and focused along the ion column through the use of an extraction electrode (shown in blue) and a series of electrostatic lenses and scanning coils. Beam blanking plates (shown in red) enable the user to obstruct the beam as required.* 45

2.6 *SEM and ion beam images of the FIB lamella preparation process utilised in this work. (a) a low magnification SEM image that shows a number of patterned top electrodes and the gas injector inserted just above the bulk sample surface. (b) an ion beam image showing a protective layer of Pt situated between two alignment cross-shaped features. (c) and (d) were acquired at the same point during the lamella preparation process;(c) was acquired from directly above the trench, whereas (d) was acquired with the sample tilted. (e) and (f) were acquired at a later point in the lamella preparation process and show the lamella, thinned to electron transparency; with respect to (e), (f) was acquired at rotation 90° and shows a top-down view of (e), as indicated by the orange arrow in (e).* 47

2.7 *Diagram showing (a) elastic and (b) inelastic electron-scattering. (a) Forward- and backward-scattering are shown by the blue and green e-beam trajectories respectively. The production of characteristic X-rays (purple wavy arrow) and Auger electrons (brown arrow) are shown in (b), where the (dashed)solid arrows represent the (de-)excitation of an inner shell electron.* 50

2.8 *Diagram showing electron-matter interaction and the generation of secondary signals. Electrons that pass through the sample un-deviated are referred to collectively as the direct beam.* 51

2.9 *Diagram showing elastic Bragg scattering (diffraction). Here the path difference between the incident and scattered waves is given by $AB + BC = 2dsin\theta$, and constructive interference is observed when the path difference is equal to an integer multiple of the electron wavelength, as described in Eqn. 2.2.* 52

2.10 *(a) Cross-section of a magnetic lens where copper coils are shown in yellow, and are enclosed within a case that can be water cooled via a water inlet and outlet. Upper and lower pole-pieces are shown in light green, and generate a* **B***-field perpendicular to the optic axis when current is supplied to the copper coils. Electron rays paths, depicting lens focusing, are shown in blue. (b) shows how electrons travelling along the optic axis are subject to helical motion under the applied* **B***-field.* 54

2.11 *Electromagnetic lens ray diagram, where electron rays are depicted as dark blue line. Principal planes are highlighted; the object, back focal, lens, and image planes are represented by green, black, yellow, and light blue dashed lines respectively. Deflected e-beams converge in the image plane at the lens focal length.* 55

2.12 *Schematic diagram showing magnetic optical system set up in CTEM mode for an aberration-corrected microscope.* 57

2.13 *Schematic diagram showing upper-objective condenser system set up for (a) broad beam and (b) probe illumination in CTEM mode.* 58

2.14 *Schematic diagram showing objective aperture set up for (a) BF and (b) DF imaging. Here the black(red) rays represent the direct(scattered) beam.* 59

2.15 *Magnetic optical system set up for STEM-EELS. In this set-up, a magnetic prism spectrometer is inserted below the viewing screen to enable the analysis of electron energies.* 61

2.16 *Spectral image (SI) data cube in which an EELS spectrum is acquired for each pixel in a scan across x and y.* 62

2.17 *STEM-EELS spectrum obtained on the TEM showing (a) low-loss and (b) high-loss data acquired simultaneously from PrCaMnO3. The low-loss spectrum comprises the ZLP and plasmon peaks and the high-loss spectrum comprises core-loss edges. In (b), oxygen and manganese core-loss edges are shown.* 63

2.18 *Normalisation process used for the quantification of EELS data included in the analysis of the tunnel RRAM device to be discussed further in Chapter 4. 2D maps, with pixel size 0.19nm^2, showing (a) Raw O K-edge intensity (b) ZLP intensity (c) $\frac{t}{\lambda}$ and (d) O K-edge intensity normalised via Eqn.2.11. The spatial distribution of (b) and (c) are shown in (e) and (f) respectively. (g) A comparison between the spatial distribution of the raw and normalised O-k edge intensity. Red vertical dashed lines highlight the interfaces between functional layers within the tunnel RRAM heterostructure.* 69

2.19 *Schematic diagram of MLLS fitting technique. (a) background-subtracted core-loss spectrum which features two overlapping core-loss edges*. (b) two separate reference spectra (S_A and S_B) that contribute to the recorded spectrum shown in (a); these references are recorded at the same energy offset and dispersion as (a). (c) resultant MLLS fit made using reference spectra shown in (b). 74

2.20 *Gatan Image Filter magnetic spectrometer employed for spectroscopic analysis of electron energy losses. Electrons with energy E_0 and $E_0 - E$ are represented by the solid and dashed blue lines respectively. A magnetic field* **B** *is applied across an electrically isolated drift tube, perpendicular to the trajectory of electrons, which causes a change in radius of curvature. Electrons with distinct energy loss are focused at points* **P** *and* **P'** *in the spectrometer dispersion plane. An aperture slit is used to select specific energy losses for imaging at the CCD detector.* 75

2.21 *Diagram showing X-ray Photoelectron Spectroscopy apparatus in which photoelectrons (represented by black curved arrows) are generated as a result of sample (shown in orange) irradiation by monochromatic X-rays (represented by green wavey arrow). These X-ray photoelectrons are accelerated through, and focused by a series of electrostatic lenses (represented by electron optics column shown in grey) before reaching the hemispherical electron analyser via an aperture slit. Within the analyser, an electric field is applied across the outer and inner hemispherical components (shown in yellow) such that the photoelectrons are deflected by 180°, and photoelectrons with different kinetic energies are separated.* 76

2.22 *An Atomic Force Microscope set up in which the cantilever-mounted tip, shown in black, scans a rough sample surface, shown in orange, and is deflected as a result. Cantilever deflection is measured using a quandrant photodiode detector that records a laser signal reflected from the cantilever. A computer interface can used to control the contact-mode of the AFM through a feedback loop, and the sample stage and tip can be moved in x- and y-directions.* 77

2.23 *5µm by 5µm AFM (a) height and (b) phase images of double-terminated* $SrTiO_3$ *vicinal surface after substrate processing. (a) A vicinal surface in which the left hand side of the image is higher with respect to the right, and each step edge is followed by a trough with height difference equal to* $\frac{1}{2}$*u.c. (b) These troughs correspond to a change in phase, and the relative phase difference is consistent with exposure of SrO in the troughs, and* TiO_2 *on the step surfaces. These images were acquired simultaneously over the same area in tapping mode* 79

2.24 *Electrical characterisation set-up used for (a) Van der Pauw and (b) RRAM device measurements. Corner electrodes are shown in peach, and patterened electrodes are shown in lilac.* 81

3.1 *(a) cubic rocksalt (b) cubic zinc blende and (c) hexagonal wurzite ZnO structures. The blue and red spheres represent Zn and O atoms respectively.* 90

3.2 *Structural zone model adapted from [57] that depicts the dependence of thin film morphology on substrate temperature.* 97

3.3 *ZnO RRAM device heterostructures: Si/SiO_x/Ti/Pt/ZnO/Ti/Pt.* . . . 105

3.4 *AFM images acquired over 1μm$\times$1μm for 100nm of polycrystalline ZnO deposited at P_{O_2} =100mTorr (a) room temperature (b) T_s =400K (c) T_s =490K (d) T_s =630K and (e) T_s =850K are presented. Rms average variation over substrate temperature is displayed in (f).* 107

3.5 *IV curves acquired from ZnO RRAM deposited at P_{O_2} =100mTorr and $T_s = 490K$. The colour scale, which runs from blue to red, indicates the direction of the voltage cycle in each plot. (a) Initial stable RS state. (b) Electroforming cycle. Representative RS IV curve produced after electrofoming plotted on a (c) linear and (d) semilog scale where cc=+2mA. Linear fitting of (d) is shown for the (e) SET and (f) RESET transitions, which are plotted on a double logarithmic scale for an assessment of $I \propto V^n$. Slope values next to the data present the value of the gradient for each linear fit (n).* 112

3.6 *IV curves obtained from Mn:ZnO RRAM devices in which the Mn:ZnO film was deposited at $P_{O_2} = 100mTorr$ and $T_s = 630K$. (a) Electroforming RESET transition. (b)(c) Reproducible bipolar IV curve exhibited post-electroforming. (b) is replotted in (c) on a semilog scale. (d) (e) Comparison of the representative bipolar IV curves obtained for ZnO and Mn:ZnO.* 116

3.7 *Reproducible electroformed IV curves acquired from (a) undoped ZnO and (b) Mn:ZnO devices. In both, the colour scaled dataset represents the initial cycle. The black dataset represents the (a) 30th (b) 60th cycle.* 118

3.8 *Diagrams showing the interfacial oxide thickness modulation and $V_{\ddot{O}}$ migration expected for the (a) HRS and (b) LRS states in the undoped and Mn-doped devices. $V_{\ddot{O}}$ are shown in white and black and white arrows beside (a) and (b) show the direction of electromigration for O^{2-} and $V_{\ddot{O}}$ respectively.* 121

3.9 *Diffraction patterns acquired from (a) P_{O_2} =100mTorr and (b) P_{O_2} =10mTorr devices, both pulsed laser deposited at $T_s = 490K$. In both images, the central bright spot is blocked to prevent saturation damage. In addition the yellow ring in both images highlights the diffraction spots that contributed to the hollow-cone diffraction images presented in Fig.3.10. (c) Radial distribution plot showing the average intensity of diffracted spots within each concentric ring as a function of radial distance from the central spot. Each peak is indexed and colour co-ordinated with the device heterostructure shown in the inset, which includes top electrode (TE) Pt and Au caps, the redox-formed interfacial TiO_x layer, and the adhesive Ti layer required for the Pt bottom electrode (BE). The miller indices used correspond to ZnO P63mc, Ti P63mc, TiO_2 Pbcn, Pt Fm3m, and Au Fm3m structures.* 123

3.10 *BF and DF images acquired from the (a)-(b) RS P_{O_2} =100mTorr and the (c)-(d) ohmic P_{O_2} =10mTorr undoped ZnO devices deposited at T_s =490K and the (e)-(h) RS P_{O_2} =100mTorr Mn:ZnO device deposited at $T_s = 630K$. In the DF images, yellow dashed lines are used to highlight grain boundaries for clarity.* 125

3.11 *EELS analysis of a pristine undoped ZnO RRAM device. (a) HAADF image where the EELS acquisition area is shown in red. (b) RGB composite signal map where Ti, O and Zn are shown in green, blue and red respectively. (c) Elemental map showing the spatial distribution profiles of the Ti, O and Zn signals, where a TiO_x interfacial oxide layer is highlighted with a black arrow. Black, white, yellow and pink boxes indicate regions from which reference spectra for MLLS fitting were acquired and correspond to the substrate adhesion layer, bulk ZnO, interfacial TiO_x and the contaminated top electrode respectively. (d) MLLS fitting reference spectra used to produce (e) an MLLS fit map. Here, the white dashed box shows the region used to produce (f) a normalised spatial distribution profiles of MLLS fit.* 127

3.12 *Low-magnification images of lamella extracted from (a) a pristine and (b) a programmed Mn:ZnO device. Damage to the Pt/Au top electrode cap did not appear to damage the Mn:ZnO RS layer.* 130

3.13 *EELS analysis of pristine and programmed Mn:ZnO devices. (a) HAADF overview map. Signal maps acquired from pristine devices showing (b) O, (c) Zn, (d) Ti, (e) Mn and (f) EDX-Pt signals. Blue and orange arrows are used to highlight the vertical and horizontal clustering of Ti and Mn. (g) Colour composite map of (b)-(f) where O, Zn, Ti and Mn are shown in white, red, blue and green respectively. (h) Elemental-ratio-normalised distribution profiles acquired from a programmed devices where O, Zn and Mn are shown in red, blue and black respectively. In both, the Ti line profile (green dashed line) was scaled up to evaluate Ti and O spatial overlap. (i) Comparison of EELS spectra acquired from highlighted regions in (g): the top electrode (shown in black), the adjacent interfacial* TiO_x *phase (shown in red), the substrate adhesion layer (shown in orange) and the* $Ti_xMn_yO_z$ *phase (shown in blue). Inset shows Ti-*$L_{3,2}$ *peaks. (j) Comparison of Mn-*$L_{3,2}$ *peaks acquired from the bulk Mn:ZnO (shown in green) and* $Ti_xMn_yO_z$ *(shown in blue).* . . . 132

3.14 *(a) Deconvolved spectra used to MLLS fit the data. Colour composites of the signal intensity maps associated with each phase presented in (a) is presented in (b), (d) and (f), which represent pristine, programmed (acquired from region A) and programmed (acquired from region B) respectively. The white boxes in (b), (d) and (f) highlight regions used to acquire the spatial distribution of each MLLS fit across device along the growth axis; these results are shown in (c), (e) and (g). In all subfigures, the Ti/Pt bottom electrode, bulk Mn:ZnO, TiMnO phase and TiO phase are shown in yellow, green, blue and red respectively.* . . . 136

3.15 *Comparison of elemental ratio normalised distribution of Mn (averaged over the entire width of each EELS dataset) previously shown in Fig.3.13(g).* 138

3.16 *Proposed mechanism of RS in Mn:ZnO device where $V_{\ddot{O}}$ and Mn^{2+} are represented by white and black circles respectively. (a) Pristine device that displays Mn- and $V_{\ddot{O}}$- clustering along growth-axis-aligned grain boundaries. (b) and (c) represent different regions (separated spatially) along the sample where (b) depicts a mid-point (or transition state) between (a) and (c), emphasising spatial inhomogeneity of redox activity at the electrode interfaces.* 140

4.1 *Diagram of an $Pr_xCa_{1-x}MnO_3$ perovskite oxide cubic cell. Here, Pr^{3+} and Ca^{2+} cations are shown in green, Mn cations are shown in red, and oxygen anions are shown in blue. Pr and Ca cations form the ionic lattice, which is represented by the black lines.* 158

4.2 *PCMO tunnel-RRAM device with heterostructure: Rh(3nm)/YSZ(2.8nm)/PCMO(20nm)/$SrRuO_3$ During electrical characterisation, the bottom electrode, SRO, was grounded.* 164

4.3 *Quasi-static I-V curves showing the 1st and 3rd RS cycles (represented by solid and hollow circles respectively) acquired from a bulk Rh/YSZ/PCMO/SRO device across voltage range $\pm 3V$. The same data are plotted in (a) and (b) which use linear and semi-log scales respectively. Here, the colour scale runs from blue→green→yellow→red in the direction of the source voltage to allow an assessment of RS polarity. The inset clarifies the device heterostructure (shown in Fig.4.2) and identifies the source (Rh, top electrode) and ground electrodes respectively (SRO, bottom electrode).* 165

4.4 *Scaling characteristics of bulk Rh/YSZ/PCMO/SRO device. Here the HRS (shown in red), LRS (shown in blue) and PS (shown in black) are shown as a function of (a) device area on a log-log scale and (b) YSZ tunnel oxide thickness on a semi-log scale. Image adapted from [30].* . 167

4.5 *(a) measured IV curves acquired for tunnel oxide thicknesses 20Å, 24Å, 28Å (blue lines) across $\pm 3V$ voltage sweeps, and compares them to polaron hopping (green line). Image adapted from [30].* 168

4.6 *Retention of HRS and LRS measured over 33 hours. Resistance values were obtained using 250μs READ pulses at $V_{READ} = -0.7V$ after programming using 1ms pulses at $V_{SET} = +2V$, $V_{RESET} = -3V$. Image adapted from [30].* . . . 169

4.7 *DF image of the tunnel-oxide PCMO RRAM device with (inset) Fast Fourier Transform. A protective Pt capping layer was deposited during lamella preparation prior to STEM.* . . . 171

4.8 *(a) Pr, (b) Mn and (c) O background-subtracted core-loss edges extracted from the bulk PCMO. (d) Pr (orange), (e) Mn (blue) and (f) O (purple) signal maps were generated by integrating under the core loss edge and plotting the integrated intensity for each x, y pixel (0.095nm^2) with the EELS-SI (EELS datacube). (g) normalised distribution of elements across the RRAM heterostructure, where vertical grey dashed lines are used to highlight interfacial regions and the horizontal green dashed lines represent the expected oxygen intensity, according to Eqn.2.11. (h) evolution of oxygen across the oxygen-containing layers of the device, where the colour distribution (brown→blue) indicates spectra obtained from progressively increasing(decreasing) distances from the YSZ(SRO), shown in brown(blue). All spectra were processed using PCA and were normalised to the maximum intensity peak for ease of comparison. A vertical dashed line highlights the shift of peak* **b** *across each layer.* . . . 172

4.9 (a) Cropped HAADF image of the tunnel oxide RRAM heterostructure. The rainbow-coloured arrow above the YSZ/PCMO interface, which changes from brown→yellow→green→blue, indicates which line spectra in (b), (c) and (d) correspond to which regions of the YSZ/PCMO interface. (b) Graduation of background-subtracted O K-edge, which comprises peaks **a**, **b** and **c**, and the Mn core loss edge, which comprises $L_{3,2}$ peaks, from the red line spectra, which has a larger YSZ component, to the blue line spectra, which has a larger PCMO component. In (c) and (d), the red, orange and blue line spectra at (c) Mn-$L_{3,2}$ and (d) Pr-$M_{4,5}$ are compared where the orange line spectrum represents a transition state between the YSZ-rich brown, and PCMO-rich blue line spectra. . 176

4.10 *Typical (a) Cropped HAADF image and (b) peak shift of Mn-L_3 (shown in purple) and Pr-M_5 (shown in orange) core-loss edges as a function of distance (x) across the device.* 180

4.11 *Representative comparison of HRS (red) and LRS (red) spectra acquired from two datasets at the YSZ/PCMO interface. Sub-figures show the (a) O K-edge (b) Mn-$L_{3,2}$ edge and (c) Pr-$M_{5,4}$ edge. For both spectra the acquisition parameters were identical: pixel size was 0.2nm^2 and dispersion was 0.5eV/Ch.* 183

4.12 *Normalised distribution of elements in (a) the LRS and (b) the HRS. O, Mn and Pr are shown in purple, blue and orange respectively and in (b) the Ca profile is shown in pink. The main difference between these LRS- and HRS- representative distributions is the relative change in O content between the YSZ and PCMO. The horizontal dashed green line is positioned to represented the expected O-K edge intensity, relative to the bulk PCMO, as calculated using Eqn.2.11.* 184

4.13 *Comparison of HRS (red) and LRS (blue) spectra extracted from the entire YSZ layer. Subfigures show the (a) O K-edge core-loss edge and (b) the YSZ low-loss spectra. In (a) the spectra were separated vertically for clarity.* 186

4.14 *HAXPES spectra showing (a) O-1s (b) Mn-2p (c) Rh-3d (d) Zr-3d for initial state (black) and HRS- (red) and LRS-programmed (blue) devices. An additional exposed SRO O1s peak is shown in (a).* 187

4.15 *(a) a schematic cross-section of the in-operando sample. (b) The IV-characteristics of a device measured in the UHV HAXPES chamber during collection of (c) Rh-3d*$_{5/2}$ *and Zr-3d*$-5/2$ *spectra using voltage sweep 0V→+2V→0V→-3V→0V. (d) The resulting peak shifts in the Zr-3d and Rh-3d peak positions are shown relative to the initial position, before a bias voltage was applied. The orange circle highlights the remnant peak shifts at 0V bias.* 189

4.16 *Inhomogeneous VCM-based RS mechanism in PCMO tunnel-RRAM devices where (a) and (c) depict the HRS, whilst (b) and (d) is the LRS. For (a) and (b),* $V_{\ddot{O}}$ *in the PCMO are depicted as white, whilst the dark purple regions represent* $V_{\ddot{O}}$*-rich areas in the YSZ where the local bonding environment has changed w.r.t the bulk. For (c) and (d), the accumulation/dissipation of negative charge modulates the height of the tunnel barrier, which ultimately governs the overall resistance state if the device.* 192

List of Tables

1.1 Comparison of conventional and emerging memories where F is the minimum feature size. Adapted from 2012 and 2016 publications [2, 3] 3

3.1 Oxygen pressure and substrate temperature deposition conditions for ZnO films pulsed laser deposited onto Si/SiO_x substrates for film characterisation or Ti/Pt substrates for electrical characterisation. Conditions under which Mn:ZnO thin films were also deposited are indicated by blue checkmarks. 106

3.2 *Estimated dielectric constants (ε_r) of polycrystalline undoped ZnO calculated using linear fit analysis of the HRS for SET and RESET transitions displayed in Fig.3.5. The gradient expressions for each conduction model were obtained from current density formulae in the literature [92, 94, 96] where ε_0 is the permittivity of free space, e is the charge of an electron, k is Boltzmann's constant, $T = 298K$, and film thickness is d=200nm.* 115

3.3 Acquisition information for ZnO and Mn:ZnO EELS datasets. 126

4.1 Acquisition information for contributing EELS datasets. LRS- and HRS-programmed devices are shown in blue and red respectively. 169

CHAPTER 1

Introduction

1.1 Principles of Memory Storage

In principle, a basic memory cell can be programmed to one of two discrete binary states, which can then be read and identified. Additional functionality includes the ability to erase and re-write that data. Since the 1950s, computer data storage utilised magnetic media, in which drums, tapes and disks were coated with ferromagnetic metal-oxide films (typically iron oxide) that could be magnetised into discrete states to store information. Today, magnetic Hard Disk Drives (HDDs), which comprise a spinning magnetic disk and a retractable read-write head, are still widely employed in commercial computing systems, primarily as semi-permanent storage. However, the mechanical requirements of HDDs serve as their greatest disadvantage: moving parts contribute negatively towards operating speeds, size restrictions and durability. An alternative class of technologies, Solid-State Drives (SSDs), have already begun to replace HDDs; these are Complementary Metal-Oxide Semiconductor (CMOS) technologies with no moving parts that to date commonly store memory in flash cells arrays. As with the development of HDDs, SSDs can only be improved through research dedicated to the optimisation of the metal-oxide materials that are at the heart of each memory cell. This thesis intends to contribute towards that effort through two spectroscopic studies on ZnO

and $PrCaMnO_3$ metal-oxide thin films, which were characterised for applications in an emerging class of solid-state *resistive* memory technology, Resistive Random Access Memory (RRAM).

Traditionally, memory storage is broadly categorised into two groups: Read-Only Memory (ROM), which is typically used to store permanent information, or information that does not need to be regularly updated; and RAM, which can be overwritten and erased multiple times at fast speeds. ROM is *non-volatile*, which means that it is able to retain stored information without constant power input, whereas depending on the technology, RAM can be either volatile or non-volatile.

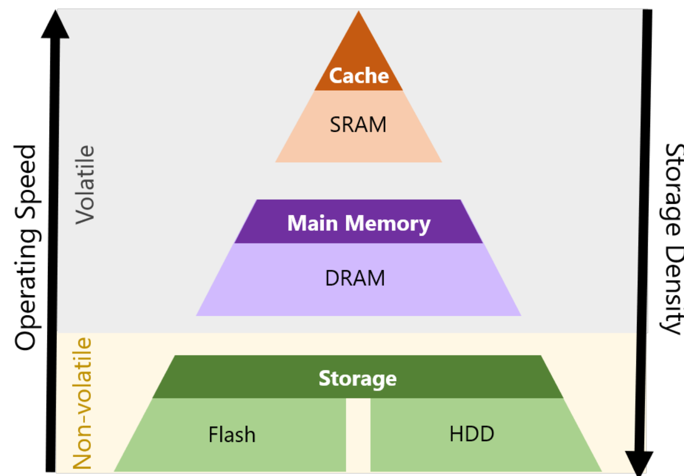

Figure 1.1: *Computer memory hierarchy. Here, cache processing requires memory technologies with extremely fast operating speeds, which have only been achieved by low density, high speed, (SSD) SRAM. Main memory has lower speed requirements than Cache, and currently employs (SSD) DRAM. In contrast to computational memory, storage technologies must be non-volatile, and have the lowest operating speed and highest storage density requirements. The most widely used storage technologies are (SSD) Flash and HDD.*

Today, computer systems contain both HDD and SSD ROM and RAM technologies which are used for different applications, as defined by the computer memory hierarchy presented in Fig.1.1. Customarily, the operating speeds, storage densities and volatilities of the technologies presented in Fig.1.1 dictate their applications. This is because traditional computer architecture operates on the basis of transferring data between physically separate data *storage*, which includes non-volatile technologies with high storage density, and computational *memory*, which includes volatile technologies with

Table 1.1: Comparison of conventional and emerging memories where F is the minimum feature size. Adapted from 2012 and 2016 publications [2, 3]

	Volatile		Non-Volatile	Emerging Non-Volatile			
Type	SRAM	DRAM	Flash	FeRAM	MRAM	PRAM	RRAM
Minimum Cell Size	$140F^2$	$6F^2$	$5F^2$	$22F^2$	$20F^2$	$4F^2$	$4F^2$
Write/Erase Speed	0.3ns/0.3ns	10ns/10ns	1ms/0.1ms	10ns/10ns	10ns/10ns	20ns/50ns	5ns/5ns
Endurance Cycles	10^{16}	10^{16}	10^{5}	10^{14}	10^{16}	10^{8}	10^{10}
Operating Voltages	<1.5V	<1.5V	5V	<1.5V	<1.5V	<3V	<1V

fast operating speeds [1]. For instance, non-volatile HDDs are employed for storage, and volatile SSD Dynamic- or Static-Random Access Memory (DRAM and SRAM respectively) are used to run and load applications that temporarily require memory. As presented in Tab.1.1, comparatively, SRAM can achieve faster read and write operations (0.3ns [2]) than DRAM (10ns [2]), however SRAM has a minimum cell size of $140F^2$ (where F is the minimum feature size), which is over 20 times greater than that of DRAM ($6F^2$) [2]. This means that high-speed, low-storage-density SRAM is employed in cache memory operations, whereas lower-speed, high-storage-density DRAM is employed as main computer memory. It should be noted that both of these technologies are volatile, as depicted in Fig.1.1.

To improve upon the limitations of volatile technologies, a large amount of research focuses on the pursuit of high-performance *non-volatile* technologies. Flash is an example of such progress, and over the past two decades, has outperformed HDDs in terms of operating speeds. Flash technology relies on the tunnelling of electrons and storage of charge in order to store information. Such tunnelling devices remain of interest in emerging technologies, and a tunnel-oxide RRAM device is presented in Chapter 4; in order to enable a comparison between the storage mechanisms of this device and that of a flash memory cell, the principles of flash will now be described. Fig.1.2(a) shows a cross-section of a flash memory cell, which has a structure similar to that of a Metal-Oxide Semiconductor Field-Effect Transistor, but utilises an additional floating-gate that is electrically insulated by insulating oxide layers (tunnel and blocking oxides). Due to its insulation, a floating-gate is able to trap (store) charge, and the presence or absence of this charge defines the memory state of the flash cell. In order to trap electrons and write (program) a flash cell, an electric field is applied across the source and drain electrode which stimulates current flow along a conduction channel, as shown in Fig.1.2(b). Fig.1.2(c) illustrates how positively biasing the control-gate stimulates

the tunnelling of electrons from the conduction channel into the floating gate. The accumulation of charge in the floating-gate modifies the voltage threshold that the control-gate requires to sustain current flow along the conduction channel, thus, the magnitude of the voltage threshold is measured to determine the memory state. Fig.1.2 illustrates how the memory state is erased; the control-gate is electrically grounded and the substrate is positively biased such that electron tunnelling from the floating-gate into the substrate is stimulated. It should be noted that Fig.1.2 presents an example of a single-level cell that can store up to 1 bit of information; today, multi-level flash cells can store up to 4 bits if operating speeds are compromised.

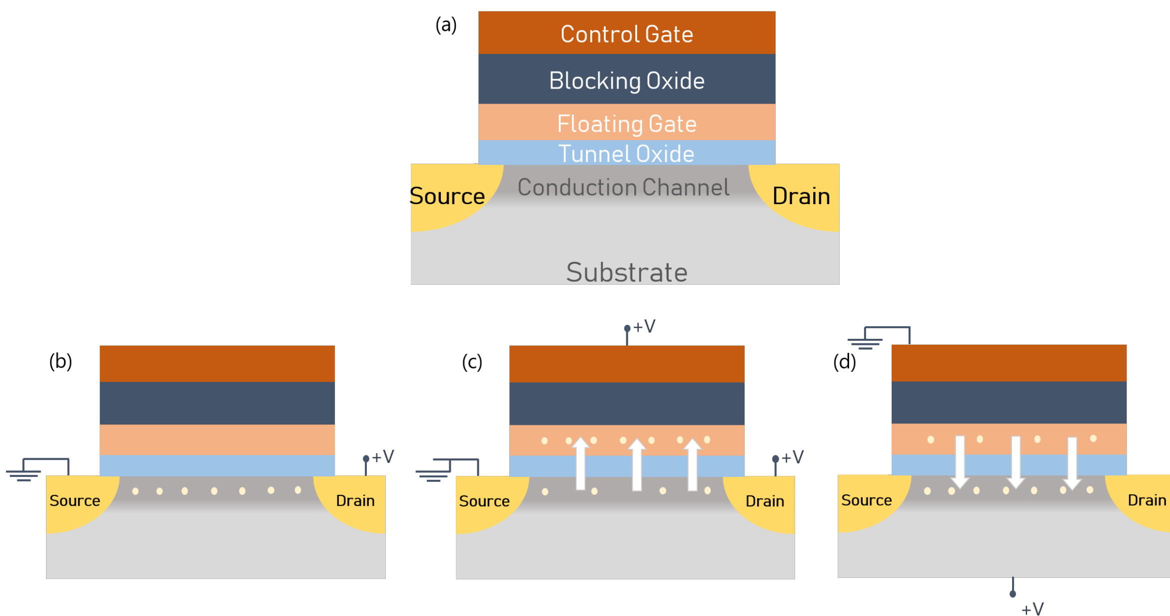

Figure 1.2: *(a) Labelled cross-section of a Flash memory cell and (b)-(d) its working principles. (b) A voltage applied across the source and drain electrodes forms a conduction channel. Charge carriers are represented by yellow circles. (c) Write process where a positive control gate voltage stimulates the tunnelling of charged carriers into the floating gate; due to the surrounding insulator layers, the charges becomes trapped. (d) Erase process in which the control gate is grounded and the substrate is positively biased. This stimulates the tunnelling of charge carriers back into the conduction channel.*

Today, flash is typically employed as *storage* technology as opposed to computational memory, which is largely due to its relatively slow operating speeds (read=1ms and write=0.1ms [2]) when compared to SRAM and DRAM. However, even as a storage technology, Flash is limited by its high operating voltage requirements (5V [4]), which will eventually fail to comply with the lowering operating voltages demanded by an ever-developing electronics industry [2, 4, 5]. In efforts to replace Flash memory and

improve upon its performance, there has been huge investment into research on emerging non-volatile solid state technologies. The four most prominent emerging technologies are Ferroelectric-RAM (FeRAM), Magnetoresistive-RAM (MRAM), Phase-Change-RAM (PRAM), and RRAM. According to the storage densities and operating speeds published in the literature (and presented in Table.1.1), not only do these technologies have the potential to replace Flash as storage, but they could also replace DRAM as main memory. Furthermore, RRAM and PRAM have high storage densities *and* high operating speeds which means they can be classed as both memory *and* storage or true memory-storage technologies.

1.1.1 Emerging Non-Volatile Memories

In an influential 2009 publication, Waser *et al.* defined the ideal characteristics of a non-volatile memory technology that could outperform Flash and compete with DRAM [5]; these were operating voltages of the order of 10^{-1}V, operating speeds faster than 100ns per write operation, and endurance (repeated write and erase processes) greater than 10^{3} cycles [5]. These characteristics are not limited to any single materials system or memory effect, and as a result, there are a number of emerging non-volatile technologies that are currently being researched which all ultimately encode data using distinct resistance states. The principles of memory storage for each of the aforementioned emerging non-volatile technologies, FeRAM, MRAM PRAM, and RRAM, will now be described.

Figure.1.3 is a simplified illustration of a FeRAM cell in which a top and bottom electrode are separated by a thin film of ferroelectric material, the active layer. Under an applied electric field, this thin film is subject to ionic polarisation, in which an ion within each unit cell is displaced. This displacement persists when the electric field is removed, resulting in the polarisation hysteresis curve shown in Fig.1.3, which is defined by the positive and negative write voltages V_{+} and V_{-}. This hysteresis allows one to define positive and negative polarisation saturation (depicted with parallel arrows in Fig.1.3) as distinct binary states. Conventionally, a FeRAM cell is read by applying a positive write voltage (here shown as V_{+}) to the top electrode, and measuring the output current generated under the saturating electric field. If the device is not in the polarisation

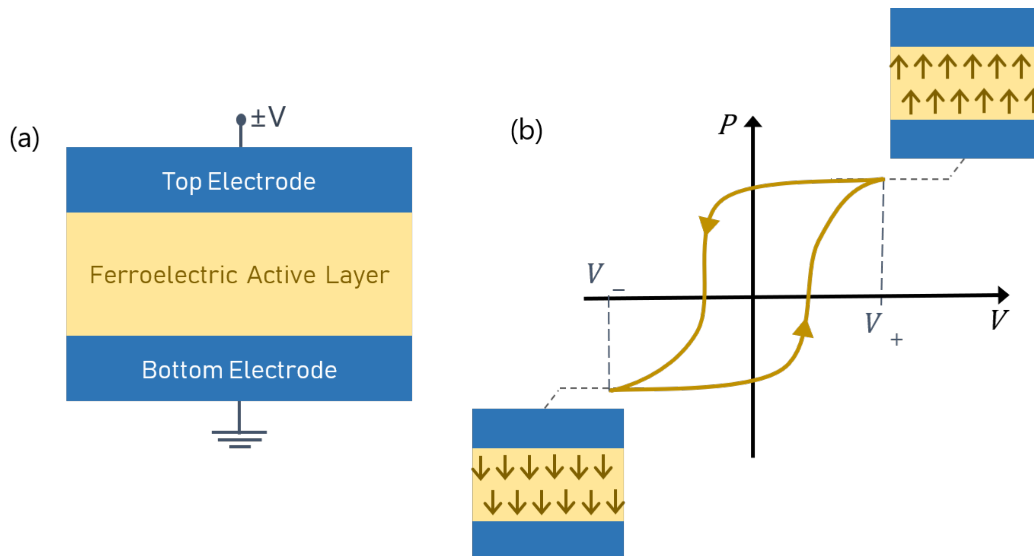

Figure 1.3: *(a) Cross-section of a FeRAM cell. (b) Evolution of the polarisation resolution as a function of the voltage applied across the top and bottom electrodes. Parallel arrows indicate the polarisation saturation of the ferroelectric active layer where distinct positive and negative saturation states are achieved at positive and negative bias respectively.*

state corresponding to that voltage, then the large resultant ion displacement causes a large change in the output current. The FeRAM read process is inherently destructive, which is a disadvantage with respect to achievable operating speeds [6]. Furthermore, ferroelectric hysteresis is subject to degradation with electrical cycling, which is caused by free charge carriers forming defect dipoles. Despite these drawbacks, FeRAM cells have fast operating speeds (read/write, 10ns/10ns [2]), which is comparable to DRAM, and have demonstrated endurance as high 10^{14} cycles.

In contrast to FeRAM, MRAM memory cells resemble Magnetic Tunnel Junctions (MTJs) and comprise two ferromagnetic active layers that are separated by a thin tunnel oxide insulator. Under an applied electric field, the magnitude of the device tunnel current is dependent on the relative magnetisation directions of the two ferromagnetic layers: when (anti)parallel, the tunnel current is (decreased)increased, and the device magnetoresistance (R_M) is (increased)decreased. In MRAM, these distinct, bistable, magnetisation-induced resistance states serve as binary memory states. Figure.1.4 presents a simplified representation of a MRAM cell, and shows its ferromagnetic response (depicted with parallel arrows) to an applied voltage cycle. It illustrates how the lower ferromagnetic layers is 'fixed' and has pinned magnetisation, whilst the other

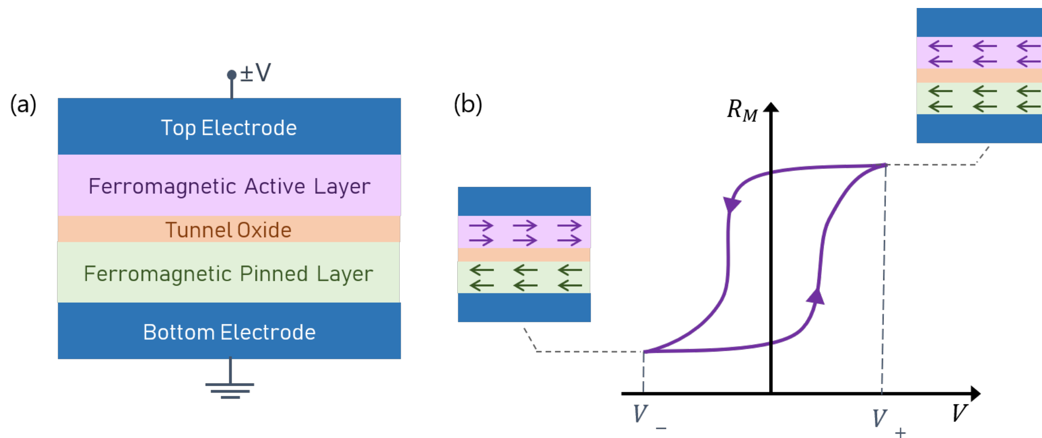

Figure 1.4: *(a) Cross-section of an MRAM cell. (b) Evolution of the magnetoresistance response to the voltage applied across the top and bottom electrodes. Whilst the pinned layer remains saturated in one direction, the ferromagnetic active layer can be saturated to the same or opposite direction, which affects the magnetoresistance.*

is 'free' and can be written into a magnetic state at sufficient write voltages, here shown as V_+ and V_-. MRAMs have operating speeds, voltages, and cell size comparable to FeRAM, however as magnetisation saturation does not require the motion of ions within a material, MRAMs do not suffer from the electrical-loading-induced degradation experienced by FeRAMs.

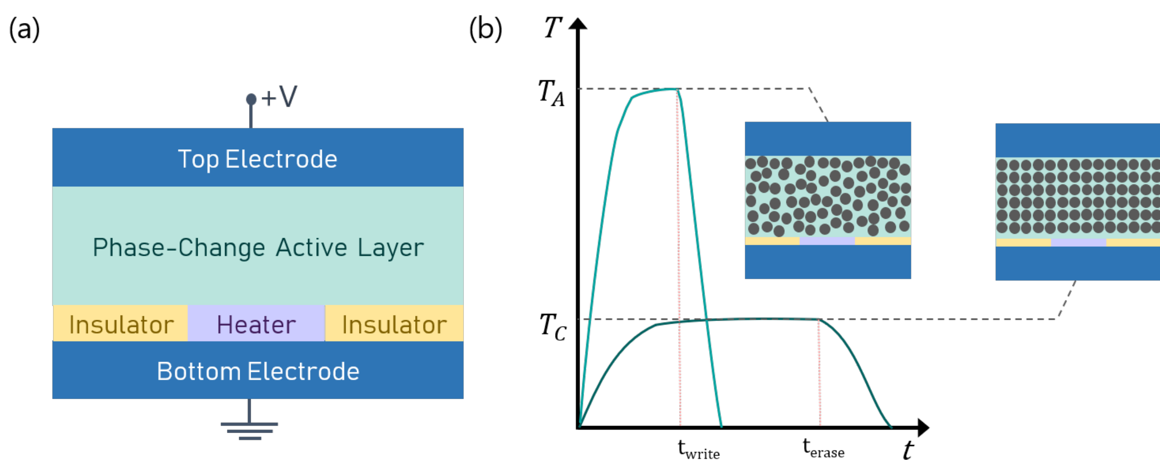

Figure 1.5: *(a) Cross-section of a PRAM cell. (b) During the set process, a short pulse length at high temperatures is sufficient to trigger a transition to the amorphous phase. In contrast, during the erase process long pulses at low temperatures stimulates a transition to the crystalline phase.*

Like MRAM, PRAM stores memory as distinct resistance states. However, unlike MRAM, this change in resistance is due to a change in the phase of the active layer. Fig.1.5 shows a simplified example of PRAM cell in which a top and bottom electrode

sandwich two adjacent insulating layers: the phase-change active layer, and an insulating layer that houses a resistive heating element. Under an applied electric field, the heating element stimulates a thermally reversible change between amorphous and crystalline phases of the active layer, which are resistive and conductive respectively. As shown in Tab.1.1 and illustrated in Fig.1.5, PRAM cells require longer erase (50ns [2]) than write (10ns [2]) processes. This is because in order to switch to the crystalline phase, the active layer is resistively heated to the temperature T_C for a length of time sufficient for the material to crystallise, whereas to change into the amorphous phase, the active layer is heated to T_A and rapidly quenched. For PRAM, the key limiting factor is the operating voltage required to stimulate a phase change, which, in comparison to other emerging technologies, is relatively high (up to 3V [3]). Despite this, PRAM outperforms Flash in terms of storage density, operating speeds and endurance.

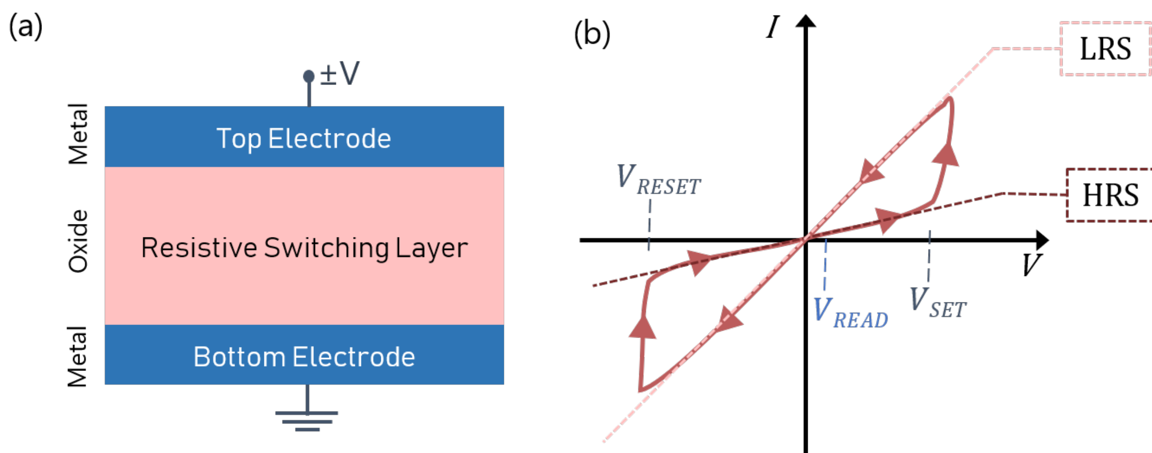

Figure 1.6: *(a) Cross-section of a Metal-Insulator-Metal RRAM cell. (b) Evolution of the resistance state as a function of the voltage applied across the top and bottom electrodes. Here, the Low Resistance State (LRS) and the High Resistance State (HRS) are highlighted by a dashed line.*

Fig.1.6 presents an example of a basic Metal-Oxide-Metal (MOM) RRAM cell. Similar to MRAM and PRAM, RRAM cells are able to store memory due to the bistability of two distinct resistance states, which are accessible under an applied electric field. For a 1 bit RRAM cell, these states are referred to as the high- and low- resistance states, which are shortened to HRS and LRS respectively. The process by which a device changes between its resistive states is referred to as *resistive switching*. RRAM devices are typically characterised by a current-voltage (I-V) curve; Fig.1.6 shows an example of

a *bipolar* resistive switching hysteresis loop, in which the device switches from the LRS to the HRS at one polarity, and then back into the LRS at the opposite polarity; these switching events occur at V_{SET} and V_{RESET} respectively. In order to read a RRAM cell, a small read voltage (V_{READ}) is applied; this is typically no greater than 10% of the write voltages required to switch the device into the HRS or LRS [5]. Using low V_{READ} voltages, it is possible to probe the resistive state of the RRAM cell *non-destructively*. Customarily, a RRAM device is also characterised by the ratio between the HRS and LRS, which is obtained at V_{READ}.

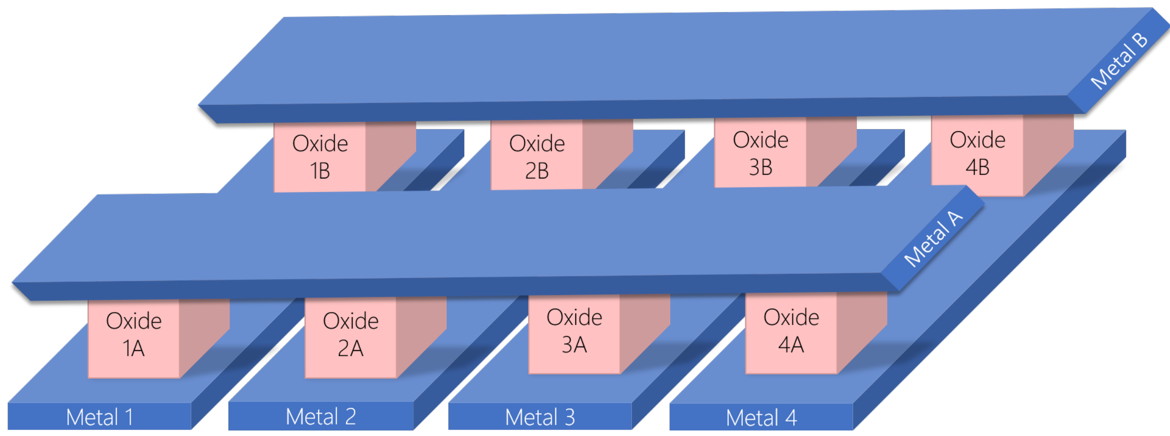

Figure 1.7: *Example of a simplified 3D RRAM Crossbar array. Here, individual RRAM cells can be accessed by isolating specific top and bottom electrode intersections.*

In comparison to other emerging non-volatile memories, RRAM has the advantage of fast operating speeds and voltages, which are less than 10ns and 1V respectively. Typically, RRAM devices display diode-like behaviour; this, coupled with the simplicity of MOM architecture, means that RRAM cells can be fabricated in CMOS-compatible 3D crossbar arrays, which are depicted in Fig.1.7. As shown in Fig.1.7, these array structures employ long metal top and bottom electrodes, where physically separated thin films of RS active layer are sandwiched between, creating multiple distinct RRAM cells. The top electrode metal bar is oriented 90° with respect to (w.r.t) the bottom electrode metal bar, such that each RRAM cell can be accessed at a defined intersection. Furthermore, owing to the diode-like electrical characteristics of RRAM, transistor elements are not required to access each cell. However, RRAM devices have not yet displayed endurance comparable to conventional memory technologies (10^{16}cycles for SRAM and DRAM, and 10^{10}cycles for RRAM [3]); this can be attributed to the variability introduced by

competing mechanisms that occur simultaneously during resistive switching, which are further described in section 1.2.2. Despite not yet outperforming SRAM and DRAM, RRAM has been shown to have greater endurance than Flash and PRAM, which have exhibited 10^5 and 10^8 cycles respectively. Taking these attributes into consideration, RRAM is arguably the most promising emerging non-volatile memory technology that is currently in development. This is the key motivation for the RRAM research presented in this thesis.

1.2 Resistive Switching

1.2.1 Memristor Theory

The theoretical basis for resistive switching dates back to 1971 when L. Chua reasoned that in addition to the resistor, the capacitor and the inductor, one could consider an additional fundamental circuit element, the memory-resistor or memristor [7, 8]. At the time, it was generally accepted that there were five mathematical relationships that paired current (i), voltage (v), charge (q) and magnetic flux (ϕ). Two of these relations show one variable as the time derivative of another, $\frac{dq}{dt} = i$ and $\frac{d\phi}{dt} = v$, whilst the other three show that one variable is a function of another: $\frac{dv}{di} = R$ describes the resistor (with resistance R); $\frac{dq}{dv} = C$ describes the capacitor (with capacitance C); and $\frac{d\phi}{di} = I$ describes the inductor (with inductance I). Chua argued that one relationship remained undefined, and postulated that the 'missing memristor' was described by the following relationship between ϕ and q: $\frac{d\phi}{dq} = M$ where M is memresistance. The key difference between a memristor and a resistor was that the memristor exhibits a non-linear response that is dependent on the device history. Five years later, Chua *et al.* published more work that broadened the memristor concept to include *memristive systems* [7]. These were a more general class of dynamic non-linear systems where a memristive response could be stimulated by any variable, and is not limited to ϕ [7].

Nearly four decades later, in a 2008 publication, Strukov *et al.* presented evidence for the first physical memristor, which was a Pt/TiO_2/Pt thin-film heterostructure. In this publication, the device displayed a memristive pinched hysteretic response to an electric field applied across the Pt electrodes [8]. Here, RS was attributed to the controlled drift

of oxygen vacancies across the device, which affected the stoichiometry of the film; this mechanism is further described in section 1.2.5. In the decade since, there has been huge investment into RRAM research; as a result, resistive switching (RS) has been observed in a wide variety of materials including organic and inorganic media [9, 10]. In this work, inorganic materials, specifically transition metal oxides, are studied.

1.2.2 Resistive Switching Mechanisms

In the decade since Strukov *et al.*'s proposed RS model, the mechanisms of RS are not yet completely understood. In fact, a number of publications have reported the observation of *multiple* distinct switching mechanisms stimulated within a single device heterostructure, as opposed to the single mechanism which was first proposed [9, 11]. If poorly understood, such complex RS contributes negatively towards device variability. In order to improve device performance, a large portion of RRAM-research, including the metal-oxides studies presented in this thesis, focuses on understanding the contributing mechanisms of RS within a variety of device heterostructures. RRAM devices are typically electrically characterised using IV curves, which provide key information including whether RS occurs due to *bipolar* or *unipolar* effects. Bipolar RS was introduced in section 1.1.1 and a conventional bipolar RS IV curve is presented in Fig.1.8(a). Here, the LRS is shown in green, the HRS is shown in red, and the resistive switching events are shown in grey. Fig.1.8(a) represents a device that is initially (at $V = 0$) in the HRS. As a positive voltage is applied, little current flows across the device, however, at V_{SET}, the SET process, highlighted by the black arrow, is triggered. In order to protect the device from damage, a compliance current (cc) limits the current flowing through the device, and is shown as a green dashed line in Fig.1.8. The device will remain in the LRS state until the voltage reaches V_{RESET}, which, for bipolar IV curves, is at opposite polarity to that of V_{SET}. In contrast, for unipolar RS, V_{SET} and V_{RESET} can occur during a *single* sweep at either polarity. Fig.1.8(b) represents a unipolar RS device that is initially in the LRS state, and undergoes a RESET switch to the HRS at low voltages. As the magnitude of the voltage increases, little current flows through the device, and at V_{SET} the device switches to the LRS.

As mentioned above, the polarity dependence exhibited by an RS device is governed

by the dominant RS mechanism. The wide breadth of RS-mechanism research has emphasised how much influence the choice of materials can have over which mechanisms of RS can be sustained during repeated cycling. Importantly, this is not limited to the RS oxide layer: RS may be dominated by interfacial effects that are dependent on both the metal-oxide *and* the electrode materials. Considering this, it is of utmost importance that devices are carefully designed to promote and sustain one particular RS mechanism above all others. For metal-oxide materials, RS is mediated via *redox-based* mechanisms that can be classified into three main groups: Electrochemical Memory (ECM), Thermochemical Memory (TCM), and Valence Change Memory (VCM), which are presented in section 1.2.3, section 1.2.4 and section 1.2.5 respectively.

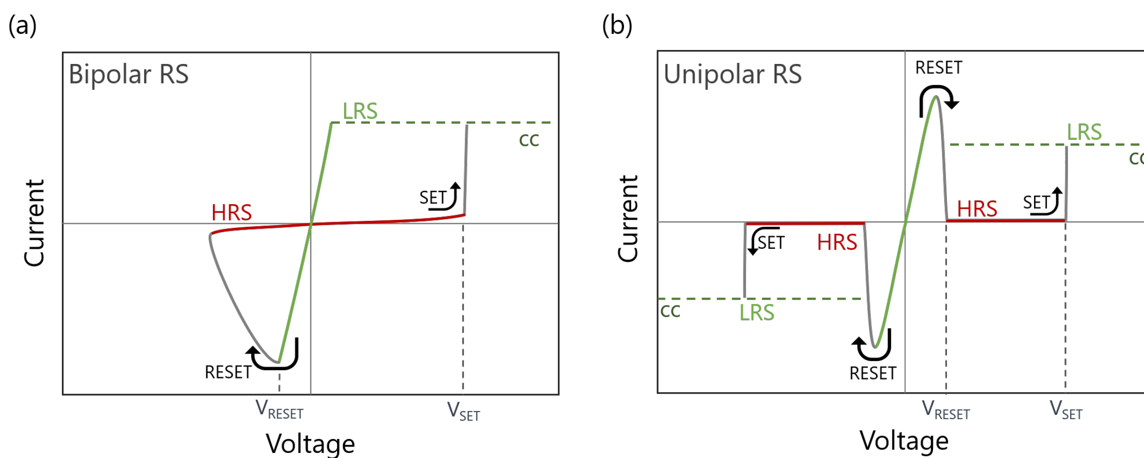

Figure 1.8: *Two basic modes of resistive switching in which the LRS and HRS are shown in green and red respectively, and the switching process is shown in grey. The SET and RESET voltages highlighted in both images, and the compliance current, used to prevent damage, is shown as a green dashed line. (a) illustrates bipolar RS, and (b) illustrates unipolar RS. Adapted from [5].*

1.2.3 Electrochemical Memory

ECM involves the electrochemical dissolution and recrystallisation of an active electrode material under an applied electric field [12]. This mechanism is also referred to as 'metallisation-' or 'conductive bridging-' memory because the dissolution process leads to the formation of a conductive metallic filament across the device. Fig.1.9 illustrates key stages of the ECM mechanism in conjunction with a bipolar I-V switching cycle. Here, the MOM cell comprises an electrochemically active electrode (shown in

dark blue) such as Ag, Cu, or Ni, a solid electrolyte insulator (shown in pink) and an inert electrode (shown in grey) such as Pt, Ir, W. Importantly, the active electrode is a metal that can be electrochemically dissolved into and conducted through the solid electrolyte; in contrast, the inert electrode cannot [12].

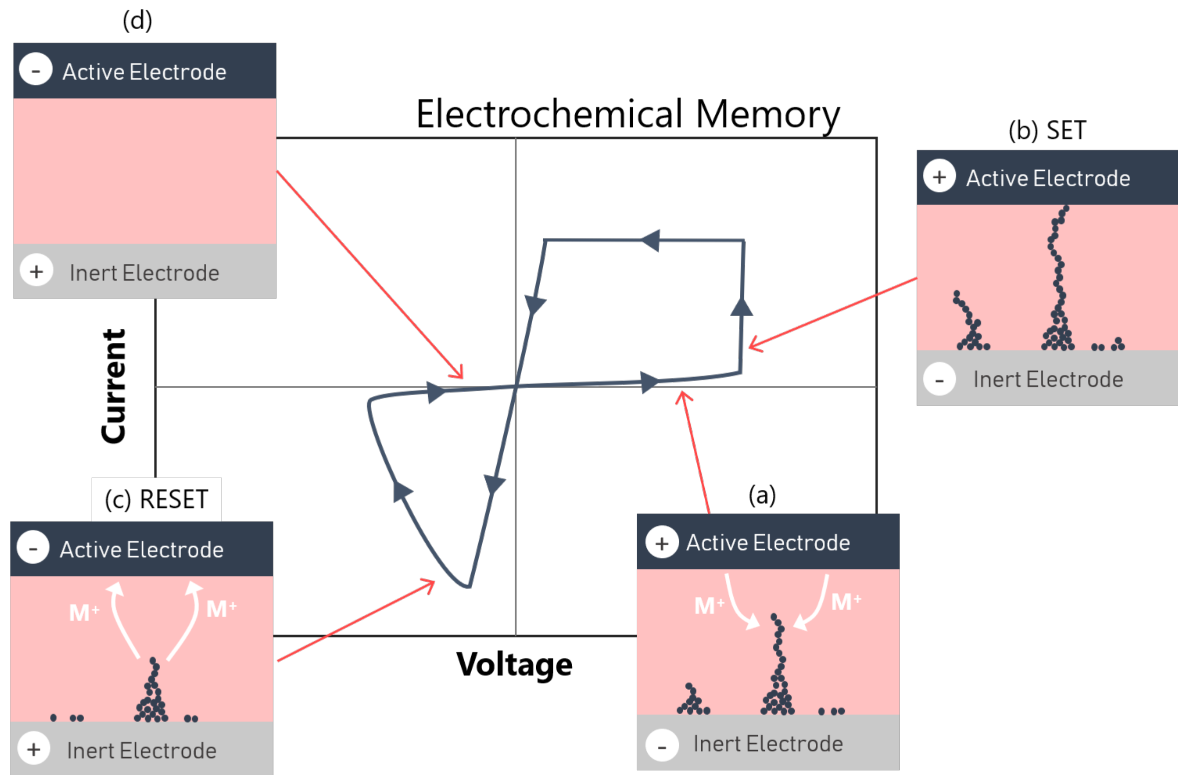

Figure 1.9: *IV curve obtained from an ECM cell in the four key stages of RS are illustrated in four device cross-sections presented in insets (a)(b)(c) and (d). In (a), a positively biased active electrode induces M^+-migration in the direction shown by the curved white arrows, where M^+ cations are represented by blue circles. In (b), the active electrode has reached a voltage sufficient to SET the device to the LRS which corresponds to the formation of a conductive M^+ filament. In (c), a sufficient negative voltage has induced M^+-migration in the direction indicated by the white arrows, rupturing the filament. Image (d) represents the final HRS reached after the full dissolution of the filament. Adapted from [5].*

In the absence of an applied field, the cell shown is initially in its HRS. However, when the inert electrode is negatively biased, the electrochemical dissolution of the anodic active electrode (M) is stimulated, which is described by the reduction reaction:

$$M \longrightarrow M^+ + e^- \tag{1.1}$$

where M^+ represents metal cations. Fig.1.9(a) shows how, under an increasing applied

field, M^+ cations drift towards the inert cathode. As a result, cathodic deposition occurs at the inert electrode/solid electrolyte interface, forming a metallic filament that grows towards the anodic active electrode. This electro-deposition is described by the oxidation reaction:

$$M^+ + e^- \longrightarrow M \tag{1.2}$$

It should be noted that through this electro-deposition process, the thinnest part of the conductive filament will be at the active electrode. Fig.1.9(b) corresponds to the voltage sufficient to SET the memory cell to the LRS state (V_{SET}). At this voltage, a *complete* conductive M^+ filament is formed that electrically shorts the active and inert electrodes. It is generally accepted that the formation of a filament is supported by defects within the solid electrolyte material such as nanopores or grain boundaries. Such a filamentary SET process is characterised by a sharp increase in device current; therefore, compliance currents are employed. An ECM RRAM cell will remain in the LRS until a sufficient RESET voltage (V_{RESET}) at opposite polarity induces the electrochemical dissolution of the conductive filament, which is shown in Fig.1.9(c). Finally, due to the electrochemical dissolution, the device enters the HRS, shown in Fig.1.9(d). Typically, $|V_{SET}| > |V_{RESET}|$, which leads to a asymmetric I-V curve. There was some speculation in the literature as to the cause of this asymmetry. However, by comparing ECM RS in solid and liquid electrolytes, Waser was able to assign this effect to the morphology of the system, referring to the filament/active electrode interface as a 'needle-to-plane' geometry [13]. In this configuration, the minimum voltage required to rupture the needle-like filament at the active electrode is much lower than the voltage required to form a complete filament that spans the entire electrolyte. At reverse polarity, as shown in Fig.1.9(a) the dissolution of the active electrode may lead to the electrodeposition of metal cation clusters that grow competitively before a complete, conductive filament is formed.

The assignment of a filamentary RS mechanism is supported by electrical characteristics which have shown that, for ECM, the LRS does not depend on the area of the top electrode. The lack of dependence on top electrode area is due to the fact that the overall resistance state of the device is governed by the needle-like tip of a

single conductive filament. This means that ECM RS cells can be scaled down to sizes that only need accommodate a single narrow filament, which is a great advantage with regards to increased storage density.

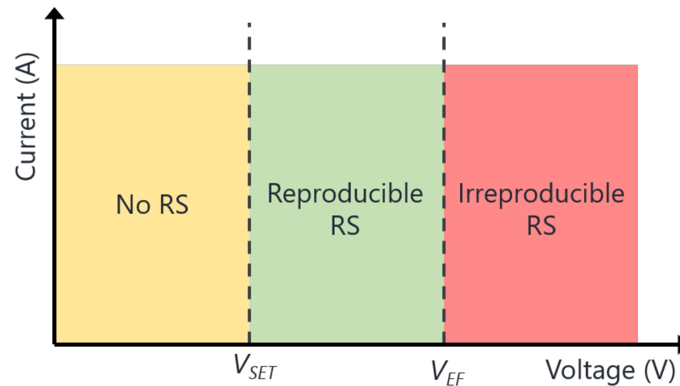

Figure 1.10: *RS reproducibility map depicting the dependence of reproducible RS on applied voltage.*

For highly resistive films in which the switching oxide is an insulator, ECM MOM cells exhibit a greater V_{SET} voltage in their first cycle than in subsequent cycles; this initial cycle is called an *electroforming* cycle. The electroforming cycle is characterised by an electroforming voltage V_{EF}, which allows one to achieve stable, lower voltage RS in subsequent cycles. The relatively high V_{EF} is ascribed to the formation of a channel that persists after the dissolution of the first conductive filament, which becomes a template for filaments generated in subsequent cycles. However, the magnitude of V_{EF} and the corresponding electroforming current are sufficiently large to damage the device. This is somewhat mitigated through the use of compliance currents, however, it has been argued that high-power-consumption electroforming is an inherently destructive process, and that the anticipation or expectation of an electroforming cycle has promoted the research of RRAM devices which display RS that is ultimately less reproducible than their electroforming-free counterparts. Fig.1.10 illustrates this argument and shows how RS reproducibility can vary with applied voltage: here, no RS is exhibited below V_{SET}; reproducible RS is exhibited at voltages between $V_{SET} \leq V < V_{EF}$; and irreproducible RS, that is, RS that is only sustainable for a few cycles, is exhibited at voltages $\geq V_{EF}$. In order to avoid irreproducible RS, it is possible to design RRAM devices to be initially conductive, and therefore, *electroforming-free*. For instance, in ECM, electroforming is only necessary if the solid electrolyte does not, in its pristine state, already contain the

metal cations required for filament formation. Further to choosing a solid electrolyte material that does, through annealing, one can stimulate the thermal diffusion of active electrode cations into the solid electrolyte prior to switching, such that an electroforming cycle is not required. However, due to the high impact of early papers, the anticipation of an electroforming cycle has guided researchers to tend towards the production of highly resistive RS films. In fact, the literature typically refers to the MOM structure as a Metal-*Insulator*-Metal (MIM) structure, which implies that RS cannot be readily achieved in more conductive films. Chapter 3 explores the electroforming process and its impact on RS further through the study of zinc oxide based thin film heterostructures.

1.2.4 Thermochemical Memory

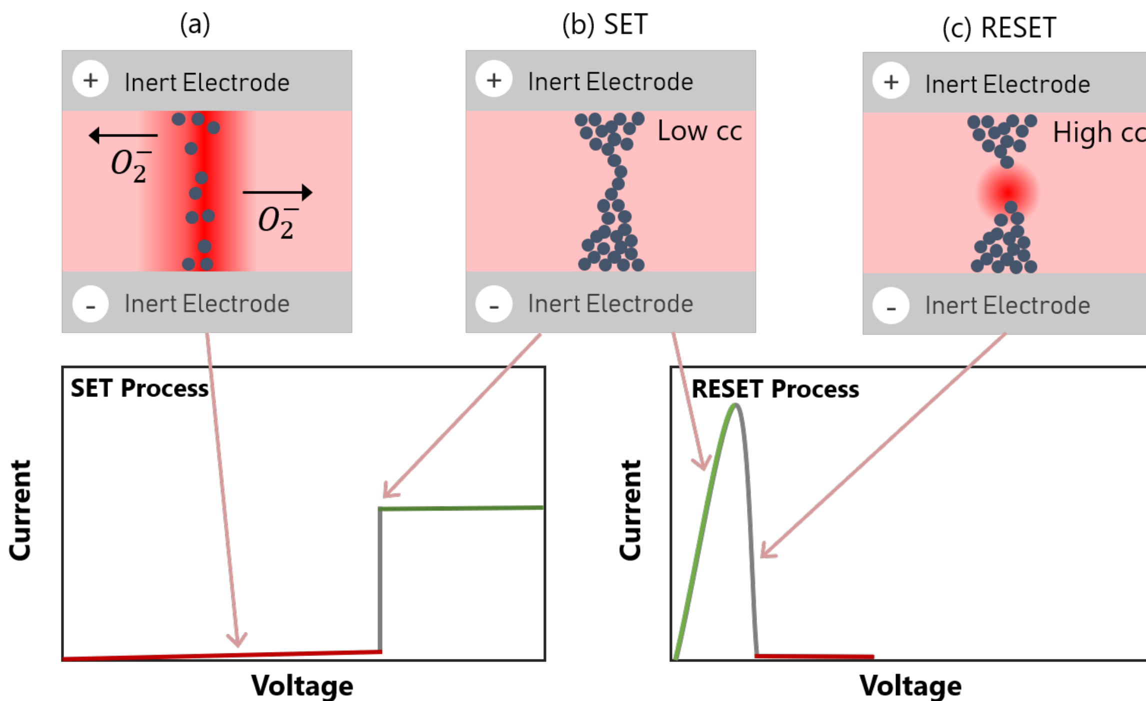

Figure 1.11: *(a)-(c) Stages of RS that occur in Joule-heat-dissolution TCM; each image corresponds to a different point in the unipolar IV curve, which has been separated into a SET voltage sweep and a RESET voltage sweep for clarity. The red region in (a) illustrates the hot conduction channel formed as a result of the thermoelectric breakdown of the insulator material, which is shown in pink. This causes oxygen anions to migrate out of the hot channel in the direction indicated by the black arrows, and leaves behind chemically reduced insulator material, which is shown in dark blue. (b) Formation of a conductive filament. (c) Localised dissolution hotspot that ruptures the filament, resetting the device.*

TCM occurs most frequently in transition metal oxides and, like ECM, is a filamentary mechanism. However, for TCM, the conductive filament generated during the SET process consists of either electrode metal cations (similar to that shown in Fig.1.9), carbon from residual organics, or reduced, non-stoichiometric insulator material [14]. Fig.1.11 depicts the case in which a metal oxide is employed as the RS material, shown in pink, and *inert metals* (Pt, Ir, W) as the electrodes. Here, reduced, non-stoichiometric oxides comprise the conductive filament, which is shown here in dark blue. Fig.1.11(a) shows how, under an applied electric field, Joule heating leads to the formation of a high temperature region within the insulator, the hot conduction channel, which is shown in red. The temperature gradient between the hot conduction channel and the surrounding insulator provides impetus for the thermodiffusion of O^{2-} out of the hot conduction channel and into the insulator. As shown in Fig.1.11, this thermally-induced migration of oxygen vacancies leads to the formation of an energetically favourable reduced oxide which acts as a conductive filament, bridging the two electrodes [5, 14, 15]. The Joule heat-induced SET transition is referred to as the thermoelectric breakdown of the transition metal oxide, and can be controlled through the use of a relatively low compliance current. As TCM is a unipolar effect, both the SET and RESET switches can be triggered in a single voltage sweep, as depicted in Fig.1.8, or in two separate voltage sweeps (a SET sweep and a RESET sweep), as shown in Fig.1.11. Fig.1.11(c) illustrates the RESET process; here, Joule heating leads to the development of a dissolution-hotspot, which is located in the middle of the filament, at its thinnest point. Within this hotspot, the local electric field and current density are increased, which leads to the dissolution and rupture of the filament. To RESET the device, high compliance currents are employed stimulate Joule heat dissolution. In subsequent RS cycles, rupture and formation in the hotspot region of the filament allows for switching.

There are a number of differences between TCM and ECM: in TCM RRAM cells RS is a *thermally-induced* effect that is governed by variations in the chemistry of the insulator, which differs from electrically-induced ECM in which RS is largely dependent on electrode materials, and occurs at an insulator/metal interface. As TCM RS is induced without the requirement of an electrochemically active electrode, inert metals such as Pt can be employed in symmetric devices, such as the well-characterised TCM system

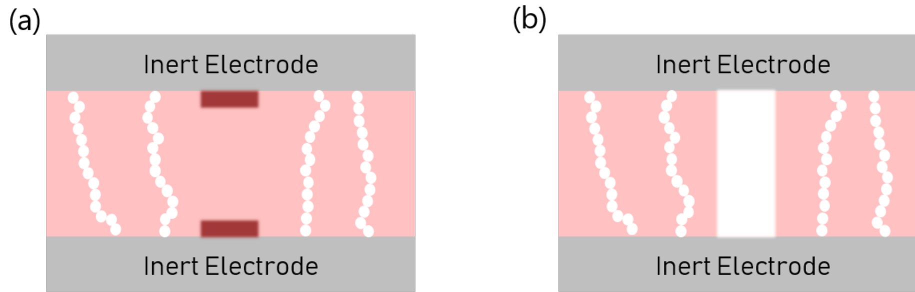

Figure 1.12: *'Faucet' model for unipolar TCM showing (a) the HRS and (b) the LRS. Here, switching is governed by a highly resistive 'faucet' region at the interface, which is shown here in dark red. Conductive regions consistent of reduced, non-stoichiometric oxide are shown here in white. In both states, multiple filaments bridge the top and bottom inert electrodes, but the 'faucet' governs the overall resistance state of the device.*

Pt/NiO/Pt [14, 16]. In contrast to ECM, the literature presents evidence (Conductive Atomic Force Microscopy, described in section 2.9) for TCM being a *multi-filamentary* effect. These characteristics are both described by Inoeu *et al.*'s TCM 'faucet' model, which is a prominent alternative model to Joule heat dissolution [5, 16]. In this model, electroforming leads to the formation of a conductive *bulk* oxide that comprises multiple filaments formed along grain boundaries, which is shown in Fig.1.12(a); however, the bulk conductivity does not dictate RS in the device [5, 16, 17]. Instead, the faucet model suggests that the current across the device must be limited by a small, highly resistive region at the electrode/oxide interface, the 'faucet', shown in Fig.1.12 by the dark red region. In the HRS, current flows homogeneously across the entire metal/oxide interface. In support of this model, the literature shows that for many systems, the HRS is dependent on the area of the top electrode, whilst the LRS is independent [16].

1.2.5 Valence Change Memory

VCM is a anion-mediated effect in which an electric field induces the redox of an insulating transition metal oxide. Specifically, the abundance or deficiency of oxygen anions (O^{2-}) affects the valence state of the transition metal cation, which causes a change in the electrical conductivity of the transition metal oxide. Taking TiO_2 as an example, the transition metal redox is governed by the reactions:

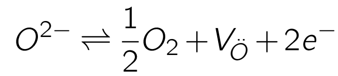

$$O^{2-} \rightleftharpoons \frac{1}{2}O_2 + V_{\ddot{O}} + 2e^-$$

$$ne^- + Ti^{4+} \rightleftharpoons Ti^{(4-n)+} \tag{1.3}$$

where n represents the number of electrons (e^-) and $V_{\ddot{O}}$ represents oxygen vacancies [5, 18, 19]. Because $V_{\ddot{O}}$ are more mobile than transition metal cations, $V_{\ddot{O}}$ mediate the switching effect. The polarity of each electrode within the MOM structure induces the migration of positively charged $V_{\ddot{O}}$ across the device. Thus, VCM RS is also a bipolar effect. For n- or p-type materials, $V_{\ddot{O}}$ act as donors and acceptors respectively [20]. This means that n-type(p-type) transition metal oxides have increased(decreased) resistivity when $V_{\ddot{O}}$-deficient.

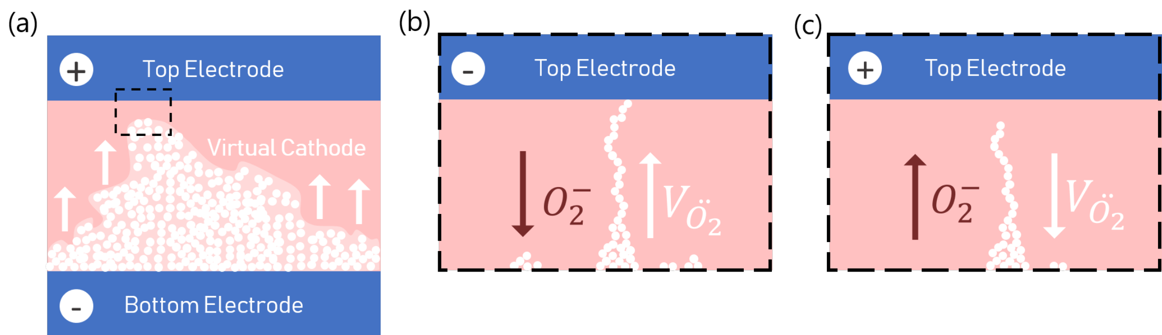

Figure 1.13: *(a) Electroforming process of a n-type oxide material and (b)(c) filamentary-VCM RS in a MOM heterostructure. This process is governed by the electromigration of $V_{\ddot{O}}$, which are shown in white, and move in the direction of the white arrows. (a) During electroforming, the migration of $V_{\ddot{O}}$ towards the anode forms a 'virtual cathode'. Within the vicinity of the anode, highlighted by the black dashed box in (a), filamentary RS occurs and is shown in (b) and (c). (b) shows the LRS in which $V_{\ddot{O}}$ migrate towards the anode (top electrode) and form a complete conductive path. At opposite polarity, (b) shows the HRS in which the $V_{\ddot{O}}$-filament is ruptured due to the migration of $V_{\ddot{O}}$ towards the cathode (anode electrode). $V_{\ddot{O}}$-migration occurs in the direction opposite to O^{2-}-migration, which is shown in brown.*

The literature has shown that VCM occurs via two geometries: filamentary-VCM and interface-VCM [5,9]. The former is shown in Fig.1.13, and is analogous to the filamentary RS exhibited in ECM; both mechanisms are independent of electrode area and have often been shown to require an electroforming cycle to sustain bipolar RS. In 1990, Baiatu *et al.* described an 'electrical degradation' mechanism that occurred with insulating transition

metal oxides which is now regarded as the electroforming process required for VCM [21]. In their publication, they proposed that the insulator/metal interfaces within a MOM structure blocked the ionic conduction of $V_{\ddot{O}}$. This created a $V_{\ddot{O}}$-gradient across the film in which $V_{\ddot{O}}$ accumulated at the cathode and O^{2-} accumulated at the anode [21]. Ultimately, the segregation of $V_{\ddot{O}}$ and O^{2-} created a p-n junction. This mechanism was later linked to RS by Hong *et al.* and Waser *et al.* who were able to visualise the formation of a field-induced p-n junction within bulk oxides through transmission optical microscopy [5, 22]. In this technique, contrast arose due to variations in valence state of the transition metal cation, which, as shown in Eq.1.3, can be used to indicate the presence of $V_{\ddot{O}}$ [5, 22]. Today, the formation of a $V_{\ddot{O}}$-rich, n-conducting region is now referred to as the formation of a *virtual cathode*, and is depicted in Fig.1.13(a). Under a continued applied field, the virtual cathode will propagate towards the anode until it is slowed by electrostatic repulsion. Due to electron-tunnelling across this interface, the resistance of the device decreases dramatically and the memory cell is electroformed [5]. It should be noted that the propagation front of virtual cathode is inherently rough as $V_{\ddot{O}}$ migration is anticipated to occur along extended defects. This means that whilst a large area of the device becomes cathodic due to $V_{\ddot{O}}$-deficiency, the propagation front is comparable to collection of individual filaments. In subsequent cycles, switching occurs across the few nm that separate the virtual cathode and physical anode. For n-type transition metal oxides, the HRS(LRS) is attained if the physical electrode is further positively(negatively) biased, whereas for p-type transition metal oxides, the LRS(HRS) is attained if the physical electrode is further positively(negatively) biased.

As opposed to filamentary-VCM, interface-VCM occurs *homogeneously* across the physical electrode. In an influential publication, Sawa *et al.* showed that interface-VCM could only occur if a Schottky contact was formed at one of the insulator/electrode interfaces, and an ohmic contact was formed at the other, which is depicted in Figs.1.14(a) and (b) [20]. Schottky contacts (or Schottky barriers) are formed at metal/semiconductor interfaces and involve the bending of energy bands within the semiconductor material to equilibriate with the Fermi energy across the interface, which is shown in Figs.1.14(c) and (d); this means that Schottky barriers have rectifying characteristics. In comparison, an ohmic contact is non-rectifying and follows Ohm's law.

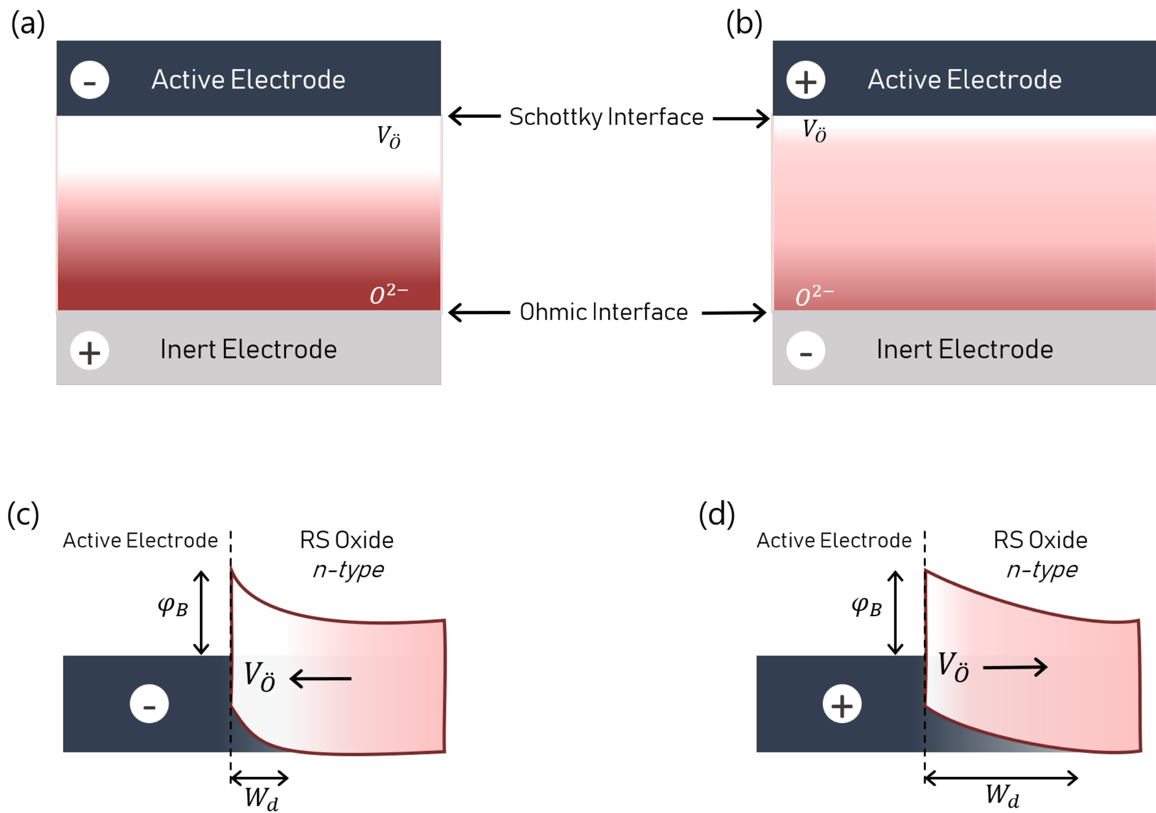

Figure 1.14: *RS in a Schottky contact/oxide/Ohmic contact MOM heterostructure in which an n-type oxide is employed. RS is depicted in terms of (a)(b) interface-VCM and (c)(d) Schottky barrier modulation. (a) and (c) represent the LRS in which* $V_{\ddot{O}}$ *-migration towards the anode leads to the accumulation of* $V_{\ddot{O}}$ *at the interface. This leads to the formation of an oxygen-rich region, which is shown here in dark red, and the reduction of the depletion width* W_d *of the Schottky Barrier, which promotes tunnelling. (b) and (d) represent the HRS at opposite polarity; here,* $V_{\ddot{O}}$*-migration in the opposite direction leads to a reduction in the number of* $V_{\ddot{O}}$ *at the Schottky interface and an increase in* W_d *which prevents tunnelling.*

Sawa *et al.*'s study proposed that the electromigration of $V_{\ddot{O}}$ governed the depletion width of a Schottky barrier which in turn varied the resistance state of the device: the LRS corresponded to a narrower depletion width that could support tunnelling, and is depicted in Fig.1.14(c); and the HRS corresponded to a wider depletion width that inhibited tunnelling, and is depicted in Fig.1.14(d). This comprehensive study also showed that, as the height of the Schottky barrier (ϕ_B) is determined by the difference between the work-function (ϕ_W) of the insulator and the metal electrode, the work-function of the active electrode metal either prevents or promotes interface-VCM-RS; this was shown for two crystalline perovskite-type oxides: p-type $PrCaMnO_3$, and n-type $Nb:SrTiO_3$, where Ti ($\phi_W = 4.3$eV), Au ($\phi_W =$5.1eV) and $SrRuO_3$ ($\phi_W = 5.3$eV) were used as top

electrodes. They found that for the p-type material, the interface resistance increased with decreasing metal work function. Conversely, for n-type material, interface resistance increased with increasing metal work function. At high(low) interface-resistance, both systems displayed rectifying(ohmic) I-V behaviour, which was attributed to the formation of a Schottky(an ohmic) contact [20, 23–25]. Sawa *et al.*'s study sparked huge interest into the effect of electrode materials on RS performance, and prompted researchers to use spectroscopic methods to investigate oxygen vacancy electromigration and interfacial chemistry, such as the studies presented in this work [20, 25–29]. In Chapter 3, n-type ZnO thin films are sandwiched between a Ti top electrode, which forms a Ohmic contact and a Pt bottom electrode, which forms an Schottky contact. A more complex ternary oxide structure was fabricated by collaborators for the $PrCaMnO_3$ study presented in Chapter 4; this device employs a dedicated interfacial oxide, the role of which will be described in section 1.2.6.

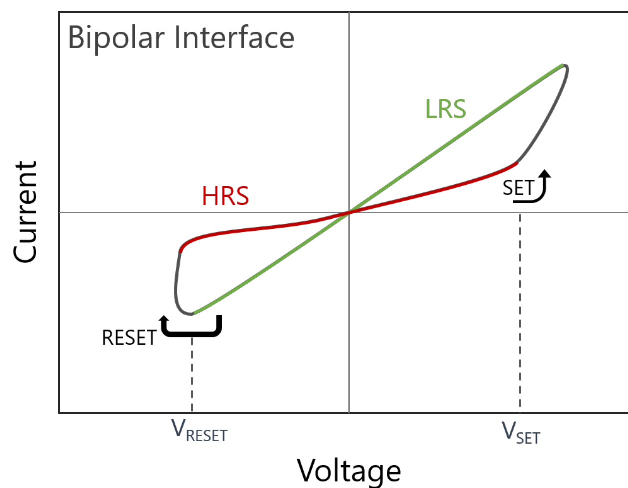

Figure 1.15: *Example of a bipolar, interface resistive switching IV curve where the LRS is highlighted in green and the HRS is highlighted in red. As current increases gradually, compliance currents are not always employed.*

Through electrical characterisation, it is possible to distinguish between filamentary- and interface-homogeneous-RS: interface-homogeneous effects produce smooth, gradual IV curves, which contrast the sharp switches produced in filamentary IV curves. Furthermore, interface-RS gives rise to a dependence on electrode area [20]. However, these two VCM geometries represent two ends of the spectrum: it is possible to show characteristics of both filamentary- *and* interface-RS. For instance, area scaling devices can show dependence on electrode area at μm scales, but independence on nm scales [5].

The $PrCaMnO_3$ device presented in Chapter 4 is an example of this. In terms of RRAM device scalability, such a geometry imposes a minimum size limit. As such, high-resolution microscopic studies are required to fully characterise such materials systems.

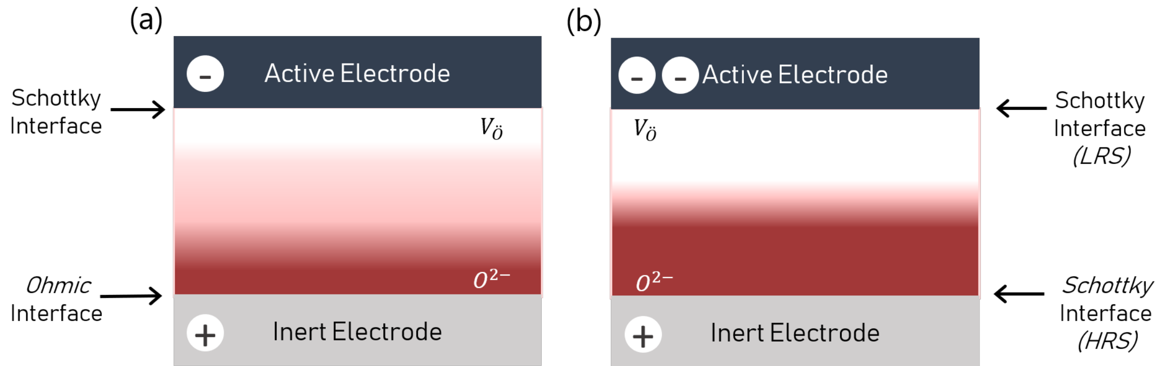

Figure 1.16: *'Reverse' valence change memory in an n-type MOM cell. $V_{\ddot{O}}$-rich regions are shown in white, and O_2-rich regions are shown in dark red. (a) LRS of an interface-VCM RS device where the Schottky interface is located below the active electrode. This is the same set-up shown in Fig.1.14(a) and is included for comparison. (b) HRS of reverse-interface-VCM RS device, which is achieved at the same polarity as (a), but at a larger voltage magnitude. This increased voltage further depletes the of an oxygen-rich ($V_{\ddot{O}}$-deficient) region at the inert electrode, forming a second Schottky interface that dictates the RS state of the device.*

It has also been shown that for interface-VCM, RS-governing processes can occur at different locations within a MOM structure. For devices designed with additional layers such as tunnel oxides, which are described further in Chapter 4, RS that is localised by design offers researchers further control over the performance of a RRAM device. It is interesting to note that differences in the location of RS-determining processes can affect the voltage polarity dependence of the device [30]. Researchers have shown that interface-VCM can exhibit bipolar RS with *opposite* polarity dependence (typically defined as clockwise or anticlockwise) to that described in Fig.1.14 [9]. For example, Dittmann *et al.* observed both clockwise and anti-clockwise RS within the same perovskite oxide $Fe:SrTiO_3$ MOM structure, where one switching regime was accessed at increased voltages with respect to the other [31, 32]. In this publication they proposed that if the insulating layer (perovskite oxide $Fe:SrTiO_3$) is much thinner than the anode, then, once the device is electroformed, sufficient negative biasing of the cathode could induce the migration of $V_{\ddot{O}}$ from the region of insulating film closest to the inert electrode, which is depicted in Fig.1.16(b). This $V_{\ddot{O}}$-depletion (O^{2-}-accumulation) leads to the formation

of a second insulating Schottky barrier at the insulator/inert electrode interface. This second Schottky interface competes with the barrier located at the insulator/active electrode interface to govern the overall resistance state of the device. However, as shown in Figs.1.14(b) and (d), a small number of $V_{\ddot{O}}$ leads to an increase in W_d which increases the resistance of the device. This means, as soon as $V_{\ddot{O}}$ begin to migrate from the inert electrode region, the device is dominated by the high resistance Schottky barrier that is immediately formed. The formation of the second, more dominating Schottky barrier shown in Fig.1.16 accounts for the observation of bipolar switching that occurs at the *reverse* polarity to that shown in Fig.1.16(b) within the same sample [9, 31]. This VCM model is consistent with the polarity dependence of bipolar electrode-area-dependent (interface-) RS that has been observed in a number of MOM structures comprising *single crystal* perovskite oxides published in the literature [20, 33, 34].

1.2.6 Interfacial oxides for Valence Change Memory

In addition to the choice of electrode materials, it is possible to improve device performance using additional non-switching layers, such as interfacial oxides. There are two types of interfacial oxides that can facilitate VCM RS: redox-formed oxides, shown in Fig.1.17(a), and dedicated oxides, shown in Fig.1.17(b). The first are formed due to the redox of an electrochemically active electrode material and can thicken during an electroforming process. Chang *et al.* showed that, in comparison to high work function metal Pt ($\phi_W \sim 5.6$eV), low work function metals Cr ($\phi_W = 4.5$eV) and Al ($\phi_W = 4.2$eV) were oxidised to form CrO_x and AlO_x interfacial oxides at the insulator/metal interface [35], which is depicted in Fig.1.17(a). Conversely, they showed that within the vicinity of the oxidisable electrode, the insulator material, ZnO, was reduced to ZnO_{1-x}. This observation proved the existence of an exchange of $V_{\ddot{O}}$ between the insulator and electrode (shown by the white arrows in Fig.1.17(a)), showing that the interfacial oxide acted as a *oxygen reservoir*. The $V_{\ddot{O}}$-exchange between the reservoir and insulator was shown to promote RS and improve device stability [35]. Through *in-situ* Transmission Electron Microscopy, these interfacial oxides have recently been shown to grow and shrink in the HRS and LRS respectively, which is consistent with Sawa *et al.*'s direction of $V_{\ddot{O}}$-migration in the Schottky VCM RS model [28]. This

type of interfacial oxide has been identified through the use of spectroscopic techniques in VCM RS devices across the literature [18, 19, 24, 28, 36]. Given the low work function of Ti, an interfacial TiO_x was also expected to contribute towards RS in the ZnO device presented in Chapter 3.

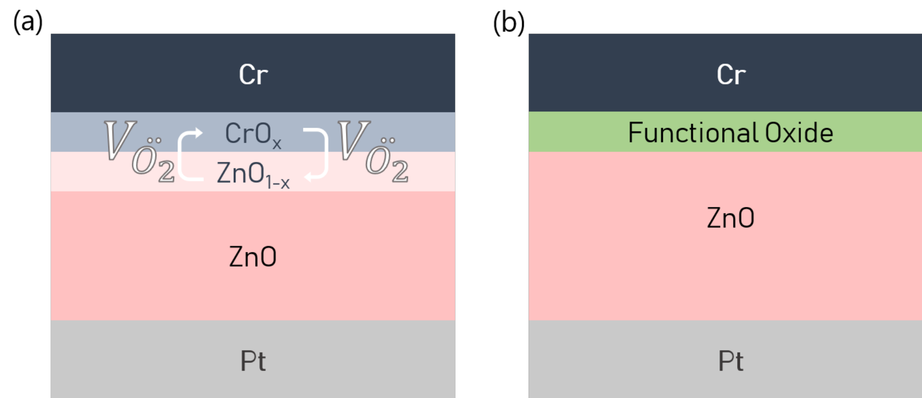

Figure 1.17: *(a) Redox-formed CrO_x interfacial oxide formed in a Cr/ZnO/Pt device discussed in [35]. Here, the oxidation of the Cr electrode causes a reduction of the nearby ZnO film, forming a ZnO_{1-x} layer. (b) Dedicated functional oxide that was deposited during fabrication.*

Fig.1.17(b) presents the second type of interfacial oxides, *dedicated* oxides. These are deliberately deposited between the RS insulator and the electrode material. As for electroformed interfacial oxides, these dedicated oxides can also serve as oxygen reservoirs. However, it should be noted that as they are not formed as a result of redox, they do not generate a non-stoichiometric region within the insulating film. When considering RRAM design, these oxides have an advantage in terms of the uniformity of the interfacial layer. For example, in comparing electroformed oxides CrO_x and AlO_x, Chang *et al.* found that the oxidation of the (Al)Cr electrode occurred (in)homogeneously, leading to a $(AlO_x)CrO_x$ film with (non-)uniform thickness that displayed (poor)excellent RS endurance [35]. The difference between these electroformed oxides was ascribed to the difference in the Gibbs free energy of oxide formation. Considering this, the deposition of dedicated oxides provides one with a greater choice of materials, as interfacial oxide formation is not limited by thermodynamics. It should be noted that dedicated oxides are not limited to the sole function of an oxygen reservoir, these can have additional functional properties that enhance the device. For example, researchers have shown that the thickness of dedicated *tunnel-oxides* can be used to tune the magnitude of

the LRS and HRS [37]. In these devices, the tunnel-barrier height is modulated by the accumulation of charged $V_{\ddot{O}}$ during VCM RS, which is similar to the $V_{\ddot{O}}$-modulated Schottky barrier formed at the oxide/metal interface described above. A tunnel-barrier device, fabricated by collaborators, was investigated and is presented in Chapter 4.

1.3 Scope of Research

In this work, Electron Energy Loss Spectroscopy (EELS), an analytical electron microscopy (AEM) technique that is sensitive to the bonding environments and valence states of probed atoms, was used to investigate RS-induced electrochemical changes in thin-film RRAM heterostructure devices incorporating polycrystalline (doped and undoped) ZnO (presented in Chapter 3) and crystalline perovskite oxide $PrCaMnO_3$ (presented in Chapter 4). With respect to RRAM and the mechanisms of RS, the degree of sensitivity provided by EELS offers valuable insight into both the presence of and the extent of redox-mediated RS effects within metal-oxide materials [18, 26, 38, 39]. Taking filamentary VCM in an n-type material as an example, EELS has been used to identify conductive filaments consisting of reduced, lower valence state material, and the surrounding, fully oxidised thin film [40], as depicted in Figs.1.13(a) and (b) and described by Eqn.1.3. Similarly, the area-homogeneous redox present in interface-VCM devices can also be identified using EELS. In fact, over the past decade, studies have presented EELS data showing evidence for just that: gradual, bipolar RS that occurs due to electric-field-stimulated redox reactions at the insulator/metal interface, consistent with the interface-VCM RS mechanism described in section 1.2.5 [18, 24, 41, 42]. However, in addition to these findings, the literature also presents an overwhelming amount of evidence for the variability of RS in terms of cycling endurance, polarity dependence and the ratio between resistance states. In many cases in the literature, these negative performance attributes and issues are not discussed, which contributes to a lack of clarity and slows progression in the field. The more comprehensive studies have shown that the increased performance variability is largely attributed to both the interfacial chemistry effects that are governed by the choice of materials employed, and the complexity of the competition between multiple simultaneous nanoscale RS mechanisms. As

such, progression in RRAM research will remain limited unless electrochemically sensitive spectroscopic techniques, such as EELS, are used in addition to electrical characterisation to fully characterise the contributing mechanisms that are responsible for RS in carefully designed RRAM structures. Furthermore, given the complex interplay between numerous simultaneous RS mechanisms, it is essential *spatially-resolved* techniques like EELS are employed to distinguish between homogeneous, in homogeneous, bulk material and interfacial effects.

The research undertaken here was 3-fold: it involved the design and fabrication, electrical characterisation and EELS analysis of VCM-type RRAM devices. This allowed for the optimisation of RRAM devices and attribution of RS characteristics to spatial, chemical and/or morphological effects. In particular, the research presented in Chapter 3 performed to fill a knowledge gap relating to the field-induced redistribution of $V_{\ddot{O}}$ across a simple MOM (Ti/Mn:ZnO/Pt) structure during RS. It had been previously proposed that such $V_{\ddot{O}}$-electromigration could be attributed to the stimulation of room temperature ferromagnetism in Mn-doped ZnO in addition to simultaneously stimulating changes in the resistive state of the film [43]. Through the EELS analysis of pristine and programmed devices, it was possible to use the valence state of the dopant Mn ions to map the redistribution of $V_{\ddot{O}}$ across the device. Such mapping showed evidence for the presence of two adjacent interfacial phases, both chemically distinct from the bulk Mn:ZnO, that acted as O^{2-}- and $V_{\ddot{O}}$-reservoirs respectively, where $V_{\ddot{O}}$ were exchanged across their shared interface. In addition, the mapping of Mn showed evidence for the clustering of Mn dopants along grain boundaries, which has been alluded to in the literature, but not confirmed. Finally, quantification analysis of the EELS spectra (described further in section 2.7.3) suggested that Mn dopants, in addition to $V_{\ddot{O}}$, underwent electromigration during RS. Similarly, in Chapter 4, the valence state of the Mn present in $PrCaMnO_3$ was used to monitor $V_{\ddot{O}}$ redistribution; these single crystal devices were fabricated and electrically characterised by collaborators in Jülich and incorporate an $V_{\ddot{O}}$-rich dedicated tunnel oxide deposited adjacent to the $PrCaMnO_3$. Owing to the sharp interface between the tunnel oxide and the $PrCaMnO_3$, the EELS analysis undertaken performed to further our understanding of the spatial homogeneity of $V_{\ddot{O}}$-electromigration. Indeed, through comparison of EELS spectra acquired from HRS-

and LRS-programmed devices, reproducible changes in Mn valence state were observed. Specifically, it was found that despite showing top electrode area scaling of electrical characteristics, the redox activity of Mn at the interface was spatially inhomogeneous, which is not typically reported in the literature.

1.3.1 Thesis Outline

Chapter 2 describes the instruments and techniques used to fabricate and characterise the ZnO and $PrCaMnO_3$ RRAM devices investigated. Chapter 2 has a particular focus on Pulsed Laser Deposition and Transmission Electron Microscopy, and presents the underlying physics describing Electron Energy Loss Spectroscopy, which is the primary spectroscopic method used to investigate RRAM mechanisms in this work. Chapter 3 presents polycrystalline undoped and Mn-doped ZnO thin-film devices that were deposited using a local Pulsed Laser Deposition system and Chapter 4 presents a crystalline $PrCaMnO_3$ device that was fabricated by collaborators at the Peter Grünberg Institute Research Center Jülich, who also characterised the device using Hard X-ray Photoelectron Spectroscopy, which is described in Section 2.8. In both results chapters, RRAM performance is discussed with respect to the structural and chemical changes revealed during electron microscopy and spectroscopic analysis. Finally, Chapter 5 summarises all conclusions and outlines future work that should be implemented in the development of this research field.

Bibliography

[1] A. Sebastian, T. Tuma, N. Papandreou, M. Le Gallo, L. Kull, T. Parnell, and E. Eleftheriou. Temporal correlation detection using computational phase-change memory. *Nature Communications*, 8(1), 2017.

[2] D. S. Jeong, R. Thomas, R. S. Katiyar, J. F. Scott, H. Kohlstedt, A. Petraru, and C. S. Hwang. Emerging memories: resistive switching mechanisms and current status. *Reports on Progress in Physics*, 75:076502, 2012.

[3] S. Yu and P. Y. Chen. Emerging Memory Technologies: Recent Trends and Prospects. *IEEE Solid-State Circuits Magazine*, 8(2):43–56, 2016.

[4] J. Meena, S. Sze, U. Chand, and T. Tseng. Overview of emerging nonvolatile memory technologies. *Nanoscale Research Letters*, 9(1):526, 2014.

[5] R. Waser, R. Dittmann, G. Staikov, and K. Szot. Redox-Based Resistive Switching Memories - Nanoionic Mechanisms, Prospects, and Challenges. *Advanced Materials*, 21(25-26):2632–2663, 2009.

[6] J. F. Scott and C. Paz de Araujo. Ferroelectric Memories. *Science*, 246:1–26, 1988.

[7] L. O. Chua. Memristor: The Missing Circuit Element. *IEEE Transactions on Circuit Theory*, 18(5):507–519, 1971.

[8] D. B. Strukov, G. S. Snider, D. R. Stewart, and R. S. Williams. The missing memristor found. *Nature*, 453(7191):80–83, 2008.

[9] F. Pan, S. Gao, C. Chen, C. Song, and F. Zeng. Recent progress in resistive random access memories: Materials, switching mechanisms, and performance. *Materials Science and Engineering: R: Reports*, 83:1–59, 2014.

[10] S. Gao, C. Song, C. Chen, F. Zeng, and F. Pan. Dynamic processes of resistive switching in metallic filament-based organic memory devices. *Journal of Physical Chemistry C*, 116(33):17955–17959, 2012.

[11] H. W. Huang, C. F. Kang, F. I. Lai, J. H. He, S. J. Lin, and Y. L. Chueh. Stability scheme of ZnO-thin film resistive switching memory: influence of defects by controllable oxygen pressure ratio. *Nanoscale research letters*, 8(1):483, 2013.

[12] I. Valov, R. Waser, J. R. Jameson, and M. N. Kozicki. Electrochemical metallization memories–fundamentals, applications, prospects. *Nanotechnology*, 22(25):254003, 2011.

[13] R. Waser. Electrochemical and Thermochemical Memories. *Technical Digest - International Electron Devices Meeting, IEDM*, 2008.

[14] D. Ielmini, R. Bruchhaus, and R. Waser. Thermochemical resistive switching: Materials, mechanisms, and scaling projections. *Phase Transitions*, 84(7):570–602, 2011.

[15] F. A. Chudnovskii, L. L. Odynets, A. L. Pergament, and G. B. Stefanovich. Electroforming and switching in oxides of transition metals: The role of metal-insulator transition in the switching mechanism. *Journal of Solid State Chemistry*, 122(1):95–99, 1996.

[16] I. H. Inoue, S. Yasuda, H. Akinaga, and H. Takagi. Nonpolar resistance switching of metal/binary-transition-metal oxides/metal sandwiches: Homogeneous/inhomogeneous transition of current distribution. *Physical Review B - Condensed Matter and Materials Physics*, 77(3):1–7, 2008.

[17] Raúl Zazpe Rz Mendioroz. *Resistive switching in Hafnium Oxide*. PhD thesis, Universidad del País Vasco, 2014.

[18] P. Parreira, G. W. Paterson, S. McVitie, and D. A. MacLaren. Stability, bistability and instability of amorphous ZrO2 resistive memory devices. *Journal of Physics D: Applied Physics*, 49(9):095111, 2016.

[19] A. Herpers, K. J. O'Shea, D. A. Maclaren, M. Noyong, B. Rösgen, U. Simon, and R. Dittmann. Competing strain relaxation mechanisms in epitaxially grown $Pr_{0.48}Ca_{0.52}MnO_3$ on $SrTiO_3$, volume = 2, year = 2014. *APL Materials*, (10):0–8.

[20] A. Sawa. Resistive switching in Transition Metal Oxides. *Materials Today*, 11(6):28–36, 2008.

[21] T. Baiatu, R. Waser, and K. H. Härdtl. dc Electrical Degradation of Perovskite-Type Titanates: III, A Model of the Mechanism. *Journal of the American Ceramic Society*, 73(6):1663–1673, 1990.

[22] D. S. Hong, Y. S. Chen, Ying Li, H. W. Yang, L. L. Wei, B. G. Shen, and J. R. Sun. Evolution of conduction channel and its effect on resistance switching for Au-WO3-x-Au devices. *Scientific Reports*, 4:1–6, 2014.

[23] B. J. Choi, D. S. Jeong, S. K. Kim, C. Rohde, S. Choi, J. H. Oh, H. J. Kim, C. S. Hwang, K. Szot, R. Waser, B. Reichenberg, and S. Tiedke. Resistive switching mechanism of TiO2 thin films grown by atomic-layer deposition. *Journal of Applied Physics*, 98(3), 2005.

[24] F. Borgatti, C. Park, A. Herpers, F. Offi, R. Egoavil, Y. Yamashita, A. Yang, M. Kobata, K. Kobayashi, J. Verbeeck, G. Panaccione, and R. Dittmann. Chemical insight into electroforming of resistive switching manganite heterostructures. *Nanoscale*, 5(9):3954–60, 2013.

[25] A. Sawa, T. Fujii, M. Kawasaki, and Y. Tokura. Hysteretic current-voltage characteristics and resistance switching at a rectifying Ti/Pr0.7Ca0.3MnO3 interface. *Applied Physics Letters*, 85(18):4073–4075, 2004.

[26] A. Herpers, C. Lenser, C. Park, F. Offi, F. Borgatti, G. Panaccione, S. Menzel, R. Waser, and R. Dittmann. Spectroscopic proof of the correlation between redox-state and charge-carrier transport at the interface of resistively switching Ti/PCMO devices. *Advanced Materials*, (26):2730–2735, 2014.

[27] Z. L. Liao, Z. Z. Wang, Y. Meng, Z. Y. Liu, P. Gao, J. L. Gang, H. W. Zhao, X. J. Liang, X. D. Bai, and D. M. Chen. Categorization of resistive switching of metal-Pr0.7Ca0.3MnO3-metal devices. *Applied Physics Letters*, 94(25):253503, 2009.

[28] K. Baek, S. Park, J. Park, Y. M. Kim, H. Hwang, and S. H. Oh. In situ TEM observation on the interface-type resistive switching by electrochemical redox reactions at a TiN/PCMO interface. *Nanoscale*, 9(2):582–593, 2017.

[29] X. B. Yin, Z. H. Tan, and X. Guo. The role of Schottky barrier in the resistive switching of SrTiO3: direct experimental evidence. *Physical Chemistry Chemical Physics*, 17(1):134–137, 2015.

[30] D. Cooper, C. Baeumer, N. Bernier, A. Marchewka, C. La Torre, R. E. Dunin-Borkowski, S. Menzel, R. Waser, and Regina Dittmann. Anomalous Resistance Hysteresis in Oxide ReRAM: Oxygen Evolution and Reincorporation Revealed by In Situ TEM. *Advanced Materials*, 29(23):1–8, 2017.

[31] Regina Dittmann, Ruth Muenstermann, Ingo Krug, Daesung Park, Tobias Menke, Joachim Mayer, Astrid Besmehn, Florian Kronast, Claus Michael Schneider, and Rainer Waser. Scaling potential of local redox processes in memristive SrTiO3 thin-film devices. *Proceedings of the IEEE*, 100(6):1979–1990, 2012.

[32] R. Muenstermann, T. Menke, R. Dittmann, and R. Waser. Coexistence of filamentary and homogeneous resistive switching in Fe-doped SrTiO3 thin-film memristive devices. *Advanced Materials*, 22(43):4819–4822, 2010.

[33] J. Park, D. H. Kwon, H. Park, C. U. Jung, and M. Kim. Role of oxygen vacancies in resistive switching in Pt/Nb-doped SrTiO3. *Applied Physics Letters*, 105(18), 2014.

[34] W. Lü, C. Li, L. Zheng, J. Xiao, W. Lin, Q. Li, X. R. Wang, Z. Huang, S. Zeng, K. Han, W. Zhou, K. Zeng, J. Chen, Ariando, W. Cao, and T. Venkatesan. Multi-Nonvolatile State Resistive Switching Arising from Ferroelectricity and Oxygen Vacancy Migration. *Advanced Materials*, 29(24):1–8, 2017.

[35] W.-Y. Chang, H.-W. Huang, W.-T. Wang, C.-H. Hou, Y.-L. Chueh, and J.-H. He. High Uniformity of Resistive Switching Characteristics in a Cr/ZnO/Pt Device. *Journal of the Electrochemical Society*, 159(3):29–32, 2012.

[36] C. Chen, S. Gao, F. Zeng, G. S. Tang, S. Z. Li, C. Song, H. D. Fu, and F. Pan. Migration of interfacial oxygen ions modulated resistive switching in oxide-based memory devices. *Journal of Applied Physics*, 114(1), 2013.

[37] R. Meyer, L. Schloss, J. Brewer, R. Lambertson, W. Kinney, J. Sanchez, and D. Rinerson. Oxide dual-layer memory element for scalable non-volatile cross-point memory technology. *Proceedings - 2008 9th Annual Non-Volatile Memory Technology Symposium, NVMTS 2008*, (C):1–5, 2008.

[38] B. Arndt, F. Borgatti, F. Offi, M. Phillips, P. Parreira, T. Meiners, S. Menzel, K. Skaja, G. Panaccione, D. A. Maclaren, R. Waser, and Regina Dittmann. Spectroscopic Indications of Tunnel Barrier Charging as the Switching Mechanism in Memristive Devices. *Advanced Functional Materials*, 1702282, 2017.

[39] W. Zhu, T. P. Chen, Y. Liu, and S. Fung. Conduction mechanisms at low- and high-resistance states in aluminum/anodic aluminum oxide/aluminum thin film structure. *Journal of Applied Physics*, 112(6), 2012.

[40] J. S. Lee, S. Lee, and T. W. Noh. Resistive switching phenomena: A review of statistical physics approaches. *Applied Physics Reviews*, 2(3), 2015.

[41] S. Asanuma and H. Akoh. Relationship between resistive switching characteristics and band diagrams of Ti/Pr(1x)Ca(x)MnO(3) junctions. *Physical Review B*, 80:1–8, 2009.

[42] Daniele Ielmini. Interface-Type Switching. In A. Sawa and R. Waser, editors, *Resistive Switching: From Fundamentals of Nanoionic Redox Processes to Memristive Device Applications, 1*, chapter 16, pages 457–482. Wiley-VCH, 2016.

[43] S. Ren, J. Dong, W. Chen, L. Zhang, J. Guo, L. Zhang, J. Zhao, and X. Zhao. Study on the oxygen vacancy redistribution and the mechanism of electrical manipulation of ferromagnetism in diluted magnetic oxides. *Journal of Applied Physics*, 118(23):233902, 2015.

CHAPTER 2

Instrumentation

A comprehensive suite of fabrication and analytical protocols were employed so that variations in RRAM device performance could be attributed to fabrication-controlled nanoscale structural and chemical characteristics. The study presented in Chapter 3 required the use of Pulsed Laser Deposition (described in Section 2.2) for the controlled deposition of zinc oxides, and a standardised patterning metallisation process which included photolithography and electron-beam evaporation techniques (described in Section 2.3) for the formation of electrical contacts. Optimisation of the deposition of oxide thin films was possible through an assessment of surface topology via Atomic Force Microscopy (described in Section 2.9) and the characterisation of electrical properties using an electrical probe station (described in Section 2.10). Analysis of the structural and chemical properties of thin film devices are presented in Chapters 3 and 4, where the data were acquired on a Transmission Electron Microscope equipped for Electron Energy Loss Spectroscopy, a set-up further described in Section 2.6. Electron-transparent lamellas suitable to loading into the Transmission Electron Microscope were created using a DualBeam Focused Ion Beam Scanning Electron Microscope system (described in Section 2.4). Hard X-ray Photo-Electron Spectroscopy was employed by collaborators in the study presented in Chapter 4 and spectroscopy technique is described in Section 2.8.

2.1 Physical Vapour Deposition

An ever increasing demand for novel, functional thin film materials in fields such as micro-electronics has required rapid development of both vacuum deposition technology and our understanding of the underlying chemical and physical processes that occur during thin film deposition and growth. A wide range of deposition technologies are available. Each of these can be broadly categorised as either a *physical* process such as Molecular Beam Epitaxy (MBE), a thermal evaporation method used for the fabrication of Si and GaAs devices, or as a *chemical* process, such as Chemical Vapour Deposition (CVD), a method widely used for applications in surface coating in which material is deposited as result of stimulated chemical reactions [1]. In this work, chemical deposition technologies were not utilised, instead, a combination of Physical Vapour Deposition (PVD) techniques were employed to fabricate multi-layer thin film devices. The use of more than one PVD method was necessary as each technique has unique advantages that best served the functional requirements of individual layers within the device heterostructure. For instance, in 1995 Gupta *et al.* published a comparison of amorphous carbon deposited via four different deposition methods, which produced a variation in mechanical properties, including hardness and elastic modulus [2].

2.2 Pulsed Laser Deposition

Also a PVD technique, Pulsed Laser Deposition (PLD) is a popular deposition method used predominantly in academic research. Its appeal is due to many aspects: its capacity for deposition under ambient gas at pressures ranging from atmosphere to 10^{-9}Torr, its ability to deposit composite materials away from thermal equilibrium, and its ability to deposit complex multiple-component materials at stoichiometry [1, 3–5]. The latter is the most important motivation for the use of PLD in this work, which includes the optimisation of stoichiometric oxide thin film deposition, which is further discussed in Chapter 3.

A PLD system allows users to focus a series of high-power laser pulses into a deposition chamber and onto a target material which vaporises, forming a plasma

comprising highly energetic species, with energies between 1 and 100eV [5, 6]. This plasma expands upwards and outwards, allowing the energetic species to condense onto the substrate surface and initiating the thin film growth process, which is described further in Chapter 3. The very first deposition of thin films using PLD was demonstrated by Smith and Turner in 1965 [7], who successfully grew compound semiconductor films and binary oxides. In 1988, a comprehensive study completed by Cheung and Sankur demonstrated the versatility of the PLD technique, reporting on a broad collection of deposited materials, including most notably, the stoichiometric deposition of complex oxide ceramics under oxygen [8]. This study was published not long after pioneering work was published by Bednorz and Muller, who demonstrated the successful production of superconducting copper-oxide-based ceramic thin films in 1986 [9]. These two significant ceramic oxide studies changed the perception of PLD from an exotic method of growth to an extremely versatile tool that could provide researchers with access to a plethora of complex, innovative materials systems [10].

A typical PLD system comprises an ultra-high vacuum (UHV) chamber capable sustaining of pressures of order 10^{-7}Pa, a high power laser, and an optical system. Fig.2.1 shows how the optical system allows one to focus the laser on the target, which is typically mounted onto a motorised target carousel with two degrees of motion. These are indicated by the purple arrows in Fig.2.1: rotation about its own axis, and movement back and forth, parallel to the target surface. The carousel grants easy access to a range of materials, permitting the deposition of multilayer thin film heterostructures. Fig.2.1 also illustrates that the chamber can be filled with background gas via a mass flow controller. Background gasses can be used to manipulate thin film growth via two effects: reactive gases can be employed to achieve the desired chemical composition, such as the use of molecular oxygen for the deposition of oxides; and background gas pressure can be varied to reduce the average kinetic energy of plume species arriving at the substrate [1]. Thin film properties are also affected by substrate temperature, which can be used to improve or retard atom mobility. Given that during plume expansion some portion of the plasma species eventually slow and stop propagating towards the substrate [11], the distance between the substrate and the target can be changed to control growth rates. As such, PLD systems users typically mount substrates onto

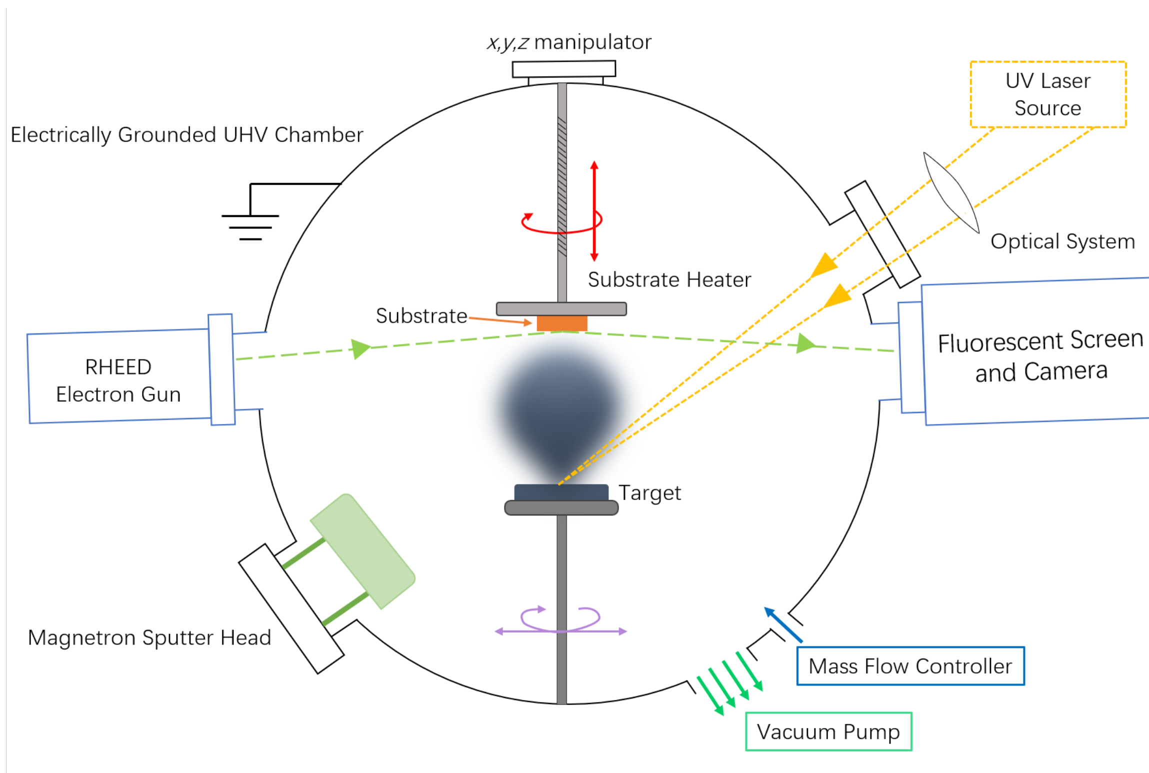

Figure 2.1: *Schematic diagram of a UHV vacuum that accommodates pulsed laser and magnetron sputtering deposition systems. Laser pulses are guided into the deposition chamber through a window and onto a target that is held on a motorised target carousel system; the purple arrows represent possible motion. The substrate is also attached to a motorised holder which can be resistively heated and can move in the directions represented by the red arrows. A turbo-molecular vacuum pump was used to evacuate the chamber via the outlet highlighted by the green arrows, and a mass flow controller was used to control gas flow into the deposition chamber through the gas inlet highlighted by the single blue arrow.*

motorised holders that can be heated as required, where the substrate can rotate about its own axis, and can be positioned along the z-axis, as shown by the red arrows in Fig.2.1.

In this work, a Neocera Pioneer PLD system was used in conjunction with a 248nm UV excimer laser (Coherent Compex Pro). The laser used has pulse duration 20ns, a typical laser fluence 1-2J/cm^2, and could be programmed to pulse at rates ranging between 1-20Hz. Evacuated by a Pfeiffer 355ls^{-1} turbo-molecular pump, which itself is backed by an Edwards 1.7ls^{-1} rough scroll pump, the deposition chamber has a base pressure of 1×10^{-5}mTorr without baking. Within the deposition chamber, up to six targets are mounted on a motorised target carousel, and the substrate is loaded into a motorised holder that features a resistive heater, allowing for the adjustment

of the target-substrate distance and substrate temperature by up to 8cm and 1000°C respectively.

Additional components can be mounted onto the UHV chamber to provide either complementary deposition techniques or *in-situ* analytical techniques. The apparatus used in this work features an additional magnetron sputter source, which allows for the deposition of metals. Furthermore, the PLD system also includes a Reflection High Energy Electron Diffraction (RHEED) system (shown in Fig.2.1) that allows for in-situ surface characterisation during deposition. This technique allows one to continuously record the diffraction pattern produced by electrons that are scattered by the substrate surface at low grazing angles ($\sim 0.5°$). In particular, the intensity of a diffracted spot relates to the reflectivity of the surface, which in turn is governed by the surface roughness [12]. During layer-by-layer growth, the surface roughness oscillates, which means that monitoring diffraction spot intensity allows for an identification of growth mode. However, RHEED data were not acquired for the studies presented in this work as epitaxial 2D growth was not required.

2.2.1 Laser-Matter Interaction

Although the principle of PLD operation itself is relatively simple, the interaction between the laser and the target material is a complex process. The earliest models assumed the interaction to be a purely thermal effect, which was later experimentally proven to be an incomplete description that could not account for resultant electron and ion emissions [1]. Today it is known that, dependent on the laser fluence at the target, the laser-matter interaction can be split into two stages: the laser-solid interaction, which is triggered at low-fluence, as shown sequentially in Figs.2.2(a)(b) and (f), and the formation and expansion of the plasma plume, which is triggered at high-fluence, as shown sequentially in Figs.2.2(a)-(e) [13]. It is the condensation of the plasma species generated at high-fluence onto the substrate surface that initiates the process of thin film growth, which is further described in Chapter 3.

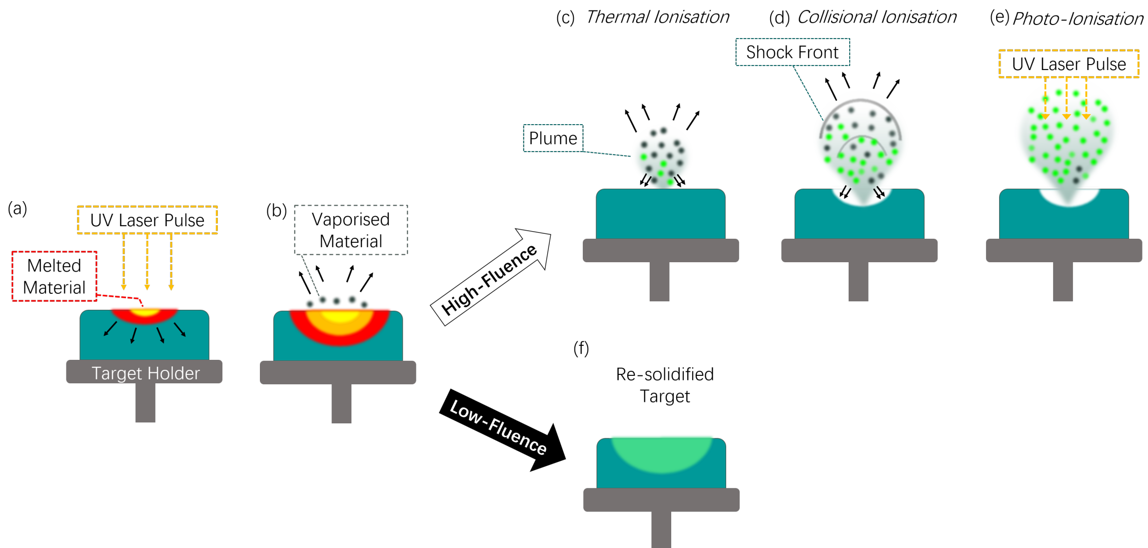

Figure 2.2: *The four stages of laser-matter interaction during the ablation of a PLD target. At high laser fluence, the interaction passes through stages (a),(b),(c),(d) and (e) consecutively, whereas at low laser fluence, stage (f) follows stage (b). Stages (a) and (b) depict the melting and subsequent vaporisation of the target, which at high-fluence is followed by the creation of a plume of ejected material, partly thermally ionised. This is followed by stages (d) and (e) where the plume becomes increasingly ionised due to shock wave collisional ionisation and further laser irradiation. In contrast, at low-fluence, the vaporisation stage is followed by the re-solidification of melted material, as shown in (f).*

At high fluence, two processes occur: as found for lower laser fluence, the melting front of the target material propagates through the target, and a luminous plume of vaporised material containing species with high kinetic energy is ejected normal to the surface of the target [10]. The vapour is produced at extremely high temperatures ($\sim 10^3$K) that support the thermal ionisation of ablated species, forming a plasma plume [5, 14]. As depicted in Fig.2.2(d), the formation of the plume effectively *sputters* the surface of the target material, where sputtering is defined as the vaporisation of a target material which is ejected as a result of energetic ion-bombardment [15–17]. For the remainder of the laser pulse, the plume absorbs laser irradiation, triggering the photo-ionisation of neutral species and increasing the extent of plume ionisation [5,13,18]. Furthermore, at sufficiently high temperature and density, the plume effectively shields the target from further irradiation, as shown in Fig.2.2(d) [14]. The degree of ionisation changes during the course of plasma expansion due to ion-electron recombination [5]. The luminosity of the plume is due the relaxation of excited positive ions that generate photons, and can be observed as the highly directional plume expands towards the

substrate [5]. During the expansion of the plasma plume, the plasma species undergo collisions with atoms in the ambient gas which cause the plasma species to slow and eventually stop. At relatively high background pressures (10-150mTorr), the plume couples with the ambient gas and undergoes shockwave propagation and features a shock front (depicted in Fig.2.2(d)). Fig.2.2(d) illustrates how shockwave propagation allows for further ionisation of the plume through collisional ionisation. Furthermore, these collisions cause an increase in the lateral spread of the ejected particles, creating a cone shaped plasma plume as shown in Figs.2.2(d)(e). In contrast to the shielding properties of a hot, dense plume, the expansion of the plume allows it to cool adiabatically. Eventually the plume becomes transparent to further laser irradiation which allows for laser-solid interaction to occur once again.

2.3 Metallisation

As described in Chapter 1, RRAM devices comprise two metallic electrode contacts sandwiching one or more active layers. In order to fabricate the devices investigated in Chapter 3, electron-beam (e-beam) evaporation was used to deposit a Ti/Pt bottom electrode layer onto Si/SiO_x substrates, where the Ti acted as an adhesion layer. The bottom electrodes served as substrates for the PLD of Mn:ZnO and ZnO thin films. To isolate RRAM devices for electrical characterisation after the deposition of continuous thin films, photolithography followed by e-beam evaporation was used to pattern a series of top electrode contacts (Ti/Pt, and Pt) on the surface of the active layer, as shown in Fig.2.4 where more details are provided. These standardised processes were undertaken in the extensive cleanroom facility available on campus, the James Watt Nano-Fabrication Center (JWNC), and will now be described.

2.3.1 Photolithography

Photolithography is a patterning technique in which the UV photo-irradiation of an organic polymer film (photoresist), spun onto a substrate surface, triggers structural changes in the photoresist film structure. Depending on the nature of the structural response, photoresists are categorised as positive or negative tone; after photo-irradiation,

positive tone photoresist undergoes chain scission, the degradation of polymer chains, which results in a *decrease* in photoresist solubility, whilst negative photoresist undergoes chain cross-linking, the bonding of polymer chains, which causes an *increase* in photoresist solubility [19]. Fig.2.3(a) shows how a patterned a mask can be used to expose specific regions of the photoresist to UV irradiation. This results in localised structural changes, as shown in Fig.2.3(b). When immersed in developer, the most soluble region of photoresist will dissolve, producing a patterned photoresist layer, as shown in Fig.2.3(c).

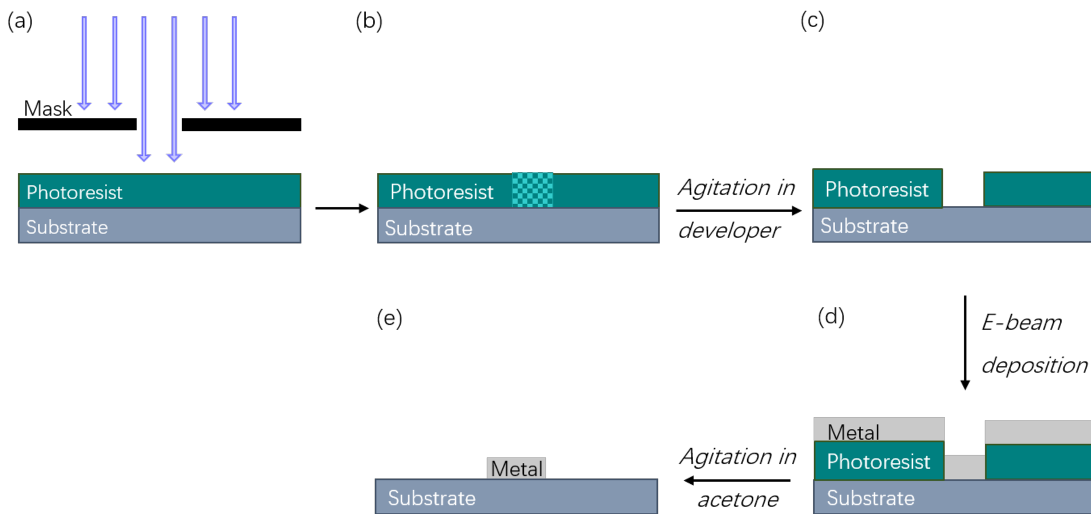

Figure 2.3: *Steps required for photolithography after photoresist spinning are shown in images (a)-(c), where (a) depicts the use of a mask to prevent/allow UV exposure on specific regions of the photoresist, (b) illustrates structural changes in the photoresist as a result of photo-irradiation, and (c) shows the remaining patterned photoresist after the dissolution of the exposed photoresist. Images (d) and (e) depict the final metallisation steps described in Section 2.3.2; (d) shows the deposition of metal onto the patterned photoresist, and (e) shows the final metallised pattern obtained after agitation in acetone.*

Microposit S1818 positive photoresist was spun onto PVD thin film heterostructures at 4000rpm for 30s, which resulted in $\sim 2\mu$m thick photoresist films. Samples were subsequently baked for 3 minutes at 115°C to remove excess solvent, before being loaded onto a SUSS MicroTec MJB4 Photolithography Mask Aligner along with the photolithography mask. The mask desgined for this work featured a series of a UV-transparent circles with diameters 10μm, 20μm, 50μm, 100μm, 200μm, and 300μm. The range of top electrode areas allowed for the mechanisms of switching to be broadly categorised as either filamentary or area-dependent processes, an important classification used in the analysis of RRAM devices (see section 1.2.2 in Chapter 1). Samples were

exposed to UV light for 5.2s in the hard-contact mode of the MJB4, in which the sample is brought into direct contact with the mask. Post-exposure, samples were manually agitated in Microposit MF-319 solution for 140s before a final immersion in a RO water bath for 1 minute. An optical microscope was used to verify the success of each patterning attempt before patterned samples were loaded into the electron-beam evaporation system for metallisation.

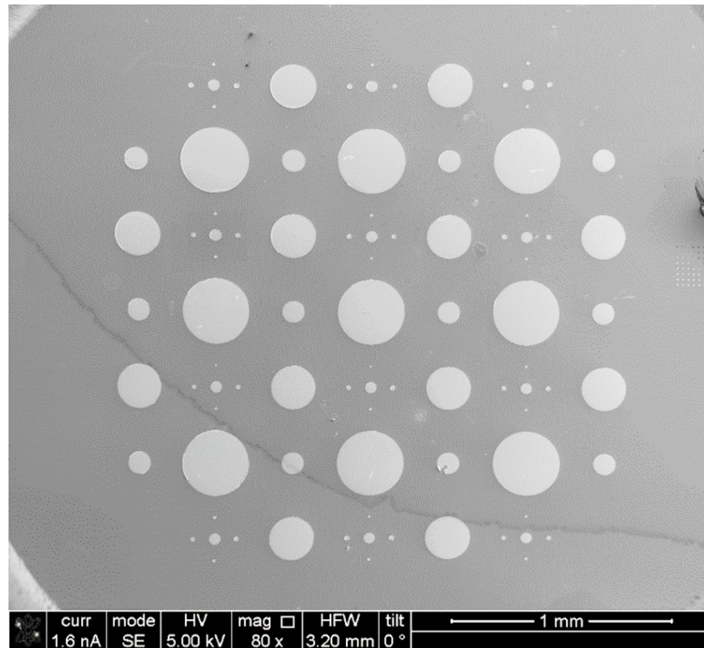

Figure 2.4: *SEM image of e-beam evaporated Ti/Pt top electrode contacts deposited after photolithographic patterning. Top electrode contacts had diameters 10µm, 20µm, 50µm, 100µm, 200µm, and 300µm*

2.3.2 Electron-beam Evaporation

For the fabrication of ZnO based RRAM devices presented in Chapter 3, a PLASSYS electron-beam (e-beam) evaporator was employed to deposit bottom electrode contacts before the deposition of the resistive switching active layer, and top electrode metal contacts after photolithographic patterning. Like PLD, e-beam evaporation is also a PVD technique and accelerates and focuses an e-beam onto a target material held in a crucible. The bombardment of high energy electrons causes thermal heating and sublimation of the target material. An advantage is that the localised heating induced by the focused e-beam produces high purity thin films in comparison to other thermal evaporation methods; in non-localised thermal evaporation, the target material and its crucible are

both heated and so the target can be subject to intermixing contamination [20]. The PLASSYS also features a quartz microbalance crystal which monitors growth rate. To create bottom electrodes for the devices presented in Chapter 3, 120nm of Ti followed by 5nm of Pt were deposited under vacuum. After the photolithographic patterning of PLD zinc oxide, 3nm and 30nm layers of Ti were deposited, followed by 5nm of Pt.

2.4 Focused Ion Beam Lamella Fabrication

A fundamental requirement for transmission electron microscopy is that the samples must be electron transparent, which corresponds to $< 100nm$ thickness at 200kV. In this work, for the investigation of multilayer RRAM devices, electron transparent lamellae were produced using an FEI DualBeam Nova Scanning Electron Microscope which included both an e-beam column and a Ga^+ ion-beam column, the latter of which is depicted schematically in Fig.2.5. In principle, this focused ion-beam instrument (FIB) allows one to mill material from a sample, held within a vacuum chamber, with high precision ($\sim$ 10nm) using Ga^+ ions, and to image this process non-destructively using the Scanning Electron Microscope (SEM), which is described in Section 2.5 [21].

An ion beam column is depicted in Fig.2.5. To create an ion beam, the extraction electrode is biased to produce a 10^8V/cm field and extract Ga^+ ions from the ion source, which is a tungsten needle wetted with liquid gallium [21]. These ions are accelerated along the length of the ion-column between 1kV and 30kV, and are focused onto the sample surface using a series of electrostatic lenses. Scanning coils allow the beam to be rastered across the sample surface, and blanking plates are used to obstruct the ion beam as required. The bombardment of energetic Ga^+ ions at the sample leads to sputtering of sample material. Secondary electrons (SE) and back-scattered electrons (BSE) are also generated during sputtering and allow for the formation of images in which contrast arises due to variations in both surface topography and atomic number. However, due to sputtering, ion-beam imaging is inherently damaging; to avoid this, the sample is imaged with a non-destructive e-beam instead, which generates SE and BSE. The FIB instrument also employs an Omniprobe needle and a gas injector. The Omniprobe needle permits the placement/removal of ion-sputtered (milled) structures,

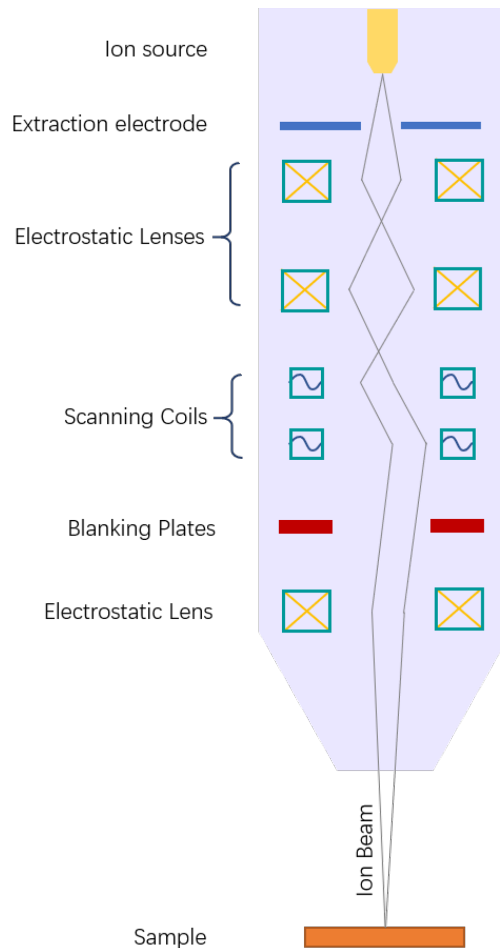

Figure 2.5: *Diagram showing vertical ion-beam column used in the FIB-SEM DualBeam instrument. A liquid metal ion source is shown in yellow and sits at the top of the column. Ga^+ ions are accelerated and focused along the ion column through the use of an extraction electrode (shown in blue) and a series of electrostatic lenses and scanning coils. Beam blanking plates (shown in red) enable the user to obstruct the beam as required.*

and the gas injector allows for chemical vapour deposition. Here, organometallic gas (for example, $W(CO_6)$) is injected within 200μm of the sample surface, where it adsorbs. When the ion beam is rastered over the desired deposition region, it decomposes the gas such that metal (W) is deposited onto the sample surface whilst waste product is removed by the vacuum system, allowing for 'maskless' patterning [22, 23]. Similarly, the e-beam can also be used to decompose organometallic gas.

In this work, a standardised FIB process was employed to produce electron transparent lamellae from bulk multilayer RRAM heterostructures and is outlined in Fig.2.6. The process was as follows: first, a RRAM device was mounted onto the sample stage, which could move in x, y, z-directions, had rotational motion and was able to tilt. Fig.2.6(a)

shows the gas injector inserted into the deposition chamber, held just above the sample surface. Fig.2.6(b) shows the result of e-beam assisted Pt deposition atop a top electrode, which served to protect the layers beneath from damage during ion-beam milling. Fig.2.6(b) also shows cross-shaped features milled into the top electrode; these were used for alignment purposes in the subsequent automated milling steps required for lamella fabrication. Figs.2.6(c) and (d) show the trench milled either side of the region protected by the e-beam deposition Pt during an automated milling process. The milled trench exposed a cross-section of the sample, which exposed each layer within the RRAM heterostructure. When tilted to the orientation shown in Fig. 2.6(d), the ion-beam was used to mill away connections between the cross-section and the bulk sample. Before complete separation from the trench, the Omniprobe needle was inserted and Pt was deposited such that the cross-section was welded to the probe. Once this was done, the final connection between the trench and cross-Section was milled away, which meant that the Omniprobe could be used to move the cross-sectional lamella away from the bulk sample. Once solely attached to the Omniprobe needle, the cross-section was thinned to electron transparency and polished: Figs.2.6(e) and (f), show the final product. Thinned, polished lamella were attached to Transmission Electron Microscopy sample holders for electron beam imaging, a technique described in Section 2.6.

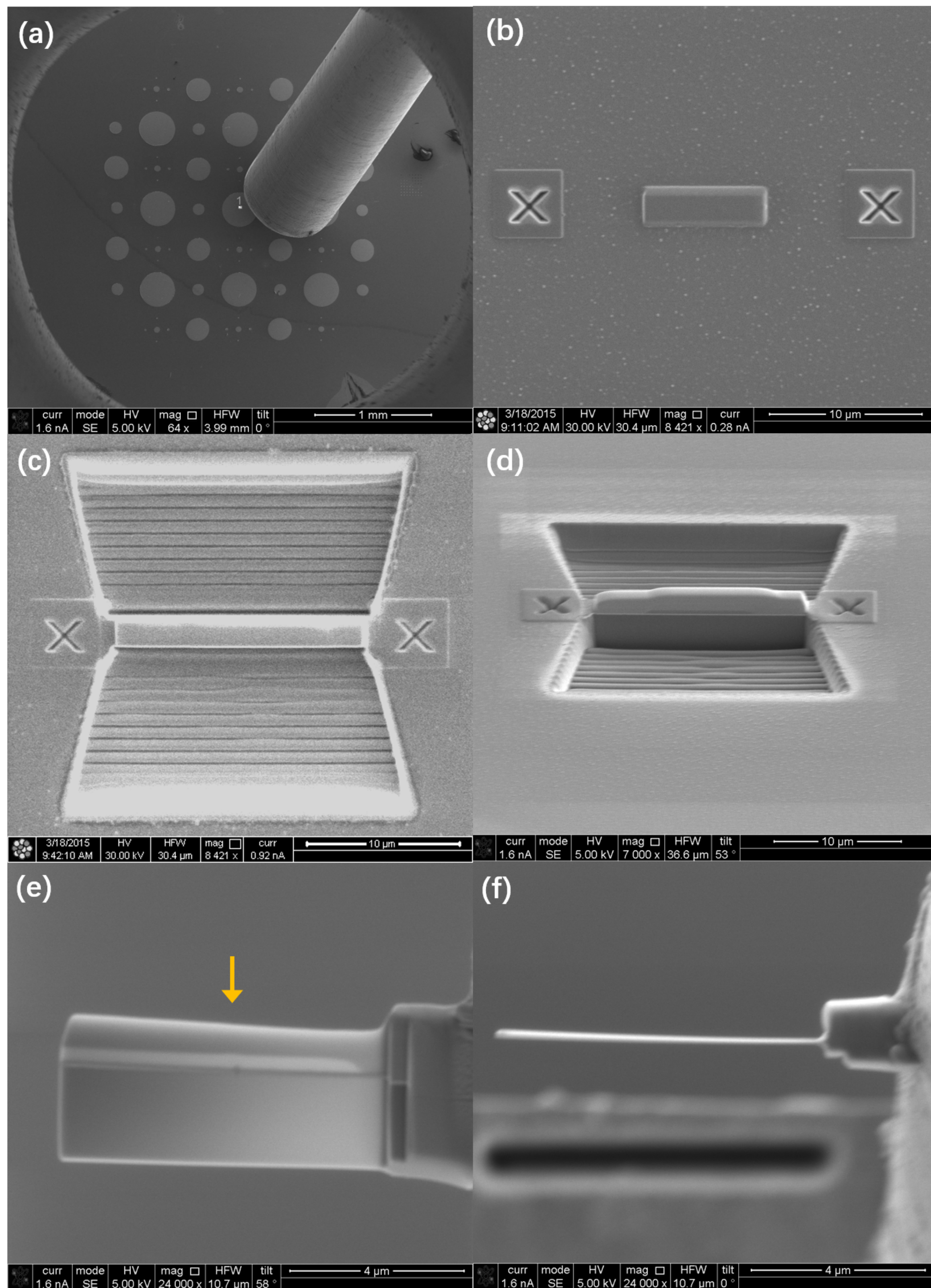

Figure 2.6: *SEM and ion beam images of the FIB lamella preparation process utilised in this work. (a) a low magnification SEM image that shows a number of patterned top electrodes and the gas injector inserted just above the bulk sample surface. (b) an ion beam image showing a protective layer of Pt situated between two alignment cross-shaped features. (c) and (d) were acquired at the same point during the lamella preparation process;(c) was acquired from directly above the trench, whereas (d) was acquired with the sample tilted. (e) and (f) were acquired at a later point in the lamella preparation process and show the lamella, thinned to electron transparency; with respect to (e), (f) was acquired at rotation 90 ° and shows a top-down view of (e), as indicated by the orange arrow in (e).*

2.5 Transmission Electron Microscopy

The spatial resolution of a conventional light microscope is restricted by the wavelength of visible light (0.4μm-0.8μm) to 250nm [24]. This limit continues to stimulate research into alternative imaging methods to enable scientists to characterise and manipulate materials for advancement in nanotechnology [24]. By far the most powerful imaging technique employed in materials science is electron microscopy, which can be used to image both surfaces and material structure; surfaces are imaged via a scanning electron beam, whereas material structure can be probed via *transmission* electron microscopy (TEM), which offers atomic resolution.

De Broglie's pioneering theory of electron wave-particle duality, published in 1925, describes how electrons can be used to image samples at higher resolution than visible light [25]. In this work, de Broglie postulated that all matter, including electrons, had wavelength (λ) proportional to its momentum (p), such that $\lambda = h/p$, where h represents Planck's constant. Following de Broglie's publication, in 1931 Ruska and Knoll constructed the world's first electron microscope, for which they were awarded a Nobel Prize some 55 years later [26].

An electron microscope comprises an electron source (described in Section 2.5.3), and an electron optical system comprising electromagnetic lenses (described in Section 2.5.4). Depending on the type of electron microscope, the arrangement of these systems will vary: in a scanning electron microscope (SEM), the electron gun and optical system are housed within an evacuated electron column which guides the electron beam to the surface of a sample located inside a vacuum chamber, and a separate detection system that collects electrons scattered from the surface of the sample. In contrast, in a TEM, an electron-transparent sample is loaded into the electron column such that the optical system transmits the electron beam through the sample and onto the detection system, which is typically located at the very base of the electron column.

Both SEMs and TEMs accelerate electrons using an accelerating voltage (V); SEMs operate at voltages up to 30kV, whereas TEMs typically operate at voltages between 30kV-300kV. When imaging using ionising radiation, there is always a balance to be struck between imaging resolution and beam damage, which both scale with accelerating

voltage. For instance, for use in high voltage transmission electron microscopy where the accelerating voltage is greater than 100KV and where the relativistic kinetic energies of electrons must be taken in account, the electron wavelength is given by:

$$\lambda = \frac{h}{\sqrt{2m_0 qV(1 + \frac{qV}{2m_0 c^2})}} \tag{2.1}$$

where h is Planck's constant, m_0 and q are the rest mass and charge of an electron, and c is the speed of light. Eqn. 2.1 shows that electrons accelerated at 200kV (the operating voltage for TEM work in this thesis) have a wavelength of $\lambda_{200kV} = 2.51$pm. Despite λ_{200kV} being smaller than interatomic distances, in practice, the resolution of the TEM is limited by aberrations in electromagnetic lenses. As mentioned above, whilst resolution is improved, beam damage, which comes in the form of sample heating, sample sputtering (the ejection of sample material), and radiolysis (the breaking of chemical bonds), also increases with accelerating voltage. Aberration-corrected TEM presents a compromise between beam damage and resolution: it allows microscopists to counter aberration effects and improve resolution whilst using lower accelerating voltages at which beam damage is low risk. The TEMs used in this work are employ aberration correction systems, which are described further in Section 2.5.4.

2.5.1 Inelastic and Elastic Scattering

Under an incident e-beam, electrons are scattered by atoms within the sample in forward (parallel to the incident beam) and backward (anti-parallel to the incident beam) directions, as shown in Fig.2.7. In an SEM, only back-scattered secondary signals can be detected, however in the TEM, forward scattered electrons are collected below the sample, and provide information about the internal structure and chemistry of the sample. These forward scattered electrons are either elastically or inelastically scattered, which refer to scattering events in which the incident electron suffers no or some loss in energy respectively.

Elastic scattering describes scattering events in which the incident electrons deviate from their path due Coulombic interactions with the nucleus and/or electron cloud and do not suffer energy loss. Frequently, small-angle deviations in incident electron

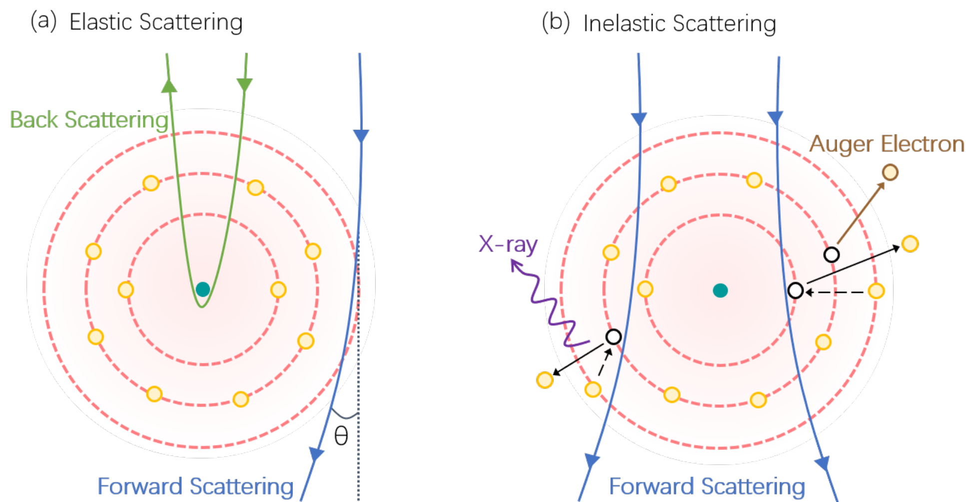

Figure 2.7: *Diagram showing (a) elastic and (b) inelastic electron-scattering. (a) Forward- and backward-scattering are shown by the blue and green e-beam trajectories respectively. The production of characteristic X-rays (purple wavy arrow) and Auger electrons (brown arrow) are shown in (b), where the (dashed)solid arrows represent the (de-)excitation of an inner shell electron.*

path occur as a result of elastic scattering, where the scattering angles increase with atomic number, Z [27]. In some cases, Coulombic interactions can be sufficiently strong to cause the back-scattering of incident electrons, in which the incident electron is subject to a deflection greater than 90°, as depicted by the green trajectory shown in in Fig.2.7(a) [27].

Inelastic scattering refers to events in which incident electrons interact with atomic electrons and lose energy as a result. These inelastic events produce a number of secondary signals including secondary electrons and X-rays (depicted in Fig. 2.8) in either back- or forward-scattered directions. X-rays are produced when secondary electrons are ejected from the valence and conduction bands, or from atomic inner-shells. The former typically have energies <50eV, which means that only those that are generated near the surface of the sample have sufficient energy to escape. This characteristic makes secondary electrons extremely useful for imaging the sample surface, which is done in SEM. However, secondary electrons emitted from the conduction and valence bands do not provide elemental information about the sample; in contrast, those ejected from atomic inner-shells, Auger electrons, and characteristic X-rays, do carry such information, which allows for *analytical* electron microscopy techniques. Fig.2.7(b) illustrates how the incident e-beam transfers energy to inner-shell electrons, causing

its ejection (represented by the solid black arrows). To relax from an ionised state, an electron is de-excited to a lower energy level (represented by the black dashed arrows), which produces characteristic X-rays (represented by a purple arrow) and Auger electrons (represented by a brown arrow). Furthermore, e-beam electrons can undergo inelastic scattering with collective atoms within the solid, creating an oscillation of valence electron density. This longitudinal wave is referred to as plasmon resonance. Fig.2.8 shows that there are multiple additional electron-matter interactions that can result in the generation of a variety of secondary signals. However, these extend beyond the scope of this thesis, and are explained in external texts [28, 29]. Given that these events cause the respective incident electron to undergo a loss of energy, electron energy loss spectroscopy can be used to determine the chemistry of the sample, as done in Chapter 4.

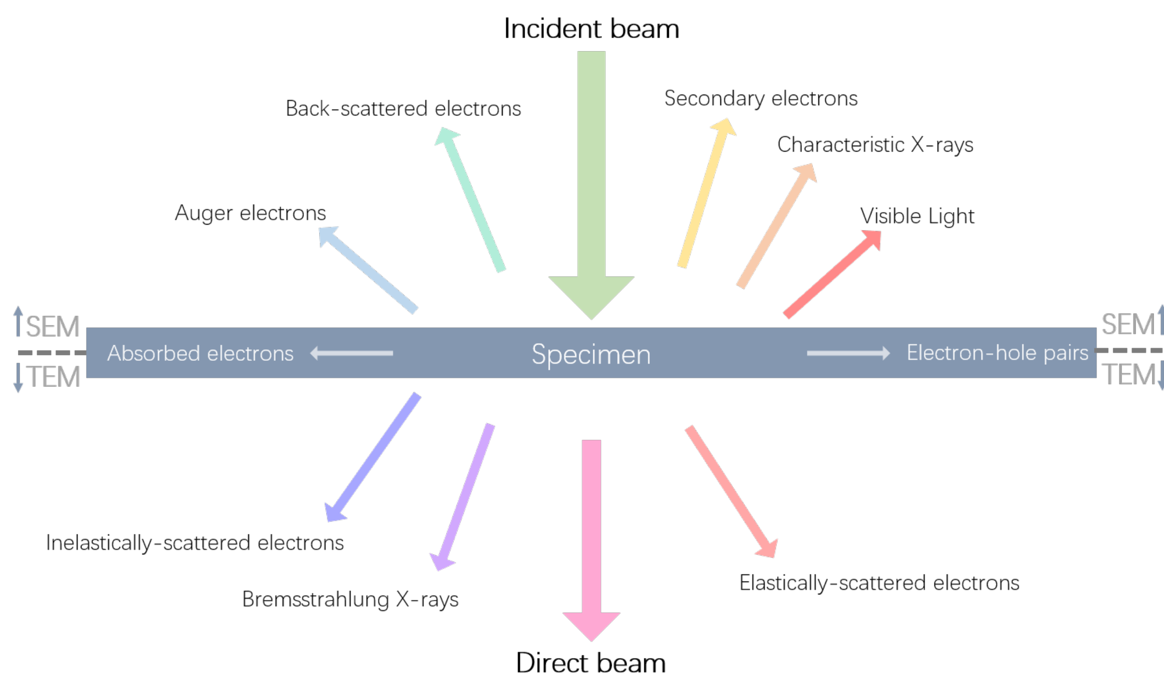

Figure 2.8: *Diagram showing electron-matter interaction and the generation of secondary signals. Electrons that pass through the sample un-deviated are referred to collectively as the direct beam.*

2.5.2 Diffraction

Section 2.5.1 described isolated single atom scattering events, however, practically, in a specimen, collective scattering from multiple atoms occurs. Fig.2.9 illustrates how,

for a crystalline sample in which the atomic planes are separated by distance d, elastically scattered electrons follow Bragg's law:

$$n\lambda = 2dsin\theta \quad (2.2)$$

where n is a positive integer and θ is the angle of the incident e-beam(wave) (measured w.r.t. the atomic plane). This type of elastic Bragg scattering is referred to as diffraction, and generates patterns in which the constructive interference of scattered (diffracted) electron waves produce an angular distribution of bright spots. Here, the distance between diffraction spots is governed by unit cell size and shape, whereas the intensity is governed by the distribution, number, and types of atoms within the sample. Therefore, through the measurement of diffraction spot intensity and position, it is possible to assess the structure of a given sample material. Diffraction scattering and analysis of elastically scattered *X-rays* can also be used to assess sample structure. In Chapter 3, X-ray diffraction is discussed in conjunction with the literature on the growth and morphology of ZnO thin films.

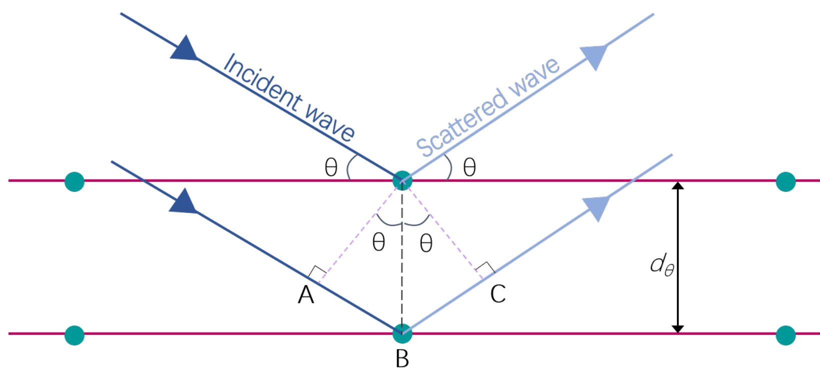

Figure 2.9: *Diagram showing elastic Bragg scattering (diffraction). Here the path difference between the incident and scattered waves is given by $AB + BC = 2dsin\theta$, and constructive interference is observed when the path difference is equal to an integer multiple of the electron wavelength, as described in Eqn. 2.2.*

Quantitatively, the degree of crystallinity of a given material is usually determined using X-ray diffraction (XRD). For polycrystalline materials, the many, distinct crystalline regions (grains) produce XRD spectra containing multiple diffraction peaks at various θ_B, as defined in Eq.2.2. The relative intensity of these peaks is proportional to the fraction of the film it corresponds to, so XRD spectra acquired from more crystalline

(less mosaic) thin films exhibit an intense diffraction peak corresponding to the preferred crystallographic orientation. The relationship between the grain width (L) and the FWHM of the diffraction peak is described by the Debye-Scherrer equation in which grain width (L) is equal to

$$L = \frac{K\lambda_x}{B\cos\theta_B} \tag{2.3}$$

where K is a constant approximately equal to 0.9, B is the broadening of the peak and λ_x is the X-ray wavelength [30]. This equation shows that with increasing grain width, the FWHM decreases.

2.5.3 Electron Sources

Electron microscopes employ electron guns that emit electrons via either thermionic or field emission. The **FEI Tecnai T20** (T20) TEM (employed in Chapter 3) uses a thermionic emission source, in which the source material (typically LaB_6 crystal) is heated such that electrons gain sufficient energy to overcome the work function of the material. The **FEI Nova DualBeam** FIB-SEM and **JEOL ARM 200cF** (ARM) TEM (employed in Chapters 3 and 4)used in this work employ field emission guns (FEGs) in which the source material (typically tungsten) is negatively biased. The use of a sharpened tungsten tip enhances the local electric field, enabling electron emission through tunnelling. Both electron guns apply an electric field to focus off-axis electrons to a gun cross-over point that is centered along the optic axis, which is shown as a red dashed vertical line in the diagrams presented in this work. Respectively, the FEG achieves better spatial coherency, brightness (defined as the current density per unit area of the source per unit solid angle) and energy spread than thermionic emission guns due to its small source size, which makes it preferable for use in analytical and high resolution transmission electron microscopy [28]. However, the reduced FEG source size provides poor illumination for low magnification imaging ($\leq 100,000\times$), making thermionic emission sources the preferred choice for routine imaging [28]. As such, in this work, samples were typically imaged using the T20 before analytical probing is undertaken using the ARM.

2.5.4 Electromagnetic Lenses

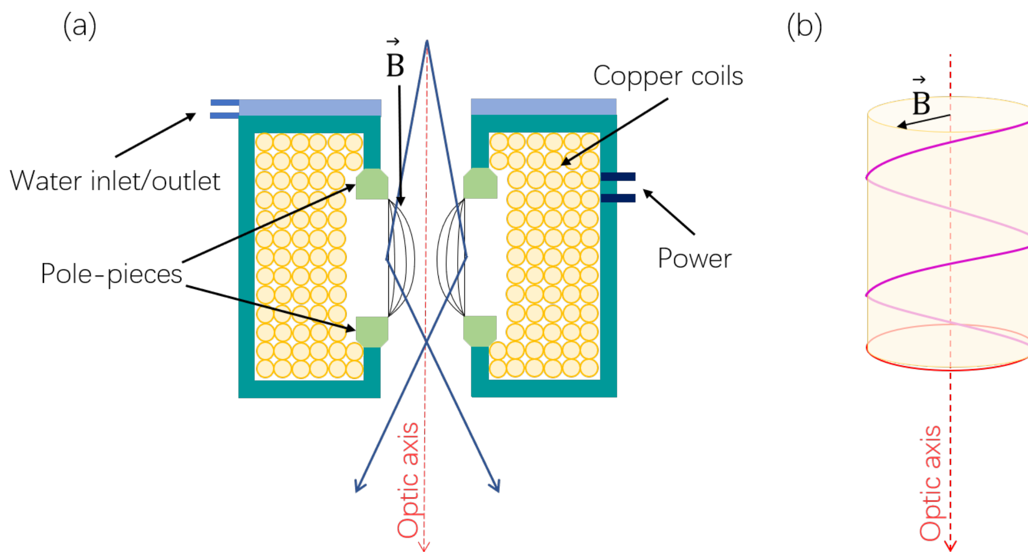

Figure 2.10: *(a) Cross-section of a magnetic lens where copper coils are shown in yellow, and are enclosed within a case that can be water cooled via a water inlet and outlet. Upper and lower pole-pieces are shown in light green, and generate a* **B***-field perpendicular to the optic axis when current is supplied to the copper coils. Electron rays paths, depicting lens focusing, are shown in blue. (b) shows how electrons travelling along the optic axis are subject to helical motion under the applied* **B***-field.*

At the time of the development of Ernst and Knoll's electron microscope, it was already known that a charged particle moving through an electrostatic (**E**) and/or magnetic field (**B**) is subject to the Lorentz force (**F**)

$$\mathbf{F} = q(\mathbf{E} + \mathbf{v} \times \mathbf{B}) \tag{2.4}$$

where **v** is the velocity of a charged particle. This showed that either an electrostatic field or a magnetic field can be employed to focus and deflect an electron beam. Indeed, the Wenhelt electrode in a thermionic emission gun is an electrostatic lens that acts to focus the electrons at a cross-over point. However, electrostatic lenses can suffer from high-voltage breakdown; this restriction stimulated research into the development of electromagnetic lenses, which are used in modern electron microscopes. Fig.2.10(a) shows a cross section of an electromagnetic lens; here, two (upper and lower) cylindrically symmetrical pole pieces form a bore along the optic axis through which an electron beam can pass. Copper coils surround the pole-pieces, and generate an axially symmetric

magnetic field when current is supplied. In the case of an electromagnetic lens, Eqn. 2.4 is modified such that $\mathbf{E} = 0$, and electrons are subject to helical motion about the optic axis whilst they pass through the lens, as illustrated by the purple line shown in Fig.2.10(b).

The effect of an electromagnetic lens on an e-beam is analogous to that of a *convex* glass lens on incoming light rays: both lenses act to converge off-axis rays to a single focal point. In an electromagnetic lens, the strength of this effect depends on the perpendicular **B**-field, which is governed by the magnitude of the current supplied to the lens. Typically, electron optics are depicted using vertical ray diagrams; Fig.2.11 is an example of this. An image of an object located in the object plane (shown in green in Fig.2.11) is formed below the electromagnetic lens in the image plane (shown in light blue in Fig.2.11). A diffraction pattern, however, is formed in the back focal plane of the lens, which is highlighted by the yellow line in Fig.2.11. By varying the current supplied to an electromagnetic lens, the **B**-field can be adjusted increase or reduce the angle of convergence.

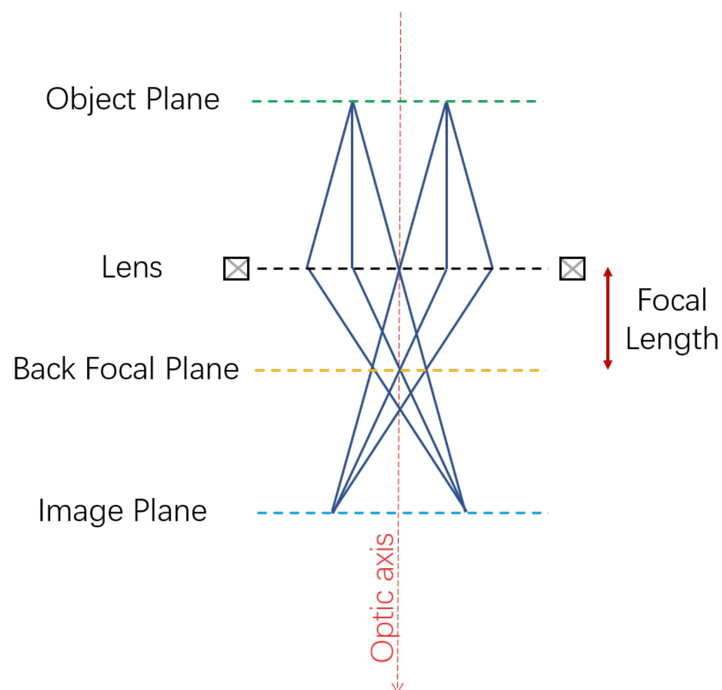

Figure 2.11: *Electromagnetic lens ray diagram, where electron rays are depicted as dark blue line. Principal planes are highlighted; the object, back focal, lens, and image planes are represented by green, black, yellow, and light blue dashed lines respectively. Deflected e-beams converge in the image plane at the lens focal length.*

Fig.2.11 is an example of an ideal electromagnetic lens where all off-axis e-beam rays are deflected such that the focal length of the lens remains constant. However, as mentioned in Section 2.5, electromagnetic lenses are limited by lens defects; in order of dominance these are spherical aberration, chromatic aberration, and astigmatism [28]. Identified by Scherzer in 1949, spherical aberration (C_s) is a radial lens defect in which off-axis rays converge excessively in comparison to those closer to the optic axis [31, 32]. Due to this defect, detail is lost during magnification: for instance, a point object is imaged as a disc of finite size. To counter C_s, diverging lenses comprising multiple pole-pieces (multipoles) are employed that act to spread off-axis rays such that they converge at a single focal point [28, 33]. Chromatic aberration (C_c) is a defect that varies with the monochromaticity of the electron beam, that is, its frequency and wavelength. In this case, electrons with lower energy (higher wavelengths) converge excessively in comparison to those with higher energy, resulting in the loss of detail at high magnification, as found in C_s [28, 31]. Whilst it is true that energy spread can be minimised by choice of electron source, inelastic electron scattering also contributes to the spread of electron energies post-interaction with the sample (these processes are described in further detail in Section 2.5.1). To counter this, C_c can also be minimised by thinning the sample, which effectively reduces the number of inelastic interactions. Astigmatism is an image distortion that arises due inhomogeneities in the lens field. This, for instance, can be due to microstructural variations in the pole-piece material, and can be corrected through the use of octopole stigmators, which produce a compensating field that acts to counter the inhomogeneities that cause the astigmatism [28].

2.6 Electron Optical System

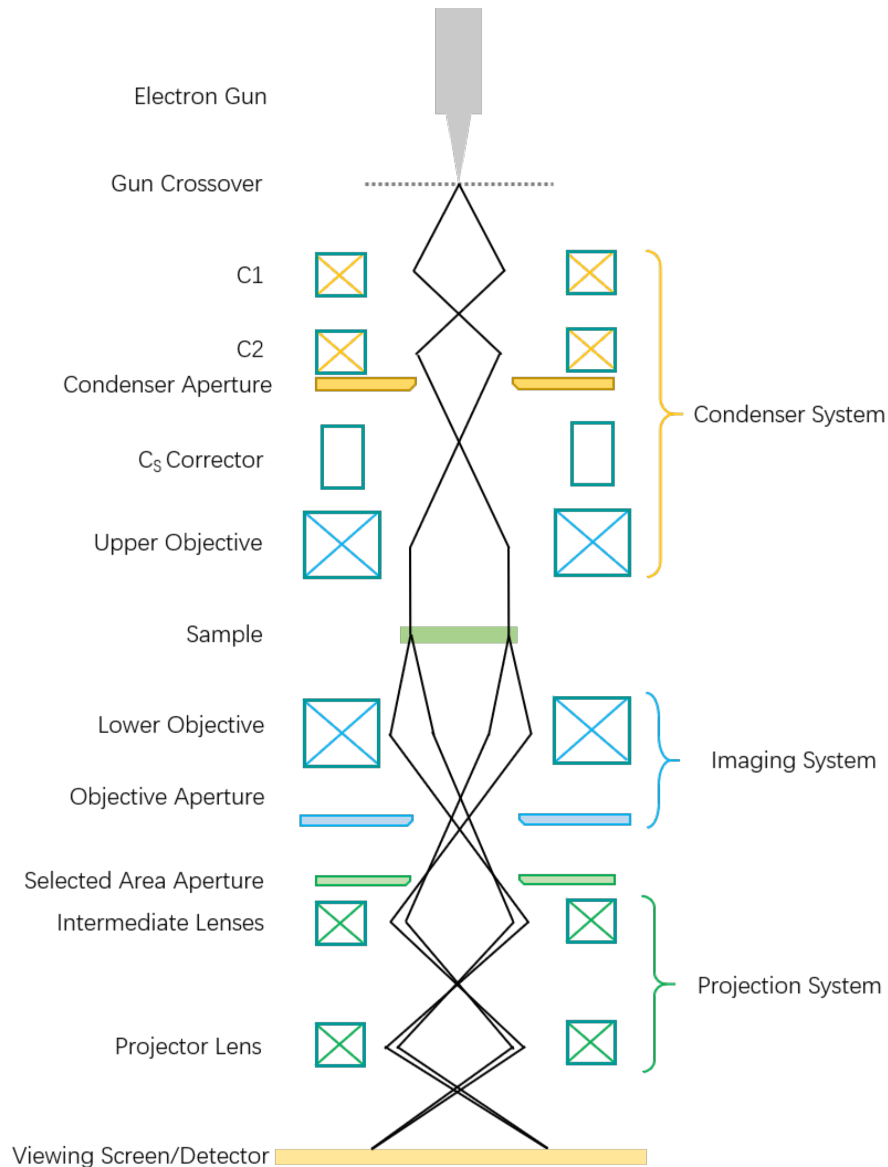

Figure 2.12: *Schematic diagram showing magnetic optical system set up in CTEM mode for an aberration-corrected microscope.*

As mentioned in Section 2.5.3, an FEI Tecnai T20 (T20) and a JEOL ARM200cF (ARM) TEM were utilised in this work, and allowed for the structural and chemical characterisation of heterostructure RRAM devices and oxide thin films. Within the electron column, the electron optical system can be divided into three sections: from top to bottom these are the condenser system, the imaging system into which the sample is loaded, and the projection system, as shown in Fig. 2.12.

Using the condenser system, a TEM can be set up to illuminate the sample in two configurations: parallel (broad beam) illumination or convergent (probe) illumination. The former is used for imaging and selected area diffraction, and is referred to as conventional transmission electron microscopy (CTEM), and the latter, when rastered, is used for scanning transmission electron microscopy (STEM), which is described in Section 2.6.2 [28]. To illuminate the sample in both modes, at least two condenser lenses are employed, as shown in Fig.2.12. In the condenser system, the gun cross-over (defined in Section 2.5.3) is positioned in the object plane of the first lens, C1, such that C1 can form its demagnified image at the C1 crossover. The second lens, C2, can be strengthened or weakened to produce either broad-beam or probe illumination. However, most TEM instruments, including the JEOL ARM used in this work, employ the upper pole piece of the objective lens to act as a third condenser lens (C3): if C2 is over-focused (strengthened), C3 can produce a parallel beam of electrons, as shown in Fig.2.13(a); if C2 is switched off, C3 can be strengthened to produce probe-illumination instead, as depicted in Fig.2.13(b). The main advantage to using C3 for probe-illumanition is that it can achieve a smaller probe size <1nm. The condenser system also includes a series of condenser correctors that counteract the effects of astigmatism and aberration, as described in Section 2.5.4.

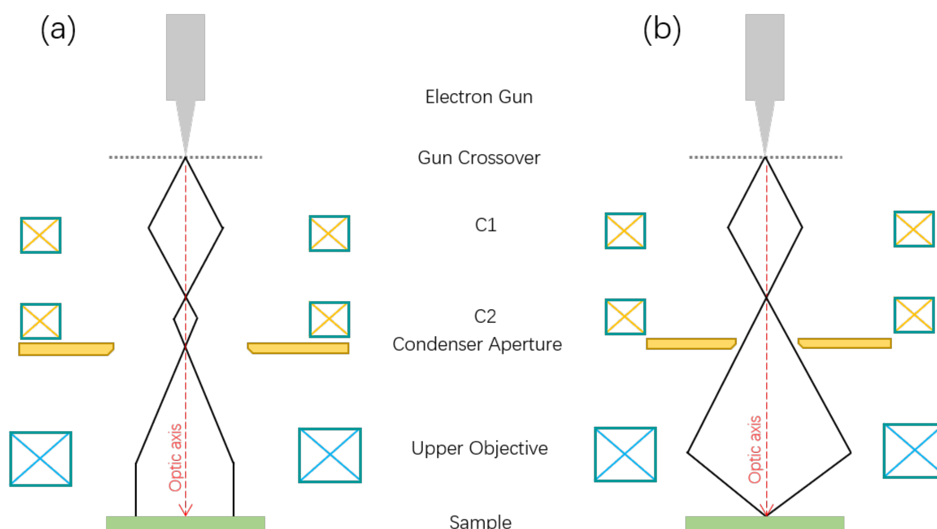

Figure 2.13: *Schematic diagram showing upper-objective condenser system set up for (a) broad beam and (b) probe illumination in CTEM mode.*

The condenser system is separated from the imaging system by the sample stage. In

the imaging system, the role of the objective lens is to form images or diffraction patterns of the sample. To produce a diffraction pattern, the strength of the intermediate lens (within the projection system) is adjusted such that its object plane is in the back focal plane of the objective lens. A selected area aperture can be introduced into the image plane of the objective lens, which allows one to obtain a diffraction pattern from a specific region of the sample as well as reducing the intensity incident at the detector. To produce an image of the sample instead, the intermediate lens is adjusted so that its object plane is in the image plane of the objective lens. Before being projected onto the viewing screen or detectors, the image is finally magnified by a projector lens.

2.6.1 Bright-Field and Dark-Field Imaging

Bright- (BF) and dark-field (DF) imaging are two of the most important CTEM modes employed in TEM, and are used in this work. The terms 'bright' and 'dark' refer to the use of an objective aperture to isolate the direct beam and diffracted beam respectively. Fig.2.14(a) illustrates the set-up for BF imaging; here, the black rays represent the unobstructed direct beam, and the red rays represent the obstructed scattered beam. In contrast, Fig.2.14(b) shows how the direct beam can be tilted to the effect that the scattered beam is parallel to the optic axis and is isolated by the objective aperture. DF imaging isolates particular crystallographic orientations with a given sample, producing diffraction contrast, which allows for an assessment of defects and grain size, as presented in Chapter 3.

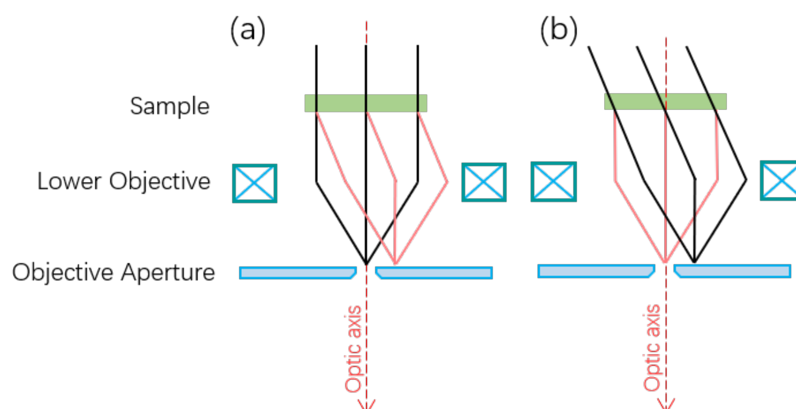

Figure 2.14: *Schematic diagram showing objective aperture set up for (a) BF and (b) DF imaging. Here the black(red) rays represent the direct(scattered) beam.*

2.6.2 Scanning Transmission Electron Microscopy

In STEM mode, the condenser system employs the upper-objective lens to produce a fine e-beam probe (0.2 to 5nm in diameter [28]) that rasters across the sample. Fig.2.15 illustrates how this rastering motion is enabled by two sets of deflector coils positioned above the upper objective lens. One of the major benefits to using STEM mode is that lenses are not used to magnify a STEM image, meaning that lens defects in the imaging system are avoided; instead, the transmitted electron beam is collected at the detector pixel-by-pixel.

As in CTEM, BF and DF images can be obtained, however different detectors are used to isolate the direct or diffracted beams as opposed to an objective aperture. In STEM, *annular* dark field (ADF) images are obtained using a ring-shaped detector centered around the optic axis. An ADF detector collects beams scattered to $\theta \approx 10$mrad. In addition to this, another annular detector can be added to surround the first to detect electrons scattered at higher angles ($\theta \geq 100$mrad), and produces *high angle* annular dark field (HAADF) images [34]. These high angle electrons are scattered via Rutherford scattering and produce Z-contrast images, which are particularly useful in the imaging of complex compound materials such as perovskite oxides.

Fig.2.15 depicts the TEM instrument used for STEM-coupled Electron Energy Loss Spectroscopy (STEM-EELS), in which a 90° magnetic prism spectrometer (described further in Section 2.7.7) is used to analyse the energy spread of transmitted electrons. As described in Section 2.17, the energy lost by inelastically scattered electrons provides information about the chemistry of a given material. Due to its fine probe size, STEM is particularly well suited for this analytical electron microscopy technique, as it allows one to investigate the spatial distribution of chemical changes within the sample at high resolution. STEM-EELS was employed for the studies presented in Chapters 3 and 4 in this work.

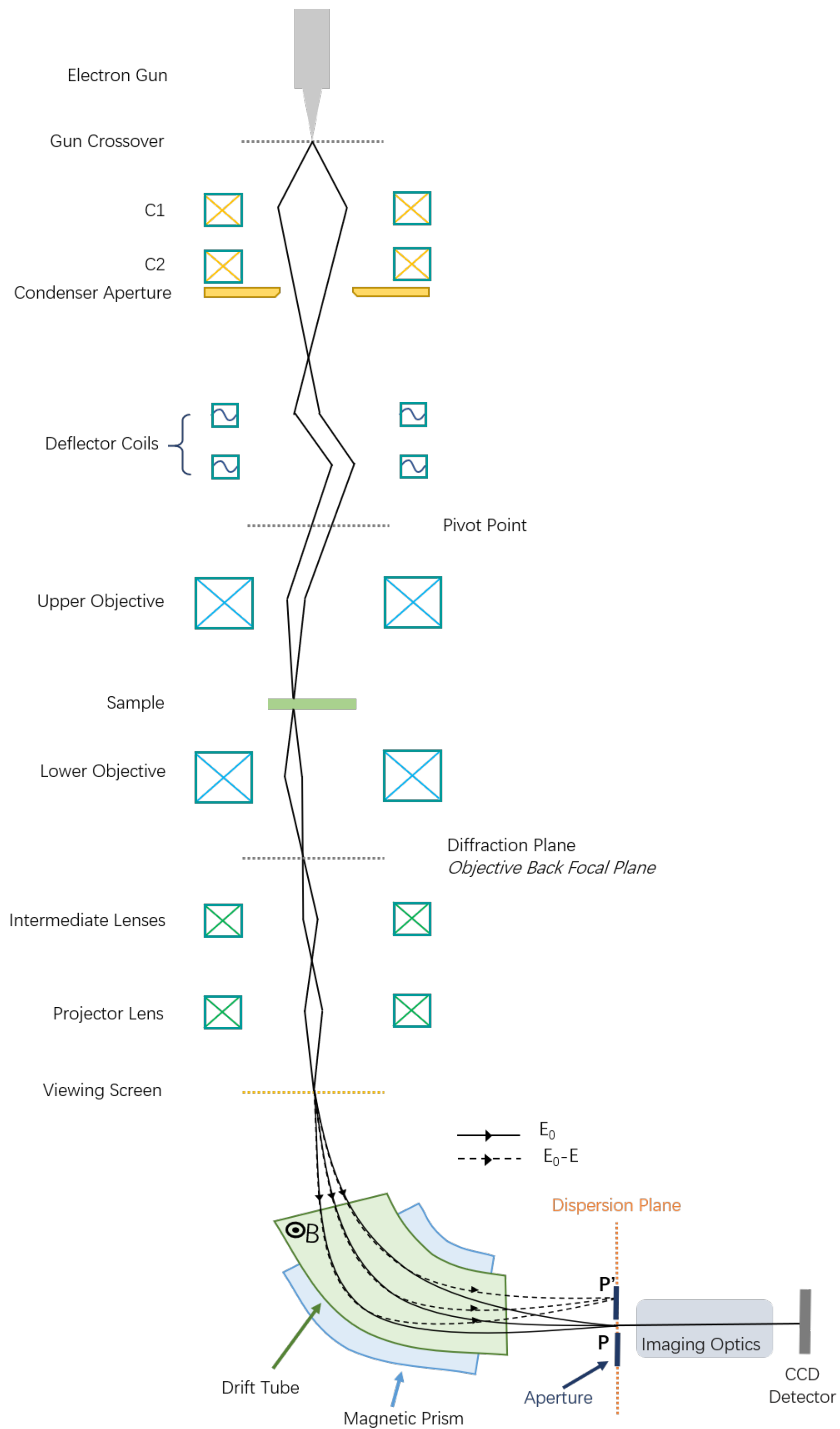

Figure 2.15: *Magnetic optical system set up for STEM-EELS. In this set-up, a magnetic prism spectrometer is inserted below the viewing screen to enable the analysis of electron energies.*

2.7 Electron Energy Loss Spectroscopy

On the ARM TEM, EELS is carried out in STEM mode in the configuration shown in Fig.2.15, where a magnetic spectrometer (described in section 2.7.7) collects inelastically scattered electrons. STEM-EELS mode involves the scanning of a fine e-beam probe across the sample in a pixel-by-pixel rastering motion, commonly referred to as spectrum imaging, which allows one to acquire an entire spectrum for each x, y coordinate within the scan. This builds a spectral image data cube which has dimensions x, y and ΔE (where ΔE is energy loss), as depicted in Fig.2.16.

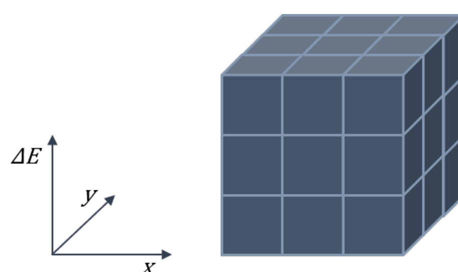

Figure 2.16: *Spectral image (SI) data cube in which an EELS spectrum is acquired for each pixel in a scan across x and y.*

2.7.1 Electron Energy Loss Spectrum

An EELS spectrum is typically described with reference to the low-loss spectrum, shown in Fig.2.17(a), which includes energy losses $\leq$ 50eV and he high-loss (core-loss) spectrum, shown in Fig.2.17(b), which extends from 50eV to $\sim$ 1keV. The low-loss spectrum is dominated by an intense Zero-Loss Peak (ZLP) at 0eV, which is highlighted by the yellow arrow in Fig.2.17(a). This comprises unscattered electrons and those that have been subject to elastic scattering and suffered no energy loss. The FWHM of the ZLP is limited by the energy spread of the electron source, which governs the overall resolution of the EELS spectrum. In this work, the ARM was used to acquire STEM-EELS data as it employs a cold-FEG source that achieves $\sim$0.3eV resolution. In addition to the ZLP, the low-loss spectrum features resonance peaks that have arisen due to plasmon excitation, and are highlighted by the orange arrow in Fig.2.17(a). The energy of a plasmon peak is governed by the density of valence electrons present in the

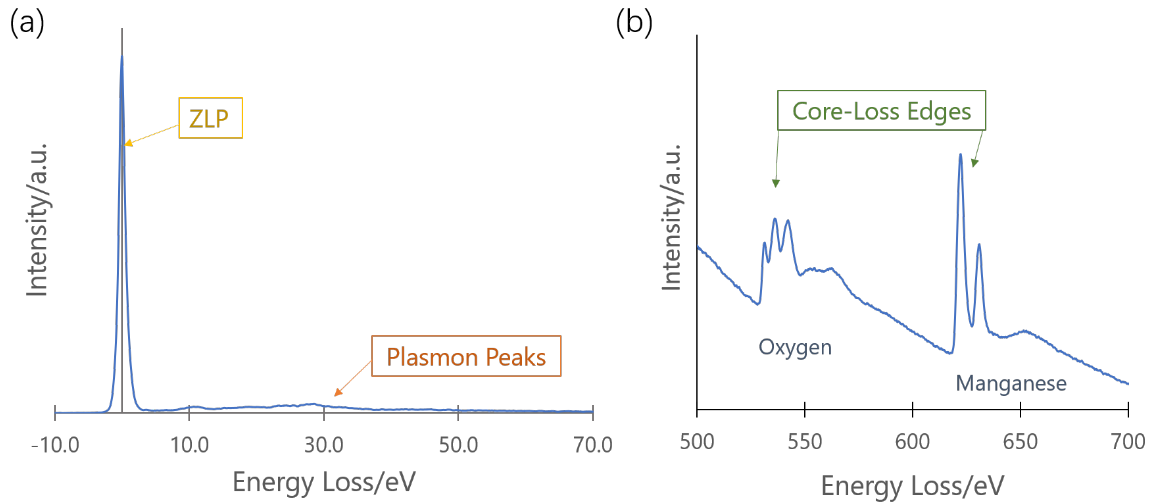

Figure 2.17: *STEM-EELS spectrum obtained on the TEM showing (a) low-loss and (b) high-loss data acquired simultaneously from PrCaMnO3. The low-loss spectrum comprises the ZLP and plasmon peaks and the high-loss spectrum comprises core-loss edges. In (b), oxygen and manganese core-loss edges are shown.*

sample. In insulator and semiconductor materials, further plasmon peaks arise due to interband transitions, which correspond to valence electron excitations to unoccupied energy states above the Fermi level [35]. In general, the overall shape of the low-loss spectrum is typically used to assess the electronic nature of a sample. Although low-loss analysis is not typically used in RRAM research as it features overlapping plasmon peaks from multiple contributions that complicate analysis, a comparison of the low-loss spectra acquired from devices programmed to the LRS and HRS could offer further insight into the mechanisms of RS [18, 36]; in Chapter 4, the low-loss spectra acquired from LRS- and HRS- programmed devices are compared and discussed and reveal reproducible differences. In the high loss spectrum, peaks corresponding to the energy required to excite an inner-(core-)shell electron to unoccupied energy states above the Fermi level. As these energies are characteristic quantities, core-loss features (edges) can be used to identify the elements present in a given sample; Fig.2.17(b) highlights the oxygen and manganese edges obtained from a $PrCaMnO_3$ sample, which correspond to energy losses of 532eV and 640eV respectively. Core-loss edges are superimposed onto the tail of the plasmon peaks, which are roughly eight times greater in magnitude than the core-loss edges [37]. This tail can be described as a decreasing logarithmic background that follows the form $I = AE^{-r}$ (where I is intensity, E is energy, and A and r are fitting

parameters [38]), and must be removed before quantification. For a *single* scattering event, k, the intensity of a given core-loss edge, I_k, is described by

$$I_k = I_0 N \sigma_k \tag{2.5}$$

where I_0 is the intensity of the ZLP, N is the number of atoms per unit area, and σ_k is the scattering cross-section, which represents the intrinsic probability of a scattering event occurring for a particular atom. σ_k is dependent on the incident beam energy, the atomic number (Z) and the scattering angle. However, the calculation accuracy of σ_k is limited to roughly 30% [39]; this is because irregularities in the dependence of σ_k on Z arise due to the outer shell structure of a given atom. Furthermore, σ_k is calculated based a scattering event from a single *isolated atom*, which does not reflect variations in bonding environments in bulk and, for crystalline materials, does not compensate for diffraction effects, which dramatically modify the angular dependence of scattering [29, 40]. For the *absolute* quantification of EELS data, the accuracy of σ_k is a limiting factor; the Hartree-Slater model for σ_k, which is commonly used throughout the field, has systematic errors of 5%, 15% for energy losses corresponding to the excitation of 1s and 2p electrons [40, 41]. In an attempt to improve on this, some EELS researchers, including those working within the Materials and Condensed Matter Group at the University of Glasgow, experimentally measure σ_k using stoichiometric samples of known thickness and achieve an accuracy to within a few percent [40]. The absolute quantification of EELS data is outwith the scope of this thesis, however the quantification of *relative* ratios between elements were evaluates; the elemental ratio quantification method used in this work and its limitations are described in section 2.7.3.

In practice, the thickness of a lamella governs whether or not *multiple* inelastic scattering events occur. Such independent events obey Poisson statistics, which means that the probability that a transmitted electron undergoes n scattering events,P_n, which can also be expressed as the ratio between the integrated n-fold scattering I_n, and the total integrated plasmon intensity I_t, is given by:

$$P_n = \frac{I_n}{I_t} = \left(\frac{1}{n!}\right)\left(\frac{t}{\lambda}\right)^n exp\left(-\frac{t}{\lambda}\right) \tag{2.6}$$

where t is the thickness of the lamellae, λ mean free path for inelastic scattering events. For the unscattered electrons that comprise the ZLP, $n = 0$ and Eqn.2.6 can be rearranged to produce

$$\frac{t}{\lambda} = ln\left(\frac{I_t}{I_0}\right) \quad (2.7)$$

where I_0 is the intensity of the ZLP. Conventionally, $\frac{t}{\lambda}$ is used as a parameter to assess sample thickness, where for $\frac{t}{\lambda} > 0.5$, thickness effects are expected to affect the spectrum and the quantification thereof [35]. With regards to the low-loss, *multiple* plasmons are excited by an incident electron, which manifests as additional resonance peaks at integer multiples of the plasmon energy [37]. In the high-loss spectrum, plural inelastic scattering events can dramatically affect the intensity and shape of core-loss peaks. Therefore, in order to compare core-loss edge shapes acquired from different samples accurately, these plural scattering effects must be minimised via Fourier transform deconvolution, which produces a single-scattering distribution [37, 42].

High-loss spectra also reveal detailed peaks extending up to 50eV beyond the core-loss edge; these pronounced features are referred to as the energy loss near-edge structure (ELNES). There are number of interpretations that have been used to explain the principles of ELNES in the literature, however it can be understood via a band structure model for a single-electron-excitation approximation [28, 37, 38]. Here, ELNES modulations in intensity ($J(E)$) are governed by Fermi's Golden Rule which states that the probability of an electron transitioning from its initial state (i) to a final state (k) is proportional to the product of atomic transition matrix element ($M(E)^i_k$) and the density of final states ($\rho(E)_k$):

$$J(E)^i_k \propto \frac{2\pi}{\hbar} \left|M(E)^i_k\right|^2 |\rho(E)_k| \quad (2.8)$$

$M(E)^i_k$ is determined by atomic physics and therefore represents the overall shape of the core-loss edge. In contrast, $\rho(E)_k$ is determined by the chemical and crystallographic environment of the excited atom, therefore, modulations in $J(E)^i_k$ represent variations in the density of final states above the Fermi level. This model can be used to describe ELNES if the following qualifications apply: $\rho(E)_k$ represents the *local* density of *unoccupied* states, i.e. different elements in the same compound have a distinct set of

unoccupied final states; and the strength of $M(E)_k^i$ is dependent on the dipole selection rule, $\Delta l = \pm 1$, where $\Delta l = +1$ transitions are predominant [35]. The latter means that for example, in high-loss spectra acquired from $PrCaMnO_3$, modulations in the Mn-$L_{2,3}$ peaks are governed by Mn-3d final states, which is discussed with respect to RS induced Mn-redox in Chapter 4. This sensitivity is one of the most useful aspects of EELS with regards to redox-based RS. The careful analysis of ELNES provides information about the valence state of an atom: a change in the effective charge of a metal cation leads to a change in the screening of the electrostatic field surrounding the nucleus which causes a change in binding energy which manifests as the 'chemical shift' of the core-loss edge. In addition, when there is a strong interaction between the excited core-shell electron and its corresponding core-hole, the intensity of ELNES peaks will also vary with valence state. Such strongly-interacting transitions correspond to $L_{2,3}$ peaks of transition metals, and $M_{5,4}$ peaks of rare-earth metals; the ratio between the intensities of these peaks is typically referred to as the white-line ratio. Thus, both the chemical shift and white-line ratio are used in Chapter 4 to distinguish between distinct valence states of a transition metal cation, which, as explained in section 1.2.2, are expected to change in transition metal oxides that display RS.

2.7.2 Basic EELS Processing Steps

All EELS datasets were processed using Gatan Digital Micrograph 2.3 (DM) software. With regards to basic EELS processing, in the first instance, to compensate for any drift induced by instrumental instabilities, both the low- and high-loss spectra are aligned using an 'Align by Peak' function on the ZLP. Both spectra are then calibrated to ensure that the ZLP is centered about 0eV. Finally, using DM's 'Remove X-rays' function, X-ray spikes which are spurious single-pixel peaks are isolated and removed. These basic EELS processing steps were always used, however more advanced techniques, such as deconvolution, principle component analysis, multiple linear least-squares fitting and elemental ratio normalisation can be applied; these are described in Sections 2.7.3, 2.7.4, 2.7.5, and 2.7.6 respectively.

2.7.3 Elemental Ratio Normalisation

In Egerton's influential text on EELS, it was shown that for the same irradiated volume in a given SI dataset, the stoichiometric ratio between elements A and B with core-loss edge intensities I_A and I_B respectively is

$$\frac{n_A}{n_B} = \frac{I_A(\Delta_A)\sigma_B(\Delta_B)}{I_B(\Delta_B)\sigma_A(\Delta_A)} \tag{2.9}$$

where n_k is the number of atoms (of type 'k') per unit volume and Δ_k is the width of the energy window used to integrate over core-loss edge with intensity I_k [29]. As noted above, Eqn.2.9 can be applied for a single material in one dataset, however, to compare stoichiometry across multiple distinct materials, for instance, across all the layers within RRAM thin film heterostructures, or to compare stoichiometry across multiple datasets it is important to normalise to account for other parameters that may influence I_k such as variations in thickness, zero-loss intensity, inelastic mean free path and ratio between low- and core-loss acquisition times. This can be done through the manipulation of Eqn.2.5 (presented on page 64): by substituting N for nt and multiplying by $\frac{\lambda}{\lambda}$, Eqn.2.5 can be expressed as

$$n_k\lambda = \left(\frac{I_k}{\sigma_k}\right)\left(\frac{1}{I_0}\right)\left(\frac{\lambda}{t}\right)\left(\frac{s_{CL}}{s_{LL}}\right) = I_{k,N} \tag{2.10}$$

where s_{CL} and s_{LL} represent the acquisition times for the core- and low-loss respectively, t represents lamella thickness and $I_{k,N}$ represents *normalised* I_k. This normalisation of I_k can be achieved using DM, which has plugins that produce 2D maps of three of the bracketed components in Eqn.2.10: I_0 is extracted using a reflected tail model that assumes the ZLP is symmetric about its maximum; $\frac{t}{\lambda}$ is calculated according to Eqn.2.7 (presented on page 65); and $\left(\frac{I_k}{\sigma_k}\right)$ is produced via an elemental quantification tool, which deconvolutes the spectra using the corresponding low-loss spectra and uses the Hartree-Slater model to calculate σ_k [37].

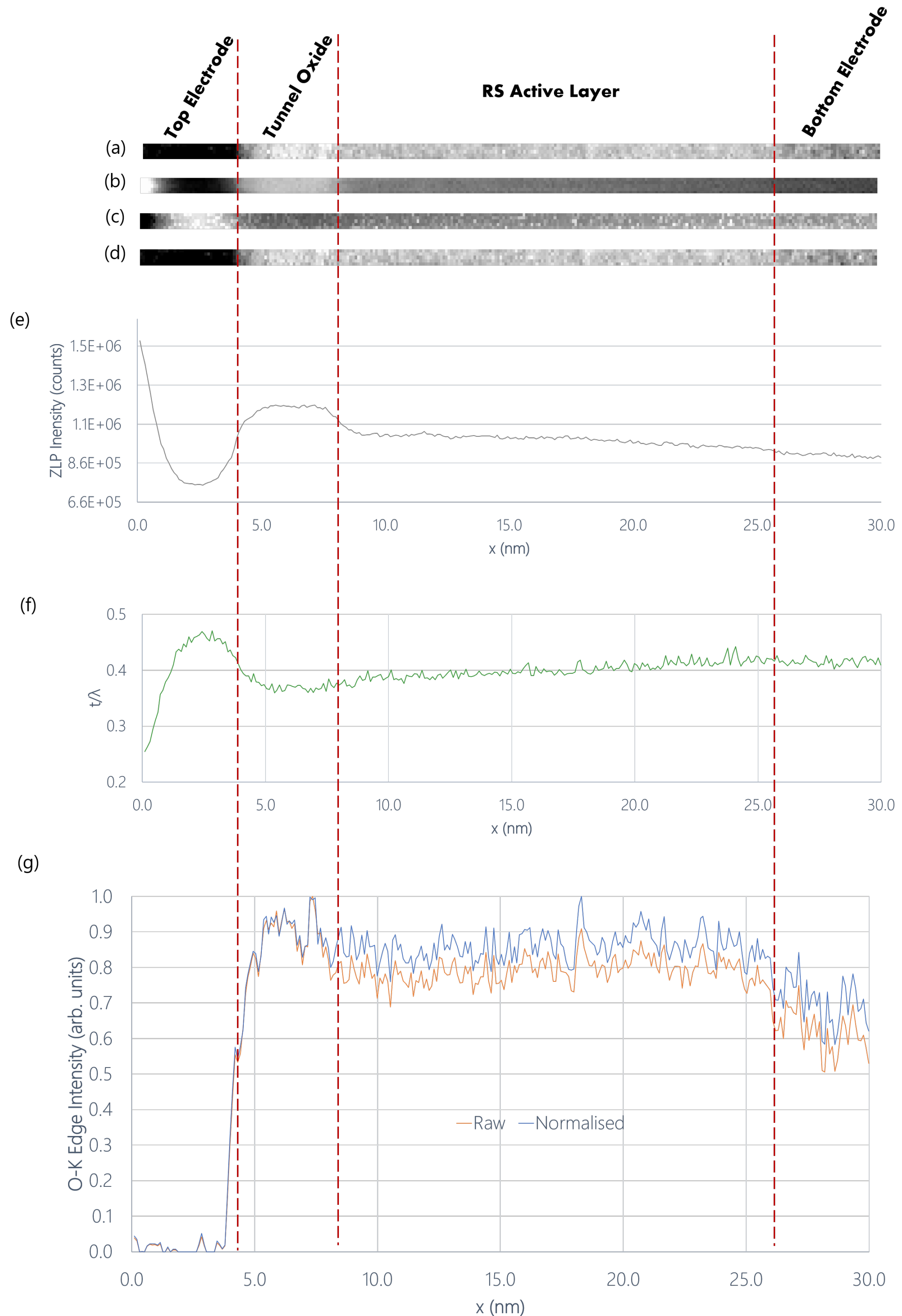

Figure 2.18: *Normalisation process used for the quantification of EELS data included in the analysis of the tunnel RRAM device to be discussed further in Chapter 4. 2D maps, with pixel size 0.19nm^2, showing (a) Raw O K-edge intensity (b) ZLP intensity (c) $\frac{t}{\lambda}$ and (d) O K-edge intensity normalised via Eqn.2.11. The spatial distribution of (b) and (c) are shown in (e) and (f) respectively. (g) A comparison between the spatial distribution of the raw and normalised O-k edge intensity. Red vertical dashed lines highlight the interfaces between functional layers within the tunnel RRAM heterostructure.*

Fig.2.18 shows an representative example of the 2D maps (Figs.2.18(a)-(d)) and corresponding averaged (in the *y*-axis) spatial distributions (Figs.2.18(e)-(g)) involved in the normalisation process for an EELS dataset acquired from the single crystal epitaxial device to be presented and discussed further in Chapter 4. All of the images in Fig.2.18 are aligned along the *x*-axis so that they can be directly compared. In addition, red vertical dashed lines are used to highlight the interfaces between different functional layers of the heterostructure, which include the top electrode, the dedicated tunnel oxide, the RS active layer and the bottom electrode. Fig.2.18(a) presents the raw Oxygen K-edge intensity (I_{Ox}) map, which includes contributions from the ZLP intensity, the lamella thickness and the inelastic mean free path of each material incorporated into the heterostructure; here the intensity of the oxygen K-edge in the bulk RS active layer is increased with respect to the bottom electrode but reduced with respect to the tunnel oxide. Fig.2.18(b) presents the ZLP intensity (I_0) map; here, the variation in intensity across the oxygen-containing layers matches that observed in the raw data, consistent with the direct proportionality relationship between I_{Ox} and I_0 shown in Eqn.2.5. For clarity, the spatial distribution of I_0 is also presented in Fig.2.18(e), where the relative variations in intensity are easily observed. Fig.2.18(c) presents the $\frac{t}{\lambda}$ map and the corresponding spatial distribution is shown in Fig.2.18(f). Here, the top electrode and the tunnel oxide are shown to be the thickest and thinnest regions of the lamella and both come under the threshold $\frac{t}{\lambda}$=0.5 for quantification. Fig.2.18(d) presents the O-K 2D map, which has been normalised according to Eqn.2.10 to account for changes in $\frac{t}{\lambda}$ and the ZLP across the devices and, for an evaluation of the ratio between elements, can be scaled by the oxygen K-edge cross-section, σ_{Ox}. As shown in Eqn.2.10, the normalised value of each pixel presented in Fig.2.18(d) corresponds to the product $n_{Ox}\lambda$, where λ is distinct for each material layer. Finally, the spatial distribution of the raw and normalised oxygen K-edge intensity are presented in Fig.2.18(g). Here, both spatial distributions have to scaled to their respective maximums to allow for direct comparison of any changes to the *shape* of the distribution. It is the shape of the normalised oxygen intensity distributions that were used to evaluate the RS-induced electromigration of $V_{\ddot{O}}$ between the tunnel oxide and the bulk RS layer. For the dataset presented in Fig.2.18(g), the main difference caused by the normalisation process is the relative increase in the

intensity of the O K-edge in the RS active layer and bottom electrode with respect to the tunnel oxide. However, a comparison of spectra extracted from programmed devices showed a reproducible change in the shape of the oxygen K-edge distribution between the LRS and HRS.

Combining Eqns.2.9 and 2.10 produces

$$\frac{n_A \lambda_Y}{n_B \lambda_Z} = \frac{I_{A,N}(\Delta_A)\sigma_B(\Delta_B)}{I_{B,N}(\Delta_B)\sigma_A(\Delta_A)} \tag{2.11}$$

where it should be noted that the inelastic mean free path is a property of a material, therefore the subscripted λ_Y and λ_Z used in Eqn.2.11 represent a comparison of the intensity of core-loss edges acquired in two materials, denoted Y and Z. In this work, inelastic mean free paths were calculated using the Iakoubovskii *et al.*'s log-ratio model parameterisation in which $\lambda \propto \rho^{-0.3}$, where ρ is the density of a given material [43]. In Chapter 3, Eqn.2.11 is used to identify the spatial redistribution of Mn within a RS Mn-doped ZnO film and in Chapter 4, it is used to compare field-induced changes in the distribution of oxygen across three different oxides in a tunnel-RRAM heterostructure.

It is important to note that there are some limitations that can restrict absolute quantification and a number of these relate to σ_k: the Hartree-Slater model used for calculations of σ_k in this work is based on isolated atoms and therefore does not include any of the (environment-dependent) ELNES features obtained experimentally, introducing error [44]; furthermore, whilst σ_k is accurate for light elements which have K-edges at accessible energies (<2keV), uncertainty on σ_k increases greatly for heavier elements with inaccessible K-edges [40]; finally, as the uncertainty on σ_k is a systematic error, the ratio between two edges of different types (for instance, K-type and L-type) have greater uncertainty than that of two edges of the same type [40]. In addition, the log-ratio method used to calculate $\frac{t}{\lambda}$ has accuracy 20% [39]. As described in section 1.3, the *absolute* quantification of EELS data is limited by uncertainties in σ_k and $\frac{t}{\lambda}$; for this reason, the analysis presented in this work focuses on the *relative* quantification of EELS data, that is, in this work, the *ratio* between elements is compared within single SI datasets as well as across different SI datasets using Eqs. 2.10 and 2.11. This elemental ratio normalisation was used in Chapter 3 to compare the Mn and Zn L-type edges and suggested that the Mn:ZnO film had a higher Mn dopant level than expected, which

could be attributed to the high defect density of the irregular polycrystalline films. In Chapter 4, the elemental normalisation confirmed the expected stoichiometry of the single crystal $Pr_{0.48}Ca_{0.52}MnO_3$, showing a Pr:Ca:Mn ratio of 0.5:0.5:1. The Mn:O ratio, however, was greater than expected (1:3.8 instead of 1:3). As the edges involved in the Mn and O relative quantification were L- and K- type respectively, as noted above, inaccuracies in the quantification could, in part, be due to the increased systematic error introduced when comparing edges of different type [35, 40].

2.7.4 Deconvolution

Fourier deconvolution methods in DM allow one to deconvolute DualEELS low- and high-loss spectra to remove plural scattering effects induced by lamellae thickness [45]. Where possible, deconvolution is typically used before a comparison of core-loss ELNES features, as the shape and intensity of a given peak has been shown to vary substantially with plural scattering effects [37]. If direct deconvolution is not possible, due to the generation of artefacts, it is also possible to use DM *quantification* scripts, which are specifically designed to model the core-loss ELNES based on the corresponding low-loss spectra. This quantification tool was used in Chapter 4 to assess the stoichiomentry of ternary complex oxide $PrCaMnO_3$.

2.7.5 Principle Component Analysis

Principal Component Analysis (PCA) is a multivariate statistical analysis method often used to reduce random noise from spectroscopic images. In PCA, a spectroscopic image is decomposed into a number of components of which, only a fraction are reconstructed. This is based on the assumption that the principal components are *strongly* correlated, whereas random noise are *weakly* correlated and can be discarded. PCA is an optional procedure that is typically used tentatively as a cross-referencing tool between the raw and reconstructed data. This is because weakly correlated, yet relevant spectral features may be discarded during processing, and conversely artefacts may also be introduced during reconstruction [46, 47]. In this work PCA was only used in some instances of elemental distribution mapping, and to show the gradual appearance of spectral features confirmed as real in the raw data.

2.7.6 Multiple Linear Least-Squares Fitting

Multiple Linear Least-Squares (MLLS) fitting is a technique primarily used to separate overlapping edges in core-loss EELS spectra [48, 49]; this fitting process is depicted as a schematic in Fig.2.19. Here, an example of a background-subtracted experimentally recorded spectrum, which features overlapping edges, is shown in Fig.2.19(a). Two reference spectra, which represent pure phases that are known to contribute to the experimentally recorded spectrum shown in Fig.2.19(a), are shown in Fig.2.19(b) and labelled S_A and S_B. These reference spectra were used to produce the MLLS fit shown in Fig.2.19(c), which is expressed $F(E) = C_A S_A + C_B S_B$, where C_A and C_B are scaling coefficients for S_A and S_B respectively. In DM, MLLS fits are produced for each pixel in an EELS SI, which means that for each reference spectra, S_x, an x, y-map is produced where the intensity is given by its corresponding scaling coefficient, C_x. In addition, the DM MLLS script also outputs residual- and reduced Chi^2-maps which reflect the quality of the MLLS fit, which is particularly useful for the assessment of the quality of an interface between two phases. For instance, regions of an SI that could not be well fitted using a the linear combination of S_A and S_B could be indicative of the presence of an additional chemically distinct interfacial phase. For this reason, in addition to separating overlapping core-loss edges, MLLS fitting is used to evaluate the spatial distribution of multiple phases [50]. MLLS fitting proved essential in this work: in Chapter 3, this technique was used to map the spatial distribution of two chemically distinct interfacial phases present at the rough interface between polycrystalline Mn-doped ZnO and a strongly reducing Ti top electrode.

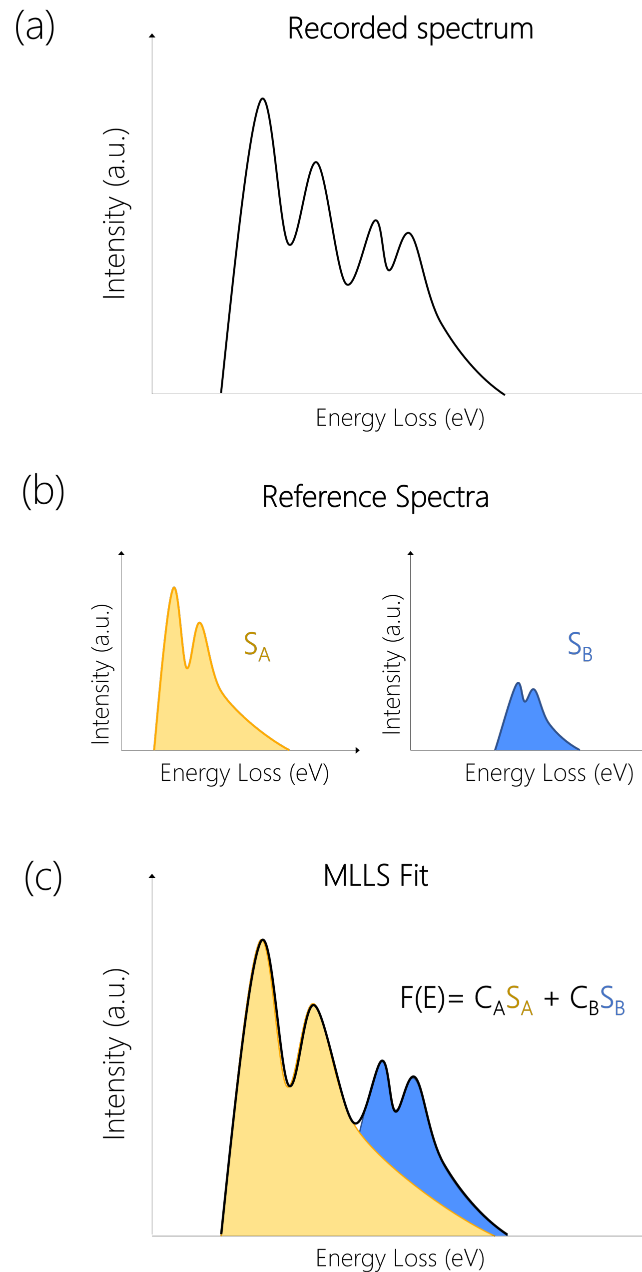

Figure 2.19: *Schematic diagram of MLLS fitting technique. (a) background-subtracted core-loss spectrum which features two overlapping core-loss edges*. (b) two separate reference spectra (S_A and S_B) that contribute to the recorded spectrum shown in (a); these references are recorded at the same energy offset and dispersion as (a). (c) resultant MLLS fit made using reference spectra shown in (b).

2.7.7 Electron Energy Loss Magnetic Spectrometer

Both the T20 and ARM are equipped with post-column Gatan Image Filter (GIF) magnetic prism spectrometers. Within the GIF spectrometer, electrons are deflected by a perpendicular **B** field, which causes those travelling with velocity v to follow a path

with radius of curvature R given by:

$$R = \frac{m_0 v}{qB}\left(1 - \frac{v^2}{c^2}\right)^{-1/2} \tag{2.12}$$

where m_0 and q are the mass and charge of an electron respectively, and c is the speed of light. Equation 2.12 shows that electrons that have undergone larger(smaller) energy loss and have lower(higher) velocity as a result will be subject to a smaller(larger) radius of curvature. This difference in curvature produces multiple distinct points of focus in the dispersion plane of the spectrometer, which directly correspond to separation in energy loss, as depicted by points **P** and **P'** in Fig.2.20 [28]. To acquire a *full* spectrum in STEM mode, the electrically isolated drift tube, shown in Fig.2.20, is biased such that the kinetic energy of electrons incident at the Charge-Coupled Device (CCD) can be adjusted as desired. An aberration corrector and magnifying lenses are positioned between the dispersion plane and a CCD detector.

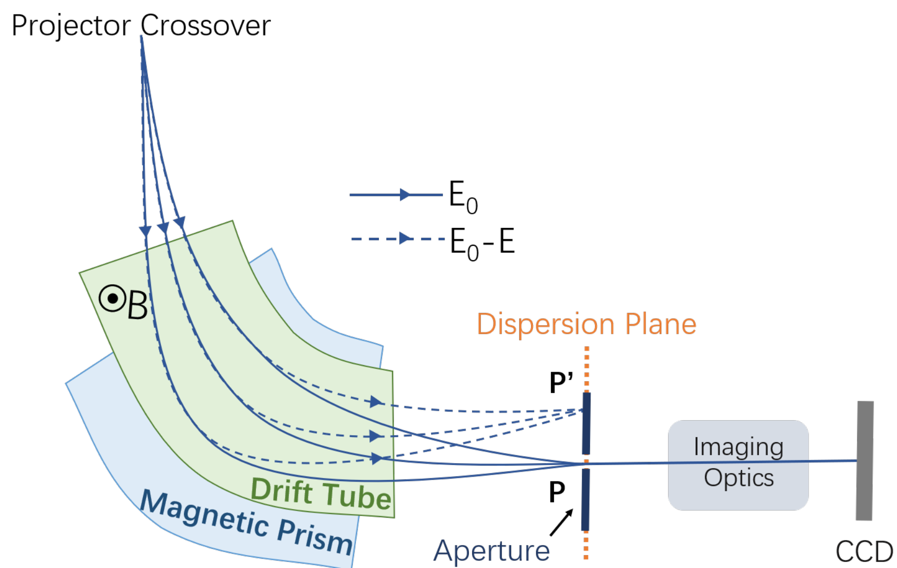

Figure 2.20: *Gatan Image Filter magnetic spectrometer employed for spectroscopic analysis of electron energy losses. Electrons with energy E_0 and $E_0 - E$ are represented by the solid and dashed blue lines respectively. A magnetic field* **B** *is applied across an electrically isolated drift tube, perpendicular to the trajectory of electrons, which causes a change in radius of curvature. Electrons with distinct energy loss are focused at points* **P** *and* **P'** *in the spectrometer dispersion plane. An aperture slit is used to select specific energy losses for imaging at the CCD detector.*

2.8 Hard X-Ray Photoelectron Spectroscopy

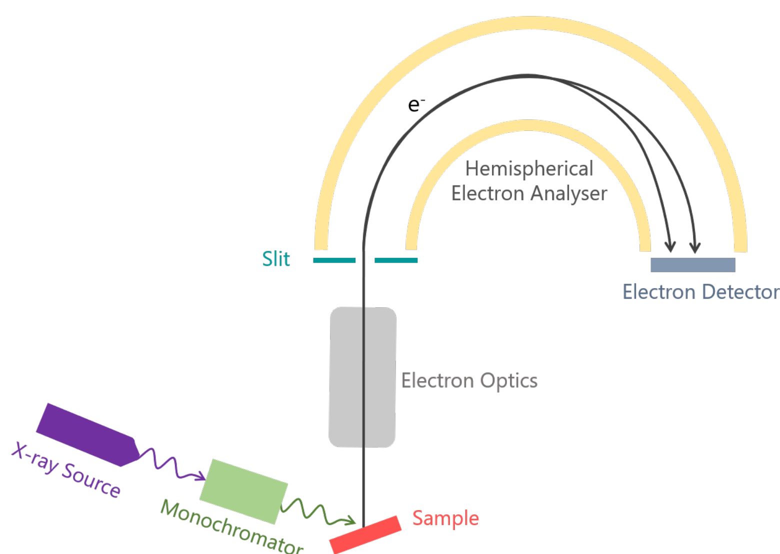

Figure 2.21: *Diagram showing X-ray Photoelectron Spectroscopy apparatus in which photoelectrons (represented by black curved arrows) are generated as a result of sample (shown in orange) irradiation by monochromatic X-rays (represented by green wavey arrow). These X-ray photoelectrons are accelerated through, and focused by a series of electrostatic lenses (represented by electron optics column shown in grey) before reaching the hemispherical electron analyser via an aperture slit. Within the analyser, an electric field is applied across the outer and inner hemispherical components (shown in yellow) such that the photoelectrons are deflected by 180°, and photoelectrons with different kinetic energies are separated.*

Another UHV spectroscopic technique presented in Chapter 4, but undertaken by collaborators in Jülich, is Hard X-Ray Photoelectron Spectroscopy (HAXPES), which measures the kinetic energy spread of electrons emitted from an X-ray irradiated sample due to the photoelectric effect [51]. The measurement of photo-emitted electron (photoelectron) energies provides information about the electronic structure of the sample because photoelectrons have kinetic energy:

$$E_k = h\nu - E_B - \Phi \qquad (2.13)$$

where h is Planck's constant, ν is the frequency of the photon, E_B is the binding energy of a core shell electron and Φ is the work function of the electron analyser [52–54]. For insulating materials, the emission of photoelectrons leads to an accumulation of

positive charge at the sample surface; as a result, E_k is further reduced, which results in a shift, of the corresponding photoelectron peak, to lower energies. Fig.2.21 shows how generated photoelectrons are deflected through 180° along a hemispherical electron analyser column before registration at an electron detector. The outer and inner hemispherical components (shown in yellow in Fig.2.21) are held at positive and negative potential, and can be adjusted to isolate electrons within a specific range of kinetic energies, allowing one to scan a full spectrum.

The inelastic mean free path of each photoelectron, defined as the distance a photoelectron travels through a material before losing its energy, is dependent on the energy of the photons that generated it: higher(lower) energy X-rays produce photoelectrons with larger(smaller) mean free paths. This means that by tuning the incident X-ray energy, it is possible to tune the X-ray probing depth [55]. *Hard* X-ray Photoelectron Spectroscopy refers to X-rays with energies exceeding 2kV, which probe material within 10nm beneath the sample surface. This probing depth proved particularly useful for investigating shallow-buried heterointerfaces within the RRAM devices that are presented in Chapter 4.

2.9 Atomic Force Microscopy

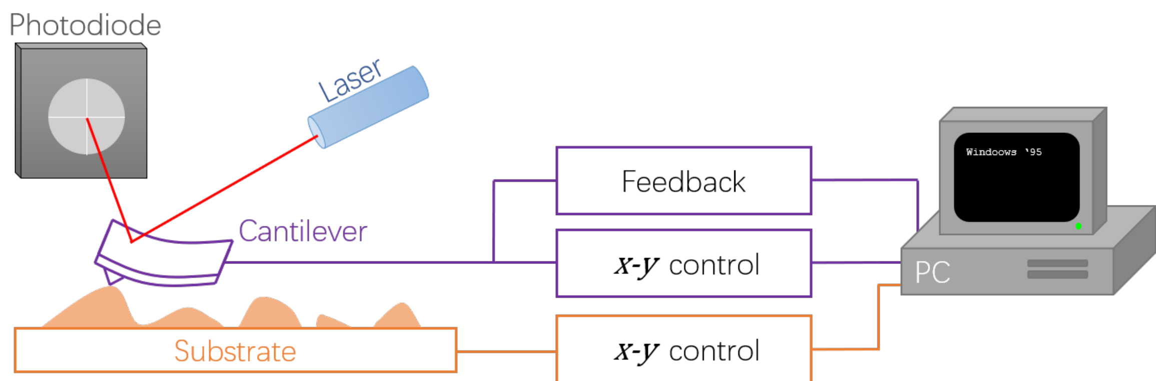

Figure 2.22: *An Atomic Force Microscope set up in which the cantilever-mounted tip, shown in black, scans a rough sample surface, shown in orange, and is deflected as a result. Cantilever deflection is measured using a quandrant photodiode detector that records a laser signal reflected from the cantilever. A computer interface can used to control the contact-mode of the AFM through a feedback loop, and the sample stage and tip can be moved in x- and y-directions.*

Atomic Force Microscopy (AFM), developed by Binnig *et al.* in 1986, is a surface sensitive technique widely used to characterise substrate and thin film surfaces in materials science. In principle, the AFM rasters a sharp, cantilever-mounted tip across the sample surface and measures cantilever deflection due to Van der Waals interactions between the sample surface and tip [56]. Fig.2.22 illustrates how the reflection of a laser, incident on the deflected cantilever, is recorded on a quadrant photodiode as the tip scans the sample surface. There are several modes in which the AFM can operate; through feedback control, the tip can be remain in constant contact with the surface, or it can oscillate above it within close proximity. For the studies presented in this work, non-destructive tapping-mode was employed. In tapping-mode, the cantilever is oscillated at its resonant frequency, and tip-sample interaction causes a change in its amplitude and phase. In non-contact mode, used to image soft, easily damaged samples, the tip also oscillates at resonant frequency and change in amplitude is measured, however the tip oscillates above the sample surface. Furthermore, through the use of functionalised tips, the principle of AFM can be applied to magnetic-, kelvin-probe-(sensitive to work function) force microscopy to name a few; in general, variations on this technique are referred to collectively as scanning probe microscopy.

Atomic force microscopy is a effective technique for use in conjunction with thin film deposition, as it can be used to assess the substrate surface before deposition, as well as the deposited film surface, and requires no functional properties of the sample. Substrate assessment prior to deposition is incredibly important for the deposition of single crystal films as the substrate provides a crystallographic foundation for subsequent growth. An example of this is the crystalline perovskite oxide RRAM device presented in Chapter 4 that comprises a thin film of single crystal $Pr_{0.48}Ca_{0.52}MnO_3$ deposited on a crystalline $SrTiO_3$ substrate that had first been subject to processing steps to facilitate 2D layer-by-layer growth. As it is possible to expose planes of SrO, TiO_2, or a mixture of both on the $SrTiO_3$ surface, there is a wealth of literature on processing methods for $SrTiO_3$, a majority of which use AFM height and phase imaging for surface characterisation. As an illustration, Fig.2.23 presents work undertaken on the optimisation of $SrTiO_3$ substrate processing for deposition of $LaSrMnO_3$ via 2D growth modes on the local PLD system, which is similar to the substrate preparation processes required for the

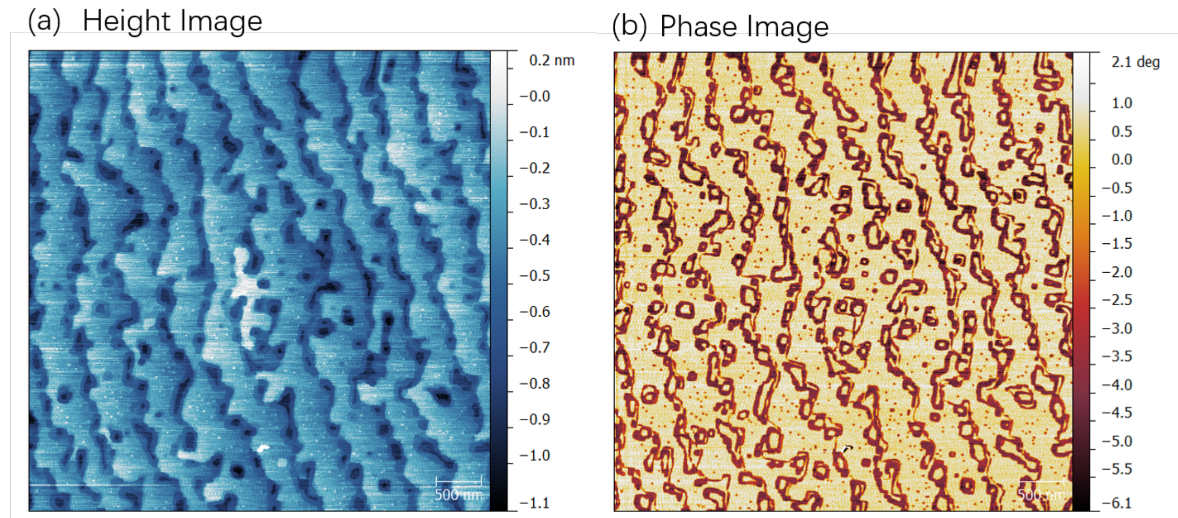

Figure 2.23: *5µm by 5µm AFM (a) height and (b) phase images of double-terminated $SrTiO_3$ vicinal surface after substrate processing. (a) A vicinal surface in which the left hand side of the image is higher with respect to the right, and each step edge is followed by a trough with height difference equal to $\frac{1}{2}$u.c. (b) These troughs correspond to a change in phase, and the relative phase difference is consistent with exposure of SrO in the troughs, and TiO_2 on the step surfaces. These images were acquired simultaneously over the same area in tapping mode*

fabrication of the crystalline perovskite oxide device presented in Chapter 4. Here, the surface presented in Fig.2.23 was produced after the substrate was first annealed at 1000°C for 2 hours, then etched in reverse-osmosis water at 90°C for 10 minutes, and finally annealed again under the same conditions. In the preparation of $SrTiO_3$, high-temperature anneals are used to induce the migration of SrO to the substrate surface. Submerging the substrate in water then forms SrO-hydroxyls that can be etched away in either water or buffered hyrdofluoric acid. The removal of SrO promotes a TiO_2 singly-terminated surface, which, in its chemical uniformity, is suitable for deposition, however etching typically results in a roughened surface that can be improved upon with a final 're-crystallisation' anneal. However, for the substrate presented in Fig.2.23, the final anneal caused excessive migration of SrO to the substrate surface, which is evident in both the height and phase images. The height image shown in Fig.2.23(a) reveals a vicinal (stepped) surface where each step-edge features a trough that is $\frac{1}{2}$ of a unit cell (u.c.) deep; these troughs appear darker than the step surfaces. As SrO and TiO_2 planes are separated by $\frac{1}{2}$u.c., this image shows evidence for doubly-terminated $SrTiO_3$ (i.e two phases, as opposed to one, are exposed on the substrate surface). Furthermore,

the phase image shown in Fig.2.23 revealed two distinct phases on the substrate surface, which are consistent with TiO_2-terminated steps, and SrO-terminated troughs.

2.10 Electrical Probe Station

An electrical probe station was used to electrically characterise thin films and RRAM devices. A Keithley sourcemeter sourced current or voltage to probes that were mounted onto micro-manipulator stages, which permitted access to electrode contacts. The probes and sample mount were housed within a glove box to allow for oxygen to be purged before sample measurements. Fig.2.24(a) shows how, for the electrical characterisation of thin films, four-probe Van der Pauw measurements were undertaken to assess sheet resistivity R_s. Van der Pauw's method requires four small electrical contacts to be deposited onto a thin film of uniform thickness. If a potential difference is applied across two contacts ($V_{3,4}$), the current measured across the two contacts on the opposite side ($I_{1,2}$) can be probed and a resistance value can be derived ($R_{12,34}$); these resistances can be substituted into Van der Pauw's formula [57]:

$$exp[-\pi R_{vertical}/R_s] + exp[-\pi R_{horizontal}/R_s] = 1 \tag{2.14}$$

to find R_s, where $R_{vertical} = \frac{1}{2}(R_{12,34} + R_{34,12})$, and $R_{horizontal} = \frac{1}{2}(R_{23,41} + R_{41,23})$.

To characterise RRAM devices two probes were used; one to probe the top electrode contacts patterned onto the surface of bulk RRAM devices (imaged in Fig.2.4 in Section 2.3), and one to probe the bottom electrode thin film that was purposefully left exposed during the pulsed laser deposition of subsequent layers, as shown in Fig.2.24(b). A LabVIEW script created specifically for RRAM measurements was used, and permitted control over compliance current, applied voltage, and voltage polarity, which was particularly useful for the characterisation of the bipolar RRAM devices presented in this work.

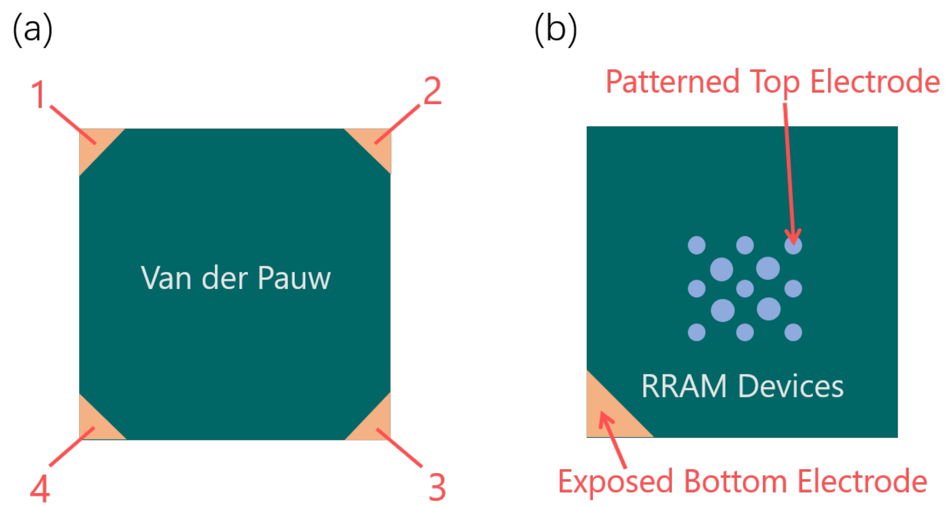

Figure 2.24: *Electrical characterisation set-up used for (a) Van der Pauw and (b) RRAM device measurements. Corner electrodes are shown in peach, and patterened electrodes are shown in lilac.*

Bibliography

[1] G. K Hubler and D. B. Chrisey. *Pulsed laser deposition of thin films*. New York: J. Wiley, 1994.

[2] B.K. Gupta and B. Bhushan. Micromechanical properties of amorphous carbon coatings deposited by different deposition techniques. *Thin Solid Films*, 270(1-2):391–398, 1995.

[3] D. H. A. Blank, M. Dekkers, and G. Rijnders. Pulsed laser deposition in Twente: from research tool towards industrial deposition. *Journal of Physics D-Applied Physics*, 034006(47):1–8, 2013.

[4] M. R. R. Vaziri, F. Hajiesmaeilbaigi, and M. H. Maleki. Monte Carlo simulation of the subsurface growth mode during pulsed laser deposition. *Journal of Applied Physics*, 110(043304), 2011.

[5] P. Willmott and J. Huber. Pulsed laser vaporization and deposition. *Reviews of Modern Physics*, 72(1):315–328, 2000.

[6] J. M. Warrender and M. J. Aziz. Kinetic energy effects on morphology evolution during pulsed laser deposition of metal-on-insulator films. *Physical Review B*, 75(1):1–11, 2007.

[7] H. M. Smith and A. F. Turner. Vacuum Deposited Thin Films Using a Ruby Laser. *Applied Optics*, 4(1):147–148, 1965.

[8] J. T. Cheung and H. Sankur. Growth of thin films by laser-induced evaporation. *CRC Critical Reviews in Solid State and Materials Sciences*, 15(1), 1988.

[9] J. G. Bednorz and K. A. Miiller. Possible High Tc Superconductivity in the Ba-La-Cu-O System. *Zeitschrift fur Physik B - Condensed Matter*, 64:189–193, 1986.

[10] C. Belouet. Thin film growth by the pulsed laser assisted deposition technique. *Applied Surface Science*, 96-98:630–642, 1996.

[11] M. Strikovski and J. H. Miller. Pulsed laser deposition of oxides: Why the optimum rate is about 1 Å per pulse. *Applied Physics Letters*, 73(12):1733–1735, 1998.

[12] D. H. A. Blank, G. J. Rijnders, G. Koster, and H. Rogalla. In-situ monitoring during pulsed laser deposition using RHEED at high pressure. *Applied Surface Science*, 127-129:633–638, 1998.

[13] E. G. Gamaly, A. V. Rode, and B. Luther-Davies. Ultrafast Laser Ablation and Film Deposition. *Pulsed Laser Deposition of Thin Films*, pages 99–129, 2006.

[14] M. Stafe, A. Marcu, and N. Puscas. *Pulsed Laser Ablation of Solids: Basics, Theory and Applications*. Springer-Verlag Berlin Heidelberg, 1 edition, 2013.

[15] J. Sarkar. Chapter 1 - sputtering targets and sputtered films for the microelectronic industry. In J. Sarkar, editor, *Sputtering Materials for VLSI and Thin Film Devices*, pages 1 – 92. William Andrew Publishing, Boston, 2014.

[16] J. A. Thornton. High rate thick film growth. *Annual Reviews in Materials Science*, 7:239–260, 1977.

[17] J. E. Greene. Review Article: Tracing the recorded history of thin-film sputter deposition: From the 1800s to 2017. *Journal of Vacuum Science & Technology A: Vacuum, Surfaces, and Films*, 35(5), 2017.

[18] P. Parreira, G. W. Paterson, S. McVitie, and D. A. MacLaren. Stability, bistability and instability of amorphous ZrO2 resistive memory devices. *Journal of Physics D: Applied Physics*, 49(9):095111, 2016.

[19] M. Geissler and Y. Xia. Patterning: Principles and Some New Developments. *Advanced Materials*, 16(15):1249–1269, 2004.

[20] C. A. Bishop. Electron beam (e-beam) evaporation. In C. A. Bishop, editor, *Vacuum Deposition onto Webs, Films and Foils (Second Edition)*, pages 261 – 272. William Andrew Publishing, Oxford, second edition edition, 2011.

[21] L. A. Giannuzzi and F. A. Stevie. A review of focused ion beam milling techniques for TEM specimen preparation. *Micron*, 30:197–204, 1999.

[22] S. Reyntjens and R. Puers. A review of focused ion beam applications in microsystem technology. *Journal of Micromechanics and Microengineering*, 11:287–300, 2001.

[23] C. A. Volkert and A. M. Minor. Focused Ion Beam Micromachining. *MRS Bulletin*, 32(May):389–399, 2007.

[24] D. Richards. Near-field microscopy: throwing light on the nanoworld. *Philosophical Transactions of the Royal Society of London*, A(361):2843–2857, 2003.

[25] L. D. Broglie. Recherches sur la theorie des Quanta Louis De Broglie. *Annales de Physique*, 3(10), 1925.

[26] 1986 nobel prize. `https://www.nobelprize.org/prizes/physics/1986/summary/`. Accessed: 201-12-29.

[27] E. Rutherford. The Scattering of α and β Particles by Matter and the Structure of the Atom. *Philosophical Magazine*, 6(21):1–24, 1911.

[28] D. B. Williams and C. B. Carter. *Transmission Electron Microscopy*. Springer, 2 edition, 2009.

[29] R. F. Egerton. Electron energy-loss spectroscopy in the TEM. *Reports on Progress in Physics*, 72(1):016502, 2009.

[30] A. L. Patterson. The scherrer formula for X-ray particle size determination. *Physical Review*, 56(10):978–982, 1939.

[31] O. Scherzer. The Theoretical Resolution Limit of the Electron Microscope. *Journal of Applied Physics*, 20(20), 1949.

[32] J. Thomas and T. Gemming. What should we know about electron optics and the construction of an electron microscope? In *Analytical Transmission Electron Microscopy: An Introduction for Operators*, pages 11–39. Springer Netherlands, Dordrecht, 2014.

[33] M. Haider, H. Rose, S. Uhlemann, E. Schwan, B. Kabius, and K. Urban. A spherical-aberration-corrected 200 kV transmission electron microscope. *Ultramicroscopy*, 75:53–60, 1998.

[34] S. J. Pennycook. A Scan Through the History of STEM. In S. J. Pennycook and P. D. Nellist, editors, *Scanning Transmission Electron Microscopy: Imaging and Analysis*, chapter 1, pages 1—-90. Springer, 2011.

[35] R.F. Egerton. *Electron Energy-Loss Spectroscopy in the Electron Microscope*, volume 72. Springer, 3 edition, 2011.

[36] B. Arndt, F. Borgatti, F. Offi, M. Phillips, P. Parreira, T. Meiners, S. Menzel, K. Skaja, G. Panaccione, D. A. Maclaren, R. Waser, and Regina Dittmann. Spectroscopic Indications of Tunnel Barrier Charging as the Switching Mechanism in Memristive Devices. *Advanced Functional Materials*, 1702282, 2017.

[37] R. F. Egerton. Limits to the spatial, energy and momentum resolution of electron energy-loss spectroscopy. *Ultramicroscopy*, 107:575–586, 2007.

[38] Aaron B. Naden. *Resolving Structure-Function Relations in Advanced Materials by Scanning Probe and Electron Microscopies*. PhD thesis, Univeristy of Glagow, 2015.

[39] R. F. Egerton, F. Wang, and P. A. Crozier. Beam-induced damage to thin specimens in an intense electron probe. *Microscopy and Microanalysis*, 12(1):65–71, 2006.

[40] A. J. Craven, J. Bobynko, B. Sala, and I. MacLaren. Accurate measurement of absolute experimental inelastic mean free paths and EELS differential cross-sections. *Ultramicroscopy*, 170:113–127, 2016.

[41] Kirsty J. Annand. *The Nanoscale Mechanisms of Zircaloy-4 Corrosion in Simulated Nuclear Reactor Conditions*. PhD thesis, University of Glasgow, 2018.

[42] R. Brydson. A brief review of quantitative aspects of electron energy loss spectroscopy and imaging. *Materials Science and Technology*, 16(October):1187–1198, 2000.

[43] K. Iakoubovskii, K. Mitsuishi, Y. Nakayama, and K. Furuya. Thickness Measurements With Electron Energy Loss Spectroscopy. 631:626–631, 2008.

[44] A. J. Craven, B. Sala, J. Bobynko, and I. MacLaren. Spectrum imaging of complex nanostructures using DualEELS: II. Absolute quantification using standards. *Ultramicroscopy*, 186:66–81, 2018.

[45] Gatan. DigitalMicrograph EELS Analysis User's Guide. Technical Report 1.2.1, 2004.

[46] M. Varela, M. P. Oxley, W. Luo, J. Tao, M. Watanabe, A. R. Lupini, S. T. Pantelides, and S. J. Pennycook. Atomic-resolution imaging of oxidation states in manganites. *Physical Review B - Condensed Matter and Materials Physics*, 79(8):1–14, 2009.

[47] J. Bobynko, I. MacLaren, and A. J. Craven. Spectrum imaging of complex nanostructures using DualEELS: I. digital extraction replicas. *Ultramicroscopy*, 149:9–20, 2015.

[48] A. Maigné and R. D. Twesten. Review of recent advances in spectrum imaging and its extension to reciprocal space. *Journal of Electron Microscopy*, 58(3):99–109, 2009.

[49] R D Leapman and C R Swyt. Separation of Overlapping Core EDGES in Electron Energy Loss Spectra. *Ultramicroscopy*, 26:393–404, 1988.

[50] Kirsty Annand. *The Nanoscale Mechanisms of Zircaloy-4 Corrosion in Simulated Nuclear Reactor Conditions*. PhD thesis, University of Glasgow, 2017.

[51] C. Nordling, E. Sokolowski, and K. Siegbahn. Precision Method for Obtaining Absolute Values of Atomic Binding Energies. *Physical Review*, 105(5):1676–1677, 1957.

[52] C. Weiland, A. K. Rumaiz, P. Pianetta, and J. C. Woicik. Recent applications of hard x-ray photoelectron spectroscopy. *Journal of Vacuum Science & Technology A: Vacuum, Surfaces, and Films*, 34(3):030801, 2016.

[53] J. Azoulay. Photoelectron spectroscopy-principles and applications. *Vacuum*, 33(4):211–213, 1983.

[54] J. C. Woicik. *Hard X-ray Photoelectron Spectroscopy (HAXPES)*, volume 59. Springer, 2016.

[55] B. Pal, S. Mukherjee, and D. D. Sarma. Probing complex heterostructures using hard X-ray photoelectron spectroscopy (HAXPES). *Journal of Electron Spectroscopy and Related Phenomena*, 200:332–339, 2015.

[56] G. Binnig and C. F. Quate. Atomic Force Microscope. *Physical Review Letters*, 56(9):930–933, 1986.

[57] L. Van Der Pauw. A method of measuring resistivity and Hall effect of lamellae of arbitrary shape. *Philips Tech Rev*, 20(I):220–224, 1958.

CHAPTER 3

Polycrystalline Manganese-Doped Zinc Oxide RRAM Device

This chapter focuses on the optimisation of pulsed laser deposited zinc oxide and manganese-doped zinc oxide thin films for applications in RRAM. Binary oxides, such as ZnO, TiO_2, WO_x and TaO_x, have been of particular interest for applications in RRAM due to their CMOS compatibility and simple composition [1]. In this chapter, a comparison of RS in undoped and 5% Mn-doped ZnO is made. Whilst RS in undoped ZnO is well characterised in the literature, a few recent studies have demonstrated that for Mn-doped ZnO, it is possible to switch the magnetic and resistive properties of the material simultaneously under an applied electric field, highlighting the potential for applications in multifunctional spintronic devices [2, 3]. Despite these findings, there is little literature on the morphology and stoichiometry of 5% Mn-doped ZnO thin films that display RS. In this study, both ZnO-based thin films were deposited via PLD over a range of deposition temperatures and pressures and were characterised using a number of techniques: AFM was used for the assessment of surface topology post-deposition, providing information on surface roughness, grain size and, indirectly, crystallinity; electrical characterisation allowed for the evaluation of resistive switching behaviour; and finally TEM and TEM-EELS were used to confirm film morphology and evaluate film stoichiometry respectively. Through this characterisation, RS in both undoped and Mn-doped ZnO was found to be consistent with oxygen vacancy ($V_{\ddot{O}}$)-

mediated VCM-type RS in which interfacial oxides, formed between the active electrode and ZnO films, facilitated switching. All deposited films were shown to be polycrystalline, and interestingly, in the Mn-doped ZnO films, Mn was found to accumulate along grain boundaries. Furthermore, the investigation revealed evidence for field-induced redistribution of Mn throughout the film, which is not typically observed in polycrystalline Mn-doped ZnO in the literature [4].

3.1 Properties of Zinc Oxide

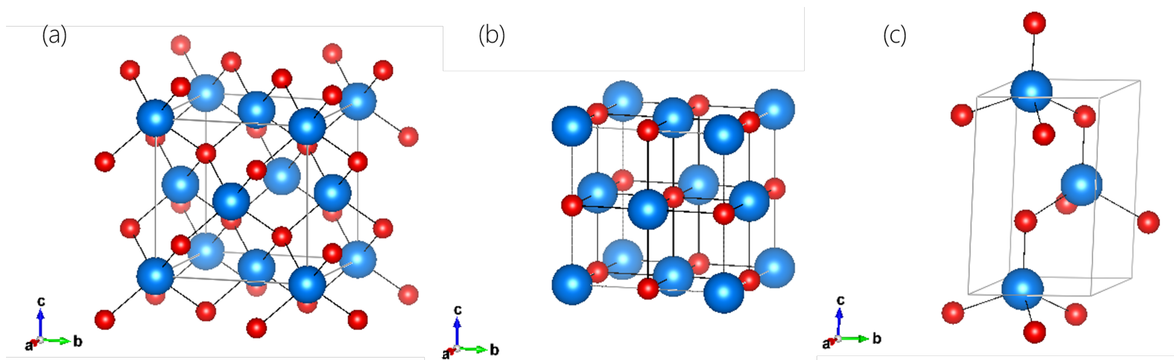

Figure 3.1: *(a) cubic rocksalt (b) cubic zinc blende and (c) hexagonal wurzite ZnO structures. The blue and red spheres represent Zn and O atoms respectively.*

Zinc oxide (ZnO) is a II-VI semiconductor material which can have a cubic rocksalt (F m -3 m), cubic zinc blende (F -4 3 m), or hexagonal wurzite (P 63 m c) crystal structure, as shown in Fig.3.1, which have lattice parameters $a = 4.3$, $a = 4.$ and $a = 3.3$, $c = 5.2$ respectively [5,6]. Both the zinc blende and wurzite structures are made up of tetragonally coordinated Zn [7], however, of these structures, only wurzite ZnO is thermodynamically stable under ambient conditions [5]. Wurzite ZnO has a wide, direct band gap (3.37eV at 300K [8]) and a large exciton binding energy (60meV [9]). These findings permitted the realisation of ZnO UV-light emitters in 1996 and prompted worldwide research into ZnO for further applications in optoelectronics [9]. To its advantage, ZnO can be deposited via a number of physical and chemical vapour deposition techniques: whilst polycrystalline ZnO is typically deposited onto amorphous glass and silicon/silicon oxide (Si/SiO_x) substrates via conventional magnetron sputtering [10], sol-gel techniques [11], and chemical vapour deposition [12, 13], single crystal ZnO has been deposited onto

sapphire, quartz and silicon substrates via molecular beam epitaxy [14], RF magnetron sputtering [5] and pulsed laser deposition [15]. This, coupled with the wide range of deposition techniques available, means that ZnO currently is employed in research across multiple disciplines such as chemical and bio-sensing, optical waveguides, transparent conductive oxides, piezoelectric transducers, varistors, and RRAM memory storage [5].

In its undoped state, ZnO has n-type conductivity due to the presence of intrinsic defects, oxygen vacancies and Zn interstitials [5, 16, 17]. Through doping, it is possible to control the number of charge carriers and tune the electrical properties of ZnO from insulating to metallic. Furthermore, doping can also be used to manipulate the magnetic properties of ZnO [5]. In particular, doping with 3d-transition metal ions such as Mn, Fe, Cr or Co into ZnO produces Dilute Magnetic Semiconductors (DMS), a group of materials which have applications in spintronics [18]. With regards to RRAM, such DMS materials offer an exciting opportunity for the pursuit of *multifunctional* RS devices, in which magnetic as well as electronic properties of the ZnO undergo reversible changes with applied voltage. Since Dietl *et al.*'s 2000 prediction that at 5% doping, Mn-doped ZnO (Mn:ZnO) would be ferromagnetic at room temperature, a vast amount of literature presenting experimental observations of the room temperature ferromagnetic hysteresis of Mn:ZnO has built up [19–21]. The theoretical study attributed room temperature ferromagnetism (RT-FM) in Mn-doped DMS to the substitution of Mn^{2+} for Zn. In this valence state, Mn has a half-filled 3d subshell in which all five orbitals contain a single electron which, according to Hund's rule, have parallel spin. Given the considerable energy required to add an electron with anti-parallel spin to an orbital, this half-filled $3d^5$ orbital has comparable stability to that of a complete subshell and results in a strong magnetic moment. Dietl *et al.* proposed that in these Mn:ZnO systems, strong coupling between the transition metal $3d^5$ spins and free charge carriers allows for carrier-mediated ferromagnetism [5]. However, since then, in addition to the experimental publications that have shown evidence for RT-FM in Mn:ZnO, there are those publications that also show no evidence for RT-FM, as well as others that have demonstrated the existence of RT-FM in *undoped* and non-magnetically-doped ZnO films; in the latter, RT-FM has been attributed to $V_{\ddot{O}}$-concentration [22], Zn-vacancy concentration [23], Zn interstitials [24] and O interstitials [25], which implies

that RT-FM is not solely dependent on magnetic coupling between spin polarised Mn atoms and free charge carriers as Dietl *et al.* proposed [26]. In addition, whether intentionally or unintentionally, these intrinsic defects can also be produced in Mn:ZnO, which further complicates our ability to fully describe RT-FM. However both theoretical and experimental studies have presented evidence demonstrating that the number of $V_{\ddot{O}}$ present in Mn:ZnO affect the presence and stabilisation of RT-FM in Mn:ZnO [26, 27]. This dependence was explained by Coey *et al.* who proposed that that magnetic polarons are bound at $V_{\ddot{O}}$ within the crystal lattice and these polarons allow for the ferromagnetic exchange coupling of Mn dopant cations [27]. Despite these findings, due to the lack of reproducibility of RT-FM in Mn:ZnO structures across the literature, its exact cause remains controversial. Much of the controversy may be caused by the difference in deposition and preparation methods used across the literature [26, 27]: as mentioned above, ZnO can be deposited by a wide choice of techniques. Considering previous works, which emphasise the importance of the control over the density of $V_{\ddot{O}}$ throughout the material, in this work, 5% Mn:ZnO was fabricated using PLD and probed used EELS, where the stoichiometry could be controlled and evaluated. An optimisation study, used to identify the ideal deposition conditions for producing stable RS in ZnO and Mn:ZnO, was undertaken and is presented in this chapter. There has been relatively little investigation of RS in ferromagnetic ZnO [28–31]; of these, so far only two studies have demonstrated the *coexistence* of simultaneous resistive and magnetic switching in Mn:ZnO [2, 3], which indicates the urgent need for exploration in this area. This study focuses on the *chemistry* of RS Mn:ZnO devices designed for direct comparison to those shown in the literature to display the simultaneous co-switching of resistivity and magnetisation. Here, the mechanism of RS in both doped and undoped ZnO RRAM devices through electrical, morphological and spectroscopic characterisation. In particular, through a TEM-EELS evaluation of the valence state of manganese dopants [2, 32], it was possible to assess redox activity due to $V_{\ddot{O}}$-migration and identify the formation of $Ti_xMn_yO_z$ interfacial oxides. Ferromagnetic resonance measurements were also attempted, however no magnetisation was measured; this could be due to the relatively low Mn-dopant levels used in this work, which may require higher probing sensitivity.

3.2 Resistive Switching in Zinc Oxide

Resistive switching in ZnO was first demonstrated in 2008 by Chang *et al.* within a symmetrical, inert electrode Pt/ZnO/Pt heterostructure [33]; they showed that in such a structure, polycrystalline ZnO films exhibited unipolar RS, and attributed this to the formation and rupture of conductive filaments which formed along the grain boundaries between crystalline regions within the ZnO film [33]. Importantly, they proposed that the conductive filaments comprised $V_{\ddot{O}}$, a conclusion that has since been supported by later experimental studies that focused on the effect of ZnO oxygen content on RS performance [1, 34]. According to the description presented in Section 1.2.4, Chang *et al.*'s device is fully described by the TCM RS mechanism, however, in the literature, there is some debate as to whether or not this should be classified as VCM, due its dependence on $V_{\ddot{O}}$, or TCM, given its compliance current dependent unipolar RS behaviour. For the purpose of clarity, in this work, all instances of unipolar RS will be ascribed to the TCM mechanism, as done in the most prominent review papers [35, 36]. Since Chang *et al.*'s work, one of the most notable studies on RS in another Pt/ZnO/Pt structure was performed by Huang *et al.* [37]; their study revealed that, if probed under forward *and* reverse bias, they could drive a transformation from reproducible unipolar, filamentary TCM RS, as seen by Chang *et al.*, to sustainable, homogeneous, bipolar VCM RS, which was a switching mode that had not been observed in ZnO systems previously [37]. Specifically, Huang *et al.* proposed that whilst moderate, positive voltages and compliance currents sustained unipolar RS, larger, negative voltages stimulated a mass $V_{\ddot{O}}$-migration away from the cathode and towards the anode [37]; this $V_{\ddot{O}}$-migration created a oxygen-deficient region near the cathode which acted as a reservoir to sustain VCM RS [37]. Notably, this study quite clearly demonstrated that the manner in which RRAM heterostructures are electrically probed has huge influence on the exhibited RS behaviour, and that as well as careful RRAM heterostructure design, electrical probing can be used to isolate and promote a single RS mechanism above other competing mechanisms. Despite these findings, since then, the effect of electrical probing on the type of RS mechanism is rarely investigated or accounted for in the literature. Instead, most experimental studies tend to focus on the reproducibility of a

single RS mechanism, typically the mechanism described in a prominent early paper, and do not usually investigate the possibility of sustaining other mechanisms. Furthermore, as noted in Chapter 1, in this field, there is also an expectation that RRAM devices initially require a filamentary electroforming process; this expectation prompts experimentalists to apply high forming voltages to their RRAM heterostructures, a process which, although often successful, may prevent the observation of alternative RS mechanisms that do not correspond to filamentary RS. In fact, a majority of the literature describing RS in ZnO (symmetrical and asymmetrical heterostructures) report a *filamentary* TCM or VCM switching mechanism, whilst very few report *homogeneous* VCM RS; this difference could be due to the fact the filamentary switching is typically observed after electroforming, whereas homogeneous switching can be stimulated without electroforming [38–43].

In addition to $V_{\ddot{O}}$-mediated VCM and TCM, ZnO heterostructures that employ Ag or Au electrodes have also been shown to exhibit bipolar ECM RS, in which metal cations from the electrode form metallic filaments under an applied field that bridge the top and bottom electrodes [1, 38, 44–47]. The stimulation of all three RS mechanisms (ECM,TCM and VCM) in ZnO is reflected in the broad and abundant literature on ZnO RRAM, which presents a wide variety of novel ZnO structures that can sustain RS [48]. Such flexibility in RS stresses the importance of careful design, fabrication and electrical probing in ZnO systems. However, the flexibility of ZnO RS is not wholly a negative attribute. It means that ZnO offers a wide range of parameters which can be adjusted such that power consumption can be minimised whilst reproducibility and resistance ratio are maximised. For this reason, the literature that focuses on the *optimisation* of ZnO RS is most informative. For instance, in an optimisation study, Huang *et al.* were able to demonstrate that for RF magnetron sputtered polycrystalline ZnO in Pt/ZnO/Pt, the unipolar RS characteristics varied with the oxygen partial pressure, which ranged from 0% to 100%: with increasing oxygen pressure, the HRS became more resistive due to a decrease in the $V_{\ddot{O}}$-concentration and the resistance window increased, which proved the importance of stoichiometric control in $V_{\ddot{O}}$-mediated RS [34]. Furthermore, through TEM, the study also showed that films deposited at 10% oxygen partial pressure featured the largest crystalline grain size and the most stable RS, revealing that in addition to stoichiometry, thin film morphology had influence over the stability of RS [34].

The study presented in this chapter aims to build upon the work of Huang *et al.* by using TEM to discuss the effects of stoichiometry and thin film morphology on RS characteristics in undoped ZnO and Mn(5%):ZnO. With regards to RS, Mn-doping in ZnO is commonly used to increase the resistivity of the HRS and, in turn, increase the resistance window [28, 47]. This increased resistivity is achieved because Mn is a deep donor in ZnO, and acts to trap intrinsic donors such as $V_{\ddot{O}}$ in the film [47, 49–51]. This means that one can expect to use both Mn-doping in addition to oxygen deposition pressure to control the $V_{\ddot{O}}$ carrier concentration in ZnO thin films, which in turn controls RS performance (for $V_{\ddot{O}}$-mediated VCM or TCM).

3.2.1 Simultaneous Magnetisation- and Resistive-Switching in Mn:ZnO

Whilst a number of studies have successfully obtained RS in Mn:ZnO heterostructures, only two have demonstrated the electric-field-driven simultaneous *co-switching* of magnetic and resistive properties [2, 3]; Ren *et al.* stimulated this in an asymmetrical Pt/Mn(5%):ZnO/Ti structure, which exhibited filamentary bipolar switching after an electroforming cycle [2]. Magnetisation hysteresis measurements revealed that in the LRS, the magnetic moment was 5.4 times larger than that measured in the initial state, and was non-volatile, lasting for at least 30 days. In fact, the same co-switching of magnetisation and resistive state was observed in ZnO films doped with Ni:ZnO, however this material exhibited a slightly lower ratio between the magnetic moment of the LRS and the initial (also called pristine) state (IS) than Mn:ZnO. It was proposed that in Mn:ZnO, RT-FM was observed due to the presence of multiple Mn-clusters, aligned along the growth axis, which constitute a secondary phase that can be magnetised under an applied electric field [2]. Using X-ray photoelectron spectroscopy depth profiling, a redistribution of $V_{\ddot{O}}$ throughout the Mn:ZnO film was observed [2]. The measured Mn-2p$_{3/2}$ peak was used to quantify the contribution from Mn^{2+} and Mn^{4+}, which represented an abundance and deficit of $V_{\ddot{O}}$ in the film respectively. In addition, fitting to the O-1s peaks indicated the presence of lattice oxygen and $V_{\ddot{O}}$ respectively. Thus, they showed that in the pristine state, there was an abundance of $V_{\ddot{O}}$ and Mn^{2+} at the top (Ti) and bottom (Pt) electrodes, however, the bulk Mn:ZnO was $V_{\ddot{O}}$-deficient and contained more oxidised Mn^{4+} [2]. In contrast, devices programmed to the LRS showed

a clear gradual change in $V_{\ddot{O}}$-concentration and Mn valence state across the depth of the film: the Mn:ZnO near the top electrode contained more oxidised Mn^{4+}, whilst the Mn^{2+} contribution became more dominant at the bottom electrode [2]. Considering the polarity of RS, it was proposed that when the top electrode was positively biased, the $V_{\ddot{O}}$ initially present beneath the top electrode migrated towards the bottom electrode, creating conductive filaments that spanned across the Mn:ZnO, which preferentially formed along the secondary phase Mn-clusters [2]. Furthermore, it was argued that the high concentration of Mn and $V_{\ddot{O}}$ along the conductive filaments allowed for the ferromagnetic ordering of Mn ions [2], consistent with the percolation of $_{\ddot{O}}$-bound magnetic polarons in the RT-FM model proposed by Coey *et al.* [27]. Surprisingly, no discussion of film morphology was made despite the fact that the literature overwhelmingly agrees that $V_{\ddot{O}}$-filaments are typically formed along grain boundaries. Considering this proposed mechanism, one might expect that these secondary phase Mn-clusters form along grain boundaries, in the same regions that contain a higher concentration of $V_{\ddot{O}}$. In order to verify the presence of and spatial distribution of secondary phases, further microscopic and spectroscopic investigations are required. The work in this chapter aims to contribute to this area of research through the use of TEM and EELS, which will allow us to describe RS in Pt/Mn:ZnO/Ti through a discussion of thin film morphology and $V_{\ddot{O}}$-stoichiometry. This focus on the *chemical effects* that occur due to RS allowed for the proposal of an RS mechanism and provided evidence to support the proposed magnetisation switching mechanism offered by Ren *et al.* [2].

3.3 Principles of Thin Film Growth

In this work, a combination of physical vapour deposition techniques were used to fabricate ZnO-based RRAM heterostructures: PLD was used to deposit (un)doped ZnO as the active RS layer and e-beam deposition was used to create top and bottom metal electrodes. For both of these deposition techniques, the same principles of thin growth apply, and can be tuned such that the deposited material achieves a desired function. In the initial stages of growth, atoms and molecules are transferred from a source material onto the substrate surface and undergo surface diffusion and/or desorption. As a result

of this motion, adatoms aggregate to form islands (also referred to as clusters), which, with an increasing influx of adatoms to the surface, may eventually coalesce to form a continuous film. Adatoms can also attach onto existing surface features such as atomic step edges or kinks [52, 53]. A number of classic growth modes, which describe initial growth onto *single crystal* substrates, are defined in external texts [52, 54]. These demonstrate that growth modes are largely influenced by the difference between the lattice constant of the substrate surface and that of the deposited material because the substrate acts as a seed structure for adatoms: well lattice-matched substrates promote the *epitaxial* layer-by-layer growth of single crystal materials, whilst lattice-mismatched substrates tend to promote the formation of clusters. In the deposition of hexagonal ZnO, sapphire, quartz and silicon substrates are commonly used for heteroepitaxial growth [55, 56], whereas non-epitaxial ZnO films are typically deposited on amorphous glass and silicon/silicon oxide (Si/SiO_x) substrates. In this work, epitaxial ZnO thin films were not pursued, therefore, Si/SiO_x substrates and $Si/SiO_x/Ti/Pt$ were employed.

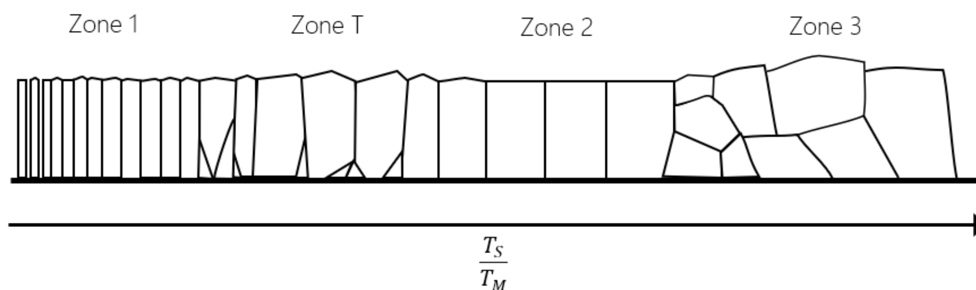

Figure 3.2: *Structural zone model adapted from [57] that depicts the dependence of thin film morphology on substrate temperature.*

The initial stages of growth describe the first few nanometers of growth. In the later stages of growth (>10nm), the morphology (or microstructure) of a thin film is largely governed by substrate temperature. Fig.3.2 presents a structural zone model (SZM) and is an adaptation from a publication by Kaiser *et al.* who studied the deposition of Al under high-vacuum [57, 58]. The SZM reveals the evolution of thin film morphology with substrate temperature in which film morphology is affected by four temperature-moderated processes: surface diffusion, dominant at moderate temperatures, which includes adatom diffusion across boundaries that separate regions of uniform crystallinity (grains); shadowing, dominant at low temperatures, which occurs due to the interaction between surface roughness and surface features with an incoming flux of atoms and

molecules; bulk diffusion, dominant at high temperatures, which describes the mobility of adatoms within single grains; and recrystallisation, also dominant at high temperatures, in which a structural transformation from one crystallographic orientation to another occurs [54, 57]. Through careful choice of homologous temperature, which describes the ratio between the temperature of a material (T_S) and its melting temperature (T_M), these four processes can be manipulated to produce an optimised morphology for desired applications. Early studies on thin film growth via sputtering developed the first SZMs in the late 1960s; today, these remain relevant to a wide selection of materials including metals (typically deposited under Argon) and metal oxides (typically deposited under oxygen) [54, 58–60]. It should be noted that, in particular, it is sputter deposition studies that have informed our understanding of film microstructure and morphology. When applying this understanding to films deposited via PLD, differences between the two techniques that must be taken into account. For instance, the deposition rate, which for PLD is high, instantaneous and intermittent, contrasts the low and steady rate achieved with sputtering. The literature on PLD shows that, between pulses, during the dissipation of the plasma plume, any unstable adatom clusters (formed during the pulse) dissociate into mobile species and migrate to form larger, energetically favourable clusters [61, 62]. Importantly, this means that for PLD, the pulse frequency can be adjusted to promote different growth modes [61]. In addition, parameters such as pulse energy and background gas pressure also have influence over growth mode and film morphology. In this work, the effects of oxygen deposition pressure on ZnO morphology was evaluated; the results suggested that increased oxygen pressures reduced the average adatom energy and mobility, promoting cluster formation and irregular grain size and orientation. Although sputtering is not the only technique used to deposit ZnO, SZMs provide a well-defined, broad overview of key thin film morphologies and, as such, are frequently used to classify the morphology of ZnO thin films grown via a wide variety of deposition techniques.

In general, the homologous temperature determines the nucleation density of adatom clusters, which limits the width of growing grains. This is shown in the SZM in Fig.3.2, where the black lines represent grain boundaries that enclose crystalline regions of material. The overall microstructure can be subdivided into four distinct zones which

are labelled in Fig.3.2: Zones 1, 2, T and 3. Porous, void-separated, columnar thin film structures with rounded, dome-like profiles define Zone 1, and are produced at low temperatures where surface diffusion is limited and shadowing is dominant. This is because a low surface diffusion coefficient (D_s) creates films with a high nucleation density, which in turn causes columnar growth where growing crystal grains shadow their surrounding grains, limiting growth in the lateral direction. In Zone 2, increased substrate temperature increases D_s, and the effects of shadowing are limited; in comparison to Zone 1, these films have lower nucleation density and have grains with larger lateral sizes and flat surface profiles that are no longer separated by voids. The wider grains exemplified by Zone 2 are typically associated with an overall increase in film crystallinity when compared to narrow (lower lateral width) grains that define Zone 1. In both Zones 1 and 2, the crystallographic orientation of the film is largely influenced by the preferred orientation of the substrate. In this study, Si/SiO_x/Ti/Pt substrates were used and the columnar polycrystalline structure of the Ti adhesion layers promoted the growth of columnar ZnO. The final columnar morphology in the SZM is Zone T; this microstructure is obtained at substrate temperatures between those of Zones 1 and 2 in which surface diffusion is dominant. Here, the difference in D_s between grains with distinct crystallographic orientation creates a *competitive* growth mode. The crystallographic orientation with the lowest D_s incorporates the largest fraction of incoming material and therefore grows fastest; in contrast, high D_s, slow-growing orientations are eventually enveloped by the fast-growing orientations [63]. As depicted in Fig.3.2, this results in a change in film structure along the growth axis where films feature small, randomly-oriented grains (high mosaicity) near the substrate surface which sit beneath larger cone-shaped grains that have maximum lateral width near the film surface [58]. Zone T films have grains with dome-like profiles, but due to the high mosaicity near the base of the film, tend to exhibit a greater variation in peak-to-trough distance (i.e. difference in height between the top of each dome and an adjacent grain boundary) than Zone 1 or 2 films [54, 58]. Zones 1, 2 and T constitute the *basic* SZM and are the foundation of every SZM presented in the literature, however, a further high mosaicity morphology, Zone 3, which was characterised by randomly oriented, faceted grain profiles, was later ascribed to different formation mechanisms. Thornton *et al*'s

early publication attributed Zone 3 morphology to increased bulk diffusion that could only be produced at heightened temperatures, as shown in Fig.3.2: such heightened temperatures were shown to be sufficient to stimulate a transition from columnar grains, which are elongated along the growth axis, to equiaxed grains, where the axes defining each grain are of equal length [54]. In contrast, Barna *et al.* later showed that Zone 3 morphology could be produced at any temperature, but that the average grain size decreased with increasing impurity level due to the periodic blocking of growth [57, 58]. Both studies produced SZMs based on the deposition of metals in which oxygen is considered an impurity. Although oxygen is not an impurity in the deposition of metal oxides, both the basic- and the impurity-SZM are used to evaluate ZnO morphology in the literature. For instance, Huang *et al.* showed that for sputtered ZnO thin films, with increasing oxygen partial pressure, the morphology gradually changed from Zone 2 of the basic SZM, which is characterised by grain boundaries aligned along the growth axis, to Zone 2 of the low-impurity-level SZM, which is characterised by sloping, off-axis grain boundaries [34].

With regards to applications in RS, *polycrystalline* ZnO films are considered more desirable than amorphous or single crystal films. This is largely due to the fact that grain boundaries act as sinks for $V_{\ddot{O}}$ and Zn interstitials, and these are known to facilitate RS [64]. Therefore, one might expect to manipulate the RS characteristics of a ZnO RRAM device by controlling the crystallinity of the film, which in turn affects the number of grain boundaries present. With this approach, there are some considerations that must be taken in account. For instance, given that during filamentary RS, conductive filaments form preferentially along grain boundaries, for non-uniform polycrystalline morphologies, such as Zones T and 3, non-uniform filaments form and may cause RS instability.

For wurzite ZnO thin films with $c-$axis structure, the intensity of the (002) diffraction peak is typically used as an indicator for crystalline quality and in polycrystalline ZnO, the FWHM of the (002) peak reveals information about the average lateral width of (002) columnar grains. According to Eqn. 2.3 this means that high quality crystalline ZnO films are characterised by a strengthened and narrowed (002) peak [5, 11, 15]. Such high quality films are most often produced through deposition at temperatures exceeding

670K; in addition, at these heightened temperatures, post-deposition anneals can be employed to improve on the crystallinity of films that were originally deposited at lower temperatures by stimulating a surface-diffusion-mediated transition from Zone T to Zone 2 of the SZM.

3.4 Thin Film Considerations for Zinc Oxide RRAM

There are few previous studies that optimise the deposition of ZnO thin films for both oxygen deposition pressure (P_{O_2}) or substrate temperature (T_S) [34, 65, 66]. Despite this, across all deposition techniques, the effect of T_s remains as defined in the SZM shown in Fig.3.2: with increased T_s, ZnO films tend towards increased lateral columnar width, which is typically associated with an overall increase in film crystallinity. A majority of the publications on P_{O_2} are PLD studies. Of these are the works of Choopun *et al.* and Vispute *et al.*, who examined ZnO thin films grown heteroepitaxially onto sapphire substrates at low oxygen pressures and high temperatures: $P_{O_2} = 10^{-2} - 10^{-3}$mTorr, $T_s = 970 - 1020$K [67,68]. Using AFM, they revealed that these conditions produced well-defined hexagonal terraced features across the film surface, which, when probed using XRD, were consistent with (002) crystallographic orientation. Interestingly, Choopun *et al.* also observed a sudden increase in roughness at heightened pressure due to a change in film morphology: heightened P_{O_2} allowed for the *columnar* growth of ZnO. It is now understood that the heightened pressure increased the number of collisional interactions between the plasma and ambient oxygen, which lowered the energy of the ablated species and thus reduced the mobility of adatoms deposited onto the substrate surface. As a result, a columnar film with high nucleation density formed. Furthermore, the same study showed that at $P_{O_2} = 100$mTorr one could produce the smooth, hexagonal morphology at lower pressures through the initial deposition of a seed layer [67]. This demonstrated one of the basic principles of growth, that the nucleation stage, the first few nanometers of growth, governs the morphology of the entire film. At these high pressures, the literature presents further evidence for the influence of oxygen pressure on film morphology. Using XRD on PLD-ZnO, Im *et al.* showed that at pressures between $P_{O_2} = 1 - 200$mTorr, columnar films with (002) *c*-axis crystallographic orientation were produced, whilst at

higher pressures ($P_{O_2} = 500$mTorr), a proportion of each film develops with a (101) *a*-axis orientation which had a flake-like surface topology [66]. Imaging via SEM revealed that at these pressures, *c*-axis oriented columns had dome-like surface profiles, which contrasted with the irregular flake-like topology of *a*-axis oriented films, which means that in the absence of XRD measurements, AFM measurements of surface topology of a ZnO polycrystalline film can be used as a preliminary means of assessing the dominant crystallographic orientation.

In addition to providing some insight into crystallographic orientation, AFM measurements of ZnO films allow one to assess the surface roughness; this is an important parameter to measure because the roughness of each thin film layer in a RRAM heterostructure can affect the quality of electrode/ZnO contacts, which can lead to an increase in device variability, and is an important parameter that should be minimised during RRAM device fabrication. Surface roughness has been shown to depend on both T_s and P_{O_2}, and it is usually evaluated through a calculation of the root-mean-square average (rms) of an AFM height image. Typically, ZnO films with rms=1-2nm are generally considered to be 'smooth', and are often produced as a result of heteroepitaxial deposition onto sapphire or silicon substrates [67, 69–71]. Studies have shown that for a given film, roughness is minimised for a small range of T_s but that this temperature varies with P_{O_2}. For example, in separate studies, Water *et al.* and Her *et al.* showed that for magnetron sputtered films deposited at $P_{O_2} = 3$mTorr and $P_{O_2} = 1.5$mTorr, roughness was minimised at $T_s = 570$K [72] and $T_s =$370K [73] respectively. In both cases, depositions at higher and lower T_s produced films with increased surface roughness. Unlike studies on P_{O_2}, wide ranges of T_s are accessible for many deposition techniques; comparatively, atomic layer deposition (ALD) has been shown to produce the smoothest ZnO films with sub-nm rms (0.61nm at $T_s =$420K, $P_{O_2} = 600$mTorr) [74], whilst the smoothest films produced via magnetron sputtering and PLD have only attained rms=1-2nm [69, 71–73, 75]. Despite achieving comparable rms, the effects of P_{O_2} on surface roughness are not well defined. Some evidence suggests that for PLD, surface roughness increases with P_{O_2}, whilst for magnetron sputtering, the opposite trend has been reported [76, 77]. Here, the most suitable P_{O_2} for the deposition of polycrystalline ZnO thin films for applications in RRAM was identified by evaluating the effect of P_{O_2}

on the electrical properties of ZnO.

In addition to affecting film roughness, P_{O_2} is expected to alter a film's conductivity: as ZnO is a n-type material, an abundance of $V_{\ddot{O}}$ is expected to decrease the resistivity of the film. A substantial fraction of the oxygen present in PLD-grown oxides is incorporated from the ambient oxygen, such that PLD P_{O_2} can be used to manipulate ZnO stoichiometry and RS performance. However, there is some contradiction in the literature over the effect of P_{O_2} on ZnO resistivity. For example, Masuda *et al.* published evidence for non-linear dependence on P_{O_2}, where resistivity was maximised at 5mTorr and decreased at higher and lower pressures [78]; whereas a majority of publications showed that resistivity increased, with increasing P_{O_2} [66, 76, 79]. Notably, there are few studies dedicated to the examination of the effect of T_s on ZnO resistivity. One of these studies showed that resistivity generally increased with T_s, and that films deposited at 5mTorr and 50mTorr exhibited comparable resistivity for $T_s < 770$K, but showed greater disparity at higher T_s; this quite clearly reveals that both T_s and P_{O_2} combined govern the electrical properties of the film [80]. Annealing under vacuum can also be used to reduce the resistivity to measurable levels, which is likely due to an increase in the concentration of $V_{\ddot{O}}$ as oxygen is liberated [81, 82]. Conversely, high temperature anneals under flowing oxygen reduce the $V_{\ddot{O}}$-concentration, making ZnO films more resistive [83]. With regards to structural changes, recent literature has shown that the average grain size decreases if the film is annealed under vacuum and increases under flowing oxygen. Given that the number of grain boundaries is inversely proportional to the average grain size, it stands to reason that $V_{\ddot{O}}$-concentration is increased as grain size decreases. For highly mosaic morphologies where grain boundaries are oriented at all angles with respect to the growth axis (like those depicted in the high impurity SZM in Fig.3.2(d)), increases in conductivity may be limited by the complex path from the bottom to the top of the film. However, for *columnar* films, where the grain boundaries run (near) parallel to the growth axis, conductive paths are largely unobstructed between the substrate and film surface, which would result in a very low resistivity film (measured perpendicular to the substrate). In fact, Zhuge *et al.* compared the RS characteristics of two ZnO films sputtered at $T_s = 770$K under vacuum and flowing oxygen and showed that RS was only achieved for the vacuum deposited films that comprised smaller grains ($\approx$40nm) and had

higher initial resistivity ($10^{11}\Omega$), but no RS hysteresis was observed in the comparative ZnO film deposited under oxygen, which had a larger average grain size (>100nm) [84]. Importantly, this study highlighted that not all deposition conditions will support RS, and that the film must fall within a 'switchable' range of *initial* resistivities. In Zhuge *et al.*'s case, switchable devices were identified by extremely high initial resistance values, which would change abruptly to the LRS during an electroforming process; this observation is reflected throughout the literature on RS in ZnO [29, 84, 85]. However, as mentioned in Chapter 1, electroforming-free devices can also display RS, which means that some intermediate $V_{\ddot{O}}$-concentration may sustain RS in a device with a moderate initial resistance that does not require electroforming, and this may be advantageous in terms of reproducibility. Alternatively, dopants can be used to vary the $V_{\ddot{O}}$-concentration.

Clearly, in order to fabricate ZnO-based RRAM devices, a compromise between thin film crystallinity, resistivity and surface roughness must be reached, and this will require the optimisation of both P_{O_2} and T_s. Based on the above review of the literature, ideal PLD-ZnO films for applications in RRAM were deposited at temperatures $T_s \leq 770$K and pressures $P_{O_2} \leq$200mTorr. These upper limits are put in place to ensure the production of a (sufficiently) resistive polycrystalline columnar film with a dominant (002) orientation. At higher T_s, the number of grain boundaries is expected to reduce, which could be detrimental to $V_{\ddot{O}}$-mediated RS. Given the non-linear relationship between T_s and surface roughness, the temperature that produces the smoothest film will need to be determined through AFM.

3.5 Zinc Oxide and Manganese-doped Zinc Oxide RRAM

The ZnO and Mn:ZnO RRAM investigation presented in this chapter aims to further the literature on RS in Mn:ZnO, which is lacking in TEM and spectroscopic studies. Specifically, the RRAM devices investigated here were designed to be comparable to the co-switching, PLD-grown transition metal doped ZnO device presented in Ren *et al.*'s work, which was introduced in Section 3.2.1 [2]. In this study, ZnO thin films were deposited onto Si/SiO_x substrates over a range of T_s and P_{O_2} and characterised using AFM.

3.5.1 RRAM Heterostructure Fabrication

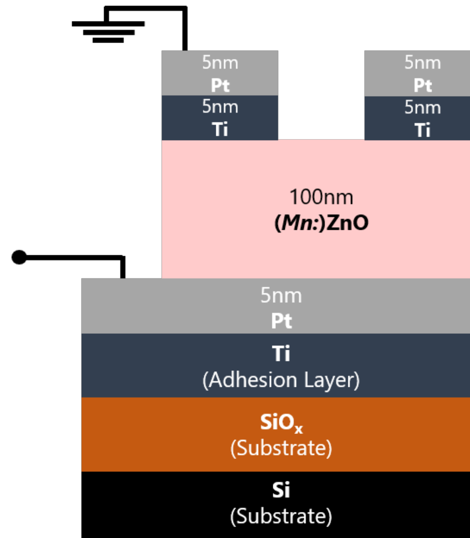

Figure 3.3: *ZnO RRAM device heterostructures: Si/SiO$_x$/Ti/Pt/ZnO/Ti/Pt.*

In this study, ZnO and Mn:ZnO thin films (ranging between 70-200nm) were employed as resistive switching layers within Si/SiO$_x$/Ti/Pt(5nm)/Ti(3nm)/Mn:ZnO/Pt(5nm) patterned RRAM heterostructures, as illustrated in Fig.3.3. Here, Ti/Pt top and bottom electrodes were deposited via e-beam evaporation such that ZnO thin films were sandwiched between an asymmetric Pt/ZnO/Ti heterostructure. Before deposition, the Si/SiO$_x$ substrates were sonically agitated in acetone and propanol to remove surface contaminants. ZnO thin films were pulsed laser deposited at T_s ranging between room temperature (RT) and 850K and at P_{O_2} ranging from 1 to 100mTorr, as detailed in Table 3.1. The combinations of P_{O_2} and T_s were used on the basis that an initial deposition of undoped ZnO over a range of T_s at P_{O_2}=100mTorr produced reproducible RS at T_s=490K. At this temperature, further comparable films were deposited over a range of P_{O_2} to assess its on RS; it was found that reproducible RS was only attained at P_{O_2}=100mTorr. The doped ZnO films were initially deposited at the deposition pressure and subtrate temperature that produced reproducible RS in undoped ZnO, however to optimise RS in the doped material, T_s was varied to the temperature above and below and it was found that reproducible RS was attained at $T_s = 630$K. To reduce the effects of contamination during the surface characterisation of ZnO, identical films were deposited on Si/SiO$_x$ substrates for this sole purpose. All films were deposited at a laser repetition rate of 5Hz and with a target-substrate distance of 96.5mm. In practice, we

found that, even at lower laser energies, ZnO would grow at moderate rates ($0.5s^{-1}$); in this work the laser energy used to deposit the films listed in Table 3.1 ranged from 20mJ to 170mJ.

In the RRAM heterostructure displayed in Fig.3.3, the Pt/ZnO interface is expected to form an ohmic contact, whereas the strongly reducing Ti top electrode is expected reduce the ZnO closest to the electrode and form interfacial TiO_x with Schottky-barrier-like, highly resistive properties. As explained in Chapter 1 section 1.2.6, interfacial oxides are known to facilitate VCM RS, and are expected to thicken and thin with the direction of $V_{\ddot{O}}$-migration under an applied bias. This means that this structure is designed to promote bipolar VCM, which can be either a filamentary or area-homogeneous effect.

Table 3.1: Oxygen pressure and substrate temperature deposition conditions for ZnO films pulsed laser deposited onto Si/SiO_x substrates for film characterisation or Ti/Pt substrates for electrical characterisation. Conditions under which Mn:ZnO thin films were also deposited are indicated by blue checkmarks.

	RT	400K	490K	630K	850K
1mTorr			✓		
10mTorr			✓		
100mTorr	✓	✓	✓	✓	✓

3.5.2 AFM Analysis

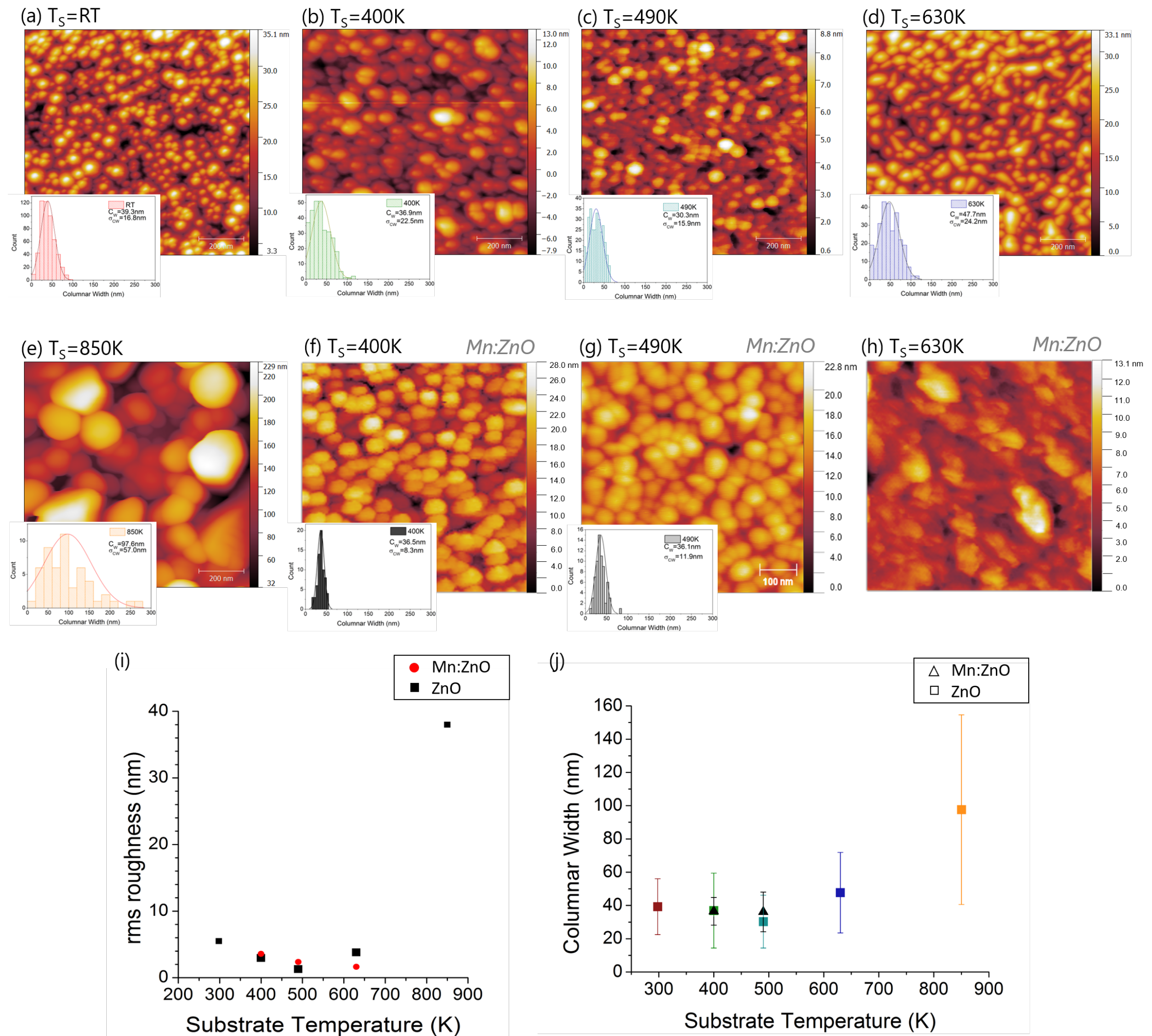

Figure 3.4: *AFM images acquired over 1µm×1µm for 100nm of polycrystalline ZnO deposited at* P_{O_2} *=100mTorr (a) room temperature (b)* T_s *=400K (c)* T_s *=490K (d)* T_s *=630K and (e)* T_s *=850K are presented. Rms average variation over substrate temperature is displayed in (f).*

ZnO and Mn:ZnO films were deposited onto Si/SiO$_x$ substrates to assess their sheet resistivity via Van der Pauw's 4-probe method but these measurements proved inconclusive, which was likely due to the poor quality electrical contacts used. Initial device resistance (R_i) was therefore assessed via the same 2-probe method used to electrically characterise the resistive switching behaviour and is described in Section 2.10. ZnO Si/SiO$_x$ films were also used to assess surface topology, as described below.

Fig.3.4 presents AFM images that were collected over 1µm×1µm areas from ZnO

(Fig.3.4(a)-(e)) and Mn:ZnO (Figs.3.4(f)-(h)) films deposited at 100mTorr onto Si/SiO_x substrates at a range of substrate temperatures. Most of the ZnO and Mn:ZnO images are consistent with films constituting densely packed columnar structures, where each column had a dome-like profile, consistent with the (002)-oriented polycrystalline films expected for the range of P_{O_2} used. However, the Mn:ZnO film deposited at 630K (shown in Fig.3.4(h)) shows no clear columnar structure or distinction between grains, which could be indicative of Zone 3 morphology (shown in Fig.3.2 on page 97). Fig.3.4(i) presents a comparison of the rms roughness values for undoped ZnO and Mn:ZnO calculated from the AFM images in Figs.3.4(a)-(h). In line with the literature [72, 73], the smoothest undoped ZnO film had rms≤2nm, and was produced at $T_s = 490K$; at higher and lower temperatures, these films became rougher. The Mn:ZnO films deposited at 400K and 490K show comparable roughness to the corresponding undoped films deposited at the same temperature, however the smoothest Mn:ZnO film was deposited at 630K, as shown in Fig.3.4(i). For the undoped ZnO films, most notably, the roughness rapidly rose to ∼40nm at $T_s = 850$K. Choopun *et al.* observed a similarly abrupt roughening (from rms=1-2nm to rms=40nm) as P_{O_2} was increased from 10mTorr to 100mTorr [67]. Given that Choopun *et al.*'s rough film was produced at a high T_s at $P_{O_2} = 100$mTorr, it can be compared to the roughest PLD film produced in the study presented in this work (deposited at P_{O_2} =100mTorr, T_s =850K); these results provide evidence for a reproducible phase change stimulated at high temperatures and pressures. The XRD literature presents no evidence for temperature-induced *crystalline* phase transitions at temperatures above T_s =570K, which suggests that this ZnO film retains its (002)-orientation, consistent with a temperature-stimulated transformation from Zone 2 to Zone 3, as shown in Fig.3.2. The literature also notes that at heightened temperatures (T_s >770K), re-evaporation of adatoms from the film surface leads to the degradation of the crystalline quality of (002)-oriented ZnO and roughens the surface [15, 86]. It is likely that the ZnO morphological phase obtained at T_s >770K is due to a combination of thermally activated re-evaporation *and* bulk-diffusion, which act to mediate a transformation from Zone 2 to Zone 3 and drastically roughen the film surface. Following this logic, temperatures below T_s <770K (shown in Fig.3.4(a)-(d)) are likely to produce Zones 1, 2 and T films. However, not all of these morphologies are

desirable for RRAM applications. For instance, porous Zone 1 films (typically deposited at low T_s) would lead to the formation of a short circuit. In addition, although Zone T and Zone 2 ZnO thin films typically exhibit comparable surface roughness, Zone T films have been shown to display greater RS variability than Zone 2 films, which is has been attributed to the complex, irregular grain boundary paths that are characteristic of Zone T [34].

Lateral grain size was determined using the AFM images shown in Fig.3.4(a)-(h); columnar width distributions are presented as insets for each AFM image and the variation of average columnar width (C_W) and standard deviation (σ_{C_W}) as a function of substrate temperature is shown in Fig.3.4(j). It should be noted that, given the lack of clear grain boundaries for the Mn:ZnO film shown in Fig.3.4(h), this film was not included in grain size analysis. Considering the literature, one might expect that for an optimised deposition that produces a uniform Zone 2 film, C_W would be maximised whilst σ_{C_W} would be minimised [66], however this was not observed in this work. Here, the variation of C_W with T_s mirrored that found for the rms surface roughness: the smallest average grain size ($C_W = 30nm$) for undoped ZnO was produced at $T_s = 490K$, but grain size increased with higher and lower T_s; and at T_s =850K, the Zone 3 morphology shown in Fig.3.4(e) was characterised by the largest average grain size and standard deviation ($C_W = 98$nm, σ_{C_W}=60nm), setting it apart from the ZnO and Mn:ZnO films deposited at lower T_s which, as observed in Fig.3.4, were all roughly comparable. At these low temperatures, σ_{C_W} showed no clear dependence on C_W or T_s, which could be due to the occurrence of a temperature-induced phase transition between Zone T and Zone 2. However, it is not possible to confirm this particular transition using a surface sensitive technique like AFM as the SZM shows that the difference between these two morphologies only becomes evident in a comparison of the grain shapes along the growth axis: Zone T has cone-shaped grains whereas Zone 2 has growth-axis-aligned, rectangular grains. Therefore, to fully characterise the morphology of ZnO thin films and discuss the effects of ZnO microstructure on RS, TEM was employed and the results are discussed in Section 3.5.4.

3.5.3 Electrical Characterisation

Optimised deposition parameters for ZnO and Mn:ZnO RRAM were found through an electrical assessment of the resistive switching characteristics of identical ZnO and Mn:ZnO films to those presented in Fig.3.4. The electrical characterisation of ZnO and Mn:ZnO RRAM heterostructures revealed that reproducible RS was supported by undoped ZnO thin films that were deposited at P_{O_2} =100mTorr and $T_s = 490$K and by Mn:ZnO films deposited at P_{O_2} =100mTorr but at a higher substrate temperature, $T_s = 630$K. For undoped ZnO, films deposited under the same oxygen pressure (P_{O_2} =100mTorr) but deposited at different temperatures (with the exception of $T_s = 850$K, which was ohmic) exhibited non-linear IV characteristics and could not sustain reproducible resistive switching despite being probed in two manners: to avoid electroforming and to induce electroforming. Comparing the two ends of the temperature range employed in this study, RT and $T_s = 850$K, revealed that ZnO thin film resistivity has a complex dependence on T_s. Films deposited at $T_s = 850$K exhibited an ohmic response and had low initial resistance ($R_i \approx 600\Omega$), whilst room temperature deposited devices had slightly greater initial resistance ($R_i \approx 1k\Omega$) and could be electroformed. Despite undergoing the same forming process as those devices deposited at $T_s = 490$K that displayed reproducible RS, room temperature ZnO devices had poor stability, collapsing to the ON state within only 16 cycles after a gradual degradation of the HRS to lower resistivities. Given that the ZnO devices that displayed reproducible RS had significantly greater initial resistance ($R_i \approx 10k\Omega$) than those that displayed no RS or irreproducible RS, it is likely that the instability of RS increases with decreased resistivity of ZnO. This would mean that in addition to displaying non-linear IV behaviour, films must have sufficient initial resistivity (which in this case was $R_i \sim 10k\Omega$) to sustain reproducible RS. In a similar fashion, the effect of P_{O_2} on electrical characteristics of ZnO RRAM devices deposited at T_s=490K was also investigated. Preliminary AFM measurements revealed that films deposited on Si/SiO$_x$ became smoother with lower deposition pressure, reaching sub-nm rms at both lower pressures. ZnO films deposited at P_{O_2} =10mTorr exhibited ohmic behaviour and devices had extremely low initial resistance ($R_i = 40\Omega$), whilst those deposited at P_{O_2} =1mTorr exhibited unstable, non-linear characteristics and had slightly greater initial resistance ($R_i \approx 100\Omega$), although this was still far below the

(above mentioned) threshold for stable RS in ZnO. These results support the general consensus in RRAM that states that devices must be sufficiently resistive to sustain reproducible RS and that ZnO films with relatively low initial resistance ($R_i < 1k\Omega$) are likely to display an ohmic, non-switching response or irreproducible RS [36].

Undoped ZnO

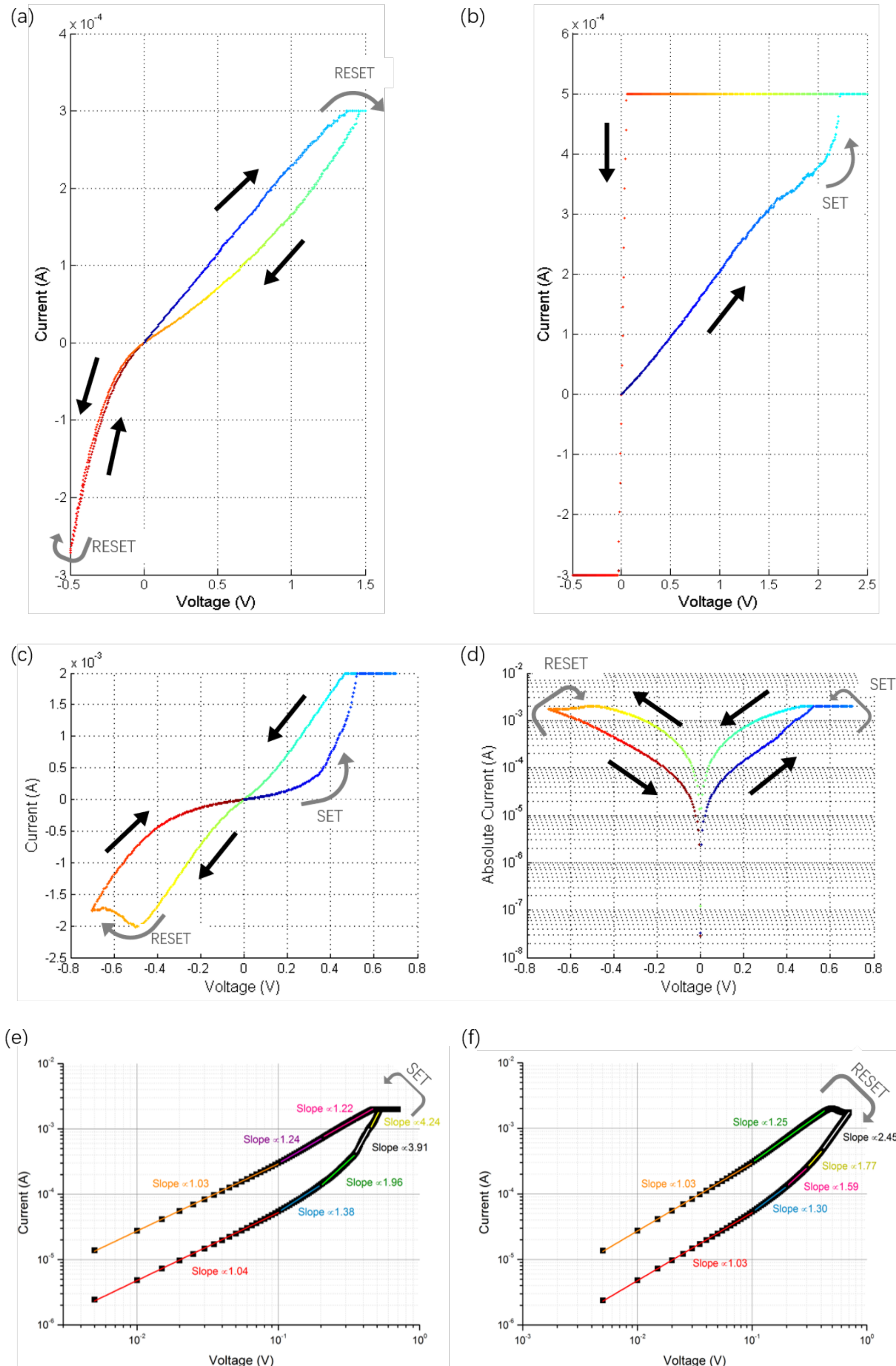

Figure 3.5: *IV curves acquired from ZnO RRAM deposited at* P_{O_2} *=100mTorr and* $T_s = 490K$*. The colour scale, which runs from blue to red, indicates the direction of the voltage cycle in each plot. (a) Initial stable RS state. (b) Electroforming cycle. Representative RS IV curve produced after electrofoming plotted on a (c) linear and (d) semilog scale where cc=+2mA. Linear fitting of (d) is shown for the (e) SET and (f) RESET transitions, which are plotted on a double logarithmic scale for an assessment of* $I \propto V^n$*. Slope values next to the data present the value of the gradient for each linear fit (n).*

For undoped ZnO, the devices were initially in a highly resistive state: using simple 2-probe measurements, the initial resistances of multiple patterned devices were found to be of the order of $R_i = 10\text{k}\Omega$ and showed some variation across the film, which is likely due to the film's polycrystalline morphology (see Fig.3.4(c)). To obtain *reproducible* RS, the devices were electroformed via a typical high voltage filamentary process, as seen in the literature. Interestingly, before electroforming, the device exhibited a *preliminary* form of reproducible resistive switching, in which the device switched at opposite polarity to that exhibited post-electroforming; the preliminary RS and forming cycles are shown in Figs.3.5(a) and (b) respectively. In the preliminary state, even at moderate voltages (higher than those displayed in Fig.3.5(a)), relatively low currents flowed across the device, and at $V_{READ} = 0.1$V, the resistance window was a low as $\sim$1.5. These were relatively poor performance parameters, however, the stability of the preliminary RS state indicated that if probed differently, the device may have been able to sustain a second stable form of RS. Upon increasing the magnitude of the positive voltage sweep, the device underwent a filament electroforming process at $V_{EF} = +2.2$V. Fig.3.5(b) reveals how instead of undergoing a RESET process during the positive sweep, as exhibited during preliminary RS, the device underwent a SET transition, reaching the compliance current, which was limited to cc=0.5mA. After electroforming, the device reached a reproducible *second* RS state, which is shown in Figs.3.5(c) and (d) on linear and semilog scales respectively; here, the ZnO device displayed bipolar, gradual RS, with a resistance window of ~ 8 measured at $V_{READ} = 0.1$V. The smooth and gradual RS displayed is only observed for VCM RS mechanisms, confirming that $V_{\ddot{O}}$-electromigration, as opposed to filamentary ECM or TCM, governs switching in these devices. In Figs.3.5(a) and (b), the direction of switching (highlighted with arrows and the colour scale) is counter-clockwise, in which the SET process occurs at positive voltages, and the RESET process occurs at negative voltages. Due to the gradual nature of RS there is no clear V_{SET}. In contrast V_{RESET} very clearly occurs at -0.5V and is easy to identify due to the occurrence of Negative Differential Resistance (NDR), a term used to describe the phenomenon in which current flow decreases with increasing voltage. NDR was originally observed in voltage cycled Au/SiO/Au MOM structures, where it was proposed that the migration of Au^+ ions into the SiO led to the formation of deep charge traps upon

which charge accumulation could lead to space charge that limits current flow across the device [87, 88]. Similarly, photoluminescence studies have shown that intrinsic Zn, O defects (including $V_{\ddot{O}}$) and charged dopant ions form charge traps in ZnO [89–91], and it is proposed here that these could result in NDR.

It is possible to assess RRAM conduction mechanisms by fitting IV data to conduction models, which in this case, can be used to identify specific conduction mechanisms [92,93]. In undoped ZnO RRAM, the LRS typically exhibits ohmic conduction, in which $I \propto V$, however, several conduction mechanisms have been ascribed to the HRS and these are field dependent [94]. In general, at low voltages, the HRS also exhibits ohmic conduction, but a higher voltages, Poole-Frenkel (PF), Schottky Emission (SE) and Space-Charge-Limited Current (SCLC) have been observed, and $I \propto V^2$ respectively [39, 46, 94, 95]. PF is a model in which conduction across a device is enhanced through the field induced lowering of the ionisation energy of donors or acceptors and can be identified by the relationship $Log(\frac{I}{V}) \propto \sqrt{V}$ [39]. SE is a model in which electrons are able to surpass the energy barrier present at a metal-dielectric interface through thermal activation and has a $Log(I) \propto \sqrt{V}$ relationship [92]. A double logarithmic IV plot, such as those shown in Figs.3.5(c) and (d), is commonly used as an initial assessment for the relationship $I \propto V^n$, as on this plot, the gradient of a linear fit is equal to the exponent n, which is particularly useful in the assessment of SCLC conduction. In this model, the IV characteristic can be divided into three field-dependent distinct $I \propto V^n$ relationships: at low fields, $n = 1$ and conduction is ohmic, which means that the number of thermally generated free carriers in the oxide is greater than the number of carriers injected from the electrode; at high fields, $n = 2$, which, in contrast to ohmic conduction, indicates that the number of injected charge carriers is greater than the number of thermally generated carriers; in some cases, $n > 2$, which corresponds to *trap-limited* (also called *trap-filled*) SCLC in which a portion of the injected charge carriers become trapped at defect trapping sites [43, 92]. It should be noted that it is possible to transition from trap-free SCLC ($I \propto V^n$ for $n \leq 2$) to trap-filled SCLC ($I \propto V^n$ for $n \geq 2$) and back [92].

In Fig.3.5, the (c) SET and (d) RESET datasets are separated into multiple linear fitting regions, each labelled with their corresponding gradient (n). The LRS in both transitions is consistent with ohmic conduction($n = 1$). In contrast, the HRS only

Conduction Model	Proportionality	Gradient Expression	Dataset	R^2	m	Estimated ε_r
SCLC	$I \propto V^2$	$m = \frac{9}{8d^3}\mu\varepsilon_0\varepsilon_r\theta$	SET	0.9777	0.011	-
			RESET	0.9988	0.004	-
Schottky Emission	$Log(\frac{I}{V}) \propto \sqrt{V}$	$m = \frac{e}{kT}\sqrt{\frac{e}{4\pi\varepsilon_0\varepsilon_r d}}$	SET	0.9945	4.660	0.50
			RESET	0.9986	2.001	1.29
Poole-Frenkel	$Log(I) \propto \sqrt{V}$	$m = \frac{e}{kT}\sqrt{\frac{e}{\pi\varepsilon_0\varepsilon_r d}}$	SET	0.9886	3.380	3.81
			RESET	0.9985	1.716	14.79

Table 3.2: *Estimated dielectric constants (ε_r) of polycrystalline undoped ZnO calculated using linear fit analysis of the HRS for SET and RESET transitions displayed in Fig.3.5. The gradient expressions for each conduction model were obtained from current density formulae in the literature [92, 94, 96] where ε_0 is the permittivity of free space, e is the charge of an electron, k is Boltzmann's constant, $T = 298K$, and film thickness is d=200nm.*

exhibits ohmic conduction at low voltages ($V < 0.1V$). Between $0.1V < V < 0.4V$, n increases to 2, consistent with *trap-free* SCLC. At even higher voltages ($V > 0.4$), $n > 2$, consistent with trap-limited SCLC. For the RESET transition presented in Fig.3.5(d), this increase is modest (n increases to 2.45), but for the SET transition shown in Fig.3.5(e), n increases to 4 before the device reaches the 2mA compliance current. The observation of these three distinct $I \propto V^n$ regions are consistent with a transition from trap-free to trap-limited SCLC conduction, which has previously been observed in complex oxides such as $PrCaMnO_3$, a material investigated in Chapter 4 [43].

Multiple conduction models can be used to describe IV characteristics of the HRS state. Here, for trap-limited-SCLC conduction, where $n > 2$, further evaluation of the dominant conduction mechanism was undertaken. The HRS data corresponding to these trap-limited-SCLC regions, which range between $0.3V < V < 0.5V$ and $0.4V < V < 0.7V$ for the SET and RESET transitions respectively, were fitted to trap-free SCLC, SE and PF conduction models via the proportionality relationships detailed in Table.3.2 [94, 96]. The R^2 value can be to identify the best linear fit for each conduction model, and the fitting parameters can be used to estimate the static dielectric constant ε_r at room temperature, which has been shown to be $\varepsilon_r = 1.86$ for amorphous ZnO and to range between $4 < \varepsilon_r < 11$ for crystalline ZnO [96, 97]. The results of this fitting process are presented in Tab.3.2. However, given similarity of R^2 values and the fact that ε_r was not measured in this work, the fitting process was not found to be a robust discriminator for identifying the dominant conduction mechanism.

Mn:ZnO

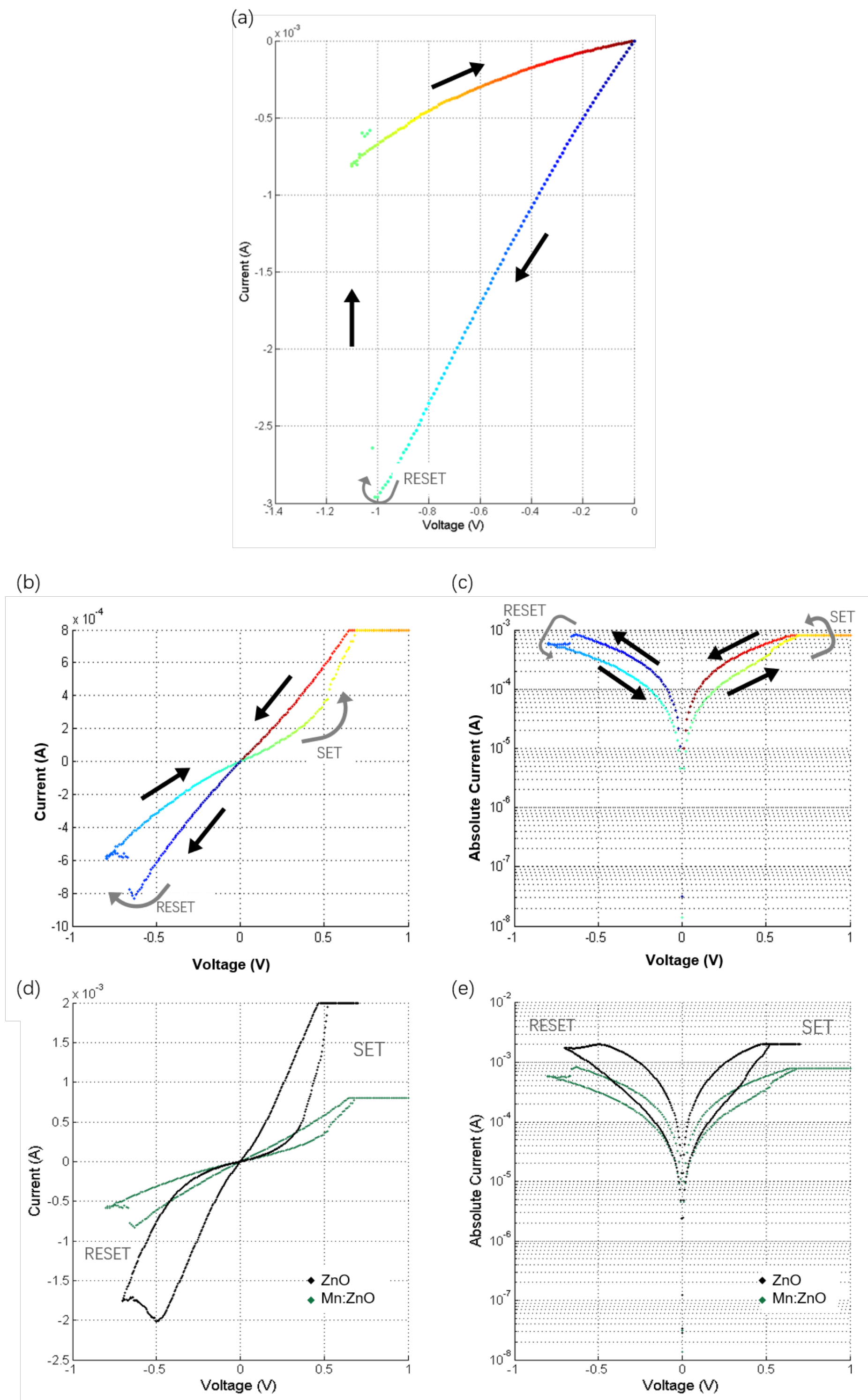

Figure 3.6: *IV curves obtained from Mn:ZnO RRAM devices in which the Mn:ZnO film was deposited at* $P_{O_2} = 100mTorr$ *and* $T_s = 630K$. *(a) Electroforming RESET transition. (b)(c) Reproducible bipolar IV curve exhibited post-electroforming. (b) is replotted in (c) on a semilog scale. (d) (e) Comparison of the representative bipolar IV curves obtained for ZnO and Mn:ZnO.*

Mn:ZnO RRAM devices were fabricated using the same PLD deposition conditions used to produce reproducible RS in undoped ZnO, $P_{O_2} = 100$mTorr and $T_s = 490$K; however, these devices displayed irreproducible bipolar RS. Devices fabricated using films deposited at $T_s = 400$K also displayed irreproducible RS but those made using films deposited at $T_s = 630$K exhibited reproducible bipolar RS after an electroforming *RESET* process at *negative* voltages. This is particularly interesting because in the literature, electroforming steps generally describe a process in which an initially resistive device becomes significantly less resistive due to the formation of a conductive filament. Whilst electroforming SET transitions have been observed at both polarities, electroforming is largely described as a *SET* process. As discussed in the introduction, multiple early reports of electrofoming SET processes has influenced researchers in the field to create highly resistive films that require such a process. Here, we observed the opposite: an initial RESET process was required to sustain bipolar RS in relatively conductive Mn:ZnO films that exhibited $R_i = 300\Omega$, which significantly smaller than the $R_i = 10k\Omega$ required for stable switching in undoped ZnO. An example of this electroforming RESET is shown in Fig.3.6(a); the abruptness of this transition is consistent with the rupture of a conductive filament. A representative example of the reproducible RS produced after an electroforming RESET is shown in Figs.3.6(b) and (c) on linear and semilog scales respectively. As observed for undoped ZnO, the Mn:ZnO displayed gradual bipolar switching in which the SET(RESET) transition occurred at positive(negative) voltages. For direct comparison, both undoped and Mn-doped ZnO devices are displayed in Figs.3.6(d) and (e) in black and green respectively; here, it is clear to see that the shape of the Mn:ZnO IV curve is similar to that exhibited by the undoped ZnO device. Both the low and high resistance states for the Mn:ZnO are more resistive than that of the undoped ZnO HRS. In fact, at $V = +0.5$V, the Mn:ZnO is approximately 4 times more resistive than the undoped ZnO, a difference that is consistent with the literature in which Mn is commonly employed to increase the resistance of the HRS in ZnO. Figs.3.6(d) and (e) also shows that different compliance currents were employed for the RRAM devices: cc=+2.0mA was used for undoped ZnO and cc=+0.8mA was used for Mn:ZnO. The comparatively reduced compliance current used for Mn:ZnO was employed in consideration of the electrical characterisation of undoped ZnO, where stable RS

was only achieved if, post-electroforming, the RS process was limited to relatively low currents (<2mA). Given that reproducible RS in Mn:ZnO was achieved for such a low compliance current, this limit was not increased. Using such a low compliance current to limit the LRS inevitably reduced the resistance window: at $V_{READ} = +0.1V$, the ratio between the LRS and HRS was only 2:1, 4 times smaller than that observed for undoped ZnO measured at higher compliance currents. With reards to the conduction mechanism, analysis of the Mn:ZnO IV curves revealed that, as in our undoped ZnO devices, these devices were consistent with trap-limited SCLC conduction.

For the small range of T_s used to evaluate RS in Mn:ZnO, all films exhibited non-linear hysteretic IV behaviour, however not all exhibited the reproducible RS shown in Fig.3.6. In fact, some devices underwent a typical electroforming *SET* process at positive voltages, as seen for undoped ZnO, and displayed *irreproducible* bipolar RS with the same voltage polarity dependence as that shown in Fig.3.6 as a result.

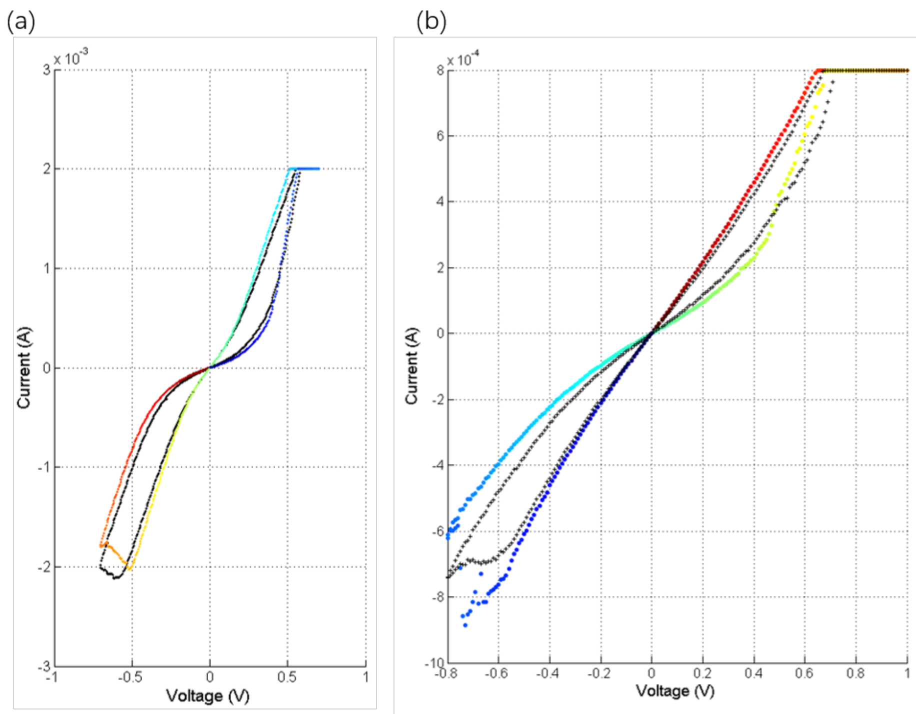

Figure 3.7: *Reproducible electroformed IV curves acquired from (a) undoped ZnO and (b) Mn:ZnO devices. In both, the colour scaled dataset represents the initial cycle. The black dataset represents the (a) 30th (b) 60th cycle.*

Fig.3.7 demonstrates the stability of RS in undoped ZnO and Mn:ZnO RRAM devices. In each subfigure, the dataset presented using the colour scale is the first cycle, whilst the dataset shown in black is, in the case of undoped ZnO, the 30th cycle, or in the case

of Mn:ZnO, the 60th cycle. In both, there is a slight degradation of resistance window due to both the HRS and LRS becoming more and less conductive respectively. In addition, for both, the NDR exhibited during the RESET process becomes less prominent during repeated cycling, which could be indicative of a reduction in the number of charge carriers becoming trapped in defect states; a reduction in the number of charge carriers involved in the RS process may also explain the reduction in resistance window.

Discussion

It should be noted that it was not possible to stimulate reproducible VCM RS across all patterned devices, which limited an assessment of top electrode area-dependency. This variation in device performance could be due to a number of reasons: given the polycrystallinity of the film, grain size and grain boundary density could vary substantially, introducing non-uniformity to each device structure and due to the roughness of the film, the quality of the top electrode contact may vary across the device and induce non-uniformity in the thickness of the interfacial TiO_x layer. In addition, as emphasised earlier, external factors, such as the electrical probing style is likely to have had an effect on device yield: electrical characterisation is an iterative process, in which each device tested provides greater context for the next, therefore devices probed incorrectly could have led to early device failure. For instance, devices cycled using cc>2mA often led to either irreproducible filamentary RS, or an irreversible transition to an ohmic LRS, therefore subsequent devices were probed in a more conservative fashion using lower compliance compliance currents. Despite these effects, the RS displayed in Figs.3.5 and 3.6 represent the most reproducible and stable form of RS achieved across all devices fabricated under the conditions and were therefore used to represent optimal RS in undoped ZnO and Mn:ZnO in this study.

Major differences between the IV curves obtained from Ren *et al.*'s RRAM devices and the Mn:ZnO devices presented here are the polarity and abrupt nature of RS: their IV curves display sharp SET and RESET transitions that occur when the Pt bottom electrode is negatively and positively biased respectively, which contrasts our observations. As described in the literature, this differences can be attributed to dissimilarities in the choice of compliance current and applied voltages; in their work, the use of much higher

compliance currents (10mA) would have allowed the application of larger voltages which would have supported filament formation across the device. A significant disadvantage of using high compliance currents and voltages is device degradation. For instance, even though our devices exhibited much poorer resistance windows they surpassed Ren *et al.*'s in terms of reproducibility, sustaining 60 cycles (as shown in Fig.3.7). In general, the *gradual* nature of the bipolar RS observed in the ZnO and Mn:ZnO devices contrasts a majority of the literature which, in most cases, reports on the observation of abrupt, filamentary RS [2, 31, 38, 39, 42, 45, 98, 99]. As mentioned in Chapter 1, of all the RS mechanisms, such gradual switching is only exhibited by devices undergoing VCM RS. Considering the polarity of the observed RS, which was the same for both devices, it is possible to describe the VCM-type mechanism with respect to the voltage biased Pt/[Mn:]ZnO/Ti structure. It is proposed here that the overall resistance state of the device is governed by the thickness of an interfacial TiO_x layer. Fig.3.8(a) shows that when the Pt bottom electrode is negatively biased, $V_{\ddot{O}}$ migrate towards it along defect-rich grain boundaries and accumulate; at the same time, O^{2-} ions migrate towards the Ti top electrode and thicken a pre-existing redox-formed interfacial layer of highly resistive TiO_x which causes the device to switch to the HRS. Conversely, Fig.3.8(b) shows that when the Pt bottom electrode is positively biased, electro-migration of $V_{\ddot{O}}$ and O^{2-} in the opposite directions cause the dissolution of the resistive TiO_x layer, which switches the device to the LRS. Furthermore, Fig.3.8(b) also shows that the dissolution of the TiO_x may allow for the formation of unobstructed conductive $V_{\ddot{O}}$ filaments between the top and bottom electrodes along grain boundaries, which may account for the ohmic nature of the LRS [100]. In both states, Fig.3.8 depicts the accumulation of positively-charged $V_{\ddot{O}}$ near the anode, as found for gradual bipolar RS ZnO films presented in the literature [34]. In Mn:ZnO, these $V_{\ddot{O}}$-rich regions are expected to contain relatively reduced Mn in comparison to the bulk material.

In both undoped and Mn:ZnO, linear fit analysis of the IV curves showed that during the SET transition, the conduction mechanism was consistent with trap-free SCLC at moderate voltages ($0.2V<V\leq0.4V$) and trap-limited SCLC at higher voltages ($>0.4V$). According to the literature, for undoped ZnO devices, these charge traps were $V_{\ddot{O}}$, whilst for Mn:ZnO device, these were both $V_{\ddot{O}}$ and Mn^{2+} dopant ions [90, 91, 101].

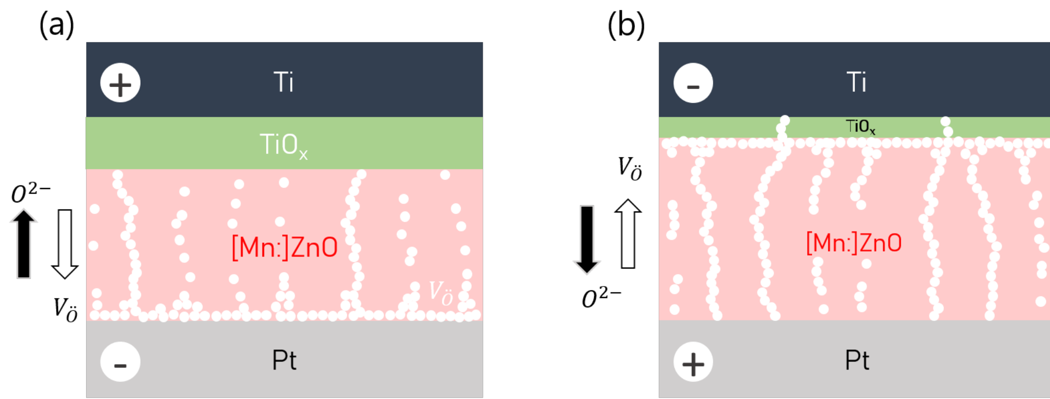

Figure 3.8: *Diagrams showing the interfacial oxide thickness modulation and $V_{\ddot{O}}$ migration expected for the (a) HRS and (b) LRS states in the undoped and Mn-doped devices. $V_{\ddot{O}}$ are shown in white and black and white arrows beside (a) and (b) show the direction of electromigration for O^{2-} and $V_{\ddot{O}}$ respectively.*

3.5.4 Electron Microscopy Characterisation

To understand the switching characteristics within the context of film morphology, FIB lamellae samples were obtained from RRAM heterostructures that displayed reproducible RS, which incorporated a 200nm undoped ZnO film deposited at P_{O_2} =100mTorr and a 70nm Mn:ZnO film deposited at P_{O_2} =100mTorr, and an ohmic device that did not display RS, which incorporated a 100nm undoped ZnO film deposited at P_{O_2} =10mTorr.

Diffraction patterns acquired from the two undoped ZnO devices are presented in Fig.3.9(a) and (b); these both had spotted ring-like diffraction patterns that are consistent with polycrystalline ZnO. By comparing the radial distribution of our measured diffraction spots with those in crystallographic databases, both films were found to be consistent with hexagonal wurzite ZnO, as expected; indexed peaks corresponding to crystallographic planes present in wurzite ZnO are highlighted in Fig.3.9(c). Additional contributions from metallic Ti, Pt and Au layers, and interfacial oxide TiO_2, which were also isolated with the selected area (SAD) aperture, were also present in the diffraction patterns and are identified in Fig.3.9(c). In Fig.3.9(c), a greater contribution from these additional layers is seen for the P_{O_2} =10mTorr film because this film was half the thickness of that deposited at P_{O_2} =100mTorr.

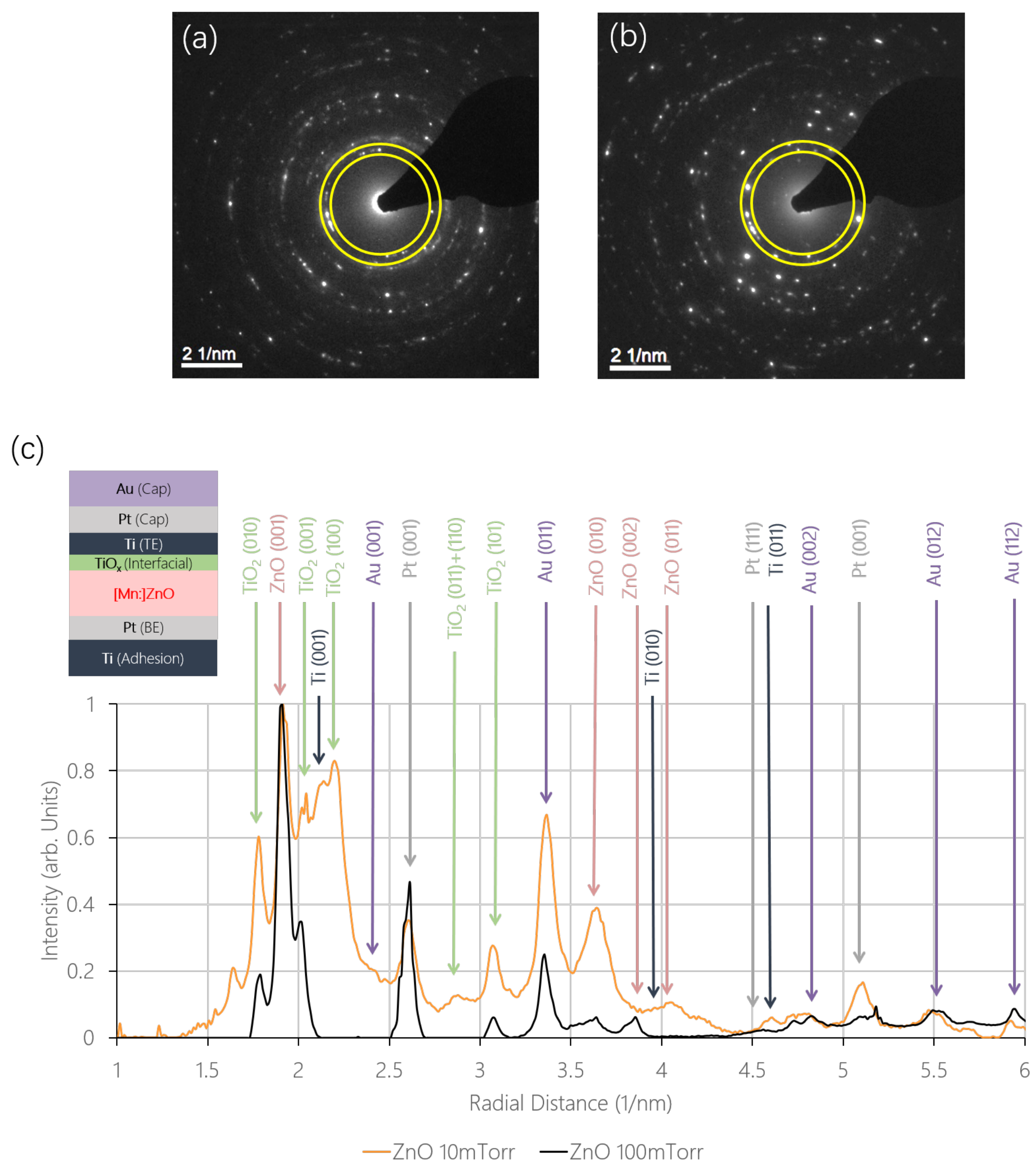

Figure 3.9: *Diffraction patterns acquired from (a) $P_{O_2}=100mTorr$ and (b) $P_{O_2}=10mTorr$ devices, both pulsed laser deposited at $T_s = 490K$. In both images, the central bright spot is blocked to prevent saturation damage. In addition the yellow ring in both images highlights the diffraction spots that contributed to the hollow-cone diffraction images presented in Fig.3.10. (c) Radial distribution plot showing the average intensity of diffracted spots within each concentric ring as a function of radial distance from the central spot. Each peak is indexed and colour co-ordinated with the device heterostructure shown in the inset, which includes top electrode (TE) Pt and Au caps, the redox-formed interfacial TiO_x layer, and the adhesive Ti layer required for the Pt bottom electrode (BE). The miller indices used correspond to ZnO P63mc, Ti P63mc, TiO_2 Pbcn, Pt Fm3m, and Au Fm3m structures.*

Fig.3.10 presents bright- and dark-field images obtained from the undoped ZnO and Mn:ZnO devices mentioned above. In the BF images, the heavy Pt bottom electrode appears dark, whereas the Ti and ZnO are near indistinguishable. These images allow for an assessment of film roughness and topology; for instance, the bright-field image of the undoped ZnO device deposited at P_{O_2} =100mTorr (shown in Fig.3.10(a)) confirms the dome-shaped grains observed using AFM and reveals that the peak-to-trough distance (highlighted in Fig.3.10(a) using red arrow and yellow dashed line) is of the order 30nm, whilst for P_{O_2} =100mTorr (shown in Fig.3.10(c)) this distance is significantly smaller (<10nm), consistent with the AFM roughness measurements which showed that roughness decreased with P_{O_2}. Figs.3.10(e) and (k) shows that unlike the undoped ZnO, the Mn:ZnO films do not display grains with smooth dome-like profiles; instead, each grain top appears to be faceted, which is consistent with the sharp contrast in surface topology between ZnO and Mn:ZnO observed using AFM (shown in Fig.3.4(h)). The peak-to-trough distance for the Mn:ZnO (20nm) is comparable to that found for ZnO. It should be noted that the contrast between the magnitude of the roughness or peak-to-trough values exhibited by these films and those presented in Fig.3.4 is due to the difference in the roughness of each substrate: Fig.3.4 presents films deposited onto smooth Si/SiO$_x$ but Fig.3.10 presents films deposited onto Si/SiO$_x$/Ti(200nm)/Pt(5nm), which was significantly rougher due to the presence of a thick Ti adhesion layer.

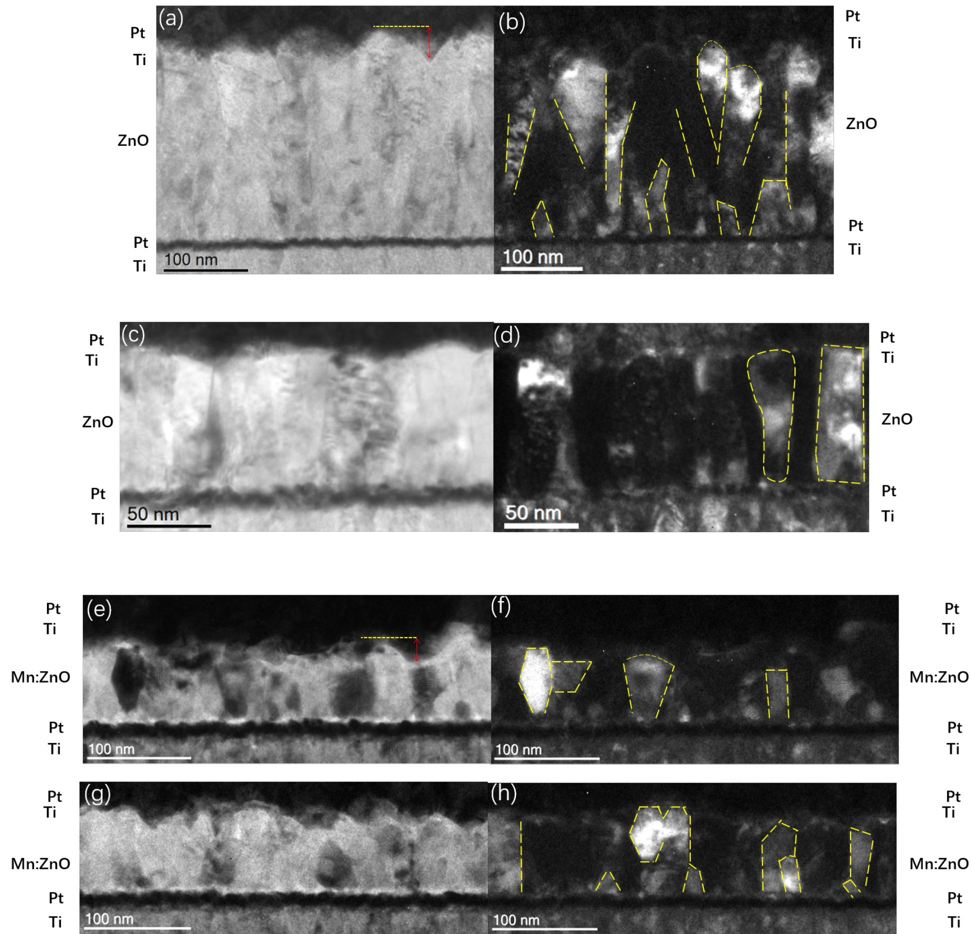

Figure 3.10: *BF and DF images acquired from the (a)-(b) RS* P_{O_2} *=100mTorr and the (c)-(d) ohmic* P_{O_2} *=10mTorr undoped ZnO devices deposited at* T_s *=490K and the (e)-(h) RS* P_{O_2} *=100mTorr Mn:ZnO device deposited at* $T_s = 630K$*. In the DF images, yellow dashed lines are used to highlight grain boundaries for clarity.*

As explained in Section 2.6.1, DF imaging allows one to isolate crystallographic orientations, as identified in a diffraction pattern, within the polycrystalline ZnO film and to enhance diffraction contrast between grains. The images shown in Figs.3.10(b), (d), (f) and (h) were produced using the hollow-cone method, in which the beam is not only tilted but rotated during the exposure, leading to a DF image that corresponds to *multiple* diffraction spots. Fig.3.10(b), which presents a DF image of the reproducible-RS device fabricated using undoped ZnO deposited at P_{O_2} =100mTorr, reveals its Zone T morphology; yellow dashed lines are used to highlight the smaller grains that populate the base of the film, close to the substrate surface, and the larger cone-shaped grains with dome-like profiles that constitute the bulk. In contrast, Fig.3.10(d) presents a DF image of the non-switching, ohmic device, which contained undoped ZnO

deposited at P_{O_2} =10mTorr; at this reduced deposition pressure, the ZnO comprised large rectangular grains that are elongated along the growth-axis, each with relatively flat profiles, consistent with Zone 2 morphology. Figs.3.10(f) and (h) present DF images obtained from the Mn:ZnO device, which exhibited reproducible RS, reveal irregular grain shapes and sizes that are not entirely consistent with the cone-shaped or rectangular grains characteristic of Zones T and 2; instead, the Mn:ZnO is consistent with Zone 3 morphology, despite having been deposited at the same pressure and temperature as the Zone T undoped ZnO film. This difference could be due to segregated Mn dopants causing the periodic blocking of growth, as explained by Barna *et al.* [58].

Discussion

Reproducible RS was not observed in devices that incorporated the Zone 2 ZnO film; it is possible that for these ohmic devices, the presence of grain boundaries aligned along the growth axis presented unobstructed $V_{\ddot{O}}$-rich conductive paths between the top and bottom electrodes that electrically shorted the device. In comparison, the films deposited at higher pressures had Zones T and 3 morphology, which present far more complex and irregular conductive paths between the top and bottom electrodes, increasing the resistivity of the film. These results are consistent with the majority of the literature on RRAM, which generally reports on the observation of reproducible RS in highly resistive films.

3.5.5 TEM-EELS Analysis

The undoped ZnO and Mn:ZnO devices that displayed reproducible RS were characterised using TEM-EELS. For the undoped ZnO, a FIB lamella was fabricated from a pristine device and for the Mn:ZnO, FIB lamellae were fabricated from pristine and programmed devices. Table 3.3 presents the acquisition information corresponding to the EELS datasets used in this work.

Table 3.3: Acquisition information for ZnO and Mn:ZnO EELS datasets.

Datasets	Offset (eV)	Dispersion (eV/Ch)	Pixel Size (nm^2)	Acquisition Time (ms)		Acquisition Ratio
				Low-Loss	High-Loss	
ZnO	300	0.5	0.99	0.10	100	1000
Mn:ZnO	300	0.5	0.99	0.25	50	200

Undoped ZnO

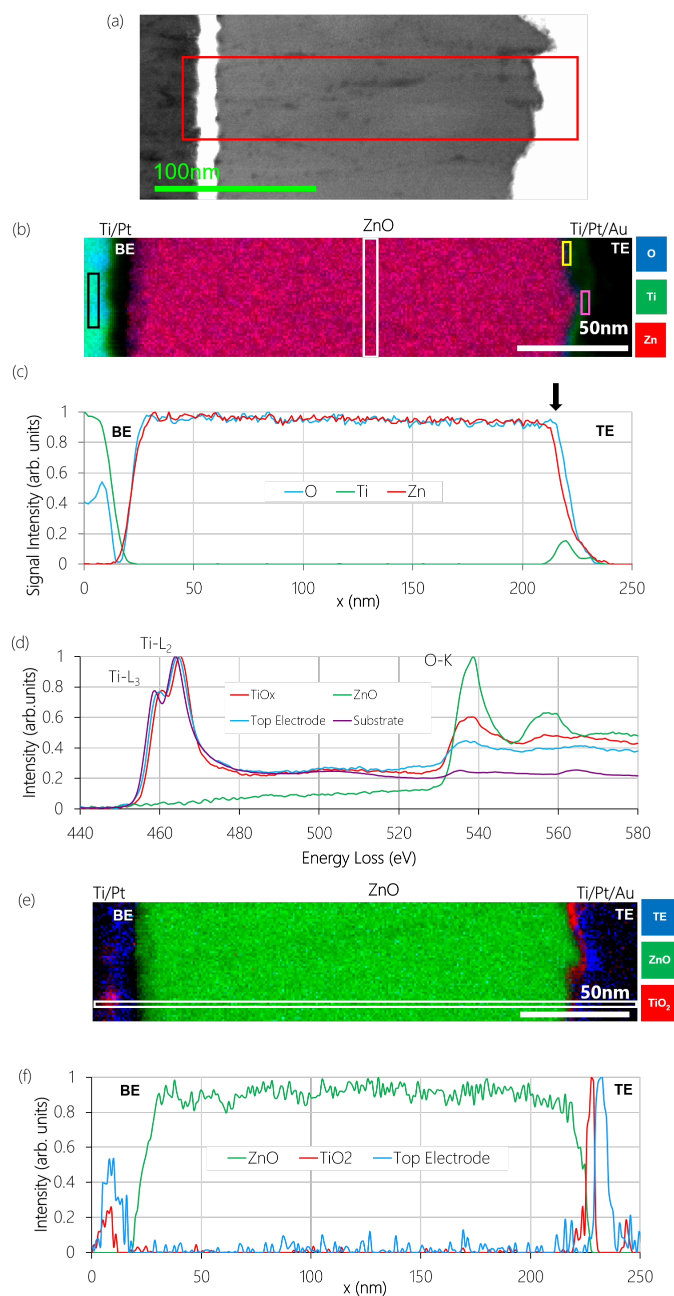

Figure 3.11: *EELS analysis of a pristine undoped ZnO RRAM device. (a) HAADF image where the EELS acquisition area is shown in red. (b) RGB composite signal map where Ti, O and Zn are shown in green, blue and red respectively. (c) Elemental map showing the spatial distribution profiles of the Ti, O and Zn signals, where a TiO_x interfacial oxide layer is highlighted with a black arrow. Black, white, yellow and pink boxes indicate regions from which reference spectra for MLLS fitting were acquired and correspond to the substrate adhesion layer, bulk ZnO, interfacial TiO_x and the contaminated top electrode respectively. (d) MLLS fitting reference spectra used to produce (e) an MLLS fit map. Here, the white dashed box shows the region used to produce (f) a normalised spatial distribution profiles of MLLS fit.*

Fig.3.11 presents a representative TEM-EELS dataset acquired from a pristine Pt/ZnO/Ti device on the same bulk sample that displayed reproducible RS. Fig.3.11(a) shows the HAADF overview image, in which diffraction contrast reveals the presence of grain boundaries, which appear dark and extend along the growth axis. In Fig.3.11(b), Ti, which is shown in green, is present in the bottom electrode (the LHS of the signal map) and the top electrode (the RHS of the signal map). The bulk ZnO appears as a bright purple due to the contribution of both blue O and red Zn in the film. Despite the confirmed Zone T structure, no significant variation in Zn:O ratio was observed at grain boundaries, which are typically thought to be O-deficient. However, Fig.3.11(b) shows that near the Ti top electrode, there is a change in Zn:O ratio: a blue, O-rich region is sandwiched between the top electrode and ZnO bulk, which is consistent with the presence of an interfacial TiO_x layer. This O-rich region can also be seen in Fig.3.11(c), which shows the distribution of Ti, O and Zn signals in Fig.3.11(b). Whilst the O and Zn signals overlap at the bottom electrode, there is a separation of $\sim$ 3nm between the O and Zn slopes at the top electrode (highlighted with the black arrow); this separation was seen across most datasets. Furthermore, Fig.3.11(c) shows that at the top electrode, the Ti signal is completely overlapped by the O signal, which suggests that the full thickness of the Ti top electrode (which was fabricated to be 5nm thick, see Fig.3.3) is in fact *fully oxidised*. This is in agreement with the analysis of the diffraction patterns, discussed in Section 3.5.4, which featured diffraction spots that were consistent with the presence of TiO_2. Given that the entire Ti top electrode was oxidised, the clear distinction between O and Ti signals at the top electrode in Fig.3.11(b) suggested that less oxidised or metallic Ti was present in the Pt/Au cap. Fig.3.11(d) presents the EELS spectra acquired from the top electrode, the substrate adhesion layer, the bulk ZnO and the interfacial TiO_x (these are highlighted in dashed boxes in Fig.3.11(b)) and reveals the presence of a TiO_x contaminant in the Pt top electrode (see blue spectra). The contamination of Pt (which most likely occurred at the point of deposition) was also observed at the bottom electrode and reached levels of up to 25%. At this relatively low level of contamination, no significant impact on RS was expected. Instead the Ti signal present in the Pt electrode and cap can be used to map the Pt indirectly.

The oxidation state of Ti in the Pt top electrode, interfacial TiO_x layer and Ti

adhesion layer can be directly assessed through comparison of the recorded Ti-$L_{3,2}$ edges with the literature [102, 103]; the recorded spectra are shown in Fig.3.11(d). Here, clear changes in Ti-$L_{3,2}$ peak position, which were greater than the dispersion (0.5eV/Ch) and therefore significant, were seen: the Ti-L_3 peak acquired from the substrate (shown in purple) has energy loss 458.7eV and is the most metallic of all TiO_x phases present in the device; the Ti contaminant present in the Pt top electrode is chemically shifted by +1eV with respect to the substrate and has Ti-L_3 peak position 459.7eV; finally, the interfacial oxide present beneath the Pt top electrode is chemically shifted by +1eV with respect to the top electrode and has a Ti-L_3 peak position 460.7eV, making it the most oxidised of all TiO_x phases present and consistent with TiO_2 and the spectra was either miscalibrated during ZLP centering or subject to dispersion scaling effects [102, 103]. According to Stoyanov *et al.*, who measured Ti-$L_{3,2}$ as a function of Ti valence state, with respect to Ti^{4+}, the contaminated Pt top electrode and substrate contain $Ti^{3.3+}$ (found in Ti_3O_5) and $Ti^{2.6+}$ respectively [102]. These spectra, as well as that acquired from the bulk ZnO, were used as principal references for MLLS fitting (described in Section 2.7.6). To improve the fit, an additional spectrum corresponding to the Au top electrode was also included, but as it does not contribute to the basic MOM heterostructure, it was not included in the analysis of RS. The MLLS fitting results are mapped in Fig.3.11(e). Here, a clear distinction between the Ti_3O_5 phase (shown in blue) present in the top electrode and TiO_2 top electrode interfacial oxide (shown in red) can be seen. A normalised line profile of the spatial distribution of the signal corresponding to each MLLS reference (except the substrate) is displayed in Fig.3.11(f), which confirms that the two TiO_x phases at the top electrode are spatially segregated and that the interfacial TiO_2 layer is ~5nm thick.

Considering the EELS analysis of the pristine device presented in Fig.3.11, with regards to the mechanism of RS, it is likely that the fully oxidised TiO_2 sandwiched between the bulk ZnO and the Pt/Au cap acts as a interfacial $V_{\ddot{O}}$-reservoir layer during RS, which, due to its high resistivity [104], governs the overall resistance state of the device, as depicted in Fig.3.8. In addition, the same reasoning can be applied to the electroforming SET transition: due to the immediate redox-induced formation of TiO_2 during deposition, the device is initially in the HRS and the dissolution of the TiO_2 layer

must be triggered before the device can be electroformed to the LRS. In contrast, the Mn:ZnO device required an electroforming *RESET* transition, which suggests that its pristine state is not identical to that observed for the undoped ZnO devices.

Mn:ZnO

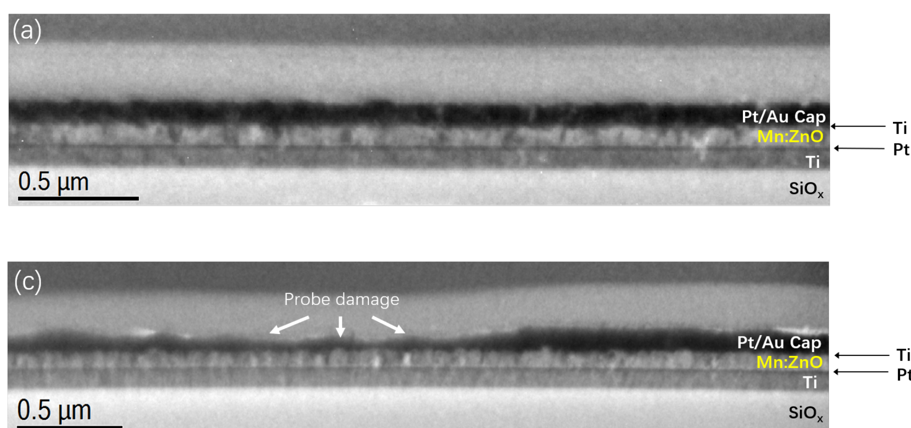

Figure 3.12: *Low-magnification images of lamella extracted from (a) a pristine and (b) a programmed Mn:ZnO device. Damage to the Pt/Au top electrode cap did not appear to damage the Mn:ZnO RS layer.*

Low magnification BF TEM images of the lamellae fabricated from a pristine and a programmed device are shown in Figs.3.12(a) and (b) respectively: in Fig.3.12(a), the heavy metal top electrode cap (which appears dark) is uniform in thickness ($\sim 1\mu$m) across the width of the device; whilst in Fig.3.12(b), the lamellae was extracted from directly beneath the region of probe damage where the top electrode cap is non-uniform in thickness. Despite damage to the Pt/Au cap, the local Mn:ZnO RS layer appears undamaged. Analysing both lammellae allows for a direct comparison of pristine and programmed devices and, in addition, allows us to compare different regions along the length of the lamella to assess the spatial uniformity of the VCM RS effect.

Fig.3.13(a) presents the HAADF overview image in which diffraction contrast appears; in addition, the region used for the acquisition of EELS data is highlighted in red. Figs.3.13(b)-(f) display the spatial distribution of O, Zn, Ti, Pt and Mn in a pristine Mn:ZnO RRAM device that was identical to those that exhibited the reproducible RS presented in Fig.3.6. Unexpectedly, in every dataset, the Ti and Mn signal maps (presented in Fig.3.13(d) and (e)) showed evidence of clustering above the Pt bottom

electrode, which suggests that the presence of an interfacial phase formed due to chemical activity during deposition. In addition, for some datasets, the *vertical* clustering of Mn (highlighted by the orange arrows in Fig.3.13(e)), presumably along grain boundaries, was revealed. The segregation of dopants at grain boundaries has been observed in the literature in a number of polycrystalline materials, but is not typically reported in the experiment-based literature on Mn:ZnO [105, 106]. In general, as found for Zn interstitials and $V_{\ddot{O}}$, grain boundaries act as sinks for impurity dopants where secondary impurity-oxide phases can form and cluster [106]. Such segregation typically occurs due to an excess of impurity dopants that cannot be accommodated within the crystalline lattice and is therefore dependent on the thermal equilibrium solubility limit of the dopant into the bulk material [107]; for Mn in ZnO, this limit is 13 mol% at 973K. However, for Mn:ZnO deposited via PLD, a non-equilibrium technique, the thermal equilibrium limit has been exceeded: solubility of Mn of up to 35% in ZnO has been achieved where the bulk material exhibited no evidence of dopant segregation [107]. The deposition and/or anneal temperature has also been shown to induce the reversible thermal diffusion of dopants out of crystalline grains into grain boundaries [108]. It is possible that at the lower substrate temperature used here, thermal diffusion was limited and insufficient for the homogeneous distribution of Mn throughout the ZnO. Although the exact cause of Mn segregation is unclear, the direct observation of the resultant vertical clustering of Mn is of particular interest as it resembles the vertical ferromagnetic sub-oxide phases proposed in Ren *et al.*'s RT-FM-RS co-switching mechanism [2].

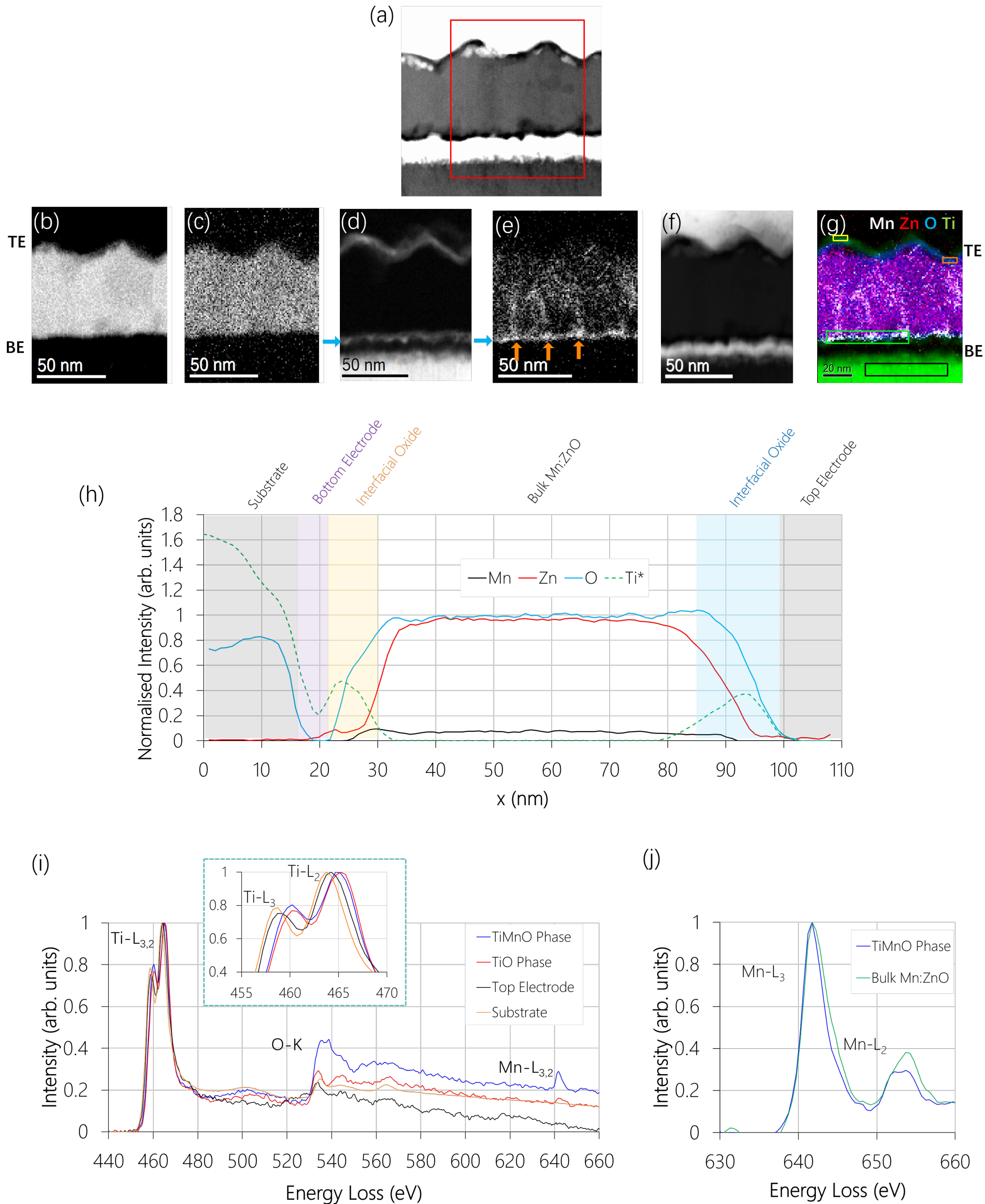

Figure 3.13: *EELS analysis of pristine and programmed Mn:ZnO devices. (a) HAADF overview map. Signal maps acquired from pristine devices showing (b) O, (c) Zn, (d) Ti, (e) Mn and (f) EDX-Pt signals. Blue and orange arrows are used to highlight the vertical and horizontal clustering of Ti and Mn. (g) Colour composite map of (b)-(f) where O, Zn, Ti and Mn are shown in white, red, blue and green respectively. (h) Elemental-ratio-normalised distribution profiles acquired from a programmed devices where O, Zn and Mn are shown in red, blue and black respectively. In both, the Ti line profile (green dashed line) was scaled up to evaluate Ti and O spatial overlap. (i) Comparison of EELS spectra acquired from highlighted regions in (g): the top electrode (shown in black), the adjacent interfacial TiO_x phase (shown in red), the substrate adhesion layer (shown in orange) and the $Ti_xMn_yO_z$ phase (shown in blue). Inset shows Ti-$L_{3,2}$ peaks. (j) Comparison of Mn-$L_{3,2}$ peaks acquired from the bulk Mn:ZnO (shown in green) and $Ti_xMn_yO_z$ (shown in blue).*

Fig.3.13(g) presents a colour composite of the Mn, Zn, O and Ti maps presented in Figs.3.13(b)-(e) and is colour coordinated to allow for direct comparison to the colour composite signal map of the undoped ZnO device shown in Fig.3.11(b). As found for the pristine undoped ZnO device, at the top electrode interface, the O signal (shown in blue) extends further towards the Ti at the top electrode (shown in green) than the Zn signal (shown in red). Furthermore, Fig.3.13(h), which was produced using the elemental ratio normalisation process described in Section 2.7.3, shows that this extension occurs at *both* electrodes (i.e. there is a $\sim$6nm separation between the rise and fall of the Zn and O signals respectively), which was only observed at the top electrode of the undoped ZnO device and corresponded to fully oxidised TiO_2. The extension of the O signal at the bottom electrode (highlighted in yellow in Fig.3.13(h)) coincides with the the Ti- and Mn-rich cluster present above the bottom electrode (shown in Figs.3.13(d) and (e)), suggesting the presence of an interfacial oxide. Figs.3.13(h) also shows that the bulk Mn:ZnO has stoichiometry $Mn_{0.1}Zn_{0.9}O$, which is a larger dopant level than expected ($Mn_{0.05}Zn_{0.95}O$).

A comparison of spectra acquired from the Pt top electrode, substrate adhesion layer, interfacial TiO_x, and the Ti- and Mn-rich cluster above the bottom electrode is shown in Fig.3.13(h). As seen in the undoped ZnO device, the Pt top electrode is contaminated with a TiO_x phase (which is used here for mapping the Pt) and there is a significant difference in Ti-L_3 peak shift (magnified in inset in Fig.3.13(i)) between the Ti present in different regions of the device: the Ti present in the interfacial oxide is fully oxidised Ti^{4+} in TiO_2, indicated by its Ti-L_3 peak at energy loss 460.7eV [102, 103]; the Ti-L_3 peak acquired from the contaminated Pt top electrode has energy loss 459.2eV, which, considering the dependence of Ti-L_3 peak shift on valence state, corresponds to Ti^{3+} in Ti_2O_3 [102]; the substrate contains the most metallic Ti present in the device, where the Ti-L_3 peak has energy loss 458.7eV, which corresponds to $Ti^{2.6+}$, indicative of the presence of both Ti^{2+} in TiO and Ti^{3+} in Ti_2O_3; finally, the Ti present in the Ti- and Mn-rich oxide phase above the Pt bottom electrode has a Ti-L_3 peak with energy loss 460.5eV, which, with respect to the position of the Ti^{4+}, is consistent with $Ti^{3.9+}$ [102]. Although not characterised in the literature, across these four spectra, the Ti-L_2 peak also displays a gradual peak shift consistent with the Ti-L_3-peak-based

evaluation of Ti valence state where the Ti-L_2 peak shifted to higher energy losses with increasing Ti valence state. Considering the EELS analysis presented above and the polarity and gradual nature of the bipolar RS exhibited by these devices, the Mn:ZnO RS mechanism is consistent with that proposed for the undoped ZnO device and depicted in Fig.3.8: the interfacial TiO_2 layer present at the top electrode acts as an $V_{\ddot{O}}$-reservoir to facilitate VCM RS. However, here we see that redox activity at the interfacial oxide near the top electrode is *spatially inhomogeneous*. In addition, the contribution from the unexpected oxide phase(s) present above the Pt bottom electrode, which is not present in the undoped ZnO device, must be evaluated. Of utmost importance is whether this is indicative of a single phase which contains both Ti and Mn or multiple chemically distinct phases containing either Ti or Mn that spatially overlap. Fig.3.13(i) allows for an assessment of this through direct comparison of the unknown bottom electrode phase (shown in blue) with other Ti-containing phases. Whilst the presence of the Mn-$L_{3,2}$ edge is not necessarily indicative of chemically distinct phase in itself (because it would also appear if an Mn-containg phase spatially overlapped with another phase), the significant difference in the shape and absolute intensity of the O-K edge observed for the Ti- and Mn-rich phase strongly suggests that this ($Ti_xMn_yO_z$) phase is distinct from the other Ti-containing phases present in the device. For example, the shape of the TiO_2 O-K edge is consistent with that observed for TiO_x in the literature, which typically feature a broad peak that rises and falls between 530eV and 535eV, whilst the shape of the O-K edge in the $Ti_xMn_yO_z$ is, in contrast, consistent with Mn^{2+} present in MnO, which is dominated by a doublet situated at energies between 530eV and 545eV [109–112]. In addition, the relative intensity of the O-K in the $Ti_xMn_yO_z$ is greater than that in TiO_2, which suggests that the ratio between Ti and O is greater than 1:2. In the literature, only two $Ti_xMn_yO_z$ phases fit this criteria: $TiMnO_3$ and $TiMn_2O_4$. Similarly, Fig.3.13(j) allows for an evaluation of the Mn valence state through a comparison of the Mn signal extracted from the bulk Mn:ZnO to that acquired from the $Ti_xMn_yO_z$ phase. Here, there is a subtle relative peak shift between the two phases: the bulk Mn:ZnO is shifted +0.5eV with respect to the $Ti_xMn_yO_z$ which, according to the literature, is indicative of a change of $Mn^{n+0.3}$ [110]. Despite this shift, the Mn-L_3 maxima occur at 641.7eV for both spectra, consistent with Mn^{3+} [110, 113],

and this is due to a clear difference in the shape of the Mn-$L_{3,2}$ edge: the Mn-L_3 in the $Ti_xMn_yO_z$ phase is more asymmetric than that in the bulk Mn:ZnO and is weighted towards lower energy losses, an effect typically observed for Mn^{2+} [113]. There are two further difference between the Mn-L−3, 2 edges: the Mn in the $Ti_xMn_yO_z$ phase has an increased L_3:L_2 peak ratio, which has been shown to increase with decreasing valence state [110, 111, 114]; and the Mn-L_2 in the $Ti_xMn_yO_z$ is broad and has a flattened top, consistent with a poorly resolved observation of the doublet typically produced for Mn^{2+} (a single sharpened Mn-L_2 peak is more consistent with Mn^{3+}) [113]. Given that the Ti in the $Ti_xMn_yO_z$ was shown to be $Ti^{3.9+}$ and that this phase is likely to be either $TiMnO_3$ and $TiMn_2O_4$, the Mn valence state can also be estimated through a simple charge balancing calculation (where oxygen is O^{2-}). Doing this, the Mn valence state is either $Mn^{2.1+}$ for $TiMnO_3$ or $Mn^{2.05+}$ for $TiMn_2O_4$; both phases are consistent with the evaluation of Mn valence state via peak shape presented above. Due to the $Mn^{n\pm0.3}$ shift between the bulk Mn:ZnO and $Ti_xMn_yO_z$ phase, it is estimated that the bulk Mn:ZnO contains $Mn^{2.3+}$. This is a slightly higher oxidation state than that predicted for homogeneously distributed Mn in single crystal Mn:ZnO, however given the presence of grain boundaries, which influence the concentration and distribution of $V_{\ddot{O}}$ and O^{2-} throughout the film, small deviations from Mn^{2+} in polycrystalline Mn:ZnO are to be expected [20].

Signal maps like that shown in Fig.3.13 allow for an evaluation of the spatial distribution of individual elements. To investigate the spatial distribution of distinct *phases*, MLLS fitting (described in Section 2.7.6) was employed; the results of which are shown in Fig.3.14. The key spectra used to create the fits are presented in Fig.3.14(a) and include the $Ti_xMn_yO_z$ phase (extracted from the above the bottom electrode), the TiO_2 interfacial oxide (extracted from beneath the top electrode), the bulk Mn:ZnO, and the bottom electrode. Given that Pt core-loss edges were not recorded, Ti-contaminant signal was used to evaluate the spatial distribution of the Pt. As noted above, this low level contamination is not expected to affect RS, which means that with regards to RRAM operation, these can be considered metallic and inert.

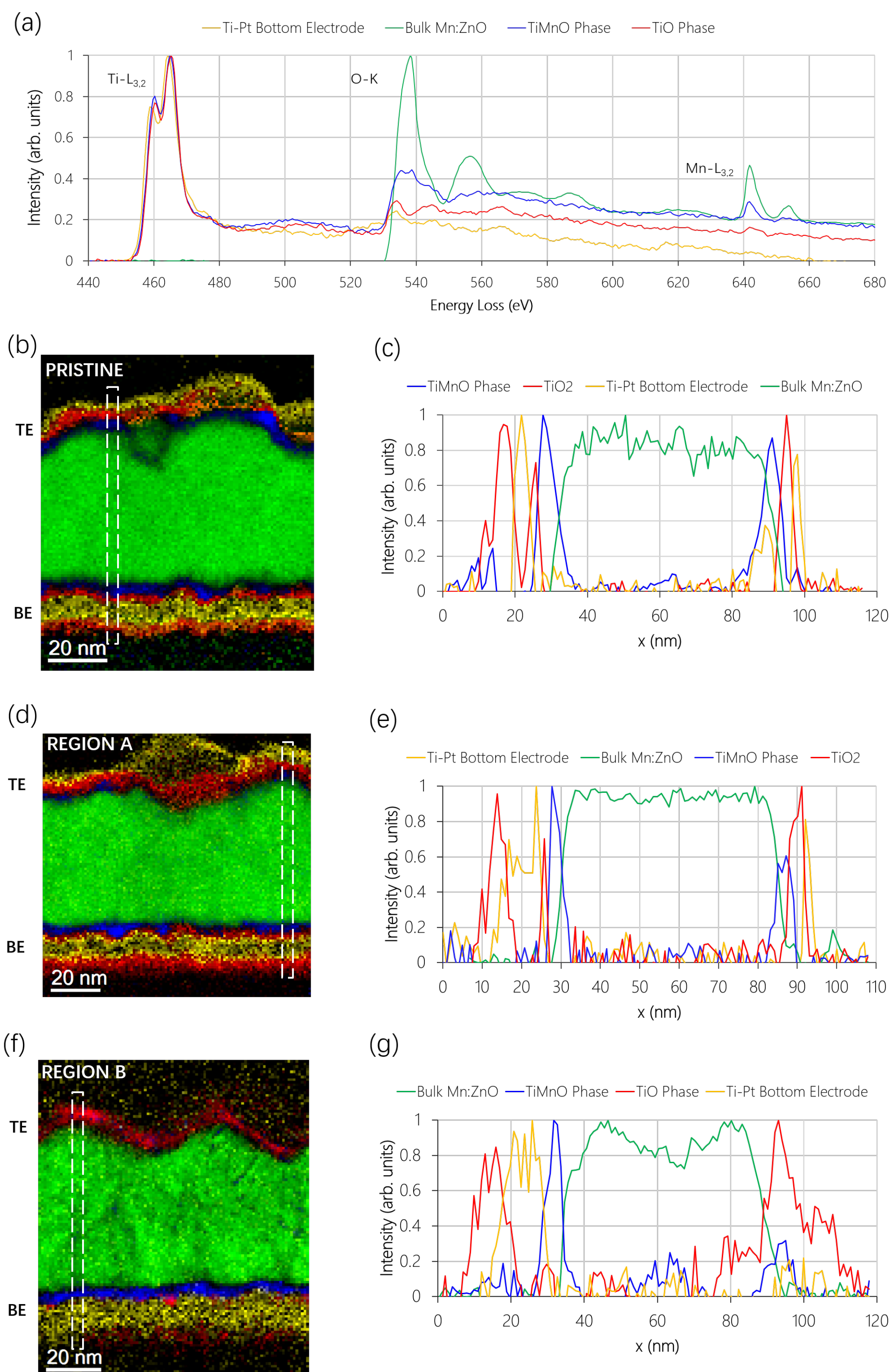

Figure 3.14: *(a) Deconvolved spectra used to MLLS fit the data. Colour composites of the signal intensity maps associated with each phase presented in (a) is presented in (b), (d) and (f), which represent pristine, programmed (acquired from region A) and programmed (acquired from region B) respectively. The white boxes in (b), (d) and (f) highlight regions used to acquire the spatial distribution of each MLLS fit across device along the growth axis; these results are shown in (c), (e) and (g). In all subfigures, the Ti/Pt bottom electrode, bulk Mn:ZnO, TiMnO phase and TiO phase are shown in yellow, green, blue and red respectively.*

Colour composite maps revealing the spatial distribution of the phases presented (and colour-coded) in Fig.3.14(a) are shown in Figs.3.14(b), (d) and (f). These are representative maps that show the phase distribution in pristine and programmed Mn:ZnO devices, where two different regions (labelled A and B) along the length of the lamella are compared for an assessment of spatial homogeneity. In addition to the colour composite MLLS fit maps, Figs.3.14(c), (e) and (g) present line profiles taken through Figs.3.14(b), (d) and (f) that show the spatial distribution of each phase along the growth axis. MLLS fitting of the pristine device (shown in Fig.3.14(b)) revealed that the Mn:ZnO RRAM device had a more complex heterostructure than that which was designed: instead of the anticipated Pt/Mn:ZnO/TiO_x/Ti structure, the devices had a Pt/TiO_2/$Ti_xMn_yO_z$/Mn:ZnO/$Ti_xMn_yO_z$/TiO_2/Pt structure. As shown in Figs.3.14(b) and (c), the $Ti_xMn_yO_z$ present above the bottom electrode was also present at the top electrode and similarly, the TiO_2 present underneath the top electrode was also present at the bottom electrode. Interestingly, Fig.3.14(b) shows that at the top electrode, the TiO_2 and $Ti_xMn_yO_z$ phases are non-uniform in thickness. Furthermore, they appear to thicken and thin in accordance with one another: regions of thick (~5nm) TiO_2 are directly adjacent to regions of thin (~2.5nm) $Ti_xMn_yO_z$ and vice versa, which suggests that the formation of these phases may be attributed to the exchange of mobile constituents between the two. The programmed devices showed reproducible changes in the spatial distribution of each phase. Fig.3.14(d) shows that the datasets acquired from different regions were largely similar to the pristine datasets, however the TiO_2 phase at the top electrode appears to have thickened at the expense of the $Ti_xMn_yO_z$. Fig.3.14(e) shows that there is nearly twice as much $Ti_xMn_yO_z$ present above the bottom electrode than there is beneath the top electrode, which is significant decrease in comparison to the pristine device shown in Fig.3.14(c). Region B of the programmed device(shown in Figs.3.14(f) and (g)) shows greater differences in comparison to the pristine device and region A of the programmed device: instead of both $Ti_xMn_yO_z$ and TiO_2 being present above and beneath the bottom and top electrodes, TiO_2 is dominant at the top electrode whilst $Ti_xMn_yO_z$ is dominant at the bottom electrode. These observations are consistent with the occurrence of spatially inhomogeneous redox activity at each electrode interface and, due to the absence of

$Ti_xMn_yO_z$ at the top electrode interface, suggests that the electromigration of Mn, in addition to $V_{\ddot{O}}$, may occur during RS, which has not previously been observed in the literature. Finally, in Fig.3.14(g), the profile of the bulk Mn:ZnO has non-uniform intensity, which contrasts Figs.3.14(c) and (e); the dip in intensity in the middle of the bulk Mn:ZnO film (at 50nm) coincides with an increase in the $Ti_xMn_yO_z$ phase. The presence of chemically distinct Mn-phase in the bulk Mn:ZnO agrees with the suggestion that in these devices, Mn ions are subject to electromigration.

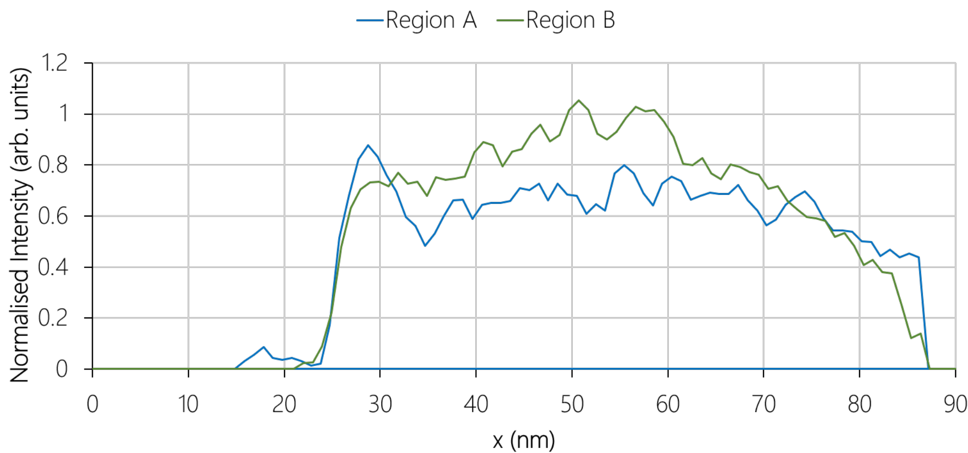

Figure 3.15: *Comparison of elemental ratio normalised distribution of Mn (averaged over the entire width of each EELS dataset) previously shown in Fig.3.13(g).*

Further inspection of the elemental-ratio-normalised Mn profiles in Figs.3.13(g) and (h) revealed more evidence of redistribution of Mn in programmed devices; the Mn profiles (averaged over the entire width of each EELS dataset) corresponding to different regions of a programmed device are shown in Fig.3.15. Here, the datasets were aligned with respect to the bottom electrode interface (centred at 25nm). For the datasets acquired from region A, there was a significant accumulation of Mn at the bottom electrode, consistent with the Mn signal map shown in Fig.3.13(e) and the increased presence of $Ti_xMn_yO_z$ at the bottom electrode shown in Fig.3.14(e). In addition, for pristine devices, the data showed that there was either an accumulation of Mn at the bottom electrode, as seen for region A, or a uniform distribution of Mn. In contrast, the datasets acquired from region B showed no accumulation of Mn at the bottom electrode; instead, there was a greater concentration of Mn in centre of the bulk Mn:ZnO film as opposed to either the top or bottom electrodes. In addition to changes presented

in Fig.3.14, changes to the normalised Mn distribution profile strongly suggest that, in addition to $V_{\ddot{O}}$, Mn ions are also *mobile* in the bulk Mn:ZnO and migrate under an applied electric field, presumably along growth-axis-aligned grain boundaries where phase segregation was observed.

3.6 Conclusion

In both the undoped and Mn:ZnO devices, TEM-EELS analysis confirmed the presence of a TiO_2 interfacial oxide, formed due to the full oxidisation of the Ti top electrode, beneath the Pt top electrode cap; it likely that this interfacial oxide acted as a source an sink for $V_{\ddot{O}}$ and facilitate VCM RS. Interestingly, in the Mn:ZnO device, an additional interfacial $Ti_xMn_yO_z$ phase (either $TiMnO_3$ or $TiMn_2O_4$) was found above the bottom electrode and appeared to have formed during deposition due to the presence of Ti contaminants at the surface of the Pt bottom electrode. Additional evidence consistent with the presence of secondary Mn phases was also found in different regions of the device: Fig.3.13(e) shows clear proof of the accumulation of Mn not only at above the bottom electrode, but along (typically $V_{\ddot{O}}$-rich) grain boundaries, a finding which has been proposed but not experimentally observed in the literature [106]. Interestingly, this supports Ren *et al.*'s publication on simultaneous resistance and magnetisation co-switching in pulsed laser deposited Pt/Mn:ZnO/Ti devices (introduced in Section 3.2.1). Although grain boundary segregation was not explicitly stated, it was proposed that secondary phase Mn-clusters aligned vertically along the growth axis and that $V_{\ddot{O}}$ conductive filaments formed within their vicinity [2]. Their paper also investigated the redistribution of $V_{\ddot{O}}$ along the *c*-axis and showed that in the pristine state, regions near the top and bottom electrodes were $V_{\ddot{O}}$-rich and contained more Mn^{2+} than Mn^{4+}; these regions contrasted the $V_{\ddot{O}}$-deficient bulk Mn:ZnO, which contained more Mn^{4+} than Mn^{2+}. In the LRS, a steady gradual change in $V_{\ddot{O}}$-concentration along the growth axis was observed. There are some similarities between Ren *et al.*'s proposal and the experimental results found here: given that the Mn present in the $Ti_xMn_yO_z$ phase was relatively reduced with respect to the bulk Mn:ZnO (see Fig.3.13(j)), this phase can be directly compared to their regions of increased Mn^{2+}. Indeed, in the pristine state

(shown in Fig.3.14(c)), the $Ti_xMn_yO_z$ phase is present above and beneath the bottom electrodes respectively and these two $V_{\ddot{O}}$-rich regions sandwich the Mn:ZnO bulk which contains relatively oxidised Mn. Although we have no direct comparison for the LRS (as fixed state LRS and HRS were not studied in this work), the heavily probe damaged region of the device shown in Fig.3.14(g) represents a state is which $V_{\ddot{O}}$ are present above the bottom electrode (indicated by the presence of $Ti_xMn_yO_z$ phase) and O^{2-} are present beneath the top electrode (indicated by the presence of TiO_2).

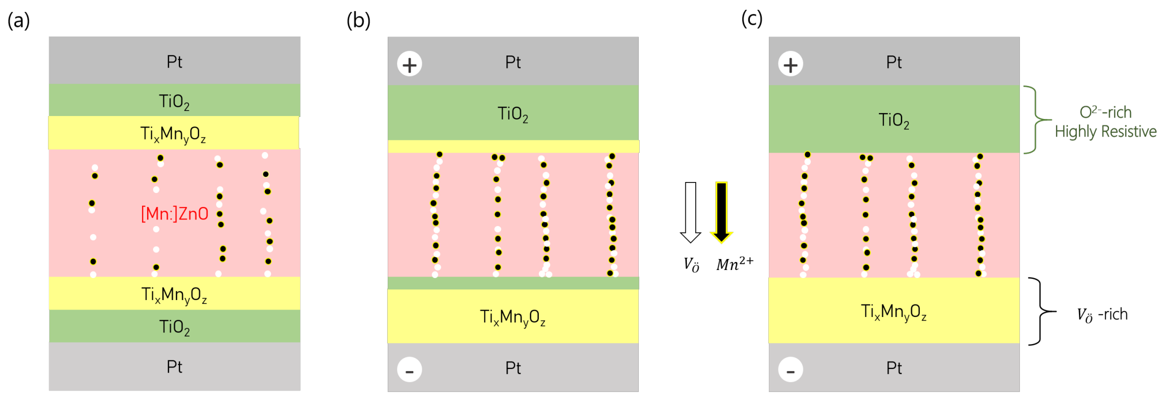

Figure 3.16: *Proposed mechanism of RS in Mn:ZnO device where $V_{\ddot{O}}$ and Mn^{2+} are represented by white and black circles respectively. (a) Pristine device that displays Mn- and $V_{\ddot{O}}$- clustering along growth-axis-aligned grain boundaries. (b) and (c) represent different regions (separated spatially) along the sample where (b) depicts a mid-point (or transition state) between (a) and (c), emphasising spatial inhomogeneity of redox activity at the electrode interfaces.*

Based on the electrical characterisation and EELS analysis presented in this chapter, an RS mechanism is proposed in Fig.3.16. Fig.3.16(a) shows the pristine device, where the Ti top electrode is fully oxidised to TiO_2. Fig.3.16(a) also depicts the experimentally observed clustering of Mn (shown in black) along *c*-axis aligned $V_{\ddot{O}}$-rich (shown in white) grain boundaries. The $Ti_xMn_yO_z$ and TiO_2 phases are shown to have equal thickness in the pristine state, however when one electrode is biased with respect to the other, these thicken or thin. As shown in Figs.3.16(b) and (c), when the top electrode is positively biased, the formation of TiO_2 beneath the top electrode and $Ti_xMn_yO_z$ above the bottom electrode is promoted. Here, based on the normalised Mn signal distribution shown in Fig.3.15, it is proposed that this interfacial oxide formation process is mediated by the electromigration of both $V_{\ddot{O}}$ and Mn^{2+} along grain boundaries. Depicting the HRS or LRS is complicated by the fact that it is unclear whether $TiMnO_3$ or $TiMn_2O_4$

is present in the device. For instance, considering the gradual nature of switching, it is likely that the resistance state is governed by the gradual formation and degradation of a highly resistive oxide layer; in the heavily probe-damaged device, this could be either the TiO_2 or the $Ti_xMn_yO_z$ phase. However, given that the RS electrical characteristics and polarity dependency exhibited by the Mn:ZnO devices were similar to that exhibited for undoped ZnO, it is likely that RS is dominated by a similar interfacial oxide effect. The common feature between these two devices is the TiO_2 interfacial oxide formed beneath the top electrode, as such, it is likely that the formation and dissolution of this phase dominates the overall resistance state. Therefore, due to the relatively thick TiO_2 present beneath the top electrode in Figs.3.16(b) and (c), these are expected to represent different regions along a Mn:ZnO that is programmed to the HRS. Furthermore, this representation of the HRS (Figs.3.16(b) and (c)) implies the pristine state (Figs.3.16(a)) is more conductive, which is consistent with the initial requirement of an electroforming RESET from the LRS observed for these devices. Given that the formation of TiO_2 at one electrode appears to be coupled with the formation of $Ti_xMn_yO_z$ at the opposite electrode, the proposed mechanism would suggest that RS could occur at either polarity, which supports the fact that the RS observed here occurred at the opposite polarity to Ren *et al.*'s devices [2].

In summary, in this chapter, the impact of film morphology on resistivity and RS was also explored; films with completely unobstructed grain boundary paths, aligned along the growth axis, such as those present in Zone 2 films, were shown to be ohmic and less resistive than films containing more irregular paths, such as Zone T and Zone 3 films. Interestingly, the Mn:ZnO devices required an unusual electroforming RESET transition, which is not typically reported in the literature as electroforming SET transitions are often sought after. The attainment of reproducible RS after an electroforming RESET demonstrates that the manner of electrical characterisation can have huge impact on the observed RS, which is not often explored or accounted for in the literature. The EELS investigation of polycrystalline ZnO-based RRAM devices presented here revealed evidence for Mn phase segregation along growth-axis aligned grain boundaries, an effect which has previously been proposed, but not observed, in order to explain the observation of RT-FM in pulsed laser deposited Mn:ZnO [2]. MLLS analysis uncovered the presence

of an unexpected $Ti_xMn_yO_z$ phase, containing chemically reduced Mn that was present beneath and above the top and bottom electrodes respectively. These findings are consistent with the XPS results published by Ren *et al.*, who also found reduced Mn present at the top and bottom of Mn:ZnO devices that exhibited the simultaneous co-switching of resistance and magnetisation.

The growth and dissolution of interfacial oxides were shown to play an important role during RS; these facilitated an exchange of $V_{\ddot{O}}$ between the bulk [Mn:]ZnO layer and the electrochemically active Ti top electrode. Although MLLS fitting allowed for the mapping of these interfacial oxide phases, due to the irregular film morphology and film roughness, further analysis of the interface was limited. To improve our understanding of interfacial chemistry during RS, contributions from morphological and chemical effects must be isolated and evaluated. As seen for the relatively smooth but ohmic ZnO films deposited at lower pressures, the compromise between film roughness and film properties will always be a limiting factor in polycrystalline RRAM devices. However, devices that incorporate highly resistive *single crystal* RS oxides provide an idealised materials system to study RS mechanisms within due to their spatial homogeneity and sharp interfaces. RS in single crystal epitaxial perovskite oxide material, $Pr_{0.48}Ca_{0.52}MnO_3$, is presented in Chapter 4.

Bibliography

[1] M. Laurenti, S. Porro, C. F. Pirri, C. Ricciardi, and A. Chiolerio. Zinc Oxide Thin Films for Memristive Devices: A Review. *Critical Reviews in Solid State and Materials Sciences*, 42(2):153–172, 2017.

[2] S. Ren, J. Dong, W. Chen, L. Zhang, J. Guo, L. Zhang, J. Zhao, and X. Zhao. Study on the oxygen vacancy redistribution and the mechanism of electrical manipulation of ferromagnetism in diluted magnetic oxides. *Journal of Applied Physics*, 118(23):233902, 2015.

[3] X. L. Wang, Q. Shao, C. W. Leung, and A. Ruotolo. Non-volatile reversible switching of the magnetic moment in Mn-doped ZnO films. 301(2013):1–4, 2013.

[4] T. C. Droubay, D. J. Keavney, T. C. Kaspar, S. M. Heald, C. M. Wang, C. A. Johnson, K. M. Whitaker, D. R. Gamelin, and S. A. Chambers. Correlated substitution in paramagnetic Mn^{2+}-doped ZnO epitaxial films. *Physical Review B - Condensed Matter and Materials Physics*, 79(15):1–9, 2009.

[5] U. Ozgur, Y. I. Alivov, C. Liu, A. Teke, M. A. Reshchikov, S. Dogan, V. Avrutin, S. J. Cho, and H. Morkoc. A comprehensive review of ZnO materials and devices. *Journal of Applied Physics*, 98(4):1–103, 2005.

[6] J. Wróbel and J. Piechota. On the structural stability of ZnO phases. *Solid State Communications*, 146(7-8):324–329, 2008.

[7] J. K. Furdyna. Diluted magnetic semiconductors. *Journal of Applied Physics*, 64(4), 1988.

[8] Y. C. Kong, D. P. Yu, B. Zhang, W. Fang, and S. Q. Feng. Ultraviolet-emitting ZnO nanowires synthesized by a physical vapor deposition approach. *Applied Physics Letters*, 78(4):407–409, 2001.

[9] D. C. Reynolds, D. C. Look, and B. Jogai. Optically pumped ultraviolet lasing from ZnO. *Solid State Communications*, 99(12):873–875, 1996.

[10] R. Ondo-Ndong, G. Ferblantier, M. Al Kalfioui, A. Boyer, and A. Foucaran. Properties of RF magnetron sputtered zinc oxide thin films. *Journal of Crystal Growth*, 255(1-2):130–135, 2003.

[11] O. Dimitrov, D. Nesheva, V. Blaskov, I. Stambolova, S. Vassilev, Z. Levi, and V. Tonchev. Gas sensitive ZnO thin films with desired (002) or (100) orientation obtained by ultrasonic spray pyrolysis. *Materials Chemistry and Physics*, 148(3):712–719, 2014.

[12] Y. Wu, R. Fan, and P. Yang. Block-by-Block Growth of Single-Crystalline Si/SiGe Superlattice Nanowires. *Nano Letters*, 2(2):83–86, 2002.

[13] W. I. Park, D. H. Kim, S. W. Jung, and Gyu Chul Yi. Metalorganic vapor-phase epitaxial growth of vertically well-aligned ZnO nanorods. *Applied Physics Letters*, 80(22):4232–4234, 2002.

[14] D. M. Bagnall, Y. F. Chen, Z. Zhu, T. Yao, S. Koyama, M. Y. Shen, and T. Goto. Optically pumped lasing of ZnO at room temperature. *Applied Physics Letters*, 70(17):2230, 1997.

[15] S. Hayamizu, H. Tabata, H. Tanaka, and T. Kawai. Preparation of crystallized zinc oxide films on amorphous glass substrates by pulsed laser deposition. *Journal of Applied Physics*, 80(2):787, 1996.

[16] M. T. Mohammad, A. A. Hashim, and M. H. Al-Maamory. Highly conductive and transparent ZnO thin films prepared by spray pyrolysis technique. *Materials Chemistry and Physics*, 99(2-3):382–387, 2006.

[17] M. Caglar, S. Ilican, Y. Caglar, and F. Yakuphanoglu. Electrical conductivity and optical properties of ZnO nanostructured thin film. *Applied Surface Science*, 255(8):4491–4496, 2009.

[18] S. A. Wolf, D. D. Awschalom, R. A. Buhrman, J. M. Daughton, S. Von Molnár, M. L. Roukes, A. Y. Chtchelkanova, and D. M. Treger. Spintronics: A spin-based electronics vision for the future. *Science*, 294(5546):1488–1495, 2001.

[19] T. Dietl, H. Ohno, F. Matsukura, J. Cibert, and D. Ferrand. Zener Model Description of Ferromagnetism in Zinc-Blende Magnetic Seminconductors. *Science*, 287:1019–1023, 2000.

[20] P. Sharma, A. Gupta, K. V. Rao, F. J. Owens, R. Sharma, R. Ahuja, J. M. O. Guillen, B. Johansson, and G. A. Gehring. Ferromagnetism above room temperature in bulk and transparent thin films of Mn-doped ZnO. *Nature Materials*, 2(10):673–677, 2003.

[21] R. K. Singhal, M. S. Dhawan, S. K. Gaur, S. N. Dolia, Sudhish Kumar, T. Shripathi, U. P. Deshpande, Y. T. Xing, Elisa Saitovitch, and K. B. Garg. Room temperature ferromagnetism in Mn-doped dilute ZnO semiconductor: An electronic structure study using X-ray photoemission. *Journal of Alloys and Compounds*, 477(1-2):379–385, 2009.

[22] R. Khan, Zulfiqar, C. I. Levartoski de Araujo, T. Khan, Muneeb-Ur-Rahman, Zia-Ur-Rehman, A. Khan, B. Ullah, and S. Fashu. Influence of oxygen vacancies on the structural, dielectric, and magnetic properties of (Mn, Co) co-doped ZnO nanostructures. *Journal of Materials Science: Materials in Electronics*, 29(12):9785–9795, 2018.

[23] M. Khalid, M. Ziese, A. Setzer, P. Esquinazi, M. Lorenz, H. Hochmuth, M. Grundmann, D. Spemann, T. Butz, G. Brauer, W. Anwand, G. Fischer, W. A. Adeagbo, W. Hergert, and A. Ernst. Defect-induced magnetic order in pure ZnO films. *Physical Review B - Condensed Matter and Materials Physics*, 80(3):1–5, 2009.

[24] G. H. Mhlongo, K. Shingange, Z. P. Tshabalala, B. P. Dhonge, F. A. Mahmoud, B. W. Mwakikunga, and D. E. Motaung. Room temperature ferromagnetism and gas sensing in ZnO nanostructures: Influence of intrinsic defects and Mn, Co, Cu doping. *Applied Surface Science*, 390:804–815, 2016.

[25] M. K. Satheesan, K. Vani, and V. Kumar. Acceptor-defect mediated room temperature ferromagnetism in (Mn2+, Nb5+) co-doped ZnO nanoparticles. *Ceramics International*, 43(11):8098–8102, 2017.

[26] M. Shatnawi, A. M. Alsmadi, I. Bsoul, B. Salameh, M. Mathai, G. Alnawashi, Gassem M. Alzoubi, F. Al-Dweri, and M. S. Bawa'aneh. Influence of Mn doping on the magnetic and optical properties of ZnO nanocrystalline particles. *Results in Physics*, 6:1064–1071, 2016.

[27] J.M.D. Coey. Dilute ferromagnetic oxides. *Local-Moment Ferromagnets. Series title "Lect. Notes Phys."*, 678:185–198, 2005.

[28] H. Y. Peng, G. P. Li, J. Y. Ye, Z. P. Wei, Z. Zhang, D. D. Wang, G. Z. Xing, and T. Wu. Electrode dependence of resistive switching in Mn-doped ZnO: Filamentary versus interfacial mechanisms. *Applied Physics Letters*, 96(19):19–21, 2010.

[29] Y. Chao Yang, F. Pan, and F. Zeng. Bipolar resistance switching in high-performance Cu/ZnO:Mn/Pt nonvolatile memories: active region and influence of Joule heating. *New Journal of Physics*, 12(2):023008, 2010.

[30] Y. Han, K. Cho, S. Park, and S. Kim. The Effects of Mn-doping and Electrode Material on the Resistive Switching Characteristics of ZnO$_x$S$_{1-x}$ Thin Films on Plastic. *Transactions on Electrical and Electronic Materials*, 15(1):24–27, 2014.

[31] S. X. Ren, G. W. Sun, J. Zhao, J. Y. Dong, Y. Wei, Z. C. Ma, X. Zhao, and W. Chen. Electric field-induced magnetic switching in Mn:ZnO film. *Applied Physics Letters*, 104(23), 2014.

[32] B. Arndt, F. Borgatti, F. Offi, M. Phillips, P. Parreira, T. Meiners, S. Menzel, K. Skaja, G. Panaccione, D. A. Maclaren, R. Waser, and Regina Dittmann. Spectroscopic Indications of Tunnel Barrier Charging as the Switching Mechanism in Memristive Devices. *Advanced Functional Materials*, 1702282, 2017.

[33] W. Y. Chang, Y. C. Lai, T. B. Wu, S. F. Wang, F. Chen, and M. J. Tsai. Unipolar resistive switching characteristics of ZnO thin films for nonvolatile memory applications. *Applied Physics Letters*, 92(2):022110 (1–3), 2008.

[34] H. W. Huang, C. F. Kang, F. I. Lai, J. H. He, S. J. Lin, and Y. L. Chueh. Stability scheme of ZnO-thin film resistive switching memory: influence of defects by controllable oxygen pressure ratio. *Nanoscale research letters*, 8(1):483, 2013.

[35] D. Ielmini, R. Bruchhaus, and R. Waser. Thermochemical resistive switching: Materials, mechanisms, and scaling projections. *Phase Transitions*, 84(7):570–602, 2011.

[36] R. Waser, R. Dittmann, G. Staikov, and K. Szot. Redox-Based Resistive Switching Memories - Nanoionic Mechanisms, Prospects, and Challenges. *Advanced Materials*, 21(25-26):2632–2663, 2009.

[37] C. H. Huang, J. S. Huang, C. C. Lai, H. W. Huang, S. J. Lin, and Y. L. Chueh. Manipulated transformation of filamentary and homogeneous resistive switching on ZnO thin film memristor with controllable multistate. *ACS Applied Materials and Interfaces*, 5(13):6017–6023, 2013.

[38] J. Zhao, F. Liu, J. Sun, and H. Huang. Low power consumption bipolar resistive switching characteristics of ZnO-based memory devices. *Chinese Optics*, 10(1):1–4, 2012.

[39] W. Y. Chang, C. S. Peng, C. H. Lin, J. M. Tsai, F. C. Chiu, and Yu-Lun Chueh. Polarity of Bipolar Resistive Switching Characteristics in ZnO Memory Films. *Journal of The Electrochemical Society*, 158(9), 2011.

[40] N. Xu, L. F. Liu, X. Sun, C. Chen, Y. Wang, D. D. Han, X. Y. Liu, R. Q. Han, J. F. Kang, and B. Yu. Bipolar switching behavior in TiN / ZnO / Pt resistive nonvolatile memory with fast switching and long. *Semiconductor Science and Technology*, 2008.

[41] F. C. Chiu, P. W. Li, W. Y. Chang, W. W. Zhuang, W. Pan, B. D. Ulrich, J. J. Lee, L. Stecker, A. Burmaster, D. R. Evans, S. T. Hsu, M. Tajiri, A. Shimaoka, K. Inoue, T. Naka, N. Awaya, K. Sakjyarma, Y. Wang, S. Q. Liu, N. J. Wu, A. Ignatiev, H. Akinaga, H. Shima, T. Zhang, X. Zhang, L. Ding, W. Zhang, R. Waser, R. Dittmann, G. Staikov, K. Szot, M. Colle, M. Buchel, D. M. de Leeuw,

S. H. Jo, K. H. Kim, W. Lu, I. G. Baek, M. S. Lee, S. Seo, M. J. Lee, D. H. Seo, D. S. Suh, J. C. Park, S. O. Park, H. S. Kim, I. K. Yoo, U. I. Chung, J. T. Moon, A. Umar, M. Moya, A. P. Samantilleke, M. Mollar, B. Mari, H. Morkoc, U. Ozgur, M. Villafuerte, S. P. Heluani, G. Juárez, G. Simonelli, G. Braunstein, S. Duhalde, W. Y. Chang, Y. C. Lai, T. B. Wu, S. F. Wang, F. Chen, M. J. Tsai, N. Xu, L. Liu, X. Sun, X. Liu, D. Han, Y. Wang, R. Han, J. Kang, B. Yu, S. Kim, H. Moon, D. Gupta, S. Yoo, Y. K. Choi, Y. Zhang, C. T. Lee, Y. C. Yang, F. Pan, Q. Liu, M. Liu, F. Zeng, Z. Ji, Q. Mao, W. Ke, S. Lee, H. Kim, J. Park, K. Yong, J. Y. M. Lee, F. C. Chiu, P. C. Juan, A. B. Djurisic, Y. H. Leung, M. Sze, M. Nakano, A. Tsukazaki, R. Y. Gunji, K. Ueno, A. Ohtomo, T. Fukumura, M. Kawasaki, D. Ielmini, F. Nardi, and C. Cagli. Reliability characteristics and conduction mechanisms in resistive switching memory devices using ZnO thin films. *Nanoscale Research Letters*, 7(1):178, 2012.

[42] H. L. Ma, Z. Q. Wang, H. Y. Xu, L. Zhang, X. N. Zhao, M. S. Han, J. G. Ma, and Y. C. Liu. Coexistence of unipolar and bipolar modes in Ag/ZnO/Pt resistive switching memory with oxygen-vacancy and metal-Ag filaments. *Chinese Physics B*, 25(12), 2016.

[43] R. Huang, K. Sun, K. S. Kiang, K. A. Morgan, and C. H. De Groot. Forming-free resistive switching of tunable ZnO films grown by atomic layer deposition. *Microelectronic Engineering*, 161:7–12, 2016.

[44] N. M. Muhammad, N. Duraisamy, K. Rahman, H. W. Dang, J. Jo, and K. H. Choi. Fabrication of printed memory device having zinc-oxide active nano-layer and investigation of resistive switching. *Current Applied Physics*, 13(1):90–96, 2013.

[45] C. N. Peng, C. W. Wang, T. C. Chan, W. Y. Chang, Y. C. Wang, H. W. Tsai, W. W. Wu, L. J. Chen, and Y. L. Chueh. Resistive switching of Au/ZnO/Au resistive memory: An in situ observation of conductive bridge formation. *Nanoscale Research Letters*, 7(1):1–6, 2012.

[46] Y. Huang, Z. Shen, Y. Wu, X. Wang, S. Zhang, X. Shi, and H. Zeng. Amorphous ZnO based resistive random access memory. *RSC Advances*, 6(22):17867–17872, 2016.

[47] Y. C. Yang, F. Pan, Q. Liu, M. Liu, and F. Zeng. Fully room temperature fabricated nonvolatile resistive memory for ultrafast and high density memory application. *Nano Letters*, 9(4):1636, 2009.

[48] F. M. Simanjuntak, O. K. Prasad, D. Panda, C. A. Lin, T. L. Tsai, K. H. Wei, and T.Y. Tseng. Impacts of Co doping on ZnO transparent switching memory device characteristics. *Applied Physics Letters*, 108(18), 2016.

[49] Cloud Nyamhere. *Characterization of process and radiation induced defects in Si and Ge using conventional deep level transient spectroscopy (DLTS) and Laplace-DLTS*. PhD thesis, University of Pretoria, 2009.

[50] V. R. Shinde, T. P. Gujar, C. D. Lokhande, R. S. Mane, and S. H. Han. Mn doped and undoped ZnO films: A comparative structural, optical and electrical properties study. *Materials Chemistry and Physics*, 96(2-3):326–330, 2006.

[51] J. Han, A. M. R. Senos, and P. Q. Mantas. Deep donors in polycrystalline Mn-doped ZnO. *Materials Chemistry and Physics*, 75(1-3):117–120, 2002.

[52] G. Rijnders and D. H. A. Blank. Growth Kinetics During Pulsed Laser Deposition. In *Pulsed Laser Deposition of Thin Films: Applications-Led Growth of Functional Materials*, chapter 8, pages 177–190. John Wiley & Sons, Inc., 2007.

[53] P. Parreira, G. W. Paterson, S. McVitie, and D. A. MacLaren. Stability, bistability and instability of amorphous ZrO2 resistive memory devices. *Journal of Physics D: Applied Physics*, 49(9):095111, 2016.

[54] J. A. Thornton. High rate thick film growth. *Annual Reviews in Materials Science*, 7:239–260, 1977.

[55] H. Kato, M. Sano, K. Miyamoto, and T. Yao. Effect of O/Zn flux ratio on crystalline quality of ZnO films grown by plasma-assisted molecular beam epitaxy.

Japanese Journal of Applied Physics, Part 1: Regular Papers and Short Notes and Review Papers, 42(4B):2241–2244, 2003.

[56] H. N. Riise, V. S. Olsen, A. Azarov, A. Galeckas, T. N. Sky, B. G. Svensson, and E. Monakhov. Local homoepitaxy of zinc oxide thin films by magnetron sputtering. *Thin Solid Films*, 601:18–21, 2016.

[57] N. Kaiser. Review of the fundamentals of thin-film growth. *Applied Optics*, 41(16):3053–3060, 2002.

[58] P. B. Barna and M. Adamik. Fundamental structure forming phenomena of polycrystalline films and the structure zone models. *Thin Solid Films*, 317(1-2):27–33, 1998.

[59] R. Messier and J. E. Yehoda. Geometry of thinfilm morphology Geometry of thin-film morphology. 58(3739), 1985.

[60] C. R. M. Grovenor, H. T. G. Hentzells, and D. A. Smith. The Development of Grain Structure During Growth of Metallic Films. *Acta Metallica*, 32(5):773–781, 1984.

[61] G. K Hubler and D. B. Chrisey. *Pulsed laser deposition of thin films*. New York: J. Wiley, 1994.

[62] D. H. A. Blank, G. J. Rijnders, G. Koster, and H. Rogalla. In-situ monitoring during pulsed laser deposition using RHEED at high pressure. *Applied Surface Science*, 127-129:633–638, 1998.

[63] I. Petrov, P. B. Barna, L. Hultman, and J. E. Greene. Microstructural evolution during film growth. *Journal of Vacuum Science & Technology A: Vacuum, Surfaces, and Films*, A 21(5):117–128, 2003.

[64] A. T. Vai, V. L. Kuznetsov, H. Jain, D. Slocombe, N. Rashidi, M. Pepper, and P. P. Edwards. The transition to the metallic state in polycrystalline n-type doped ZnO thin films. *Zeitschrift fur Anorganische und Allgemeine Chemie*, 640(6):1054–1062, 2014.

[65] S. L. Ou, F. P. Yu, and D. S. Wuu. Transformation from Film to Nanorod via a Sacrifical Layer: Pulsed Laser Deposition of ZnO for Enhancing Photodetector Performance. *Scientific Reports*, 7(1):1–11, 2017.

[66] S. Im, B. J. Jin, and S. Yi. Ultraviolet emission and microstructural evolution in pulsed-laser-deposited ZnO films. *Journal of Applied Physics*, 87:4558–4561, 2000.

[67] S. Choopun, R. D. Vispute, W. Noch, A. Balsamo, R. P. Sharma, T. Venkatesan, A. Iliadis, and D. C. Look. Oxygen pressure-tuned epitaxy and optoelectronic properties of laser-deposited ZnO films on sapphire Oxygen pressure-tuned epitaxy and optoelectronic properties of laser-deposited ZnO films on sapphire. *Applied Physics Letters*, 75(25):3947–3949, 1999.

[68] R. D. Vispute, V. Talyansky, Z. Trajanovic, S. Choopun, M. Downes, R. P. Sharma, T. Venkatesan, M. C. Woods, R. T. Lareau, K. A. Jones, and a a Iliadis. High quality crystalline ZnO buffer layers on sapphire (001) by pulsed laser deposition for III-V nitrides. *Applied Physics Letters*, 70(20):2735–2737, 1997.

[69] J. L. Zhao, X. M. Li, J. M. Bian, W. D. Yu, and X. D. Gao. Structural, optical and electrical properties of ZnO films grown by pulsed laser deposition (PLD). *Journal of Crystal Growth*, 276(3):507–512, 2005.

[70] E. Hasabeldaim, O. M. Ntwaeaborwa, R. E. Kroon, D. E. Motaung, E. Coetsee, and H. C. Swart. Effect of PLD growth atmosphere on the physical properties of ZnO:Zn thin films. *Optical Materials*, 74:76–85, 2017.

[71] B. Weng, J. Wang, P. Larson, and Y. Liu. Growth process optimization of ZnO thin film using atomic layer Deposition. *Materials Research Express*, 3(12), 2016.

[72] Walter Water and Sheng-Yuan Chu. Physical and structural properties of ZnO sputtered films. *Materials Letters*, 55(1-2):67–72, 2002.

[73] S. C. Her and T. C. Chi. Temperature Effect on Optical and Electrical Properties of ZnO Films. *Asian Journal of Chemistry*, 27(7):2619–2623, 2015.

[74] C. H. Zhai, R. J. Zhang, X. Chen, Y. X. Zheng, S. Y. Wang, J. Liu, N. Dai, and L. Y. Chen. Effects of Al Doping on the Properties of ZnO Thin Films Deposited by Atomic Layer Deposition. *Nanoscale Research Letters*, 11(1):407, 2016.

[75] E. A. Martín-Tovar, R. Castro-Rodríguez, L. G. Daza, J. Méndez-Gamboa, R. Medina-Esquivel, I. Perez-Quintana, and A. Iribarren. Structural and optical properties of ZnO thin films prepared by laser ablation using target of ZnO powder mixture with glue. *Bulletin of Materials Science*, 40(3):467–471, 2017.

[76] M. G. Tsoutsouva, C. N. Panagopoulos, D. Papadimitriou, I. Fasaki, and M. Kompitsas. ZnO thin films prepared by pulsed laser deposition. *Materials Science and Engineering B: Solid-State Materials for Advanced Technology*, 176(6):480–483, 2011.

[77] K. Ellmer, A. Klein, and B. Rech. *Transparent Conductive Zin Oxide Basic and Applications in Thin Film Solar Cells*. Springer, 2008.

[78] S. Masuda, K. Kitamura, Y. Okumura, S. Miyatake, H. Tabata, and T. Kawai. Transparent thin film transistors using ZnO as an active channel layer and their electrical properties. *Journal of Applied Physics*, 93(3):1624–1630, 2003.

[79] P. Tiwari, X. D. Wu, S. R. Foltyn, M. Q. Le, I. H. Campbell, R. C. Dye, and R. E. Muenchausen. Epitaxial $YBa_2Cu_3O_{7-\delta}$ thin films on $SrRuO_3$/Pt/MgO, volume = 64, year = 1994. *Applied Physics Letters*, (5):634–636.

[80] J. B. Franklin, B. Zou, P. Petrov, D. W. McComb, M. P. Ryan, and M. A. McLachlan. Optimised pulsed laser deposition of ZnO thin films on transparent conducting substrates. *Journal of Materials Chemistry*, 21(22):8178, 2011.

[81] N. Fujimura, T. Nishihara, S. Goto, J. Xu, and T. Ito. Control of preferred orientation for ZnOx films: control of self-texture. *Journal of Crystal Growth*, 130(1-2):269–279, 1993.

[82] X. Q. Wei, B. Y. Man, M. Liu, C. S. Xue, H. Z. Zhuang, and C. Yang. Blue luminescent centers and microstructural evaluation by XPS and Raman in ZnO

thin films annealed in vacuum, N2 and O2. *Physica B: Condensed Matter*, 388(1-2):145–152, 2007.

[83] H. B. Fan, S. Y. Yang, P. F. Zhang, H. Y. Wei, X. L. Liu, C. M. Jiao, Q. S. Zhu, Y. H. Chen, and Z. G. Wang. Investigation of Oxygen Vacancy and Interstitial Oxygen defects in ZnO films by PL and XPS. *Chinese Physics Letters*, 24(7):2108, 2007.

[84] F. Zhuge, S. Peng, C. He, X. Zhu, X. Chen, Y. Liu, and R. W. Li. Improvement of resistive switching in Cu/ZnO/Pt sandwiches by weakening the randomicity of the formation/rupture of Cu filaments. *Nanotechnology*, 22(27), 2011.

[85] Y. C. Yang, F. Pan, Q. Liu, M. Liu, and F. Zeng. Fully room-temperature-fabricated nonvolatile resistive memory for ultrafast and high-density memory application. *Nano Letters*, 9(4):1636–1643, 2009.

[86] B. Y. Man, H. Z. Xi, C. S. Chen, M. Liu, and J. Wei. XRD study on the effect of the deposition condition on pulsed laser deposition of ZnO films. *Central European Journal of Physics*, 6(3):643–647, 2008.

[87] L. D. Bozano, B. W. Kean, V. R. Deline, J. R. Salem, and J. C. Scott. Mechanism for bistability in organic memory elements. *Applied Physics Letters*, 84(4):607–609, 2004.

[88] J. G. Simmons and R. R. Verderber. New Conduction and Reversible Memory Phenomena in Thin Insulating Films. *Proceedings of the Royal Society A: Mathematical, Physical and Engineering Sciences*, 301(1464):77–102, 1967.

[89] T. J. Penfold, J. Szlachetko, F. G. Santomauro, A. Britz, W. Gawelda, G. Doumy, A. M. March, S. H. Southworth, J. Rittmann, R. Abela, M. Chergui, and C. J. Milne. Revealing hole trapping in zinc oxide nanoparticles by time-resolved X-ray spectroscopy. *Nature Communications*, 9(1):1–9, 2018.

[90] S. J. Pearton, D. P. Norton, K. Ip, Y. W. Heo, and T. Steiner. Recent progress in processing and properties of ZnO. *Superlattices and Microstructures*, 34(1-2):3–32, 2003.

[91] T. S. Herng, M. F. Wong, D. Qi, J. Yi, A. Kumar, A. Huang, F. C. Kartawidjaja, S. Smadici, P. Abbamonte, C. Sánchez-Hanke, S. Shannigrahi, J. M. Xue, J. Wang, Y. P. Feng, A. Rusydi, K. Zeng, and J. Ding. Mutual ferromagnetic-ferroelectric coupling in multiferroic copper-doped ZnO. *Advanced Materials*, 23(14):1635–1640, 2011.

[92] F. C. Chiu. A review on conduction mechanisms in dielectric films. *Advances in Materials Science and Engineering*, 2014(578168), 2014.

[93] A. Schulman, L. F. Lanosa, and C. Acha. Poole-Frenkel effect and Variable-Range Hopping conduction in metal/YBCO resistive switching devices. *Journal of Applied Physics*, 118(044511):1–16, 2015.

[94] E. W. Lim and R. Ismail. Conduction Mechanism of Valence Change Resistive Switching Memory: A Survey. *Electronics*, 4(3):586–613, 2015.

[95] F. Gul and H. Efeoglu. Bipolar resistive switching and conduction mechanism of an Al/ZnO/Al-based memristor. *Superlattices and Microstructures*, 101:172–179, 2017.

[96] D. Cheon, M. Son, M. H. Ham, and W. Lee. Resistive switching in an amorphous ZnO dielectric film prepared on a Ga-doped ZnO transparent electrode. *RSC Advances*, 6(106):103864–103871, 2016.

[97] H. Schroeder. Poole-Frenkel-effect as dominating current mechanism in thin oxide films - An illusion?! *Journal of Applied Physics*, 117(21), 2015.

[98] W.-Y. Chang, H.-W. Huang, W.-T. Wang, C.-H. Hou, Y.-L. Chueh, and J.-H. He. High Uniformity of Resistive Switching Characteristics in a Cr/ZnO/Pt Device. *Journal of the Electrochemical Society*, 159(3):29–32, 2012.

[99] H. Lv, X. Xu, H. Liu, R. Liu, Q. Liu, W. Banerjee, H. Sun, S. Long, L. Li, and M. Liu. Evolution of conductive filament and its impact on reliability issues in oxide-electrolyte based resistive random access memory. *Scientific reports*, 5:7764, 2015.

[100] Z. L. Tseng, P. C. Kao, M. F. Shih, H. H. Huang, J. Y. Wang, and S. Y. Chu. Electrical bistability in hybrid ZnO nanorod/polymethylmethacrylate heterostructures. *Applied Physics Letters*, 97(21), 2010.

[101] M. Younas, C. Xu, M. Arshad, L. P. Ho, S. Zhou, F. Azad, M. J. Akhtar, S. Su, W. Azeem, and F. C. C. Ling. Reversible Tuning of Ferromagnetism and Resistive Switching in ZnO/Cu Thin Films. *ACS Omega*, 2(12):8810–8817, 2017.

[102] E. Stoyanov, F. Langenhorst, and G. Steinle-Neumann. The effect of valence state and site geometry on Ti L3,2 and O K electron energy-loss spectra of TixOy phases. *American Mineralogist*, 92(4):577–586, 2007.

[103] R. D. Leapman, L. A. Grunes, and P. L. Fejes. Study of the L-2,3 edges in the 3d transition metals and their oxides by electron-energy-loss spectroscopy with comparisons to theory. *Physical Review B*, 26(1):614, 1982.

[104] W.M. Haynes. *CRC Handbook of Chemistry and Physics, 93rd Edition*. 100 Key Points. Taylor & Francis, 2012.

[105] B. Nasr, S. Dasgupta, D. Wang, N. Mechau, R. Kruk, and H. Hahn. Electrical resistivity of nanocrystalline Al-doped zinc oxide films as a function of Al content and the degree of its segregation at the grain boundaries. *Journal of Applied Physics*, 108(10), 2010.

[106] M. Rajagopalan, M. A. Tschopp, and K. N. Solanki. Grain boundary segregation of interstitial and substitutional impurity atoms in alpha-iron. *Journal of Minerals, Metals and Materials Society*, 2013.

[107] T. Fukumura, Z. Jin, A. Ohtomo, H. Koinuma, and M. Kawasaki. An oxide-diluted magnetic semiconductor: Mn-doped ZnO. *Applied Physics Letters*, 75(21):3366–3368, 1999.

[108] M. M. Mandurah, K. C. Saraswat, C. R. Helms, and T. I. Kamins. Dopant segregation in polycrystalline silicon. *Journal of Applied Physics*, 51(11):5755–5763, 1980.

[109] P. L. Potapov, K. Jorissen, D. Schryvers, and D. Lamoen. Effect of charge transfer on EELS integrated cross sections in Mn and Ti oxides. *Physical Review B - Condensed Matter and Materials Physics*, 70(4):1–10, 2004.

[110] D. B. Loomer, T. A. Al, L. Weaver, and S. Cogswell. Manganese valence imaging in Mn minerals at the nanoscale using STEM-EELS. *American Mineralogist*, 92(1):72–79, 2007.

[111] H. Tan, J. Verbeeck, A. Abakumov, and G. Van Tendeloo. Oxidation state and chemical shift investigation in transition metal oxides by EELS. *Ultramicroscopy*, 116:24–33, 2012.

[112] H. K. Schmid and W. Mader. Oxidation states of Mn and Fe in various compound oxide systems. *Micron*, 37(5):426–432, 2006.

[113]

[114] J. Richter, A. Braun, A. S. Harvey, P. Holtappels, T. Graule, and L. J. Gauckler. Valence changes of manganese and praseodymium in $Pr_{1-x}Sr_xMn_{1-y}In_yO_3\delta$ perovskites upon cation substitution as determined with XANES and ELNES. *Physica B: Condensed Matter*, 403:87–94, 2008.

CHAPTER 4

Crystalline $Pr_{0.48}Ca_{0.52}MnO_3$ Tunnel Oxide RRAM device

In Chapter 3, polycrystalline ZnO and Mn:ZnO was fabricated in a classic MOM heterostructure and exhibited bipolar, filamentary RS consistent with the VCM redox mechanism outlined in Chapter 1. In this chapter, a ternary, *crystalline* complex perovskite oxide material, $Pr_{1-x}Ca_xMnO_3$, that was fabricated by collaborators in Jülich, is studied. $Pr_{1-x}Ca_xMnO_3$ is a well-known RS material; in Sawa *et al.*'s prominent 2008 publication, it was used to elucidate the interface-VCM RS mechanism, a switching model that is dependent on the $V_{\ddot{O}}$-mediated formation and modulation of an interfacial oxide (at the oxide/metal interface) that acted as Schottky barrier [1]. The study presented here investigates a $Pr_{0.48}Ca_{0.52}MnO_3$ device that incorporates an Yttria-stabilised Zirconia (Y_2O_3-ZrO_2) tunnel-oxide layer for the enhanced control of RS characteristics. As outlined in Chapter 1 in section 1.2.5, the literature suggests that for tunnel-oxide RS devices, the tunnel-barrier height governs the resistance state and is modulated by the $V_{\ddot{O}}$-concentration [2]. This means that the most intriguing aspect of the crystalline perovskite oxide/tunnel-oxide RS heterostructure presented here is the interplay between Schottky- and tunnel-barrier effects, both of which have been shown to be dependent on $V_{\ddot{O}}$-electromigration. To assess the RS mechanism exhibited by this more complex device heterostructure, STEM-EELS was used to identify the spatial extent of *electrochemical* differences between LRS- and HRS-programmed devices. In addition, to understand

changes to the *electronic* properties of the active layers, collaborators probed programmed devices using HAXPES, a surface-sensitive technique, which was described in Section 2.8. Analysis of the spectroscopic results confirmed that RS was mediated by the exchange of $V_{\ddot{O}}$ across the tunnel-oxide/$Pr_{0.48}Ca_{0.52}MnO_3$ interface and that this electromigration resulted in the electrostatic modulation of the tunnel-barrier height, which ultimately governed the overall resistance state of the device during switching.

4.1 Resistive Switching in Crystalline Perovskite Oxides

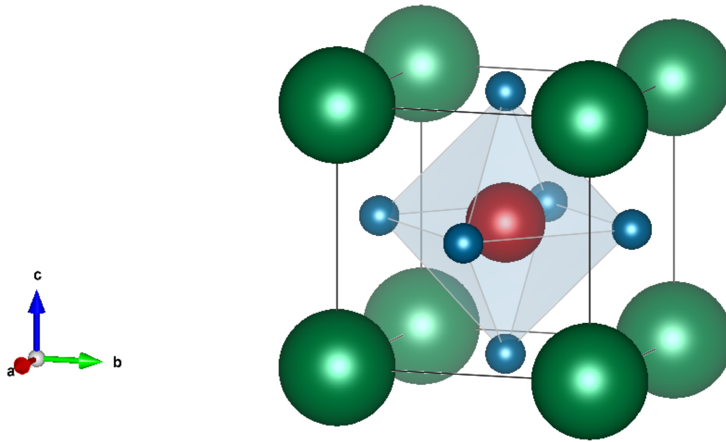

Figure 4.1: *Diagram of an $Pr_xCa_{1-x}MnO_3$ perovskite oxide cubic cell. Here, Pr^{3+} and Ca^{2+} cations are shown in green, Mn cations are shown in red, and oxygen anions are shown in blue. Pr and Ca cations form the ionic lattice, which is represented by the black lines.*

Perovskite oxide have general formula ABO_3 and adopt the structure displayed in Fig.4.1. Here, the A-site cation (shown in green) is a rare or alkali-earth metal and has 12-fold coordination with oxygen (shown in blue) and the B-site cation (shown in red) is a transition metal and has 6-fold coordination with oxygen [3, 4]. Fig. 4.1 emphasises the formation of an oxygen octahedra, which is formed at the B-site, however, although it is not shown in Fig.4.1, the A- and B-site cations form a cubic ionic lattice. The ABO_3 structure shown in Fig.4.1 can incorporate foreign substitutional A- or B-site cations and, in addition, can also support $V_{\ddot{O}}$ [3]. In RRAM research, perovskite oxides are of particular interest due to their stable crystalline structure. As single crystal devices are often used as an idealised physical model, the mechanisms of RS can more

readily be ascribed to the geometric and electronic structure of the active material. Deposition techniques such as PLD, which is described in Section 2.2, have been vital to the growth of this field as they allow researchers to fabricate epitaxial, single crystal, multilayered heterostructures of well-defined stoichiometry with atomic precision. Considering the $V_{\ddot{O}}$-mediated RS mechanisms presented in Chapter 1 in section 1.2.2, fine control over oxide stoichiometry allows one to precisely engineer RS devices to reduce variability and/or enhance RS performance. Further enhancement can be achieved via the deposition of dedicated oxides between an electrode and active RS layer, which are described in Chapter 1 in section1.2.6; these not only act as O^{2-}-reservoirs from which O^{2-} anions can be pushed and pulled during VCM RS, but can also provide additional functionality. For instance, the device presented in this chapter incorporates a dedicated yttria-stabilised zirconia (YSZ) *tunnel barrier*; this functional oxide was included as the literature shows that it can be used to tune device operating currents, an effect which is further described in section 4.3. Perovskite oxide crystals exhibit a multitude of tuneable electrical and magnetic properties including colossal magnetoresistance, ferroelectricity and superconductivity [5–10], making them favourable for applications in multifunctional RS devices in which multiple properties exhibit switching behaviour.

The earliest observations of RS in crystalline perovskite oxides attributed the switching effect to a charge-injection-induced metal-insulator transition [10–12]. In this *electronic* RS model, the oxide layer was described as a structure consisting of multiple metallic domains, and an electric-field could induce the tunnelling of charge carriers through these domains towards a biased electrode [12]. However, since then, a large number of researchers that have undertaken spectroscopic analyses of perovskite oxide RRAM devices have attributed RS in these systems to *ionic* effects, specifically bipolar $V_{\ddot{O}}$-mediated VCM RS [1, 11, 13]. Typically, this class of materials undergoes area-scaling, interface-homogeneous VCM RS, from which a gradual, bipolar IV curve is acquired, as depicted in Chapter 1 in Fig.1.15 [13–18]. Depending on the type of interfacial oxides employed in the heterostructure, perovskite oxides can display electroforming-free interface-type VCM RS; as illustrated in Fig.1.10, this means that, in comparison to devices that do require electroforming, interface VCM perovskite oxides have the potential to display highly reproducible RS at low voltages. To fully understand the mechanisms

that permit RS in a tunnel oxide YSZ-PCMO device, programmed devices and their corresponding lamellae were probed using HAXPES and EELS, which, respectively, are particularly sensitive to electronic and chemical variations within the sample.

4.1.1 Resistive Switching in Crystalline $Pr_{1-x}Ca_xMnO_3$

As noted earlier, in perovskite oxides, both the A- and B-site cations can be partially substituted with dopants to manipulate the conduction characteristics of the material; in the case of $Pr_{1-x}Ca_xMnO_3$ (PCMO), Ca^{2+} is substituted for A-site Pr^{3+}, and both of these transfer their outer electrons to complete the O-2p shell. Any excess electrons/holes present introduced due to A-site doping are primarily located in the 3d shell of the B-site transition metal cation, which, in this context, means that the valence state of the B-site Mn is controlled by the level of A-site Ca^{2+} doping [19]. A-site doping also leads to the production of $V_{\ddot{O}}$ in the material to maintain overall charge neutrality [20, 21], which is an important parameter to consider for $V_{\ddot{O}}$-mediated VCM RS. For instance, in 2009, Asanuma *et al.* investigated the RS performance of a $Pt/Pr_{1-x}Ca_xMnO_3/Ti$ structure, where x ranged between 0 and 1 (which correspond to the presence of Mn^{3+} and Mn^{4+} respectively), and showed that for all values of x an interfacial TiO_y layer formed via the reduction of PCMO at the strongly reducing Ti electrode; this redox reaction generated an abundance of $V_{\ddot{O}}$ in the PCMO which then facilitated VCM RS [22]. However, their study also showed that whilst $V_{\ddot{O}}$-migration between the TiO_y and the reduced PCMO mediated RS, the effect of $V_{\ddot{O}}$ on the carrier concentration must also be considered. For instance, in the literature, it has been shown that A-site doping can be used to tune the dominant carrier-type in perovskite oxides: Asanuma *et al.* found that for $x < 0.8$, holes dominated conduction in their PCMO, whilst for ≥ 0.8, electrons dominated instead [22]. In their work, RS was only observed for *p*-type hole-carrier dominated PCMO in which conduction is known to occur via polaron hopping along mixed valence state Mn-O-Mn bonds [23–25]. Given that in PCMO, the presence of $V_{\ddot{O}}$ decreases the Mn valence state and in doing so increases the electron-carrier concentration, the field-induced accumulation of $V_{\ddot{O}}$ in the PCMO at the interface acted as a barrier to polaron hopping, allowing the device to switch to the HRS. In contrast, RS was not observed for the *n*-type electron-carrier

because the accumulation of $V_{\ddot{O}}$ in the reduced PCMO caused no significant change to the carrier concentration. Finally, Asanuma *et al.* showed that the resistance ratio (LRS:HRS) varied with x and reached a maximum of 30:1 between $x = 0.4 - 0.5$, which was attributed there being a relatively large concentration of hole-carriers present in comparison to that found in lighter or heaving Ca^{2+}-doping. In this chapter, $PrMnO_3$ was Ca-doped at comparable levels ($x = 0.52$) to produce *p*-type $Pr_{0.48}Ca_{0.52}MnO_3$ with nominal valence states Pr^{3+}, Ca^{2+} and $Mn^{3.5+}$ [22].

In a 2014 publication, Herpers *et al.* studied RS in $Pr_{1-x}Ca_xMnO_3$ (with $x = 0.5$) in a PLD epitaxial $SrRuO_3$(SRO, 30nm)/PCMO(20nm)/Ti(4nm) device, where SRO served as an inert, ohmic, crystalline bottom electrode, and Ti served as a high work-function top electrode. Due to $V_{\ddot{O}}$-migration, the device was expected to form interfacial layers (shown in emboldened text) at the insulator/electrode interface such that the heterostructure would become SRO/$PCMO_3$/$\mathbf{PCMO}_{3-\delta}$/$\mathbf{TiO}_{\delta}$/Ti. Given the B-site oxygen octahedra formed in perovskite oxides, which in the case of PCMO is MnO_6, Herpers *et al.* expected to observe measurable changes in the Mn valence state in the PCMO in addition to changes in Ti valence between metallic and oxidised TiO_δ as a result of $V_{\ddot{O}}$-migration. To probe the redox activity of Ti and Mn at the PCMO/Ti interface (buried $\sim 10nm$ below the surface) as a function of switching, HAXPES was employed [26]. This technique revealed that the aforementioned interfacial layers were indeed formed during Ti deposition, and would later thicken during electroforming, when the Ti top electrode was positively biased. They identified four distinct resistive states; in order of magnitude, these were the pristine state, the LRS, the HRS, and the electroformed state. Of these, only the LRS and HRS were reversible. In each resistive state the Ti-2p spectrum included contributions from oxidised Ti^{4+}, and metallic Ti^0, where intensity of the Ti^{4+}(Ti^0) component increased(decreased) with increasing resistivity, consistent with the previous literature which showed that the formation of interfacial TiO_δ and reduced $PCMO_{3-\delta}$ reduces hole-carrier conduction. In addition, the O-1s spectra were shown to be the sum of contributions from the TiO_δ and PCMO layers; with increasing resistive state, the intensity of the TiO_δ component decreased as the PCMO component increased. This provided evidence for the *reversible* exchange of $V_{\ddot{O}}$ between the TiO_δ and $PCMO_{3-\delta}$ during RS [26]. Similarly, in an

in-situ, STEM-EELS study on a polycrystalline PCMO RRAM device, Baek *et al.* probed a TiN/$\mathbf{TiO_{\delta}N}$/$PCMO_{3-\delta}$ interface and showed that the interfacial oxide underwent measurable, reversible changes in thickness (of the order of a few nm) under an applied field during RS [27]. By comparing the Mn-L_3 peak position, and the Mn-L_3,L_2 white-line ratio, this study showed that the oxygen-deficient PCMO (closest to the interfacial oxide) contained reduced Mn, whilst further into the PCMO (away from the interfacial oxide), the Mn was oxidised. Despite showing the spatial extent of the variation in Mn valence state, no comparison of the Mn valence state between the LRS and HRS was made. In this regard, Herpers *et al.* provided some insight; they found that with increasing resistance, the subtle emergence of a low-energy shoulder on the Mn-2p doublet indicated a greater presence of Mn^{3+}, which was consistent with the suppression of polaron hopping due to the presence of $V_{\ddot{O}}$ and the reduction of Mn. However, no significant or reproducible change to the Mn valence state was observed between the LRS and HRS. This was attributed to the limited probing depth achievable using HAXPES, which suggests that spectroscopic techniques with larger probing depths must be used to observe the presumably subtle changes in Mn valence state that occur during VCM RS [26].

Both studies compared their IV curves with various conduction mechanism models. For the TiN/$\mathbf{TiO_{\delta}N}$/$PCMO_{3-\delta}$ polycrystalline device, a linear fit best described the data when $\ln(I/V)$ was plotted against $V^{1/2}$, indicating that Poole-Frenkel conduction was predominant, in which charge carriers hopped along defect sites within the interfacial oxide, $TiO_{\delta}N$, and that this interfacial layer governed the resistance state of the device overall [27]. In contrast, Herpers *et al.* proposed that a *combination* of conduction mechanisms characterised each resistance state. Using impedence spectroscopy, they showed that the interfacial oxide, TiO_{δ}, acted as a tunnel barrier, whilst conduction in the adjacent PCMO was dominated by field-enhanced polaron hopping [26]. In their model, for thick TiO_{δ} and oxygen-stoichiometric PCMO, polaron hopping was predominant and the device was in the LRS. However, for thin TiO_{δ} a non-stoichiometric reduced PCMO, tunnelling was predominant, switching the device to the HRS. The PCMO device presented in this chapter looks to build upon this RS model by fabricating and studying a similar device heterostructure that, instead of using a strongly reducing top electrode

to form an interfacial oxide, employs a *dedicated* tunnel oxide; this heterostructure is further described in section 4.2.

For this reason, STEM-EELS was used to probe the spatial extent of any changes to the Mn valence state across the device heterostructure; to fully characterise the RS mechanism, both LRS and HRS programmed states are compared and discussed. It should be noted that valence changes to Pr^{3+} and Ca^{2+} are not expected to occur because, as shown in Fig.4.1, they form the ionic lattice.

4.2 Crystalline Tunnel Oxide $Pr_{0.48}Ca_{0.52}MnO_3$ RRAM

As described in Chapter 1, dedicated interfacial oxides are purposefully deposited interfacial layers and do not form due to electrochemical redox activity at the interface. Their basic function is to act as an oxygen-reservoir to facilitate $V_{\ddot{O}}$-mediated RS, however if carefully chosen, dedicated oxides can offer additional functionality or control over RS characteristics, such as tunnel oxides, which are employed to promote tunnelling of charge carriers above any other contributing conduction mechanisms. Tunnel oxide RRAM devices were first developed in 2008 by UNITY Semiconductor Corporation [2]. Despite receiving little acclaim, this study notably demonstrated that the as-deposited thickness of a dedicated tunnel oxide governs the nominal current density of the device; this means that a tunnel-RRAM device can be tailored according to the requirements of high-density 3D cross-point RRAM architecture, which is described in Chapter 1 [2]. Importantly, UNITY proposed that the resistance state is dictated by the concentration of $V_{\ddot{O}}$ in the tunnel oxide. Specifically, an accumulation of negatively charged oxygen anions (which is equivalent to the dissipation of $V_{\ddot{O}}$) in the tunnel oxide was thought to increase(decrease) the tunnel barrier height and restrict(promote) tunnelling, programming the device to the HRS(LRS) [2]. Despite this insightful 2008 study, tunnel oxide RRAM devices have scarcely been investigated since; the study presented in this chapter aims to continue in this line of investigation by building upon key findings of RS outlined in UNITY's tunnel RRAM publication and Herper *et al.*'s crystalline PCMO publication. In this study, a Rh(3nm)/YSZ(2.8nm)/PCMO(20nm)/$SrRuO_3$(SRO,30nm)/$SrTiO_3$(STO) heterostructure, fabricated via PLD by collaborators in Jülich is presented. Each layer

serves a functional purpose: STO is a perovskite oxide substrate that enables epitaxial growth (which was described in Chapter3), SRO acts as an inert, ohmic, perovskite bottom electrode, PCMO is the active resistive switching layer and Rh acts as an ohmic top electrode. Here, $(Y_2O_3)_{0.08}(ZrO_2)_{0.92}$ is employed as a tunnel oxide; the replacement of Zr^{3+} with Y^{4+} leads to the formation of multiple $V_{\ddot{O}}$ through charge compensation, which makes YSZ an effective ionic conductor [28]. In fact, for dopant concentration x, the number of $V_{\ddot{O}}$ per unit cell, δ is given by $\delta = 2 - \frac{(2+x)}{(1+x)}$, which means that for the YSZ used here, $\delta = 0.07$ [29].

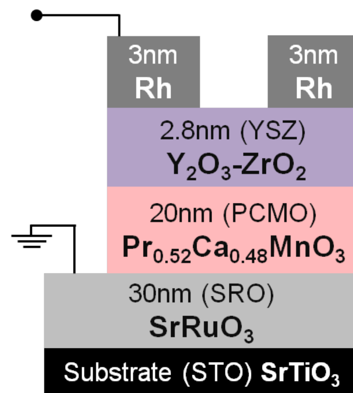

Figure 4.2: *PCMO tunnel-RRAM device with heterostructure: Rh(3nm)/YSZ(2.8nm)/PCMO(20nm)/$SrRuO_3$(SRO,30nm)/$SrTiO_3$(STO). During electrical characterisation, the bottom electrode, SRO, was grounded.*

The literature strongly suggests that RS in this tunnel-RRAM PCMO device will be mediated by the field-driven exchange of $V_{\ddot{O}}$ between the tunnel oxide and PCMO; to observe and investigate this effect, HAXPES and EELS were employed. During HAXPES, multiple devices can be irradiated at once, providing a relatively quick general assessment of the electronic proprieties of materials within the probing depth. HAXPES can also be done *in-operando*. In comparison, although EELS requires dedicated lamellae fabrication, and can only be used to probe one sample that has been programmed *ex-situ*, its high spatial and energy resolution and sensitivity allows one to probe subtle chemical changes that occur during RS. In addition, as the intensity of a deconvoluted EELS core-loss edge is proportional to the number of atoms per unit area (described by Eqn.2.5), the number of oxygen anions being exchanged between the YSZ and PCMO that effect a change in resistance state can be quantified, which is not possible using HAXPES. Furthermore, given the large amount of literature of Mn valence, EELS can

be used to assess any RS-induced redox activity at the YSZ/PCMO interface, and could potentially reveal the much anticipated differences in Mn valence state induced by RS. With regards to electrical characterisation, by fitting the IV characteristics to conduction mechanism models, it is possible to elucidate the predominant conduction mechanism(s) governing each resistive state. As explained in Chapter 2, the low-loss EELS spectra can be used to reveal some information regarding the electronic properties of the material. However, before using spectroscopy techniques to probe of the device, it was electrically characterised; these results are discussed in section 4.3.

4.3 Electrical Characterisation

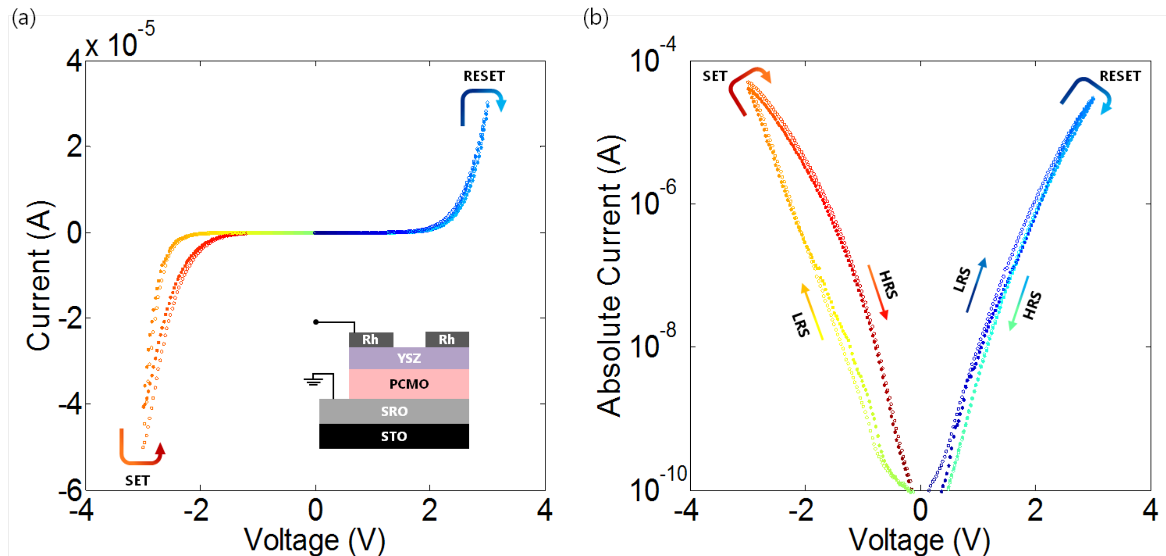

Figure 4.3: *Quasi-static I-V curves showing the 1st and 3rd RS cycles (represented by solid and hollow circles respectively) acquired from a bulk Rh/YSZ/PCMO/SRO device across voltage range ±3V. The same data are plotted in (a) and (b) which use linear and semi-log scales respectively. Here, the colour scale runs from blue→green→yellow→red in the direction of the source voltage to allow an assessment of RS polarity. The inset clarifies the device heterostructure (shown in Fig.4.2) and identifies the source (Rh, top electrode) and ground electrodes respectively (SRO, bottom electrode).*

Collaborators based in Jülich electrically characterised the device. Fig.4.3 displays representative quasi-static IV curves obtained from a bulk sample in which the SRO bottom electrode was grounded with respect to the Rh top electrode (as shown in inset in Fig.4.3(a)). Figs.4.3(a) and (b) present identical datasets, however Fig.4.3(b) employs a semi-log scale for greater clarity. Here, the direction of RS is expressed by the

colour scale: from the start to the end of the voltage cycle, the marker colour gradually changes from dark blue to green to yellow to red. Fig.4.3(b) shows that the device is initially in the LRS and that at $V_{RESET} = +3V$, the device switches into the HRS during a RESET process. At the opposite voltage polarity, the device undergoes a SET process, in which it switches from the HRS to the LRS at $V_{SET} = -3V$. The RS polarity exhibited by these tunnel-RRAM devices is consistent with that of p-type crystalline perovskite oxide devices presented in the literature [1, 25]. At $V_{READ} = -0.7V$, the resistance ratio is 1.5:1; however, this relatively small window is consistent with perovskite oxide RRAM devices presented in the literature [26]. In Fig.4.3, both the initial (represented by filled markers) and a successive (represented by empty markers) cycles are shown; both switching transitions (SET and RESET) occur at the same switching voltages for each cycle, which means these devices display good reproducibility. Furthermore, as the switching voltages remain constant in successive cycles, these devices do not require an electroforming process, which is typified by a greater initial V_{SET}. However, a third of all tested devices revealed an increased measured current during the initial cycle, which dropped in successive cycles to the current levels shown in Fig.4.3.

In Chapter 1 section 1.13, filamentary and area-homogeneous VCM RS were introduced; these two VCM geometries are typically identified by monitoring changes to the electrical characteristics as the area of the top electrode is scaled. In this work, numerous tunnel-RRAM devices were fabricated through the deposition of multiple square electrodes with side lengths 10, 20, 30, 50, 100, and 200μm. The magnitude of resistance for the pristine state (PS, shown in black), LRS (shown in blue) and HRS (shown in red) are presented in Fig.4.4(a), which shows the inverse scaling of the LRS and HRS with top electrode area, where the gradient is close to $m = -1$. This suggests that the RS effect is homogeneous and occurs over the entire area of the top electrode, which is often associated with the gradual transition between resistance states displayed in Fig.4.3. Although PS does show inverse scaling with top electrode area, it deviates from $m = -1$; this is most likely due to the contribution from the devices that displayed an increased LRS current in the during the initial sweep.

UNITY's tunnel-RRAM model was supported by evidence showing the dependence of current density on tunnel oxide thickness [2]. To determine whether our PCMO

tunnel-RRAM results are consistent with this, the effect of tunnel oxide thickness was explored, the results of which are presented in Fig.4.4(b). The use of tunnel oxide thicknesses 20Å, 24Å and 28Å revealed that the current density decreases exponentially with increased YSZ thickness, agreeing with the tunnel model. Measured IV curves acquired from devices with different YSZ thicknesses were also compared to a simplified transport model describing a series connection consisting of an ohmic resistance (which represents the SRO and other ohmic losses) and a field-accelerated polaron hopping model (which represents the PCMO) [24], and is shown in Fig. 4.5(a). The comparison highlighted the inadequacy of the simplified polaron hopping model, which outputted currents that significantly exceeded those measured. Instead, an appropriate fit was achieved after the inclusion of a tunnel barrier component, which is consistent with Herper et al's dual-component model [30, 31].

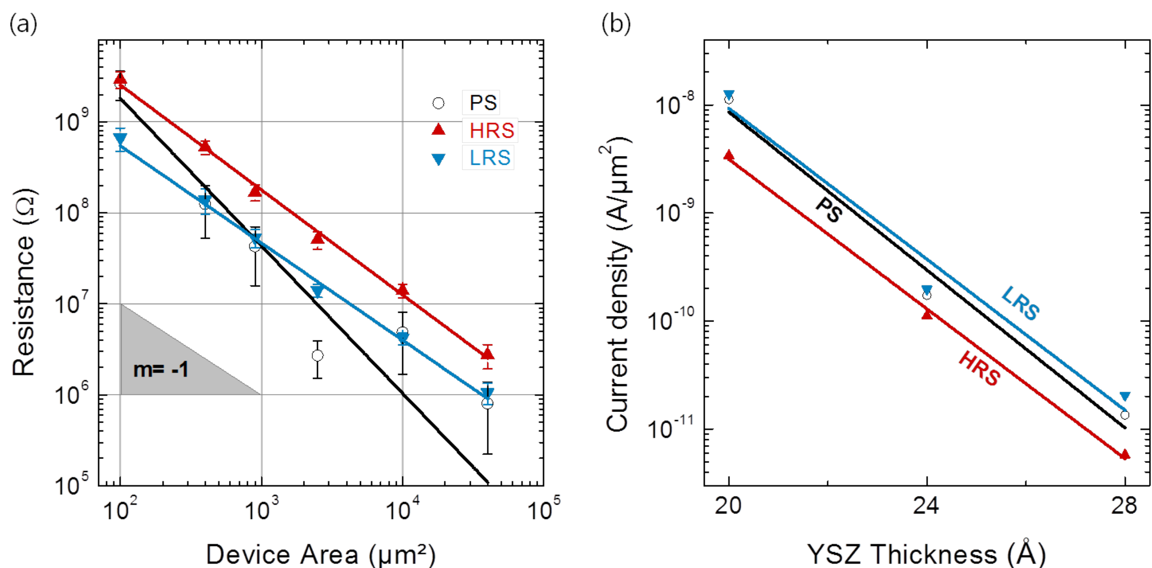

Figure 4.4: *Scaling characteristics of bulk Rh/YSZ/PCMO/SRO device. Here the HRS (shown in red), LRS (shown in blue) and PS (shown in black) are shown as a function of (a) device area on a log-log scale and (b) YSZ tunnel oxide thickness on a semi-log scale. Image adapted from [30].*

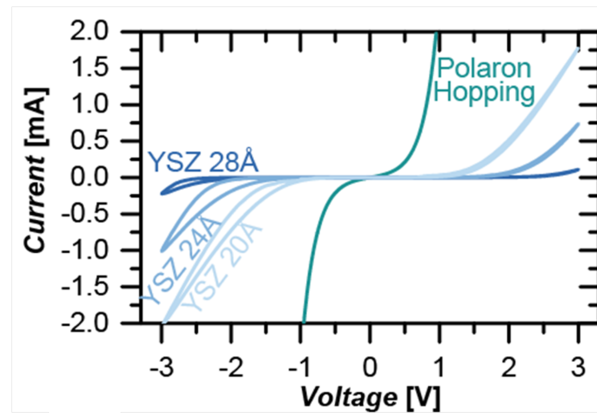

Figure 4.5: *(a) measured IV curves acquired for tunnel oxide thicknesses 20Å, 24Å, 28Å (blue lines) across ±3V voltage sweeps, and compares them to polaron hopping (green line). Image adapted from [30].*

By way of determining whether HAXPES and STEM-EELS measurements could be acquired from a programmed device, collaborators at Jülich acquired retention data over the course of 33 hours; the results are shown in Fig.4.6. During this time, a series of pulses at $V_{READ} = -0.7V$ were used to probe both LRS- and HRS-programmed devices. Whilst the HRS remained at a stable resistance of 0.25MΩ, the LRS relaxed towards a higher resistance over time, until reaching stability at 0.21MΩ. This type of PCMO LRS relaxation was previously observed in an Al/PCMO/Pt bipolar VCM device [32]. In this study, the device switched to the HRS due to the field-induced formation of an interfacial oxide, AlO_x, which acted as a Schottky barrier, and switched back to the LRS when the field was reversed at a magnitude sufficient to stimulate the dissolution of the AlO_x. Here, the metastability of the LRS was ascribed to the fact that the free energy of AlO_x formation was lower than that of the highly reducing metal Al; it was argued that this low energy of formation meant that *after* the removal of an applied AlO_x-dissipating field, a thin AlO_x layer would gradually form over time, which in turn, would gradually increase the resistance of the LRS, as observed [32]. In terms of the tunnel RRAM device presented here, it is feasible that a comparable mechanism could be the cause of the observed LRS relaxation, wherein it is energetically favourable for some portion of the migrated oxygen anions to gradually return to the YSZ after the SET process. Despite this LRS relaxation, the device proved stable for spectroscopic investigation up to 24 hours post-programming. The analysis of STEM-EELS and HAXPES spectra are presented in sections 4.4 and 4.5 respectively.

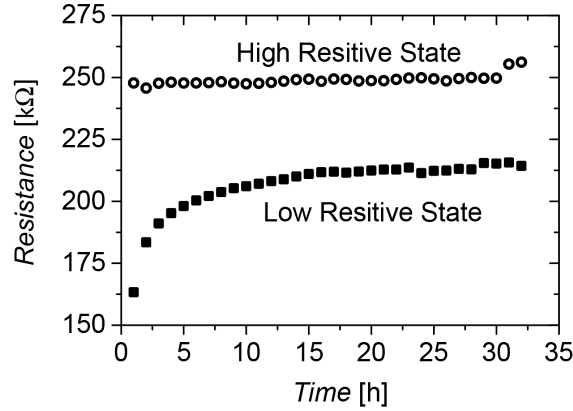

Figure 4.6: *Retention of HRS and LRS measured over 33 hours. Resistance values were obtained using* 250μs *READ pulses at* $V_{READ} = -0.7V$ *after programming using 1ms pulses at* $V_{SET} = +2V$, $V_{RESET} = -3V$. *Image adapted from [30].*

4.4 STEM-EELS Analysis

Table 4.1: Acquisition information for contributing EELS datasets. LRS- and HRS-programmed devices are shown in blue and red respectively.

Dataset	Offset (eV)	Dispersion (eV/Ch)	Acquisition Time (ms)		Acquisition Ratio	State	SI Length (nm)
			Low-Loss	High-Loss			
LRS3	535	0.25	199	0.995	200	LRS	15
LRS4	535	0.25	499	0.998	500	LRS	30
LRS5	190	0.5	49	0.980	50	LRS	15
LRS6	190	0.5	99	0.990	100	LRS	30
HRS1	190	0.5	99	0.990	100	HRS	30
HRS2	190	0.5	99	0.990	100	HRS	15
HRS3	535	0.5	499	0.998	500	HRS	30
HRS4	535	0.25	498	1.99	250	HRS	15
HRS5	190	0.5	199	0.995	200	HRS	15

Due to its high spatial and energy resolution, EELS allows one to probe the electrochemical response of *individual* active layers within a given RRAM device. With regards to our PCMO tunnel-RRAM device, the literature strongly suggests that these active layers are the YSZ tunnel oxide, and the O^{2-}-deficient PCMO, where RS is mediated by the field-induced exchange of $V_{\ddot{O}}$ across the YSZ/PCMO interface [22, 26, 27]. Considering the literature, which anticipates and alludes to measurable, reversible, $V_{\ddot{O}}$-migration-induced Mn redox activity, a notable EELS measurement would be that of the valence state of Mn^{n+} within the vicinity of the YSZ/PCMO interface [11, 19, 26]. Lamella samples, prepared using the DualBeam FIB instrument (see Chapter 2 section 2.4), were obtained from *ex-situ* programmed devices, allowing for comparison of HRS

and LRS devices. However, before RS-induced chemical changes can be identified, static device characteristics, that is, those that are irrespective of programmed state, must be understood. These static characteristics are presented in section 4.4.1, and are followed by a comparison of the HRS-programmed and LRS-programmed devices in section 4.4.2.

Table 4.1 presents the acquisition information (described in Chapter 2) corresponding to the EELS datasets that contributed to this study; LRS-programmed devices are shown in blue whilst HRS-programmed devices are shown in red. To compare between these two resistance states, datasets were first grouped according to their energy offset and dispersion. This is an essential precaution that must be taken in order to account for nonlinearities in the spectrometer; if this is not addressed, absolute quantification of the onset of a core-loss edge (i.e. the chemical shift, which is an indicator of oxidation state) is not possible. As shown in Table 4.1, the acquisition ratio (the ratio between the acquisition time used for low- and high-loss spectra) varies across the datasets; to compare across these datasets, the integrated intensity of the high-loss spectra was normalised using acquisition ratio. Finally, the datasets span different lengths across the heterostructure: the short datasets (15nm) include the Rh and YSZ layers, and the YSZ/PCMO interface, whereas the long datasets (30nm) include the Rh, YSZ and PCMO layers, and the PCMO/SRO interface.

4.4.1 Static Device Characteristics

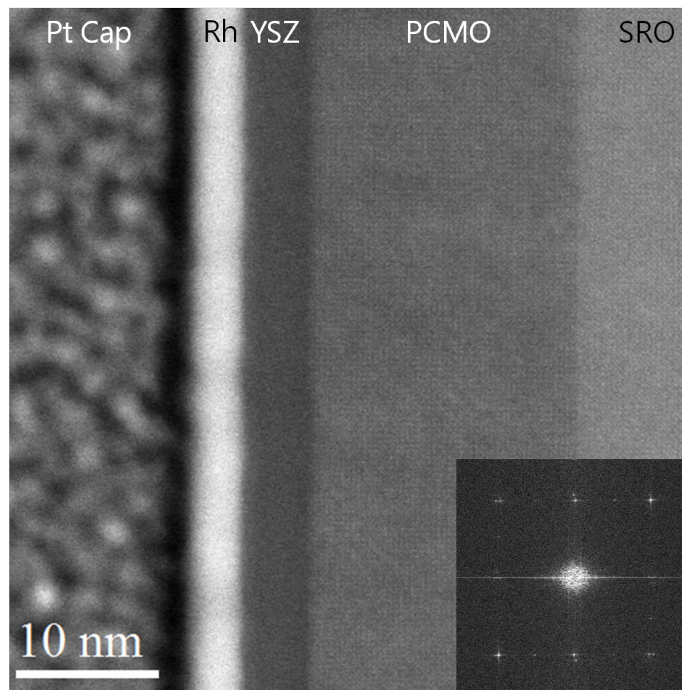

Figure 4.7: *DF image of the tunnel-oxide PCMO RRAM device with (inset) Fast Fourier Transform. A protective Pt capping layer was deposited during lamella preparation prior to STEM.*

A BF STEM image of a typical device is shown in Fig. 4.7; here, the crystalline lattice is just visible at this magnification, providing some evidence for the excellent hetero-epitaxial relationship of PCMO and SRO with the underlying STO substrate, and no dislocations are observed at the PCMO/SRO interface. No higher magnification images were procured due to time constraints. The inset FFT is dominated by a square pattern of sharp spots that are streaked along the sample normal in the (001) direction.

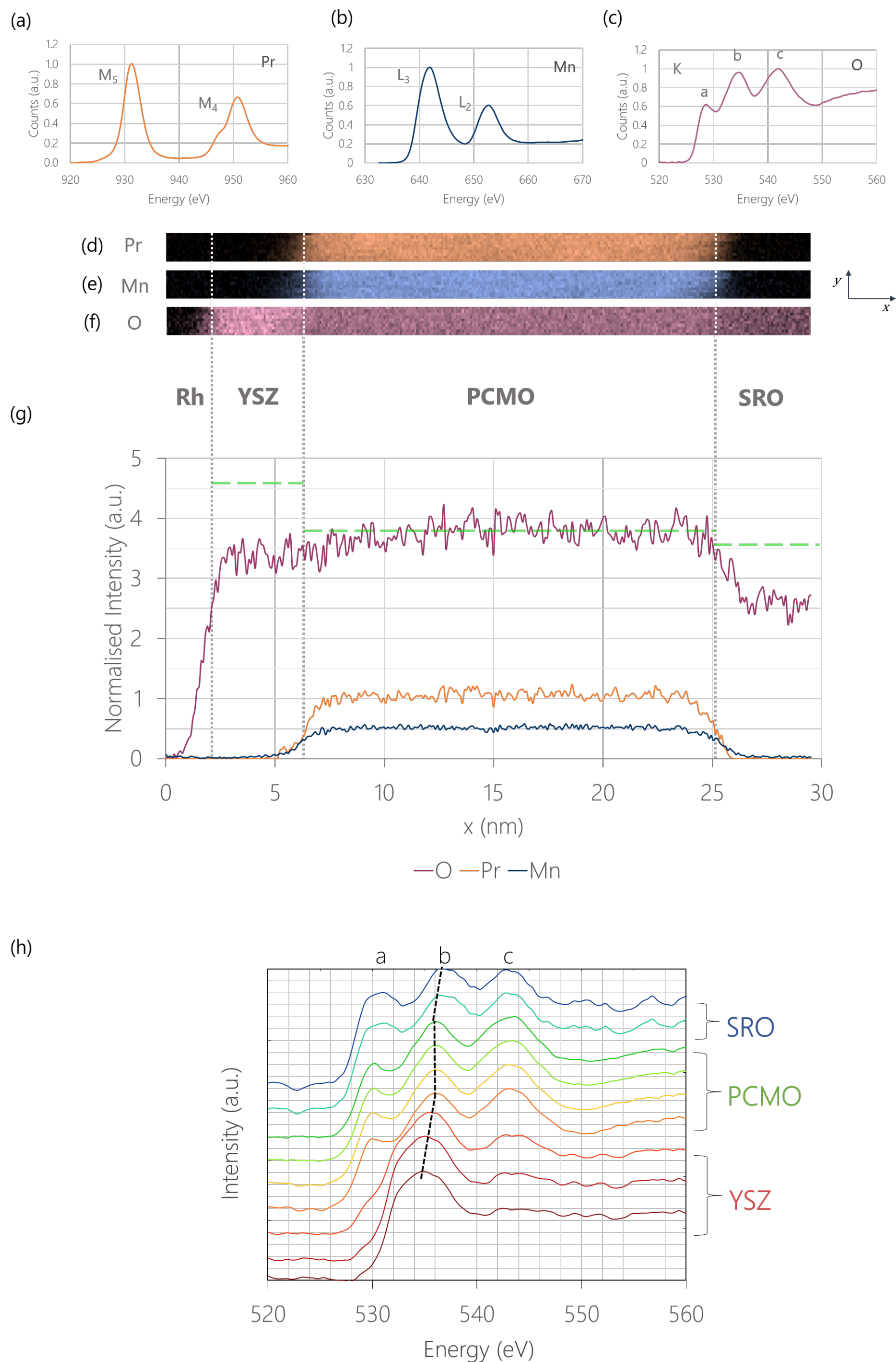

Figure 4.8: *(a) Pr, (b) Mn and (c) O background-subtracted core-loss edges extracted from the bulk PCMO. (d) Pr (orange), (e) Mn (blue) and (f) O (purple) signal maps were generated by integrating under the core loss edge and plotting the integrated intensity for each x, y pixel (0.095nm^2) with the EELS-SI (EELS datacube). (g) normalised distribution of elements across the RRAM heterostructure, where vertical grey dashed lines are used to highlight interfacial regions and the horizontal green dashed lines represent the expected oxygen intensity, according to Eqn.2.11. (h) evolution of oxygen across the oxygen-containing layers of the device, where the colour distribution (brown→blue) indicates spectra obtained from progressively increasing(decreasing) distances from the YSZ(SRO), shown in brown(blue). All spectra were processed using PCA and were normalised to the maximum intensity peak for ease of comparison. A vertical dashed line highlights the shift of peak* **b** *across each layer.*

Fig.4.8 displays the elemental distribution of O, Mn and Pr across the device heterostructure. After basic EELS processing (described in Chapter 2 Section 2.17), Pr-$M_{5,4}$, Mn-$L_{3,2}$ and O-K core-loss edges (shown in Figs.4.8(a), (b), and (c) respectively) were extracted from a $\approx$1nm^2 region of interest the middle of the PCMO layer. As stated above, all core-loss edges extend above a background signal which, in standard practice, is fitted with a power law background and then subtracted before analysis. Integrating over the energy range that isolates a particular peak (such as 930-934eV for the isolation of the Pr-M_5 peak) produces a 2D map that shows the integrated intensity within that energy range for each x, y-pixel within the SI; these signal maps are shown for Pr-M_5, Mn-L_3, and O-K (peak **b**) in Figs.4.8(d), (e), and (f) respectively. As explained in Section 2.7.3, these signal maps can be normalised in three ways to allow for comparison across multiple datasets with different acquisition conditions: to account for the variations in integrated signal intensity caused by thickness changes across the lamella; to account for the variations in intensity of the ZLP; and finally, to account for the atomic cross-section for each element. The normalised signal map for each element was summed in y to produce the profiles displayed in Fig.4.8(g), which shows the spatial distribution of and relative ratio between O, Mn and Pr across the device, where vertical grey dashed lines highlight regions corresponding to the Rh/YSZ, YSZ/PCMO and PCMO/SRO interfaces respectively. In Fig.4.8(g), the O-K signal (shown in purple) is present in the YSZ, PCMO and SRO layers and the Pr and Mn signals (shown in yellow and blue respectively) rise to maximum intensity in the bulk PCMO region, as expected. In addition, Fig.4.8(g) also shows that within the bulk PCMO, the ratio between the elements Pr:Mn:O is approximately 1:0.5:3.8, which mostly agrees with the nominal ratio (1:0.5:3), however, there is a surplus in the relative oxygen content. It is possible that this surplus could be due to the presence surface oxides that may contaminate the exposed faces of lamella, however it is also possible that oxygen may have migrated into the PCMO from the YSZ or the PCMO. As shown in Section 2.7.3, the normalisation process results in intensity that is proportional to the product of n, the number of atoms per unit volume, and λ, the mean free path. For stoichiometric 8%-YSZ, there are 1.9 O atoms per unit cell [29], which has volume V_{YSZ} =135Å^3 [33], whilst for PCMO there are three atoms per unit cell, which has volume $V_{YSZ} = 233$Å^3 [34]. Using

the Log-ratio model (formulated by Iakoubovskii *et al.* [35]), the calculated mean free paths for each layer in the RRAM heterostructure were found to be $\lambda_{YSZ} = 109$nm, $\lambda_{PCMO} = 101$nm and $\lambda_{SRO} = 96$nm; therefore, applying Eqn.2.11, the ratio between the normalised intensities of the O signal for fully stoichiometric YSZ and PCMO is given by $\frac{I_{PCMO}}{I_{YSZ}} = \left(\frac{1.9}{135}\right)\left(\frac{233}{3}\right)\left(\frac{109}{101}\right) = 1.2$. Similarly, the ratio between the normalised intensities of the O signal in the perovskite oxides PCMO and SRO is expected to be $\frac{I_{PCMO}}{I_{SRO}} = \left(\frac{96}{101}\right) = 0.95$ at full stoichiometry. In addition to the normalised O signal distribution, the calculated signal intensities for fully stoichiometric YSZ, PCMO and SRO are plotted with green dashed lines in Fig.4.8(g) and reveal a clear difference between nominal and measured stoichiometry. Given that it is unlikely that PCMO contains a surplus of O atoms, it appears that the YSZ and SRO are sub-stoichiometric. However, as these are lamella extracted from *programmed* devices, deviations from stoichiometry are expected, and, as will be discussed in Section 4.4.2, the relative density of O atoms in the YSZ ultimately showed dependency on the programmed resistive state, which is attributed to $V_{\ddot{O}}$-migration during RS. As mentioned above, Fig.4.8(g) also indicates that there is a large drop in the number of O atoms in the SRO, which is greater than that expected due to the change in mean free path; however, under closer inspection of the high-loss spectrum, it became clear than the appearance of a Ru-M_3 at 461eV affected the background subtraction window before the O-K edge, which lead to an overestimation of the background contribution to the core-loss edge; therefore, an assessment of relative oxygen density in the SRO layer is somewhat limited. The appearance of the Ru-M_3 edge also affected the Mn-$L_{3,2}$ edge, which is in close proximity to the O-K edge; this means that the apparent difference between the decay of the Mn and Pr signals at the PCMO/SRO interface should not necessarily be interpreted as a greater diffusion of Pr into the SRO than Mn.

In addition to using signal intensity to assess relative changes in oxygen density, which is the basis of the normalisation process used above and described in Section 2.7.3, the shape of the ELNES can also be used to identify the presence (or absence) of $V_{\ddot{O}}$ in a oxide given material [36, 37]. To evaluate this a comparison of the O K-edge acquired from each oxygen-containing layer (YSZ, PCMO, SRO) of the device is presented in Fig.4.8(h), where the signals were extracted after PCA processing. For perovskite

manganites, the O K-edge has fine structure comprising three main peaks: the first peak (labelled **a**), located at 530eV, corresponds to hybridised O-2p and Mn-3d states and has been shown to decrease with lowering Mn valence state and an increased concentration of $V_{\ddot{O}}$ [36, 38]; the second peak (labelled **b**), located at 536eV, is associated with bonding to Pr-4f, Pr-5d, and Ca-3d states [39, 40]; and the third peak (labelled **c**), located at 543eV is attributed to hybridised O-2p and (delocalised) Mn-4s/Mn-4p states [41]. Also a perovskite oxide, the SRO ELNES contains peaks **a**, **b** and **c**, however, in comparison to the PCMO, peaks **a** and **b** are broadened whilst peak **c** weakens; this can be seen most clearly in Fig.4.8(h). In the literature on perovskite manganites, the broadening of peak **b**, when associated with the weakening of peaks **a** and **c**, is attributed to the increased presence of $V_{\ddot{O}}$ [36, 42], however it is unclear whether this interpretation can be applied to SRO, as the effects of $V_{\ddot{O}}$ on O K-edge ELNES for different perovskite oxides vary. For instance, in the case of STO, the increased presence of $V_{\ddot{O}}$ causes an increase in peak **a**, coupled with the decrease of peaks **b** and **c**, which contrasts that observed for PCMO [43]. Therefore, in the absence of literature on SRO ELNES, it is unclear if the SRO has a greater, equal or lower $V_{\ddot{O}}$-concentration than the PCMO. There is a clear difference between the O K-edge obtained from the YSZ and the perovskite oxides, namely, the absence of peak **a**, and near negligible peak **c**. According to the literature, a YSZ oxygen K-edge is a doublet feature, in which the relative intensities of each peak and FWHM (if considered as a single intensity band) can be used to identify the crystalline phase of the YSZ [44, 45]; due to the amorphous nature of the YSZ, evident in Fig.4.7, a broad single peak is observed.

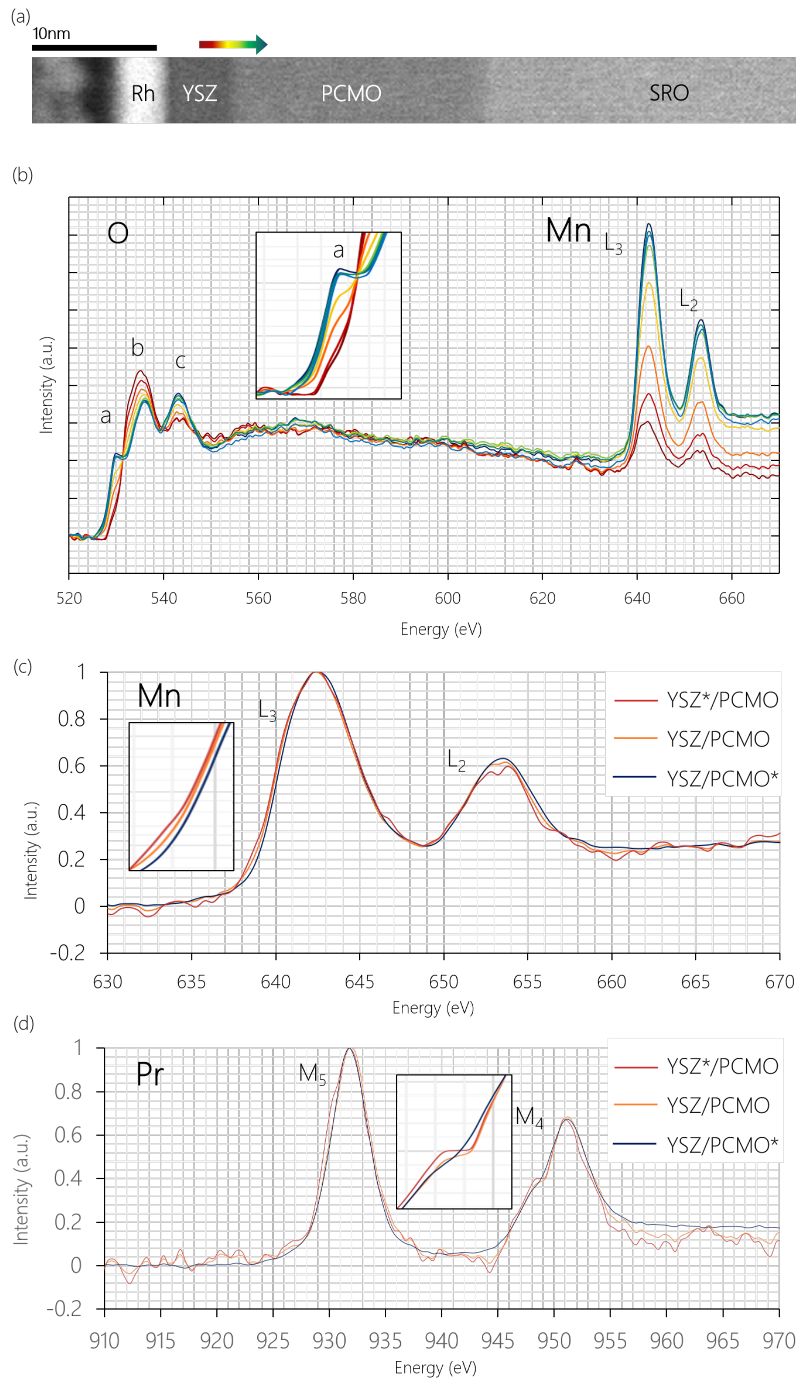

Figure 4.9: (a) Cropped HAADF image of the tunnel oxide RRAM heterostructure. The rainbow-coloured arrow above the YSZ/PCMO interface, which changes from brown→yellow→green→blue, indicates which line spectra in (b), (c) and (d) correspond to which regions of the YSZ/PCMO interface. (b) Graduation of background-subtracted O K-edge, which comprises peaks **a**, **b** and **c**, and the Mn core loss edge, which comprises $L_{3,2}$ peaks, from the red line spectra, which has a larger YSZ component, to the blue line spectra, which has a larger PCMO component. In (c) and (d), the red, orange and blue line spectra at (c) Mn-$L_{3,2}$ and (d) Pr-$M_{4,5}$ are compared where the orange line spectrum represents a transition state between the YSZ-rich brown, and PCMO-rich blue line spectra.

As highlighted earlier, $V_{\ddot{O}}$-exchange across the YSZ/PCMO interface is expected to occur during RS in PCMO tunnel-RRAM devices. Therefore, it is important to first understand the chemistry within the vicinity of this interface irrespective of programmed state. Fig.4.9 reveals such information extracted from a 4nm wide region across the YSZ/PCMO interface. It is important to note that this data was processed using PCA, the noise-reducing technique presented in section 2.7.5. The use of PCA means that the introduction of artefacts, which manifest as repeated shapes superimposed on the line spectra and must be isolated and excluded from the interpretation of results. Fig.4.9(a) is a cropped HAADF image that shows all layers within the PCMO tunnel-RRAM device, excluding the STO substrate. The rainbow coloured arrow, which graduates from brown→ orange → green → blue and is situated above the YSZ/PCMO interface, indicates which colours in Figs.4.9(b-d) represent which regions of the YSZ/PCMO interface: here, the brown(blue) end of the arrow corresponds to the part of the YSZ/PCMO interface with a larger YSZ(PCMO) component. This progression across the interface can be seen clearly in Fig.4.9(b) in which the same power-law background has been subtracted for all line traces: as we move in the direction of the rainbow arrow (brown→blue), the relative intensity of the Mn core loss edge increases. Starting in the region with the largest YSZ component, the brown trace includes a O-K edge (at 530eV) dominated by a broad peak **b**, which we take to be a characteristic of amorphous YSZ; the brown line trace also includes the lowest intensity Mn-$L_{3,2}$ peaks (at 640eV). Moving towards the PCMO, the line traces reveal a gradual increase of peaks **a**, a decrease and narrowing of peak **b** and an increase a broadening of peak **c**. These changes are consistent with the Mn being more *reduced* at the YSZ/PCMO interface than the bulk, which is consistent with $V_{\ddot{O}}$-migration from the YSZ into the PCMO (equivalent to O^{2-}-migration from the PCMO into the YSZ). However, to truly evaluate whether this is an effect of redox activity or simply a gradual change between the two materials, the Mn-$L_{3,2}$ edge (shown in Fig.4.9(c)) must be assessed in conjunction. Of all the spectra displayed in Fig.4.9(a) the red, orange and dark blue spectra, which span 3.5nm, can be used as indicator for Mn valence state; according to the literature which relates the intensity of peak **a** to the presence of $V_{\ddot{O}}$ in perovskite manganites, these spectra represent the reduced, transitioning, and oxidised phases of PCMO respectively [38].

In Fig.4.9(c), the Mn-$L_{3,2}$ peaks, which are normalised to the intensity of the Mn-L_3 peak, show a clear graduation in both the Mn-L_3 chemical shift and the Mn-$L_{3,2}$ peak ratio, effects which would only be observed if redox activity (due to $V_{\ddot{O}}$-migration) has occurred at the interface [46]. Although subtle, in Fig.4.9(c), the red trace features an Mn-L_3 peak that is shifted to lower energies: the inset shows that the red line trace rises to its maximum at consistently lower energies than the orange trace, which, in turn, rises at lower energies than the blue trace; here, the difference between the red and blue traces is 1eV, which, according to the literature, corresponds to a valence change of $Mn^{n-0.3}$ [46, 47]. With respect to the normalised intensity of the Mn-L_3 peak, the Mn-L_2 peak gradually increases from its lowest intensity in the red line trace, to its highest intensity in the blue trace. Both of these trends are consistent with the brown trace being more reduced than the orange trace, which is more reduced than the blue case. Relating this back to specific regions within the YSZ/PCMO interface, within the vicinity of the YSZ, the PCMO contains reduced Mn, which gradually becomes more oxidised further away from the interface (towards the bulk PCMO). Although a 'doublet' feature can be seen in the red line trace at the Mn-L_2 peak maximum in Fig.4.9(c), it cannot be reliably distinguished from noise and is present in peak **c** of the O-K, and as such is not interpreted as a valence-state-indicative feature, instead it is most likely a PCA-introduced artefact. Despite this, interestingly, all three line traces overlap on the incline towards the Mn-L_2 maximum yet decline (between 653eV-637eV) at different gradients, revealing a broadening of the Mn-L_2 peak as the PCMO component increases. In the literature, the relationship between the broadening of the Mn-L_2 and Mn valence state is not well characterised, however, considering the clear, graduated changes in Mn-L_3 chemical shift, Mn-L_2 white-line ratio and Mn-$L_{3,2}$ shape, broadening of the Mn-L_2 peak may be an additional effect of valence change. The gradual changes across the YSZ/PCMO interface observed in the O-K and Mn-L edges are consistent with $V_{\ddot{O}}$-migration from the YSZ into the PCMO. This direction of migration agrees with the normalised O intensity profile presented in Fig.4.8(g), which revealed that the YSZ was sub-stoichiometric and oxygen deficient.

For comparison, Pr-$M_{5,4}$ peaks, extracted from the same regions as shown in Fig.4.9(c), are shown in Fig.4.9(d). In the literature, $V_{\ddot{O}}$-migration in PCMO typically

causes a change in the Mn valence state and this change is attribute to the MnO_6 octahedron. However, surprisingly, changes to the shape of the Pr-$M_{5,4}$ peaks are observed in this work. In comparison to Mn, there is little literature that discusses how valence state manifests in Pr-$M_{5,4}$ ELNES. Of these, Herrero-Martin *et al.* showed that the Pr-M_5 peak is shifted to lower energies and the ratio between the Pr-M_5 and Pr-M_4 peaks increases for reduced Pr^{3+} in comparison to oxidised Pr^{4+} [48]; Richter *et al.* observed no change in Pr-M_5 peak position between valence states, which is likely due to the lower energy resolution used, but confirmed the trend in Pr-$M_{5,4}$ peak ratio, and further noted the appearance of a pronounced low-energy shoulder for Pr^{3+} [49]. With regards to the Pr-$M_{5,4}$ peaks extracted from the YSZ/PCMO interface shown in Fig.4.9(d), there is a clear low-energy shoulder present on the Pr-M_5 peak in the red line trace that is not present in the orange or blue traces, which could indicate the presence of a more reduced Pr phase in the region with a larger YSZ component, as seen in the literature [50]. However, the Pr-M_4 peak shows a gradual transition from a prominent Pr-M_4 low-energy shoulder in the red line trace to a weak low-energy shoulder in the blue line trace; this transition is most clearly seen in the inset. According to to Richter *et al.*, this is consistent with the gradual transition from Pr^{3+}, within the vicinity of the YSZ, towards Pr^{4+} away from the YSZ, which is an unexpected interfacial reduction effect not typically associated with interfacial redox activity in PCMO in the literature. Due to the potential for the introduction of artefacts during PCA processing and the lack of consistency in the literature, it is difficult to be confident in the PCA-analysis of the Pr-$M_{5,4}$ peak. Therefore, all further analysis presented in this chapter was processed *without* the use of PCA.

As evident from Fig.4.9, the chemical shift at the YSZ/PCMO interface can occur over a narrow range (4nm in Fig.4.9(c)) and can be difficult to distinguish by overlapping spectra. Therefore, the spatial extent of the shift of Mn-L_3 and Pr-M_5 peaks were assessed for all datasets; an example of the profile (across x) of peak shift is shown in Fig.4.10(b), where Mn-L_3(Pr-M_5) shift is shown in purple(orange). According to the literature, the -1.3eV shift of Mn-L_3 at the YSZ/PCMO interface corresponds to a change in Mn valence state equal to $Mn^{n-0.8}$, which means that if the bulk PCMO contains nominal $Mn^{+3.5}$, then $Mn^{+2.7}$ is present at the interface. Across all

datasets, at the YSZ/PCMO interface, the Mn-L_3 peak underwent negative chemical shifts that ranged between 0.4eV and 2.5eV, which corresponded to Mn valence states which ranged between $Mn^{+3.3}$ and Mn^{+2} respectively [47]; in some cases, this shift extended up to ~12nm from the YSZ/PCMO interface. These results indicate that although gradual electrode-area-scaling RS is observed, *inhomogeneous* redox activity occurs at the YSZ/PCMO interface. This is interesting because the literature largely defines VCM RS geometry as either abrupt filamentary switching or gradual, area-scaling homogeneous switching. Here, we show that in these tunnel RRAM devices, the latter represents an ideal as area-scaling, gradual RS can occur due to inhomogenous interfacial effects. Finally, no changes in peak position were observed at the PCMO/SRO interface, indicating an absence of redox activity at this bottom electrode, as expected.

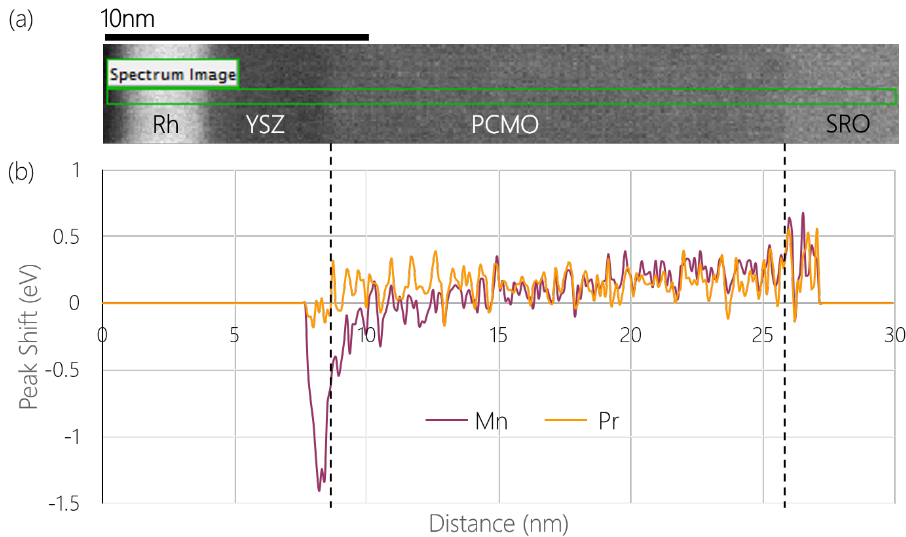

Figure 4.10: *Typical (a) Cropped HAADF image and (b) peak shift of Mn-L_3 (shown in purple) and Pr-M_5 (shown in orange) core-loss edges as a function of distance (x) across the device.*

4.4.2 Comparison of HRS and LRS

Acknowledging the literature, one would expect that during RS, in order to compensate for the migration of $V_{\ddot{O}}$ between the YSZ and PCMO, the Mn would be subject to field-induced redox activity within the vicinity of the YSZ/PCMO interface, whilst the components of the ionic lattice (here Pr and Ca) remained unchanged [22, 25, 51]. In addition, given the dependence of each resistance state on top electrode area (see Fig.4.4), this field-induced redox activity is expected to be homogeneous under the

entire electrode area. The analysis of *ex-situ* programmed devices presented in Section 4.4.1 revealed evidence of the inhomegeneous redox activity of both Mn and Pr at the YSZ/PCMO interface of all programmed devices due to $V_{\ddot{O}}$-electromigration during RS. In this section, O, Mn and Pr core-loss edges acquired at the YSZ/PCMO interface from HRS and LRS programmed devices are contrasted and presented in Fig.4.11. For many of the datasets, deconvolution was not possible due to the presence of multiple close core-loss edges. However, for those that had comparable thickness $\left(\frac{t}{\lambda}\right)$, convolution effects were assumed to be roughly equivalent, allowing for direct comparison between datasets acquired at equivalent energy offset and dispersion. For those datasets that could not be deconvoluted and did not have comparable thickness, the edge-onset (peak position) was used to determine the extent of interfacial reduction, as this parameter is not affected by convolution.

In Fig.4.11, two spectra acquired at the same energy offset and dispersion are compared; one of these was extracted from a LRS-programmed device (shown in blue), and the other was extracted from a HRS-programmed device (shown in red). Although only one line spectra representing each programmed state is shown, these are representative of a majority of the datasets acquired in this work. As mentioned earlier, the line spectra presented in Fig.4.11 have not been subject to PCA, therefore changes in shape (above noise) observed are significant and not the result of artefacts. Looking first at the O K-edge in Fig.4.11(a), both spectra reveal a wide, broadened peak that is characteristic of amorphous YSZ. The most notable difference between programmed states is the relative intensity of its two components, peak $\mathbf{b_1}$ and (normalised) peak $\mathbf{b_2}$: here, the HRS(LRS) is characterised by a strengthened(weakened) peak $\mathbf{b_1}$ and a broadened(narrowed) peak **c**. Considering the literature, this change is indicative of a change in the local bonding environment within the YSZ, and suggests that the LRS corresponds to a more *tetragonal*-like bonding environment, whereas the HRS corresponds to a more *cubic*-like environment [45]. With regards the Mn-$L_{3,2}$ edge, a number of changes were observed: the HRS line trace is shifted -0.5eV with respect to the LRS; both of the Mn-L_2 peaks were more asymmetric in the LRS than the HRS, and in the literature, such asymmetry is associated with increased presence of unoxidised Mn metal; and finally, the relative intensity of the Mn-L_2 peak is reduced in the HRS. All of

these changes are consistent with the HRS having a greater proportion of *reduced* Mn than the LRS, which has a greater proportion of *oxidised* Mn. To quantify the difference between HRS- and LRS-Mn valence states at the YSZ/PCMO interface, we can consider Loomer *et al.*'s study, which suggests that the Mn valence state difference associated with a shift of -0.5eV is $Mn^{n-0.3}$ [47]. For the HRS dataset presented in Fig.4.11, the relative peak shift between the Mn-L_3 peak acquired from the bulk PCMO and the YSZ/PCMO interface was -2.5eV, which puts the nominal valence state of the HRS at the YSZ/PCMO interface at Mn^{2+}, and the LRS at $Mn^{2.3+}$. Furthermore, if the charges are balanced, then for $Pr^{4+}_{0.48}Ca^{3+}_{0.52}Mn^{2.3+}O^{2-}_{3-\delta}$, $\delta=$0.1, and for $Pr^{4+}_{0.48}Ca^{3+}_{0.52}Mn^{2+}O^{2-}_{3-\delta}$, $\delta=$0.25, which indicates that there is an exchange of $\delta=$0.15 between programmed states. According to Goff *et al.*'s study, it is possible for tetragonal YSZ to contain $\delta=0.2$ (measured for YSZ doped at 24%), which suggests that an exchange of $\delta=$0.15 across the YSZ/PCMO interface is feasible [29]. For each dataset, relative to the bulk PCMO, the Mn underwent a peak shift of less(greater) than 1eV for the LRS(HRS) (calculated as shown in Fig.4.10(b)). In addition, a relative shift of -0.5eV, which corresponds to $Mn^{n-0.3}$, was consistently observed between the HRS and LRS, where the HRS was shifted negatively with respect to the LRS. Interestingly, as in Fig.4.9(c), the Pr-$M_{5,4}$ peaks show evidence of Pr redox activity in Fig.4.11(c): here, the HRS is shifted by -0.7eV with respect to the LRS, which, according to Herrero-Martin *et al.*, is consistent with a greater proportion of reduced Pr in the HRS than in the LRS [50]. Across all paired datasets, the negative shift of the Pr in the HRS was observed, however, in terms of peak ratio and shape, there was no clear distinction between the programmed resistance states, which is unexpected as changes in valence state cause changes in both peak shape *and* peak position. As noted in the discussion of Fig.4.9(d), the sparse and conflicting EELS literature on the valence state of Pr limits our interpretation of the results. For instance, a change in peak position could be due to non-linearities in the spectrometer dispersion that are exaggerated at higher energy loss. On the other hand, unlike Mn, Pr peak ratio and shape may not change linearly with chemical shift. In either case, it is difficult to reliably assess valence state of Pr at this time.

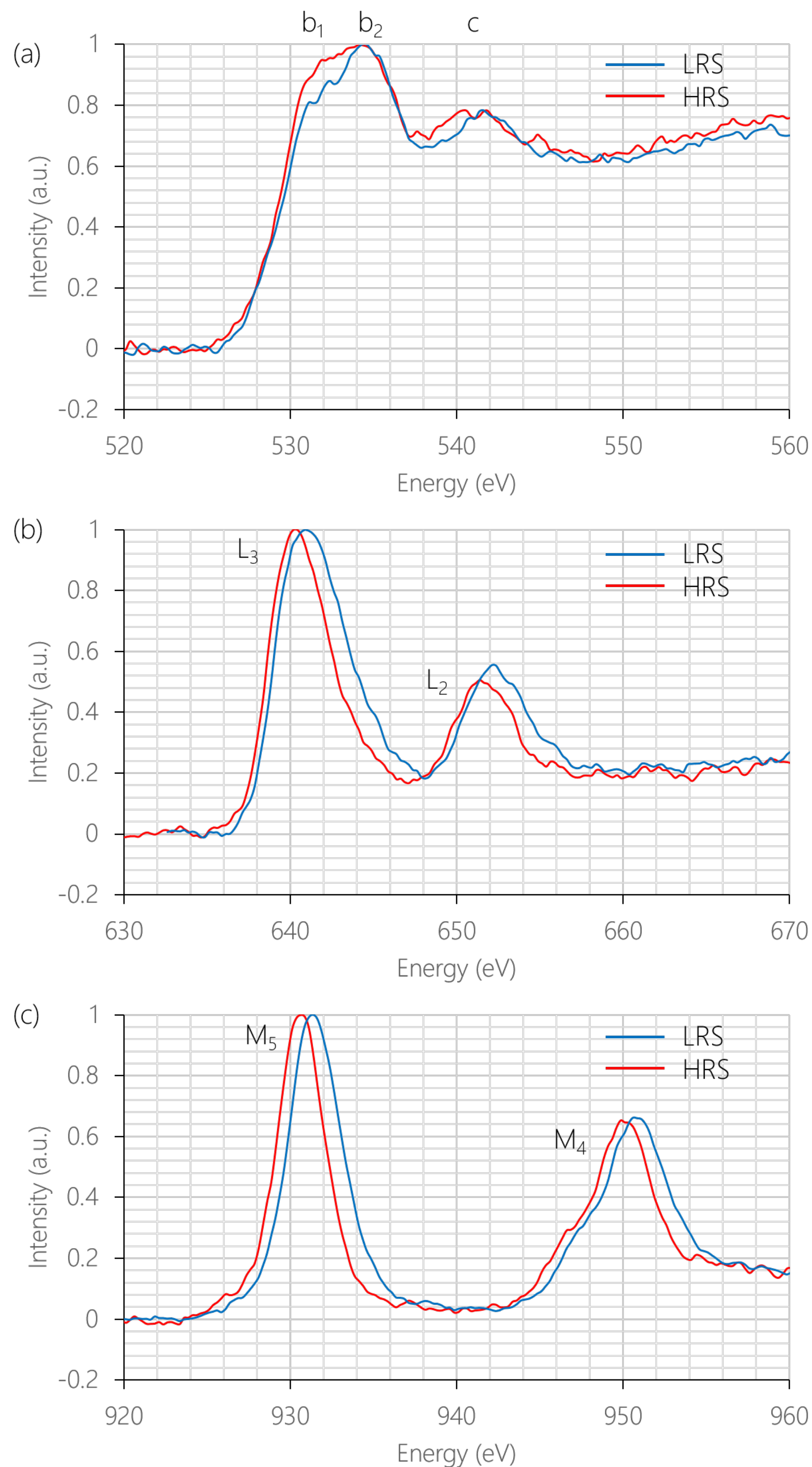

Figure 4.11: *Representative comparison of HRS (red) and LRS (red) spectra acquired from two datasets at the YSZ/PCMO interface. Sub-figures show the (a) O K-edge (b) Mn-$L_{3,2}$ edge and (c) Pr-$M_{5,4}$ edge. For both spectra the acquisition parameters were identical: pixel size was 0.2nm^2 and dispersion was 0.5eV/Ch.*

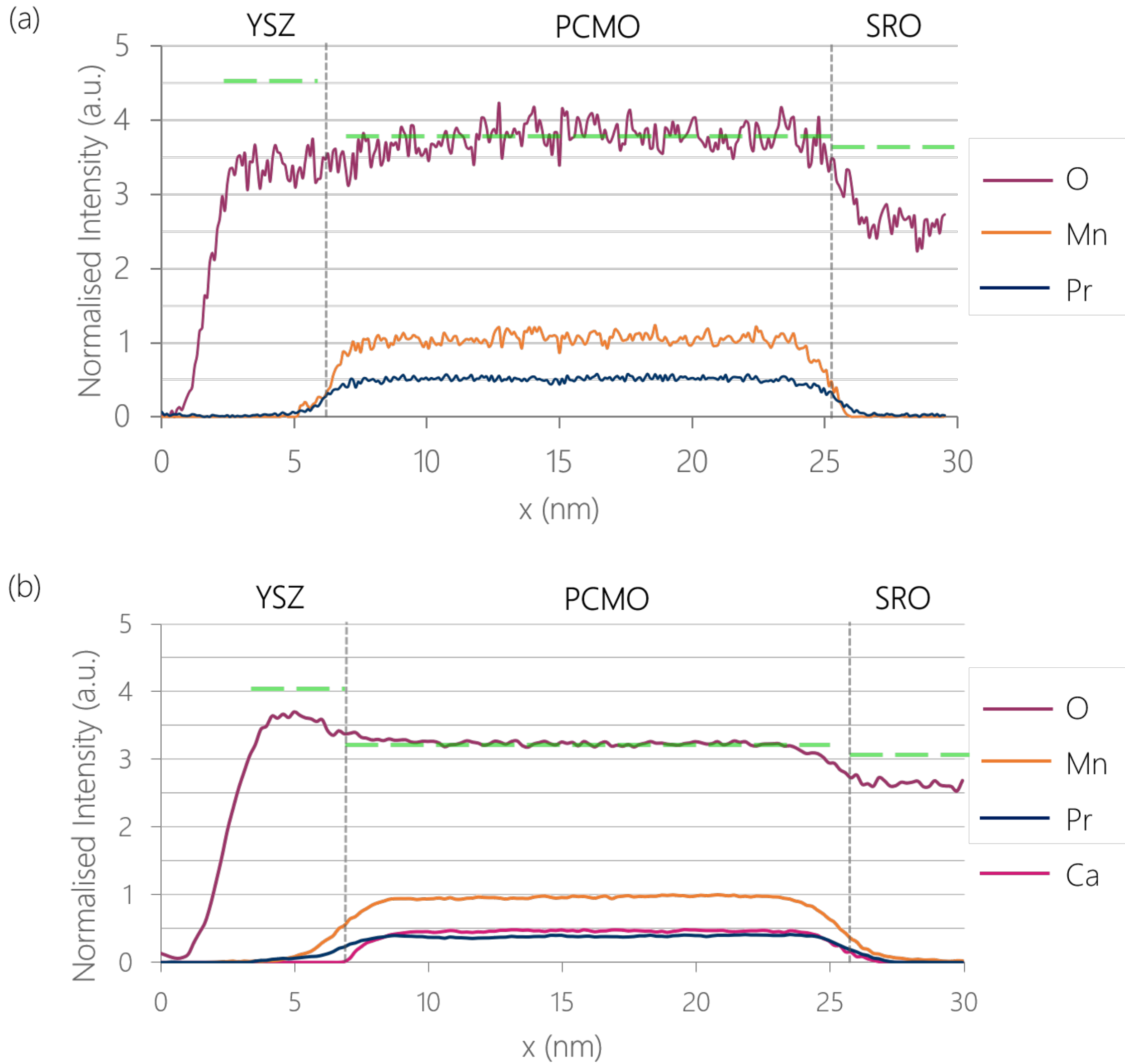

Figure 4.12: *Normalised distribution of elements in (a) the LRS and (b) the HRS. O, Mn and Pr are shown in purple, blue and orange respectively and in (b) the Ca profile is shown in pink. The main difference between these LRS- and HRS- representative distributions is the relative change in O content between the YSZ and PCMO. The horizontal dashed green line is positioned to represented the expected O-K edge intensity, relative to the bulk PCMO, as calculated using Eqn.2.11.*

Representative normalised elemental distributions of O, Mn and Pr are presented in Fig.4.12 where, as in Fig.4.8(g), the expected O intensity, relative to the bulk PCMO and calculated using Eqn.2.11, is shown for each oxide with horizontal green dashed lines. Interfaces between these materials are highlighted with grey dashed vertical lines. In the LRS and HRS (presented in Figs.4.12(a) and (b) respectively), the normalisation process resulted in an Mn:O:Pr ratio of 1:3.8:0.5 and 1:3.3:0.5 in the bulk PCMO respectively; the difference in O content could be indicative of a relative increase of

O atoms in the PCMO in the LRS in comparison to the HRS, however evidence of $V_{\ddot{O}}$-migration into and out of the PCMO must also be found to confirm this. As shown earlier (in Section 4.4.1), the expected relative change in the O signal intensity across the YSZ:PCMO:SRO in a static device is 1.2:1:0.95; in Figs.4.12(a) and (b), this expected O intensity (relative to the bulk PCMO) is presented using horizontal dashed green lines. In Fig.4.12(a), which represents the LRS, the YSZ is sub-stoichiometric with respect to the bulk PCMO. In Fig.4.12(b), which represents the HRS, the YSZ is also sub-stoichiometric with respect to the bulk PCMO, however, unlike the LRS, the O signal in the YSZ is significantly increased w.r.t. the PCMO. This change is consistent with there being more O^{2-} present in the YSZ in the HRS than there is in the LRS. Considering the fact the in the bulk PCMO, the HRS contained less O (relative to the Mn) than the HRS, then the accumulation of O^{2-} in the YSZ in the HRS is consistent with O^{2-}-migration from the PCMO into the YSZ across the YSZ/PCMO interface. Specifically, the results suggest that the HRS is programmed when the Rh top electrode is *positively* biased and O^{2-} migrate from the PCMO into the YSZ, and conversely, the LRS is programmed when the Rh top electrode is *negatively* biased and O^{2-} anions migrate from the YSZ into the PCMO. This O^{2-}-exchange between the YSZ and PCMO is seen consistently over a majority of the programmed datasets, however those that showed no significant change remain consistent with the earlier evaluation of *inhomogeneous* redox at the YSZ/PCMO interface, in which the degree of $V_{\ddot{O}}$-migration along the length of the interface would vary.

Considering the critical role of the YSZ tunnel barrier, spectra corresponding to the HRS- and LRS-programmed devices acquired from the center of the YSZ layer, away from the YSZ/PCMO interface, were also compared and are displayed in Fig.4.13. This revealed that overall, the YSZ layer underwent reproducible changes that mirrored those seen at the interface as a function of switching, however the change is more subtle. As seen at the interface (shown in Fig.4.4.2(a)), Fig.4.13(a) confirms that the LRS features a lower intensity pre-edge peak shoulder than the HRS, which is consistent with the aforementioned variation in local bonding environment in the amorphous YSZ [44, 45].

The Low-Loss EELS spectra provides information about the electronic nature of the probed material. Fig.4.13 presents a comparison of the Low-Loss spectra acquired from

the YSZ and PCMO, which, like the Core-Loss spectra, exhibit switching-dependent features. The spectra are in broad agreement with those of the literature [45, 52, 53]. Features below ∼22eV are ascribed to interband transitions from the O 2p state to empty Zr states; the broad peak around 26eV is a plasmonic excitation; and features above 30eV correspond to the Zr $N_{2,3}$ edge, ie. interband transitions from the Zr 4p state to other unoccupied Zr states [54]. One might therefore expect the greatest changes upon switching to be observed below 30 eV, where interband transitions sensitive to ZrO bonding and environment occur. As expected, there is variability in the intensity of the peak at 15 eV across all data sets but the LRS datasets tend to have a more pronounced plasmon peak that would be consistent with an increased metallic character of the YSZ. Some regions of LRS devices yield spectra which barely differ from the typical HRS spectrum in the region of the plasmon, once again suggesting the presence of chemical inhomogeneities.

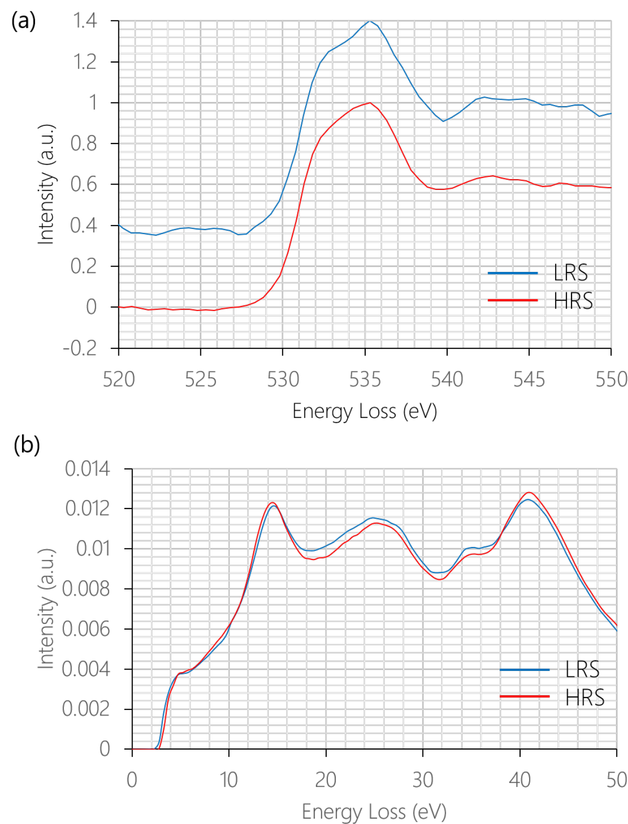

Figure 4.13: *Comparison of HRS (red) and LRS (blue) spectra extracted from the entire YSZ layer. Subfigures show the (a) O K-edge core-loss edge and (b) the YSZ low-loss spectra. In (a) the spectra were separated vertically for clarity.*

4.5 HAXPES Analysis

To understand changes to the electronic structure of YSZ and PCMO as a function of switching, collaborators at Jülich performed HAXPES both *in-operando* and on *ex-situ* devices that were programmed in advance. For pre-programmed devices, the photon energy was set to 3.2keV and a 5° grazing incidence allowed for simultaneous probing of ∼ 50 devices, meaning that the HAXPES analysis would average over local defects related to device fabrication.

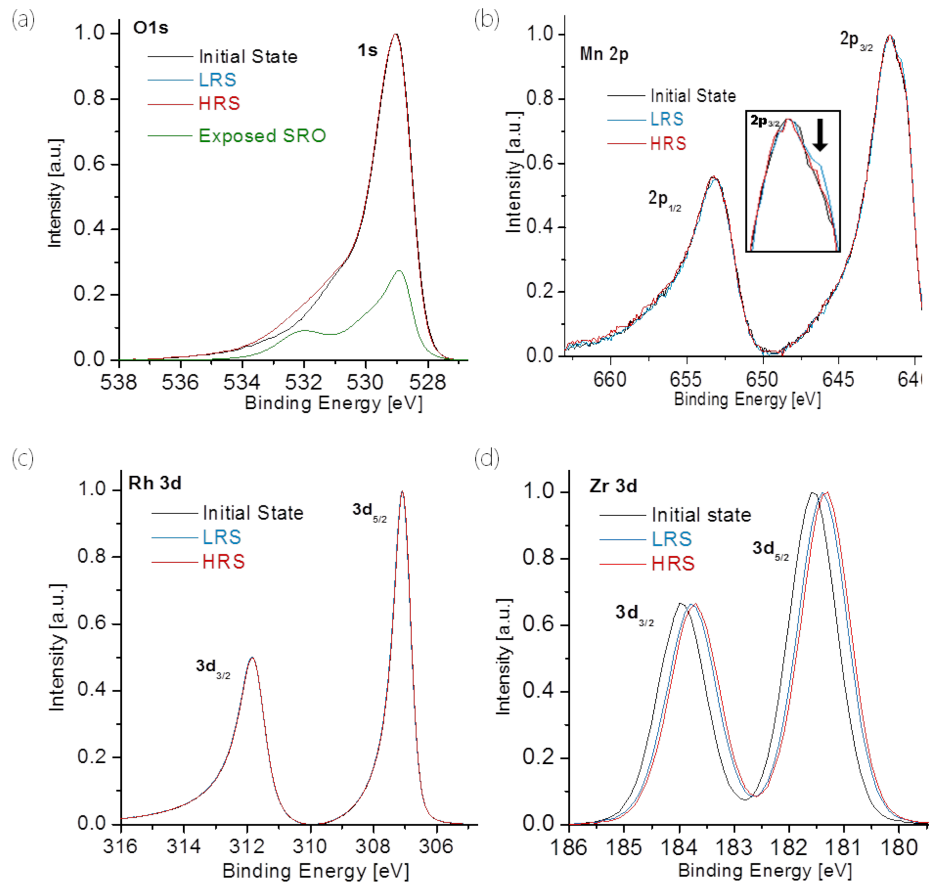

Figure 4.14: *HAXPES spectra showing (a) O-1s (b) Mn-2p (c) Rh-3d (d) Zr-3d for initial state (black) and HRS- (red) and LRS-programmed (blue) devices. An additional exposed SRO O1s peak is shown in (a).*

HAXPES spectra acquired from *ex-situ* programmed devices are shown in Fig.4.14. Fig.4.14(a) presents the O-1s peak, where no changes are seen between the LRS and HRS. Despite this, there is a notable difference in peak shape between the *initial* and programmed states: the change in shape at 532eV was attributed to the contribution from regions of exposed SRO bottom electrode, which, when probed individually, features

a high-energy shoulder at 532eV, as shown in green in Fig.4.14(a). However, the spectral weighting of the exposed SRO was expected to remain constant during the irradiation of programmed devices; evidence showing a change suggests that $V_{\ddot{O}}$-migration may occur from as far as the SRO bottom electrode. With regards to the Mn, HAXPES revealed subtle changes in the Mn-2p spectra between the HRS and LRS, which are shown in Fig.4.14(b): the low-energy shoulder on the Mn-$2p_{3/2}$ peak is weakened in the LRS, and strengthened in the HRS. This change is consistent with that observed via HAXPES in the literature, which suggests that the Mn closest to the exposed surface (which in our case is that at the YSZ/PCMO interface), is reduced in the HRS, and oxidised in the LRS [25]. Notably, the Zr-3d spectra (shown in Fig.4.14(d)) displayed significant changes as a function of switched state, where reproducible shifts in binding energy (of the order 0.1eV) were observed; these shifts were not observed for the Rh-3d peaks shown in Fig.4.14(c). As mentioned in Section 2.8, energy shifts of HAXPES peaks are indicative of charging effects in the material; the observation of shifts in the Zr-3d spectra but not the Rh-3d suggests that the charge build up in the YSZ was not due to the electrical charging of the Rh top electrode. In addition, the resistance states in Fig.4.14(d) correspond to shifts in Zr-3d binding energy such that the resistance states can be ordered IS>LRS>HRS. Critically, these shifts are interpreted as evidence for the build-up of electrostatic charge within the YSZ rather than a change in Zr oxidation state, because the latter would manifest as secondary features in the Zr-3d which were not observed. To investigate this charging effect further, HAXPES measurements of the Rh-3d and Zr-3d spectra were acquired *in-operando* for single devices during voltage sweeps, where a typical IV curve is shown in Fig.4.15(b). During biasing, the HAXPES spectra consistently moved to higher(lower) kinetic energies at negative(positive) bias, as shown in Fig. 4.15(c). To evaluate the shift in peak position with respect to the unbiased state, both spectra were fitted using Voigt and modified Donjach-Sunjich curves respectively [30]. These results are presented in Fig.4.15(d) and show that the Rh-3d peak shift is linear as a function of voltage, consistent with the HAXPES measurements acquired from the bulk array which show no change to Rh as a function of switching (Fig.4.14)(c). In contrast, the Zr-3d peak displays hysteresis consistent with the hysteresis of current exhibited in the IV curve acquired simultaneously, which

suggests a strong correlation between charge accumulation in the YSZ and overall electrical transport of the device. In addition, a remnant 0.2eV shift of the Zr-3d peak is evident at 0V, and is positive(negative) after a positive(negative) voltage sweep. These results are consistent with UNITY's proposed tunnel RRAM mechanism in which charge accumulation in the tunnel oxide governs the resistance state of the device [2] and that the retention measurements (Fig. 4.6) are in fact a measurement of the stability of the accumulated charge in the YSZ over time.

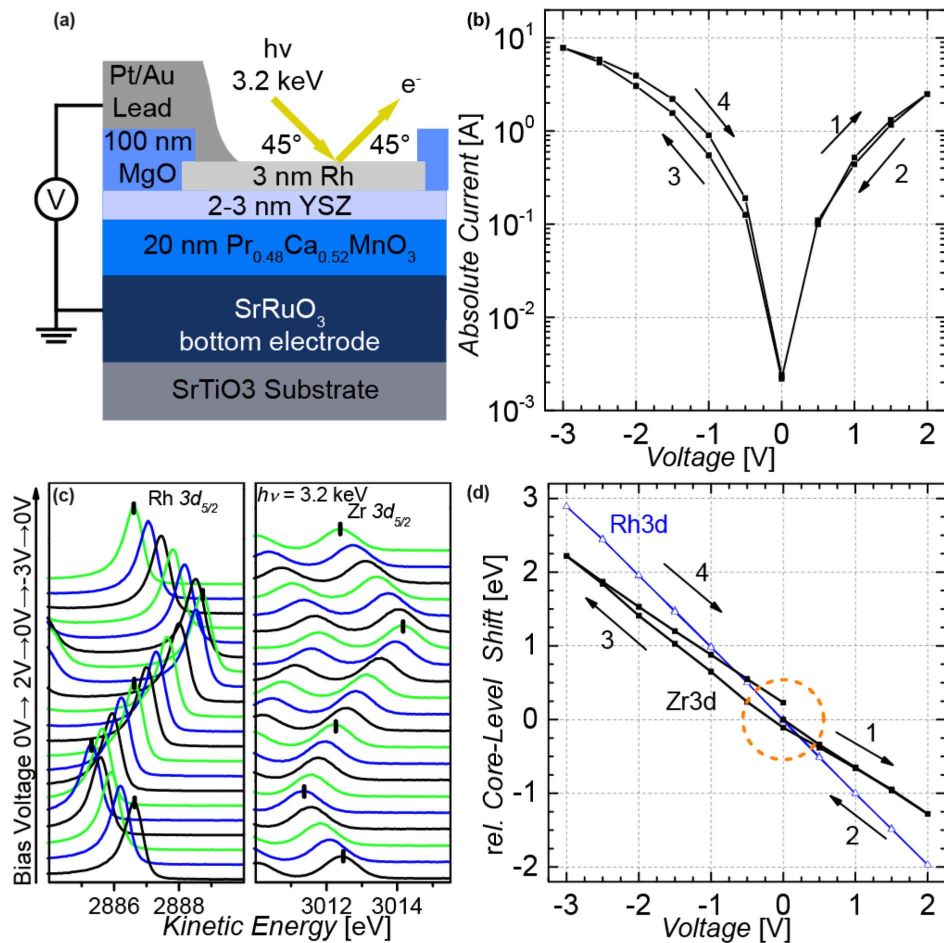

Figure 4.15: *(a) a schematic cross-section of the in-operando sample. (b) The IV-characteristics of a device measured in the UHV HAXPES chamber during collection of (c) Rh-3d$_{5/2}$ and Zr-3d–5/2 spectra using voltage sweep 0V→+2V→0V→-3V→0V. (d) The resulting peak shifts in the Zr-3d and Rh-3d peak positions are shown relative to the initial position, before a bias voltage was applied. The orange circle highlights the remnant peak shifts at 0V bias.*

4.6 Conclusion

Based on the electrical characterisation and spectroscopic analysis presented above, a charge-trapping, $V_{\ddot{O}}$-based mechanism behind the RS exhibited by crystalline PCMO tunnel-RRAM devices can be described.

EELS analysis of oxygen, manganese and praseodymium core-loss edges provided evidence for the field-induced exchange of $V_{\ddot{O}}$ across the YSZ/PCMO interface, which is expected for VCM RS. Specifically, through the analysis of peak position, shape and peak ratio, it was shown that in the HRS, Mn was more reduced than in the LRS within the vicinity of the YSZ/PCMO interface. It should be noted that the magnitude and spatial extent of this reduction varied across datasets, which were acquired from different positions along the YSZ/PCMO interface. This indicates that RS-induced interfacial redox is *inhomogeneous* despite showing area-scaling with top electrode area, which is a parameter often used in the literature to identify chemical homogeneity in RS. As stated above, at the YSZ/PCMO interface, an evaluation of chemical shift revealed that Mn had valence states ranging between Mn^{2+} and $Mn^{3.3+}$. In the dataset presented in section 4.4.2, at the YSZ/PCMO interface, the HRS was shown to contain reduced Mn^{2+}, whilst the LRS contained (relatively) oxidised $Mn^{2.3+}$, which is consistent with a change in the number of oxygen vacancies in $PCMO_{3-\delta}$ from δ =0.25 to δ =0.1 respectively. A comparison of the quantitative distributions of elements across the device for LRS- and HRS-programmed devices revealed the direction of $V_{\ddot{O}}$ migration and showed that typically, the HRS (achieved at positive bias), contained more O^{2-} in the YSZ than the PCMO and vice-versa for the LRS. This confirms that RS is governed by the *exchange* of $V_{\ddot{O}}$ between the YSZ layer and YSZ/PCMO interface. This exchange is consistent with that displayed by the IV curves in Section 4.3, which show that when the Rh top electrode is positively biased, it eventually switches to the HRS; according to the known direction of migration of charged species through an electric field, this RESET transition is due to the electromigration of positively charged $V_{\ddot{O}}$ from the YSZ into the PCMO, and conversely, the electromigration of negatively charged O^{2-} from the PCMO into the YSZ.

The simplified transport model presented in section 4.3 showed that the electrical

characteristics displayed by this heterostructure were comparable to that of a circuit comprising a tunnel barrier and a polaron hopping component connected in series, therefore, the effects of $V_{\ddot{O}}$-migration on both of these conduction mechanisms affect the electrical transport overall. In the literature, polaron hopping along Mn-O-Mn bonds in PCMO is *promoted* with the dissipation of $V_{\ddot{O}}$ (equivalent to the accumulation of O^{2-}), whilst the accumulation of *negatively charged* O^{2-} (equivalent to the dissipation of $V_{\ddot{O}}$) in the YSZ, which was supported by *in-operando* HAXPES results (section 4.5), causes an increase in the tunnel barrier height and *impedes* tunnelling through the YSZ. This means that for the same direction of $V_{\ddot{O}}$-migration, the tunnel barrier would become less resistive whilst the PCMO became more resistive, therefore tunnelling and polaron hopping are competing effects. Given that the devices switch to the HRS(LRS) at polarities that impede(promote) tunnelling, it is clear that electrical transport is ultimately governed by tunnelling through the YSZ, a conclusion that is further supported by the scaling of resistance states with tunnel oxide thickness.

Further EELS inspection of the YSZ tunnel barrier revealed a reproducible change in O K-edge ELNES between HRS- and LRS-programmed devices that was consistent with a $V_{\ddot{O}}$-induced change in the local bonding environment in the YSZ. This is consistent with the literature, which suggests that the electronic and structural properties of stabilized zirconia can be controlled by the structural disorder around the oxygen vacancies [45, 55]. Although not typically used to characterise RS device, the low-loss spectra acquired from YSZ layers within programmed devices showed differences in the electronic character of the YSZ, where the increased plasmon resonance in the LRS was consistent with a more metallic character.

Interestingly, using EELS, the praseodymium, which is typically not thought to be readily reduced or oxidised, showed evidence of reduction at the YSZ/PCMO interface. Whilst there is little literature on the topic, graduated changes to the shape of the Pr core-loss edge occurred in conjunction with graduated changes to the position, shape and peak ratio of the Mn core-loss edge. This evidence suggests that Pr may play some charge-compensation role during $V_{\ddot{O}}$-mediated RS, which has not been observed previously.

Considering all the datasets included in the study, it should be emphasised that,

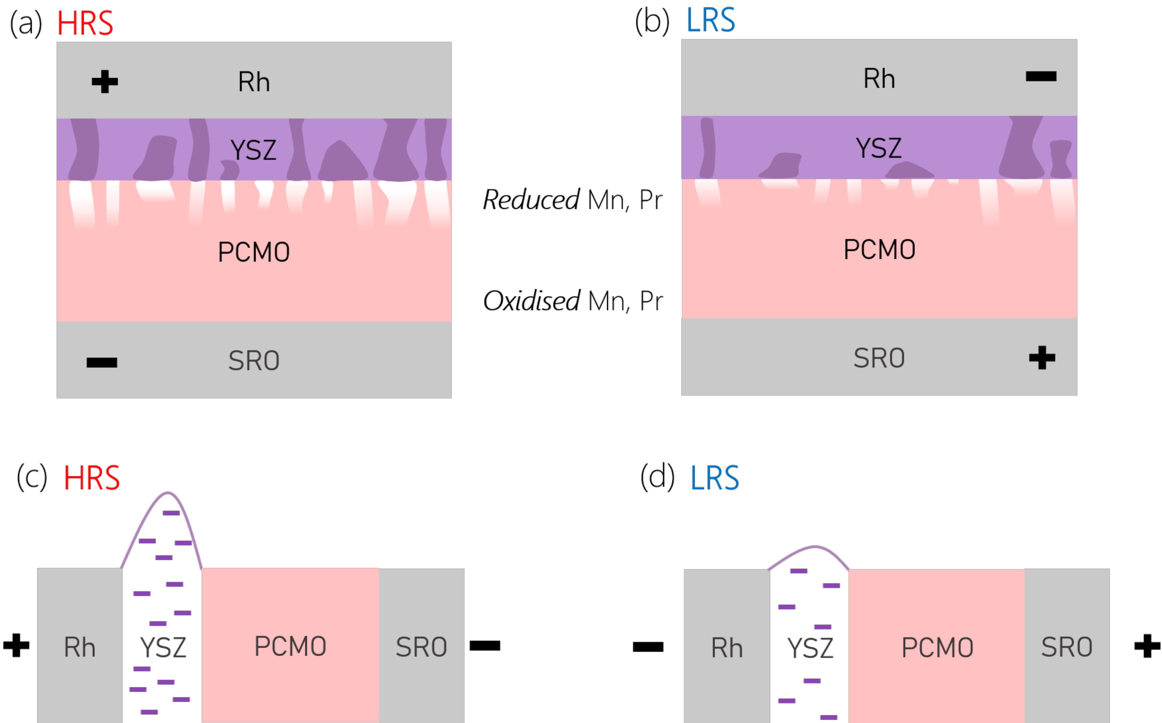

Figure 4.16: *Inhomogeneous VCM-based RS mechanism in PCMO tunnel-RRAM devices where (a) and (c) depict the HRS, whilst (b) and (d) is the LRS. For (a) and (b), $V_{\ddot{O}}$ in the PCMO are depicted as white, whilst the dark purple regions represent $V_{\ddot{O}}$-rich areas in the YSZ where the local bonding environment has changed w.r.t the bulk. For (c) and (d), the accumulation/dissipation of negative charge modulates the height of the tunnel barrier, which ultimately governs the overall resistance state if the device.*

with regards to the EELS analysis, the above stated changes did not occur to the same extent for each programmed resistance state. Instead, some effects, such as the valence state of Mn, were seen to vary in both magnitude and spatial extent at the YSZ/PCMO interface. This variation is depicted in Fig.4.16, where $V_{\ddot{O}}$ in the PCMO are shown in white and regions corresponding to local changes in bonding environment in the YSZ are shown in dark purple. The large change observed between HRS- and LRS-programmed devices seen in the O K-edge ELNES at the YSZ/PCMO interface (Fig.4.4.2) became extremely subtle when averaged over the entire YSZ layer (Fig.4.13), highlighting a degree of inhomogeneity within the YSZ layer which mirrors that seen at the interface for Mn. Despite this, electrical characterisation showed that RS was extremely reproducible. This suggests that although spatial inhomogenities may increase device variability in different RRAM heterostructures, in tunnel-RRAM, any such negative effects are minimised because, as emphasized in Fig.4.16(c) and (d), the *concentration* of $V_{\ddot{O}}$ in the YSZ governs RS and has greater impact on device performance than the

spatial distribution of $V_{\ddot{O}}$. This demonstrated lack of variability despite the presence of spatial inhomogeneities is an extremely valuable attribute when considering applications of tunnel-RRAM in memory storage, as it could mean that simpler (easier to fabricate) amorphous or polycrystalline materials systems could incorporate tunnel oxides for improved reproducibility.

Bibliography

[1] A. Sawa. Resistive switching in Transition Metal Oxides. *Materials Today*, 11(6):28–36, 2008.

[2] R. Meyer, L. Schloss, J. Brewer, R. Lambertson, W. Kinney, J. Sanchez, and D. Rinerson. Oxide dual-layer memory element for scalable non-volatile cross-point memory technology. *Proceedings - 2008 9th Annual Non-Volatile Memory Technology Symposium, NVMTS 2008*, (C):1–5, 2008.

[3] J. Zhu, H. Li, L. Zhong, P. Xiao, X. Xu, X. Yang, Z. Zhao, and J. Li. Perovskite oxides: Preparation, characterizations, and applications in heterogeneous catalysis. *ACS Catalysis*, 4(9):2917–2940, 2014.

[4] E. Grabowska. Selected perovskite oxides: Characterization, preparation and photocatalytic properties-A review. *Applied Catalysis B: Environmental*, 186:97–126, 2016.

[5] T. Goto, T. Kimura, G. Lawes, A. P. Ramirez, and Y. Tokura. Ferroelectricity and Giant Magnetocapacitance in Perovskite Rare-Earth Manganites. *Physical Review Letters*, 92(25):1–4, 2004.

[6] J. Sakai, A. Kitagawa, T. Tamada, M. Sakai, T. Hirao, and S. Iinai. Field Effect in Perovskite-Type Manganite Films on High-T_c Superconductor. 1(I):248–251, 2001.

[7] B. Lei, C. Li, D. Zhang, S. Han, and C. Zhou. Efficient synthesis and electronic studies of core-shell nanowires based on colossal magnetoresistive manganites. *Journal of Physical Chemistry B*, 109(40):18799–18803, 2005.

[8] E. Dagotto, T. Hotta, and A. Moreo. Colossal magnetoresistant materials: the key role of phase separation. *Physics Reports*, 344(1-3):1–153, 2001.

[9] D. C. Krishna and P. Venugopal Reddy. Magnetic transport behavior of nano-crystalline $Pr_{0.67}A_{0.33}MnO_3$ (A = Ca, Sr, Pb and Ba) manganites. *Journal of Alloys and Compounds*, 479(1-2):661–669, 2009.

[10] Z. B. Yan and J. M. Liu. Resistance switching memory in perovskite oxides. *Annals of Physics*, 358:206–224, 2015.

[11] R. Waser, R. Dittmann, G. Staikov, and K. Szot. Redox-Based Resistive Switching Memories - Nanoionic Mechanisms, Prospects, and Challenges. *Advanced Materials*, 21(25-26):2632–2663, 2009.

[12] M. J. Rozenberg, I. H. Inoue, and M. J. Sánchez. Strong electron correlation effects in nonvolatile electronic memory devices. *Applied Physics Letters*, 88(033510), 2006.

[13] D. Panda and T. Y. Tseng. Perovskite Oxides as Resistive Switching Memories: A Review. *Ferroelectrics*, 471(1):23–64, 2014.

[14] K. Shono, H. Kawano, T. Yokota, and M. Gomi. Origin of negative differential resistance observed on bipolar resistance switching device with Ti/$Pr_{0.7}Ca_{0.3}MnO_3$/Pt structure. *Applied Physics Express*, 1:0550021–0550023, 2008.

[15] Z. L. Liao, Z. Z. Wang, Y. Meng, Z. Y. Liu, P. Gao, J. L. Gang, H. W. Zhao, X. J. Liang, X. D. Bai, and D. M. Chen. Categorization of resistive switching of metal-Pr0.7Ca0.3MnO3-metal devices. *Applied Physics Letters*, 94(25):253503, 2009.

[16] L. Xinjun, K. Insung, S. Manzar, Md. S. Sharif, P. B. Kuyyadi, P. Sangsu, and H. Hyunsang. Resistive Switching Mechanism of a $Pr_{0.7}Ca_{0.3}MnO_3$-based Memory Device and Assessment of Its Suitability for Nano-scale Applications. *Journal of the Korean Physical Society*, 59(2):497, 2011.

[17] Daniele Ielmini. Interface-Type Switching. In A. Sawa and R. Waser, editors, *Resistive Switching: From Fundamentals of Nanoionic Redox Processes to Memristive Device Applications, 1*, chapter 16, pages 457–482. Wiley-VCH, 2016.

[18] F. Pan, S. Gao, C. Chen, C. Song, and F. Zeng. Recent progress in resistive random access memories: Materials, switching mechanisms, and performance. *Materials Science and Engineering: R: Reports*, 83:1–59, 2014.

[19] H. Lee, S. Choi, H. Park, and M. Rozenberg. A new route to the Mott-Hubbard metal-insulator transition: Strong correlations effects in $Pr_{0.7}Ca_{0.3}MnO_3$, volume = 3, year = 2013. *Scientific reports*, (April):1704.

[20] M. A. Peña and J. L G Fierro. Chemical structures and performance of perovskite oxides. *Chemical Reviews*, 101(7):1981–2017, 2001.

[21] J. Mizusaki. Nonstoichiometry, diffusion, and electrical properties of perovskite-type oxide electrode materials. *Solid State Ionics*, 52(1-3):79–91, 1992.

[22] S. Asanuma and H. Akoh. Relationship between resistive switching characteristics and band diagrams of Ti/Pr(1x)Ca(x)MnO(3) junctions. *Physical Review B*, 80:1–8, 2009.

[23] Y. Nian, J. Strozier, N. Wu, X. Chen, and a. Ignatiev. Evidence for an Oxygen Diffusion Model for the Electric Pulse Induced Resistance Change Effect in Transition-Metal Oxides. *Physical Review Letters*, 98(14):146403, 2007.

[24] S Schramm, J Hoffmann, and Ch Jooss. Transport and ordering of polarons in CER manganites PrCaMnO. *Journal of Physics: Condensed Matter*, 20(395231), 2008.

[25] A. Herpers, K. J. O'Shea, D. A. Maclaren, M. Noyong, B. Rösgen, U. Simon, and R. Dittmann. Competing strain relaxation mechanisms in epitaxially grown $Pr_{0.48}Ca_{0.52}MnO_3$ on $SrTiO_3$, volume = 2, year = 2014. *APL Materials*, (10):0–8.

[26] A. Herpers, C. Lenser, C. Park, F. Offi, F. Borgatti, G. Panaccione, S. Menzel, R. Waser, and R. Dittmann. Spectroscopic proof of the correlation between redox-state and charge-carrier transport at the interface of resistively switching Ti/PCMO devices. *Advanced Materials*, (26):2730–2735, 2014.

[27] K. Baek, S. Park, J. Park, Y. M. Kim, H. Hwang, and S. H. Oh. In-situ TEM observation on the interface-type resistive switching by electrochemical redox reactions at a TiN/PCMO interface. *Nanoscale*, 9(2):582–593, 2017.

[28] G. Knoner, K. Reimann, R. Rower, U. Sodervall, and H. E. Schaefer. Enhanced oxygen diffusivity in interfaces of nanocrystalline $ZrO_2Y_2O_3$, volume = 100, year =

2003. *Proceedings of the National Academy of Sciences of the United States of America*, (7):3870–3.

[29] J. Goff, W. Hayes, S. Hull, M. Hutchings, and K. Clausen. Defect structure of yttria-stabilized zirconia and its influence on the ionic conductivity at elevated temperatures. *Physical Review B*, 59(22):14202–14219, 1999.

[30] B. Arndt, F. Borgatti, F. Offi, M. Phillips, P. Parreira, T. Meiners, S. Menzel, K. Skaja, G. Panaccione, D. A. Maclaren, R. Waser, and Regina Dittmann. Spectroscopic Indications of Tunnel Barrier Charging as the Switching Mechanism in Memristive Devices. *Advanced Functional Materials*, 1702282, 2017.

[31] J. G. Simmons. Generalized Formula for the Electric Tunnel Effect between Similar Electrodes Separated by a Thin Insulating Film. *Journal of Applied Physics*, 34(6):1793–1803, 1963.

[32] L. Song-Lin, Z. L. Liao, J. Li, J. L. Gang, and D. N. Zheng. Resistive switching properties and low resistance state relaxation in Al/$Pr_{0.7}Ca_{0.3}MnO_3$/Pt junctions. *Journal of Physics D: Applied Physics*, 42(4):45411, 2009.

[33] J. A. Krogstad, M. Lepple, Y. Gao, D. M. Lipkin, and C. G. Levi. Effect of yttria content on the zirconia unit cell parameters. *Journal of the American Ceramic Society*, 94(12):4548–4555, 2011.

[34] J. Tikkanen, S. Kauhala, H. Huhtinen, and P. Paturi. Anomalous Thermal Expansion in (Pr,Ca)MnO3 Due to Orbital Ordering. *Physics Procedia*, 75:475–481, 2015.

[35] K. Iakoubovskii, K. Mitsuishi, Y. Nakayama, and K. Furuya. Thickness Measurements With Electron Energy Loss Spectroscopy. 631:626–631, 2008.

[36] L. Yao, S. Majumdar, L. Akaslompolo, S. Inkinen, Q. J. Qin, and S. Van Dijken. Electron-beam-induced perovskite-brownmillerite-perovskite structural phase transitions in epitaxial $La_{2/3}Sr_{1/3}MnO_3$ films. *Advanced Materials*, 26(18):2789–2793, 2014.

[37] Magnus Nord. *EELS and STEM studies of perovskite oxide heterostructures EELS and STEM studies of perovskite oxide heterostructures*. PhD thesis, Norwegian University of Science and Technology, 2016.

[38] M. Nord, P. E. Vullum, M. Moreau, J. E. Boschker, S. M. Selbach, R. Holmestad, and T. Tybell. Structural phases driven by oxygen vacancies at the $La_{0.7}Sr_{0.3}MnO_3/SrTiO_3$ hetero-interface. *Applied Physics Letters*, 106(4):0–4, 2015.

[39] J. Norpoth, D. Su, H. Inada, S. Sievers, Y. Zhu, and C. Jooss. Interfacial reconstruction and superconductivity in cuprate-manganite multilayers of $YBa_2Cu_3O_{7-\delta} and Pr_{0.68}Ca_{0.32}MnO_3$. *New Journal of Physics*, 14:0–15, 2012.

[40] M. Varela, M. P. Oxley, W. Luo, J. Tao, M. Watanabe, A. R. Lupini, S. T. Pantelides, and S. J. Pennycook. Atomic-resolution imaging of oxidation states in manganites. *Physical Review B - Condensed Matter and Materials Physics*, 79(8):1–14, 2009.

[41] H. Kurata, E. Lefevre, C. Colliex, and R. Brydson. Electron-energy-loss near-edge structures in the oxygen K-edge spectra of transition-metal oxides. *Physical Review B*, 47(20):13763–13768, 1993.

[42] M. Nord, P. E. Vullum, M. Moreau, J. E. Boschker, S. M. Selbach, R. Holmestad, and T. Tybell. Structural phases driven by oxygen vacancies at the $La_{0.7}Sr_{0.3}MnO_3/SrTiO_3$ hetero-interface. 041604(0003):1–4, 2015.

[43] D. A. Muller, N. Nakagawa, A. Ohtomo, J. Grazul, and H. Y. Hwang. Atomic-scale imaging of nanoengineered oxygen vacancy profiles in $SrTiO_3$. *Nature*, 430(August):657–661, 2004.

[44] I. M. Ross, W. M. Rainforth, A. J. Scott, A. P. Brown, R. Brydson, and D. W. McComb. Electron energy-loss spectroscopy (EELS) studies of an yttria stabilized TZP ceramic. *Journal of the European Ceramic Society*, 24(7):2023–2029, 2004.

[45] D. McComb. Bonding and electronic structure in zirconia pseudopolymorphs investigated by electron energy-loss spectroscopy. *Physical Review B*, 54(10):7094–7102, 1996.

[46]

[47] D. B. Loomer, T. A. Al, L. Weaver, and S. Cogswell. Manganese valence imaging in Mn minerals at the nanoscale using STEM-EELS. *American Mineralogist*, 92(1):72–79, 2007.

[48] J. Herrero-Martín, J. L. García-Muñoz, S. Valencia, C. Frontera, J. Blasco, a. J. Barón-González, G. Subías, R. Abrudan, F. Radu, E. Dudzik, and R. Feyerherm. Valence change of praseodymium in $Pr_{0.5}Ca_{0.5}CoO_3$. *Physical Review B*, 84(11):115131, 2011.

[49] J. Richter, A. Braun, A. S. Harvey, P. Holtappels, T. Graule, and L. J. Gauckler. Valence changes of manganese and praseodymium in $Pr_{1-x}Sr_xMn_{1-y}In_yO_3\delta$ perovskites upon cation substitution as determined with XANES and ELNES. *Physica B: Condensed Matter*, 403:87–94, 2008.

[50] S. Valencia and G. Subías. Valence change of praseodymium in $Pr_{0.5}Ca_{0.5}CoO_3$ investigated by x-ray absorption spectroscopy. 2017.

[51] Pedro Parreira. *Nanocharacterisation of zirconia based RRAM devices deposited via PLD*. PhD thesis, University of Glasgow, 2015.

[52] S. Ostanin, A. J. Craven, D. W. Mccomb, D. Vlachos, A. Alavi, M. W. Finnis, and A. T. Paxton. Effect of relaxation on the oxygen K-edge electron energy-loss near-edge structure in yttria-stabilized zirconia. *Physical Review B*, 62(22):728–735, 2000.

[53] S. Ostanin, A. J. Craven, D. W. McComb, D. Vlachos, D. Vlachos, A. Alavi, A. T. Paxton, and M. W. Finnis. Electron energy-loss near-edge shape as a probe to investigate the stabilization of yttria-stabilized zirconia. *Physical Review B - Condensed Matter and Materials Physics*, 65(22):2241091–2241099, 2002.

[54] S. Kobayashi, A. Yamasaki, and T. Fujiwara. Electronic Structure and Dielectric Properties of Cubic Zirconia. *Japanese Journal of Applied Physics*, 42(Part 1, No. 11):6946–6950, 2003.

[55] S. Fabris, A. T. Paxton, and M. W. Finnis. A stabilization mechanism of zirconia based on oxygen vacancies only. *Acta Materialia*, 50(20):5171–5178, 2002.

CHAPTER 5

Summary and Outlook

In this work, the mechanisms of resistive switching in pulsed laser deposited transition metal oxide thin film RRAM heterostructures were investigated using TEM-EELS. In both the polycrystalline ZnO-based devices (presented in Chapter 3) and the single crystal epitaxial PCMO device (presented in Chapter 4), RS was mediated by the exchange of $V_{\ddot{O}}$ between the bulk switching material and an interfacial oxide. $V_{\ddot{O}}$-mediated switching devices are traditionally classified as VCM-type [1]. However, the work presented here demonstrates that this is a relatively broad categorisation because these devices do not necessarily switch via the same mechanism. For instance, in Chapter 3, $V_{\ddot{O}}$-electromigration mediated the formation and dissolution of highly resistive TiO_2 at the interface between the bulk [Mn:]ZnO and the electrochemically active Ti top electrode. In contrast, in Chapter 4, $V_{\ddot{O}}$-electromigration mediated the charge accumulation and dissipation within an interfacial dedicated tunnel oxide, which modulated the tunnel barrier height. Interestingly, this RS mechanism has similarities with the charge-storage-based memory technology it attempts to replace, flash memory.

With regards to the tunnel oxide RS mechanism, there is no specific terminology consistently used across the field of RRAM research. This is, in part, due to the fact that RS can be produced in an extensive range of materials incorporated into basic MOM devices, which initially led to the publication of a large number of studies that

focused on the observation and categorisation of RS rather than the development of our understanding of the switching mechanism itself. One of the primary motivations for this work was to improve upon our understanding of switching mechanisms specifically by using HAXPES and TEM-EELS to evaluate the contribution of electrical and chemical effects to the observed RS in both basic and novel metal-oxide RRAM architectures. In Chapter 3, a simplistic MOM Pt/Mn:ZnO/Ti device was fabricated locally via PLD, which allowed control over nanoscale structural and chemical characteristics. This materials system was of great interest: a similar pulsed laser deposited multifunctional device had recently been shown to display simultaneous co-switching of resistance and magnetisation, an effect attributed to the redistribution of $V_{\ddot{O}}$ and ferromagnetic ordering of local Mn-clusters [2]. Their proposed mechanism was based on the results of XPS depth profiling, an inherently destructive process with relatively low spatial resolution. Here, high spatial and energy resolution EELS was used to investigate their proposed mechanism and, in general, our analysis was consistent with their proposal, showing direct evidence of Mn-clustering along $V_{\ddot{O}}$-rich grain boundaries. In Chapter 4, a more complex epitaxial perovskite oxide tunnel RRAM device, fabricated via PLD by collaborators, was investigated. The motivation behind this particular materials system was two-fold: firstly, epitaxial single crystal devices are the closest physical representation of an ideal device, where defects and spatial inhomogeneities are minimised and sharp interfaces allow for an unobstructed assessment of interfacial chemistry; secondly, the incorporation of a dedicated tunnel oxide had been shown to allow control over the current density, which meant that this device could be tailored according to technology requirements [3]. Quantitative EELS analysis of *ex-situ* programmed devices confirmed the exchange of $V_{\ddot{O}}$ between the tunnel oxide and PCMO and showed that at the interface, the resultant redox activity may not have only affected the oxidation state of the manganese, but also the praseodymium, which is not typically thought to be readily oxidised or reduced. The device exhibited top-electrode area scaling, which is typically thought to indicate the occurrence of homogeneous redox activity at a given interface. Here, an evaluation of manganese oxidation states along the sharp PCMO/tunnel oxide revealed that this redox activity was, in fact, inhomogeneous. An accurate evaluation of the homogeneity of interfacial effects is of utmost importance for the progression

of RRAM research and its mainstream implementation. For instance, for VCM-type devices the nanoscale inhomeogenity of redox activity may act to limit the minimum cell size that can be reliably cycled during RS. Therefore, spatially resolved spectroscopic investigations, such as those presented here, are crucial for understanding and furthering the scalablity of RRAM.

In addition to the lack of consistency in the terminology used to described RS, there is also a lack of clarity with regards to the methodology of electrical characterisation, which has slowed progression in the field. This was discussed in Chapters 1 and 3, which commented upon the impact the early observations of electroforming SET processes have had on the methodology of electrical characterisation in RRAM research. In particular, it was suggested that the anticipation of such a forming step has influence experimentalists to promote filamentary switching, which is often observed after such a process, above other potentially viable switching mechanisms. Whilst filamentary switching tends to yield greater resistance windows than interfacial switching, the electroforming SET processes is often coupled with high compliance currents and can lead to device damage, limiting the reproducibility of the observed RS. Even in the absence of and electroforming processes, few RS-mechanism-focused studies comment on the specific electrical characterisation approach used to generate reproducible RS or that which led to device failure. The ArC ONE memristor characterisation platform was produced by researchers at the University of Southampton and Imperial College London in efforts to standardise this approach [4]. The platform lets users to probe 32×32 crossbar arrays of two-terminal devices and so can be used across all the emerging non-volatile memory technologies presented in Chapter 1. One of its key features is its pulsed programming routine, which, step-by-step, slowly increments the voltage applied across each device and stops when a benchmark resistance level is reached, limiting device damage and permitting multistate RRAM characterisation. The growing use of technologies like the ArCONE will allow for the characterisation of switching effects that may not have otherwise been observed and will also push researcher to improve clarity with regards to electrical characterisation methodology across the field RRAM research.

Aside from electrical characterisation, there has been progress in the field *in-situ* spectroscopic characterisation of RRAM devices [5]. These investigations involve probing

of the device during electrical cyclying allow for the unambiguous attribution of effects such as chemical changes or charging to the electrical probing of the device. An example of this was performed by collaborators in Chapter 4 through HAXPES. However, locally, it was not possible to perform *in-situ* EELS characterisation of lamellae. This was largely due to time constraints and challenges regarding FIB-assisted *in-situ* lamella design. However, the design and implementation of *in-situ* switchable lamellae remains a viable option for future work.

For RRAM devices to be implemented into mainstream memory storage technologies, they must be CMOS compatible and relatively easy to fabricate. Of course, these requirements eliminate the complex epitaxial perovskite oxide structure studied in Chapter 4 which required the use of PLD, a technique that is not suited for large scale industrial applications due to its relatively slow deposition rates and its small deposition area. Despite this, the study uncovered the benefits of tunnel oxide layer incorporation: it demonstrated that the tunnel barrier allowed for the control of current density and that charge accumulation dominated the overall resistance state of the device, suggesting that the negative impact of the inhomogeneous interfacial redox activity, or, potentially, a rough interface, may be minimised in tunnel RRAM devices. Based on this, it is clear that the electrical characterisation and spectroscopic investigation of novel *CMOS-compatible tunnel RRAM* devices would be of great interest in the field in the future. Although (CMOS-compatible) [Mn:]ZnO was also deposited via PLD, it is possible to deposit these polycrystalline oxides via techniques more suited for large-scale industrial application, such as magnetron sputtering, which makes CMOS-compatible tunnel RRAM an excellent candidate for research. Whilst there is currently relatively little interest in tunnel RRAM, due to the wealth of research and spectroscopic studies in particular, such as those presented in this work, CMOS-compatible resistive memories are already in the process of being introduced to the memory storage market: in 2015 Intel and Micron embarked on a collaborative commercial project to produce '3D X-point memory', a transistor-less 3D cross-bar memory cell array (like that depicted in Fig.1.7) in which memory storage is based upon a change in the resistance of the memory cell [6]. 3D X-point currently remains in development [6]. As no further details have been released, one can only speculate as to which of the emerging resistive non-volatile technologies is employed.

However, considering its description, it is possible that 3D X-point technology is the first commercial implementation of RRAM since its conception in 1971 [7]. Given the studies presented in this work, which uncovered issues including nanoscale inhomogeneities in interfacial redox activity and the unexpected presence multiple redox-formed oxides within the heterostructure, it is likely that the development of 3D X-Point will not be released any time soon. Further research must be undertaken to fully characterise and minimise these effects, such as that undertaken in this work, to improve the device resistance windows and cycling durability to commercial standards.

Bibliography

[1] R. Waser, R. Dittmann, G. Staikov, and K. Szot. Redox-Based Resistive Switching Memories - Nanoionic Mechanisms, Prospects, and Challenges. *Advanced Materials*, 21(25-26):2632–2663, 2009.

[2] S. Ren, J. Dong, W. Chen, L. Zhang, J. Guo, L. Zhang, J. Zhao, and X. Zhao. Study on the oxygen vacancy redistribution and the mechanism of electrical manipulation of ferromagnetism in diluted magnetic oxides. *Journal of Applied Physics*, 118(23):233902, 2015.

[3] R. Meyer, L. Schloss, J. Brewer, R. Lambertson, W. Kinney, J. Sanchez, and D. Rinerson. Oxide dual-layer memory element for scalable non-volatile cross-point memory technology. *Proceedings - 2008 9th Annual Non-Volatile Memory Technology Symposium, NVMTS 2008*, (C):1–5, 2008.

[4] Radu Berdan, Alexander Serb, Ali Khiat, Anna Regoutz, Christos Papavassiliou, and Themis Prodromakis. A μ-Controller-Based System for Interfacing Selectorless RRAM Crossbar Arrays. *IEEE Transactions on Electron Devices*, 62(7):2190–2196, 2015.

[5] A. Zintler, U. Kunz, Y. Pivak, S. U. Sharath, S. Vogel, E. Hildebrandt, H. J. Kleebe, L. Alff, and L. Molina-Luna. FIB based fabrication of an operative Pt/HfO2/TiN device for resistive switching inside a transmission electron microscope. *Ultramicroscopy*, 181:144–149, 2017.

[6] ITRS. Beyond CMOS. *International Technology Roadmap for Semiconductors*, (2.0), 2015.

[7] L. O. Chua. Memristor: The Missing Circuit Element. *IEEE Transactions on Circuit Theory*, 18(5):507–519, 1971.